Fundamentals for the Dimensioning and Optimization of Prestressed Segmented Girders for Application in Bridge Crane Systems

Zur Erlangung des akademischen Grades eines

DOKTORS DER INGENIEURWISSENSCHAFTEN (Dr.-Ing.)

von der KIT-Fakultät für
Maschinenbau
des Karlsruher Instituts für Technologie (KIT)

genehmigte

DISSERTATION

von

M.Sc. Jan Oellerich
geb. in Hamburg

Zusammenfassung

Brückenkrane sind ein wichtiger Vertreter der Unstetigförderer und werden vornehmlich im industriellen Umfeld eingesetzt. Sie ermöglichen die Bewegung von hohen Transportlasten innerhalb eines definierten Arbeitsbereichs. Neben der Laufkatze spielt die sogenannte *Kranbrücke* eine zentrale Rolle in der Gesamtkonstruktion. Mit zunehmender Spannweite und Traglast nehmen auch die Abmessungen der Kranbrücke zu. Damit trägt sie den größten Teil zum Gesamtgewicht des Krans bei, woraus sich das Bestreben ergibt, im Rahmen von Optimierungsansätzen weitere Gewichtseinsparungen zu erzielen. Es müssen definierte Randbedingungen eingehalten werden, die weitgehend durch standardisierte Regelwerke vorgegeben sind. Kern dieser Arbeit ist die Konstruktion eines neuartigen Brückenkransystems, das aus einzelnen Segmenten besteht und durch ein Zugmittel exzentrisch vorgespannt wird. In diesem Zusammenhang ist es notwendig, zusätzliche Randbedingungen zu ermitteln, die durch die bestehenden Regularien nicht abgedeckt sind. Grundlage hierfür ist die Ableitung eines geeigneten mechanischen Ersatzmodells, das die Eigenschaften des Systems mit hinreichender Genauigkeit beschreibt. Anschließend können die Randbedingungen in ein Optimierungsproblem überführt werden. Dazu werden Lösungsverfahren entwickelt, die dazu dienen, die neuartigen Kranbrückenträger vor dem Hintergrund ihres Eigengewichts zu optimieren. Der Fokus dieser Doktorarbeit liegt somit auf der Erarbeitung der theoretischen Grundlagen zur Beschreibung des mechanischen Verhaltens und der Optimierung von vorgespannten, segmentierten Trägern für den zukünftigen Einsatz in Brückenkrananlagen.

Abstract

Bridge cranes are widely used as discontinuous material handling systems in industrial environments. They enable the movement of high transport loads within a defined working area. In addition to the traveling trolley, the so-called *crane bridge* plays a central role in the overall construction. With increasing span widths and load capacities, the dimensions of the crane bridge also increase. Thus, it contributes the major part to the total weight of the crane, which results in the effort to achieve further weight savings within the scope of optimization approaches. Defined boundary conditions must be met, which are largely determined by standardized regulations. The core of this work is the design of a new type of bridge crane system, which consists of individual segments and is eccentrically pretensioned by a tensile member. In this context, it is necessary to identify additional boundary conditions which are not covered by the existing rules and regulations. The basis for this is the establishment of a suitable mechanical substitute model, which describes the properties of the system with sufficient accuracy. Subsequently, the constraints can be transformed into an optimization problem. For this purpose, a solution method is developed which serves to optimize the novel crane bridge girders against the background of their self-weights. Hence, the main focus of this doctoral thesis is the development of the theoretical basis for the description of the mechanical behavior and the optimization of prestressed, segmented girders for future application in bridge crane systems.

Danksagung

auch meinem ehemaligen Physiklehrer Herrn GERHARD RAUSCH herzlich danken. Durch sein Engagement wurde in mir die Begeisterung für die Mathematik und Physik geweckt, die ausschlaggebend für den Beginn des Maschinenbaustudiums nach dem Abitur war.

Abschließend möchte ich einem ganz besonderen Menschen, meiner Partnerin ALEXANDRA MIFTIKHITDINOVA, danken. Sie hat nie an mir gezweifelt und mich auch in den schwierigsten Phasen immer wieder aufgebaut und mir Mut zugesprochen. Ihr ist es zu verdanken, dass ich durch ihre Inspiration, ihren Rückhalt und ihre Geduld die notwendige Kraft und Ausdauer habe aufbringen können, um diese Arbeit zu verfassen. Danke, dass Du bei mir bist.

Karlsruhe, im Juli 2021 *Jan Oellerich*

Table of Contents

List of Figures

List of Tables

1 Introduction

Paths are made by walking.

- F. KAFKA

In the course of increasing globalization, economic interdependencies between states are growing and with them the trade of goods. More and more goods have to be transported, which requires the construction of more intralogistic systems. These include production facilities, port facilities or distribution centers. In this context, intralogistics describes not only the physical flow of materials and goods but also their organization, execution and control within a defined company site [12, p. 6]. For goods handling, elements must be provided that are capable of moving them. In the field of material handling, these technical devices are primarily divided into continuous and discontinuous conveyors. Whereas continuous conveyors operate continuously over a longer period of time (as is the case with bulk material transport), discontinuous conveyors are characterized by discontinuous working cycles. This means that a load cycle is usually followed by an empty cycle [13, p. 3].

Cranes, together with floor conveyors, form a significant group of representatives of discontinuous conveyors, which can move goods in a limited working area. They enable the transport of heavy loads and are assigned to different groups depending on their design. The so-called *bridge crane* is often used for handling unit loads in, for instance, assembly halls as well as workshops and is one of the most widespread crane designs. It plays a central role in this work. With the increasing span width, the requirements in terms of manufacturing as well as transportation from the production site to the desired place of operation increase. Sufficient space must be available for the production, as the crane usually passes through various stations during its manufacturing. In addition,

the large dimensions and the resulting weight may require heavy-duty transport [14, p. 228].

The analysis of the challenges mentioned above resulted in the idea of developing a new type of bridge crane system at the Institute for Materials Handling and Logistics (IFL) of the Karlsruhe Institute of Technology (KIT), based on the approach of assembling the crane from standardized individual parts and connect them by means of tension and compression. The advantage of this is that the dimensions of the individual parts on one hand reduce the manufacturing effort and that they can be transported more easily (on EUR-pallets for example) on the other hand. By applying the axial force, the initially loose joints are pressed together. Only by this pretensioning the structure is able to transfer bending moments and shear forces, which is essential for a safe operation. Here, the crane bridge is designed as a truss with tie rods running in the hollow profiles of the upper and lower chord, with which the required pretensioning forces can be transmitted to the joints via stop pieces. With the help of a prototype it could be shown that the use of such a concept is conceivable. The system also offers the possibility of being upgraded to a modular system, in order to extend the use of the available components to a broad spectrum with regard to the span widths and load capacities to be achieved [3].

In contrast to the concept mentioned previously, the use of an *eccentrically* prestressed beam structure is to be investigated in the present work. The concept envisages for the beam to be composed of different uniform segments, which are then pressed together by pretensioning a tensile member that is eccentrically located with respect to the centroid axis. In analogy to the truss construction method, the joints are thus closed by means of form closure and the structure is capable of transmitting bending moments. In this connection, several components come into operation which fulfill different functions. Of particular interest is the development and application of design regulations combined with the desire of a construction of minimum weight.

1.1   Problem Description

The economic implementation of a new crane concept requires the existence of dimensioning regulations that provide recommendations for the design and thus enable safe operation of the crane. In this context, the system must be able to withstand the loads occurring during operation. This includes, in particular, compliance with strength and temperature limits as well as the avoidance of elastic instability of the components involved. The external load effects lead in turn to loads on the structure and thus to stresses on the used material. These can be roughly divided into static and dynamic loads.

For conventional crane systems, the standard norm DIN EN 13001-3-1 provides the basics for dimensioning, but this does not cover, for instance, the additional use of traction equipment in order to apply the necessary pretensioning forces. Therefore, the problem arises that no investigations or findings regarding the mechanical dimensioning of such a new type of system have been made so far. It also remains to be clarified which failure mechanisms can occur and which additional constraints must be considered within the design in comparison to conventional bridge crane girders. Furthermore, questions regarding a simultaneous weight optimization during the design of this new type of structure used remain unanswered so far as well.

This leads to several central questions that are to be answered within the framework of this doctoral thesis.

1. How can an eccentrically prestressed girder in segmented construction be designed and what functions do the individual components perform?

2. How can a suitable dimensioning procedure be designed that leads to solutions which meet both the defined constraints and are of minimum weight?

3. With what quality can a local minimum be approximated by the developed methods?

These risen questions form the basis for the doctoral thesis. On the one hand, the answers to these should close current research gaps and on the other hand lay the foundation for future research activities.

1.2 Scope and Structure of the Doctoral Thesis

Both the analysis and the subsequent answering of the questions mentioned in the previous section require a systematic approach. In addition, due to the prevailing complexity and the large scale of the problem, the scope of action must be limited to a defined framework in order to enable reliable statements.

1.2.1 Structure

The presented work is divided into seven chapters, which build on each other chronologically and in terms of content. This ensures a targeted and comprehensible treatment of the questions.

In the first chapter, the central problems are first formulated and the framework of the doctoral thesis is defined. The following chapter 2 reviews the state of the art, with a focus on the use of segmented and prestressed structures and the findings to date. In this connection, basics of engineering mechanics and current design regulations in crane construction are provided. The field of the structural optimization of box girder profiles is also one of the relevant aspects in the literature research. Here, the selected strategies and the underlying constraints are to be mentioned in particular. Furthermore, the term *optimization* used for the work is additionally specified in more detail.

The description of the reference structure to be investigated and the components used forms the core of the third chapter and aims to answer the first research question. The possible segmentation strategies as well as the structure of the segmented girder are explained. The assumptions made in this context are furthermore the starting point for the subsequent modeling.

In chapter 4, the development of constraints by means of analytical models which are to be met by the segmented girder are described. They are mandatory for the mathematical formulation of the underlying optimization problem. The solution approach is then developed in the subsequent chapter 5 and provides answers to the second research question. In addition, appropriate parameter settings can be identified which lead to most suitable solutions in terms of approximation of the local minimum. Then, the third research guiding question can be answered as well.

Chapter 6 additionally deals with the concrete application of the developed methods, focusing on the investigation of their suitability for practical implementation. The calculated profiles are validated in FE analyses using the ABAQUS$^{©}$ code and verified for compliance with the previously defined constraints. In addition, design notes can be derived by means of detailed studies of the structural behavior under the defined loads.

In the seventh and final chapter of the doctoral thesis, the major findings of the work are summarized. In an outlook, future research topics and related questions in the field of prestressed segmented support structures are outlined, whereby the contents and results of this thesis form the basis.

1.2.2 Scope of the Thesis

As the title of the thesis indicates, the main task of the doctoral thesis is to develop the fundamentals that should be applied to design an eccentrically prestressed girder in segmented construction with simultaneous weight optimization. Since the entire spectrum of this research field is both of high complexity and extremely extensive, restrictions must be made so that the work and the associated answers to the research questions remain manageable.

For this reason, the mechanical problems mentioned are restricted to the field of elastostatics, which focuses on elastic deformation on the one hand and on the mechanical stresses occurring on the other. Accordingly, only elastostatic problems are considered and those of dynamics

are neglected. Furthermore, contact problems that rise are marginally taken into account in order to include them in the procedures. This also covers the consideration of possible stability problems and the phenomena of local load application. The main focus is the global behavior of the structure, especially the avoidance of excessive deflections and material yielding.

For the construction of a prestressed girder in segmented design, the use of only one eccentrically mounted tensile member running inside the segments is taken into account. It can be assumed, that the extension of the structure to several parallel arranged tensile members with the same bases can be carried out. However, further constraints must be defined, such as the consideration of the additional space requirement.

The prestressed structure is also limited to a single-girder design, i.e. the trolley travels on only one girder, although double-girder designs are generally also conceivable. Furthermore, it is assumed that the structure is used in a covered system (e.g. in an assembly hall), i.e. additional influences such as weather conditions or stochastically distributed loads caused by the occurrence of wind loads in outdoor operation are neglected and therefore not considered in the design. This is also accompanied by the fact that a constant room temperature level is assumed and thus changes in the axial force due to temperature-related expansions are ignored.

2 Basics and State of Research

*One never notices what has been
done, one can only see what remains
to be done.*
- M. Curie

In the course of the investigation of the state of research, section 2.1
first introduces the *bridge crane* as well as its involved components and
the currently applied dimensioning regulations. In this context, a short
aggregation of the fundamentals of engineering mechanics relevant for
the work serves to introduce important concepts and principles (section
2.2).

On this basis it is necessary to clarify whether applications already exist
where a crane girder composed of different segments is used. The focus
here is on the use of a traction device mounted eccentrically to the
centroid axis of the main beam and the possibility of non-destructive
dismantling of the crane bridge.

Based on these findings, the current research results regarding the gen-
eral use of eccentrically prestressed beams will be discussed in more
detail in the following section 2.3.1 to identify possible interfaces to the
topic of the thesis. In this connection, it is of particular interest, which
types of tension means are selected and which modeling strategies are
applied. Here, it also will be examined whether structural optimization
approaches have already been undertaken and which constraints have
been defined in these cases.

The subject of structural optimization plays an important role in the
present work and is to be defined terminologically first. Subsequently,
it is mandatory to analyze the field of optimization of geometric cross-
sectional quantities in crane construction, see section 2.4. Here, the

selected optimization strategies and the corresponding constraints are in the foreground as well.

A short summary at the end of chapter 2 gives an overview of the collected findings. The prevailing research gap can be identified and a delimitation to the current state of research can be made.

2.1 Bridge Crane Systems

The bridge crane is a classic material handling system for moving heavy loads. Despite the large number of possible applications, these usually have the same basic structure. The single elements that play a central role within a bridge crane system are explained in section 2.1.1. In order to be able to guarantee a safe operation, dimensioning regulations are used in this context, which provide assistance in the design of the individual components. Those are discussed more in detail in section 2.1.2.

2.1.1 Configurations and Components

The essential components of a bridge crane system include the *crane bridge* (main girder), the *endcarriages*, in which the wheels of the crane trolley are mounted and run on the crane runways, and the *traveling trolley* that can travel along the girder. By moving the trolley, the position of the hoisting cable is changeable and thus loads can be attached within the defined working range of the crane. In general, there are two dominating bridge crane types available:

- single beam bridge cranes and

- double beam bridge cranes.

These are depicted in figure 2.1 together with the involved elements. Usually, the girders of single beam bridge cranes are designed as rolled-steel joists, such as I-shaped beams, for working loads up to $12.50\,\text{t}$ and span widths up to $12.00\,\text{m}$ or welded box girders while these are

Single beam bridge crane

Traveling trolley   Crane runway

Double beam bridge crane   Main girder(s)

Hoisting
cable

Endcarriage
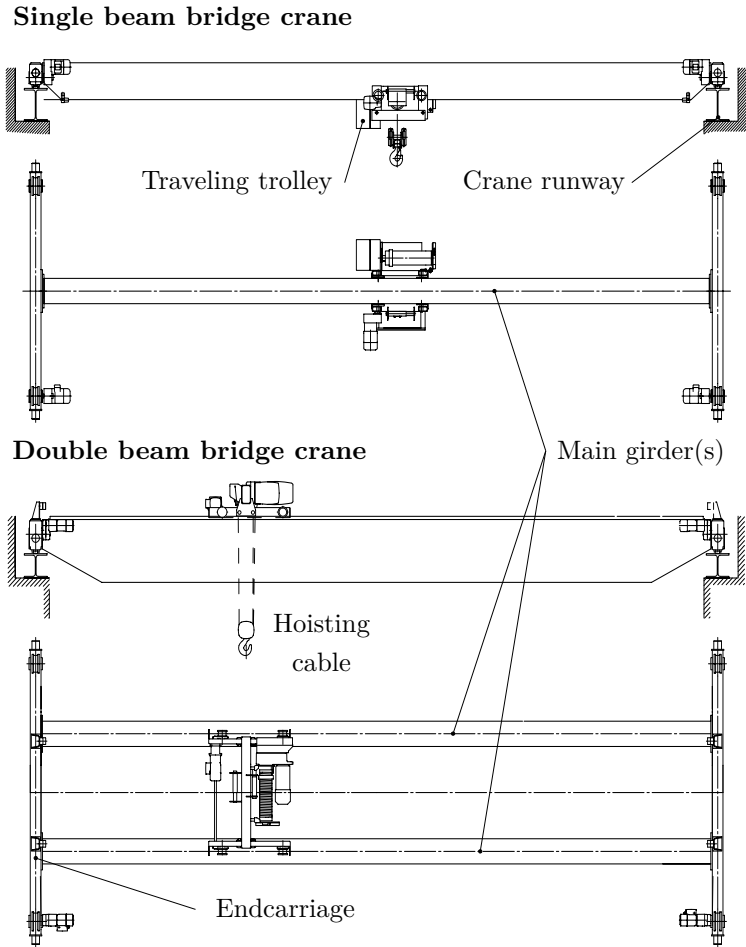
Figure 2.1: Common configurations of bridge crane systems [1, p. 8]

especially applied for high working loads and large span widths. In
addition, they offer the advantage of comparatively simple manufactur-
ing and lightweight construction [13, p. 131–132]. The main differences
in geometry of the geometric properties between the mentioned girder

9

types are shown in figure 2.2. Owing to the closed form, box sections

I-shaped girder   **Box section girder**
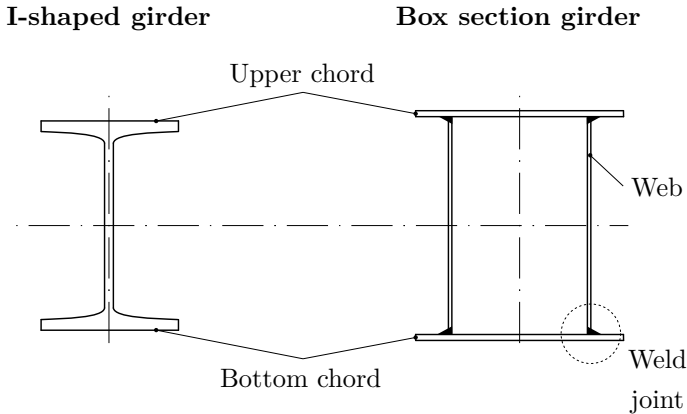
Figure 2.2: Dominating cross-sections in bridge crane systems

possess a high torsional stiffness and are more resistant to *torsional flexural buckling*[1] compared to open profiles, such as I-shaped girders. Nevertheless, they are vulnerable to *plate buckling* due to the relatively thin web plates, see figure 2.3. In this context, failure modes of elastic stability can be divided into *global* and *local* failures where global means that the entire structure deflects while local failures only lead to deflections of the respective failed regions or components. Here, especially thin axially loaded plates are at risk of local buckling. This important aspect must be taken into account and for this reason the profiles are usually reinforced in the boxes with both welded-in bulkhead plates and buckling stiffeners [13, p. 131]. The phenomena of elastic behavior and stability are discussed more in detail in section 2.2.

2.1.2 Applied Dimensioning Regulations

In the previous section 2.1.1 it was already pointed out that failures in terms of elastic stability might occur during operation. Besides elastic

---

[1] Variant of elastic stability failure.

Global deflection of the beam
(torsional lateral buckling)

Local deflection of the
web plate due to high axial load
(buckling of plates)
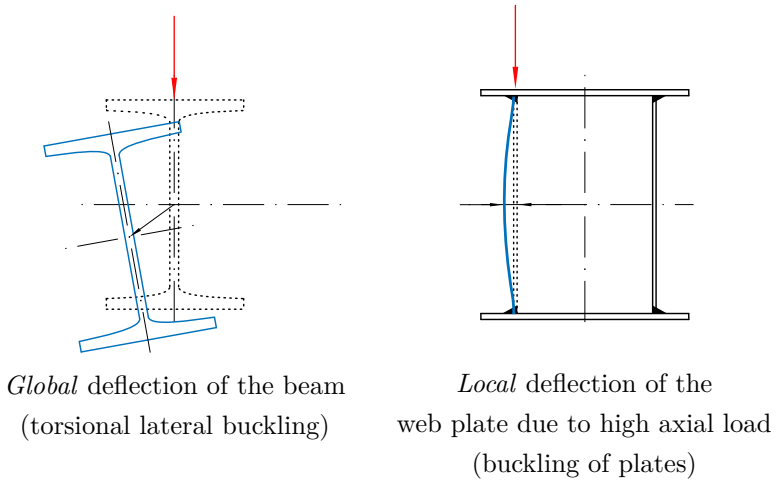
Figure 2.3: Failures of elastic stability of the considered cross-sections

stability further failure types must be considered. This includes especially a possible exceeding of specified strength values of the materials used as well as the proof of fatigue strength, i.e. that no material fatigue due to dynamic loads occurs. Thus, knowledge of the loads to be expected during operation is significant for dimensioning the crane system. It is the task of the design engineer to identify these and calculate them accordingly.

In the field of bridge crane construction at the present time three main dimensioning regulations regarding the crane bridge are used for its design. These are in particular:

- DIN EN 13001-3-1: Cranes – General design – Part 3.1 – Limit states and proof competence of steel structure [15]

- DIN EN 13001-3-3: Cranes – General design – Part 3.3 – Limit states and proof of wheel / rail contacts [16]

- DIN EN 1993-6: Eurocode 3: Design of steel structures – Part 6: Crane supporting structures [9]

Within DIN EN 13001-3-1 requirements as well as procedures are included which are to be applied in order to avoid mechanical hazards caused by the crane. These hazards, which are considered, cover in general a possible exceeding of material strengths (such as yielding, destruction and material fatigue), an exceeding of limits with respect to temperature induced loads and the elastic stability of the crane and its components. Besides the global loads, the handling of local influences due to the wheel-flange contact of the traveling trolley running on the girder are described in the annex of DIN EN 13001-3-1 but only in case that the trolley runs on the upper chord of the main girder [15]. Once a traveling trolley is designed to run on the lower chord DIN EN 1993-6 offers amongst others procedures in order to assess the local stresses acting in the flanges [9] of an I-shaped girder due to the wheel contact. Moreover DIN EN 13001-3-3 gives instructions regarding the design of the wheel-flange contact where the dimensions of both the rails and wheels are considered [16].

Basically, the references included in DIN EN 13001-3-1 and DIN EN 1993-6 are important for the following work.

2.2 Basics of Engineering Mechanics

In order to apply the before mentioned standards, an in-depth knowledge of engineering mechanics is indispensable. For this purpose, in the following section, the basics are summarized in a condensed form and essential terms are defined. For further information, reference is made to the relevant technical literature.

As the oldest and most developed discipline of physics, the task of engineering mechanics is to predict both the movement and the deformation of bodies while hereby the *force* F is of great importance. It is a physical quantity based on the observations of daily experience [17, p. 7] and is interpreted as a vectorial quantity. The force F possesses the unit *Newton* [N], named after the English natural scientist Sir ISAAC NEWTON. With the introduction of the concept of force, other types of loads can be introduced, such as *distributed loads* and *moments*.

If forces act on a body in different points and if they are of opposite direction they form a pair. The resulting physical effect is called moment $\boldsymbol{M}$ and possesses the unit [Nm]. Choosing a reference point "A", the moment is obtained as follows.

$$\boldsymbol{M}^{(\mathrm{A})} = \boldsymbol{r} \times \boldsymbol{F} \qquad (2.1)$$

Here, $\boldsymbol{r}$ describes the vector from the reference point "A" to any point on the line of action of $\boldsymbol{F}$ [17, p. 90].

In case that forces act continuously distributed along a line, they are referred to as *distributed loads* $\boldsymbol{q}_0$ [N/m]. For two-dimensional problems, external influences such as wind loads can be interpreted as distributed loads. Further information regarding the definition of loads can be found in the relevant specialized literature such as [17], [18] or [19].

The field of engineering mechanics is of large scope, for this reason the knowledge necessary for the work is to be recorded compactly hereinafter and mainly reduced to elastostatic problems, i.e. theory and description of deformable bodies.

2.2.1 Mechanical Stresses

Once a body gets loaded by external loads, such as single forces $\boldsymbol{F}_i$ or distributed loads $\boldsymbol{q}_0$ and moments $\boldsymbol{M}_i$, the outer loads lead to inner forces. By means of a theoretical cut through the body (s-s) they can be visualized and are distributed over the entire cut surface A. These inner forces are called *stresses* and possess the unit [N/mm^2]. Here, point P is included in the surface element ΔA and in turn, the force $\Delta \boldsymbol{F}_i$ acts on the surface element. The quotient $\Delta \boldsymbol{F}_i / \Delta A$ defines the mean stress relating to the surface element ΔA. We postulate that this quotient reaches a finite limit for $\Delta A \to 0$ and we find the following expression.

$$\boldsymbol{t} = \lim_{\Delta A \to 0} \frac{\Delta \boldsymbol{F}}{\Delta A} = \frac{\mathrm{d}\boldsymbol{F}}{\mathrm{d}A} \qquad (2.2)$$
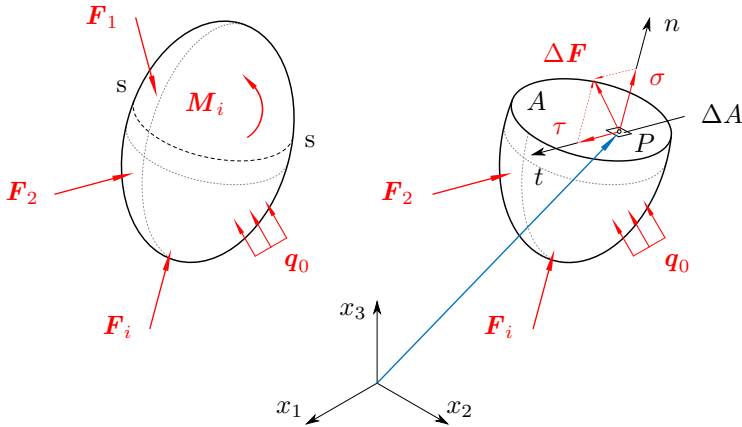
Figure 2.4: Loaded body, based on [2, p. 43]

The limit of the quotient t is called *stress vector* which can be further divided into two separate components. The first component σ is related to the part acting in normal direction n corresponding to the cutting area and will be called *normal stress*, while the other component τ relates to the parts acting inside in the cutting area in tangential direction t and will be called *shear stress* (see figure 2.4). Both components are perpendicular to each other and form the stress vector t. It can be easily seen, that the vectorial components of t depend on the direction of the cut s-s. By application of three cutting planes, which are orientated orthogonally to each other, all possible components can be identified with respect to the axes x_1, x_2 and x_3. These are summarized in the symmetric stress tensor (eq. 2.3) which fully defines the stress state at a certain point P in a body [2, p. 43–46].

$$
\underline{\underline{\sigma}} = \begin{bmatrix} \sigma_{11} & \tau_{12} & \tau_{13} \\ \tau_{21} & \sigma_{22} & \tau_{23} \\ \tau_{31} & \tau_{32} & \sigma_{33} \end{bmatrix} \tag{2.3}
$$

Knowledge of the mechanical stresses is essential in technical applications. They provide information on the extent to which the material of a body is loaded.

In steel construction, the so-called MISES yield criterion is of particular importance [20, p. 11]. Since in reality mostly multi-axial stress states occur, the basic idea is to trace them back to a uniaxial stress state that results in the same load. With the components of the stress tensor (eq. 2.3), the equivalent stress σ_M then follows to

$$\sigma_\mathrm{M} = \sqrt{\sigma_{11}^2 + \sigma_{22}^2 + \sigma_{33}^2 - \sigma_{11}\sigma_{22} - \sigma_{11}\sigma_{33} - \sigma_{22}\sigma_{33} + 3(\tau_{12}^2 + \tau_{13}^2 + \tau_{23}^2)}$$

(2.4)

and applies to a certain point of the body [21, p. 118–129].

2.2.2 Deformation of Elastic Bodies

In the previous section, it was stated that external loads lead to inner stresses of the body. Experience shows that the body then reacts in the form of a deformation and changes its shape. It can be further observed that the extent of the resulting deformation depends on the properties of the considered material. By means of a constitutive equation, the relation between the external influences and the response of the material can be described. In this context, HOOKE's Law is important due to the fact that it describes the relation between mechanical stresses and strains for steel closely. If a steel rod is loaded uniaxially and the stress is plotted over the dimensionless strain[2] $\varepsilon\,[-]$, a linear relationship can be established experimentally. The gradient of the straight line is called YOUNG's Modulus $E\,[\mathrm{N/mm^2}]$ and depends on the material, see figure 2.5. For a uniaxial tensile load in x_1-direction, the relationship between mechanical stress and strain is

$$\sigma_{11} = E\varepsilon_{11}.$$

(2.5)

---

[2] Relation between initial length and length change.

If POISSON's ratio[3] ν

$$\nu = -\frac{\varepsilon_{22}}{\varepsilon_{11}} \qquad (2.6)$$

and the coefficient of thermal expansion α_T [1/K] (relevant for changes in temperatures denoted by ΔT) are also introduced, HOOKE's law for the three-dimensional case results in

$$E\varepsilon_{11} = \sigma_{11} - \nu(\sigma_{22} + \sigma_{33}) + E\alpha_\mathrm{T}\Delta T. \qquad (2.7)$$

It is a special case of the *law of elasticity* and is valid in the so-called linear-elastic range which means that after removal of the load no permanent elongation remains [2, p. 76–79]. As soon as a significant value of stress is exceeded, the material begins yielding, i.e. that the material will be permanently deformed and changes its properties. Once the load is still increased the material will be destructed. It is the task of experimental investigation to determine these specific material characteristics. Usually the stresses are plotted against the strains in a *stress-strain curve*, qualitatively depicted in figure 2.5. Here, the stress value refers to the dimensions of the initial cross-section of the specimen. For a purely uniaxial load, the stress is given by $\sigma = N/A$. As the load increases, the steel bar becomes increasingly constricted, which means that the cross-sectional area also changes and the real stress increases. For most applications this specific value of stress is relevant and marks the possible range of operation. It is denoted by R_e [N/mm^2]. By adding a dimensionless safety factor $\gamma_{\mathrm{M}1}$ we obtain

$$f_\mathrm{y} = \frac{R_\mathrm{e}}{\gamma_{\mathrm{M}1}} \qquad (2.8)$$

which is usually used in crane construction [15, p. 15]. It should be mentioned at this point that the theory of elasticity is a field in its own right and is reduced to its essential contents in the course of the thesis. The theory of elasticity and behavior of materials are discussed in detail for instance in [22]. During its service life, a crane is exposed to loads that

---

[3] Describes the behavior of a body loaded by axial forces and the relation between the strains ε_{11} and ε_{22} in x_1-, respectively x_2-direction.
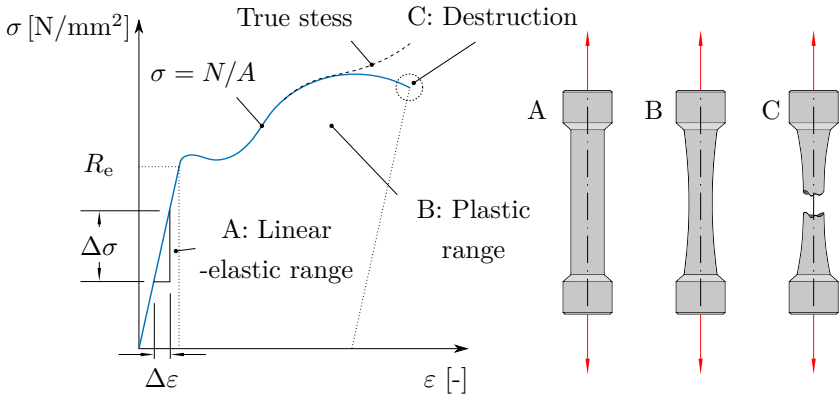
Figure 2.5: Stress-strain curve of a loaded axial rod [2, p. 15]

are largely determined by the movement of goods being transported. Every lifting movement causes deformations in the main girder which, although hardly visible to the naked eye, have a major impact on the entire structural performance due to the already described circumstance of internal material stresses. For example, the international standard ISO 22986 defines the limit values for maximum permissible deflections of crane girders [23]. In order to be able to describe the deformation of the crane bridge, an appropriate mechanical substitute model must be developed that is capable of describing the observed phenomena with sufficient accuracy.

A suitable way of describing a crane bridge is to reduce it to a *beam*. As a fundamental mechanical element the beam is capable of transmitting forces and moments transverse to its centroid axis. Another characteristic of a beam is that its cross-sectional dimensions are much smaller compared to its length [2, p. 89]. In this context, we introduce the following right-handed coordinate system with its axes x_1, x_2 and x_3 to describe the spatial extent of a beam. This type of designation is common in the theory of strength of materials [24, p. 5] and can also be found in simulation software, such as ABAQUS©. By means of a theoretical cut, both the resulting forces and moments can be identified at the cutting point in analogy to section 2.2.1. Splitting these into
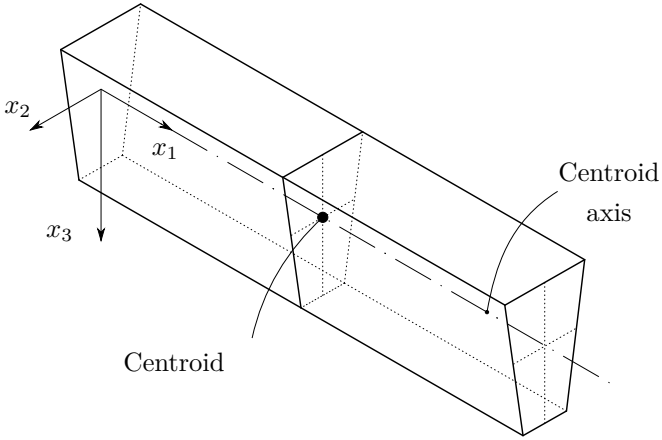
Figure 2.6: Coordinate system and defined beam axes

individual components results in a component that is directed along the centroid axis, another component transverse to and a moment that acts at this point. In this connection, the beam theory deals with the
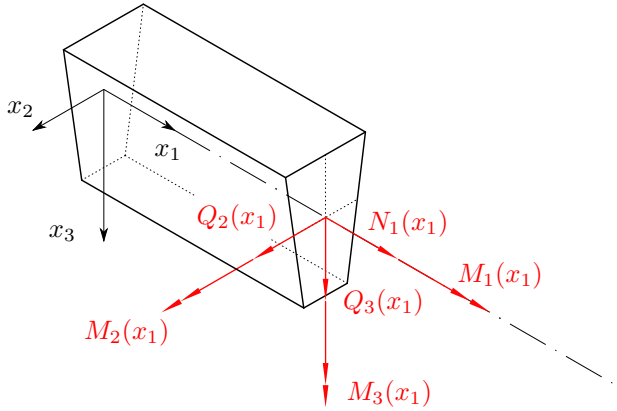
Figure 2.7: Visualization of inner forces and moments at x_1

description and calculation of the deformations and the corresponding stresses of beams. With the aid of the equations provided, conclusions can be drawn in advance about the behavior of loaded beams. Hereby, the geometry of the considered cross-section, the stresses and the law of elasticity play an important role. The relevant relations can be identified by combining them [2, p. 108].

Characteristics of Bending Problems

Within the framework of bending problems, a total of six different characteristics can be taken into account as a basis under which the problem is considered [25, p. 96–98]. These are briefly summarized below.

Shear force   In principle, a distinction is made in bending between pure bending and bending under transverse force. In case of pure bending, only external moments occur at the ends of the beam, which lead to constant moments about the beam axes x_2 and x_3 while the shear forces do not appear. In contrast, bending under shear forces leads to transverse forces in addition to bending moments.

Normal force   In case that the beam is additionally loaded by an external normal force an additional inner normal force occurs. Depending on the resulting deformations, the normal force may have to be taken into account within the frame of higher order theories (see paragraph *Deformation due to bending* below).

External loads   The orientation of the plane in which the loads act in and the plane regarding the deflection depends on the direction of the loads. If the loads act in one plane, the deformations take place in the same plane. Then the planes are parallel to each other. Otherwise the so-called *oblique bending* is present.

Geometry   In terms of geometric features, beams are divided into three different categories:

- *straight* beams,

- *slightly curved* beams and

- *curved* beams.

They vary in the amount of the radius of curvature ρ_c, see figure 2.8.
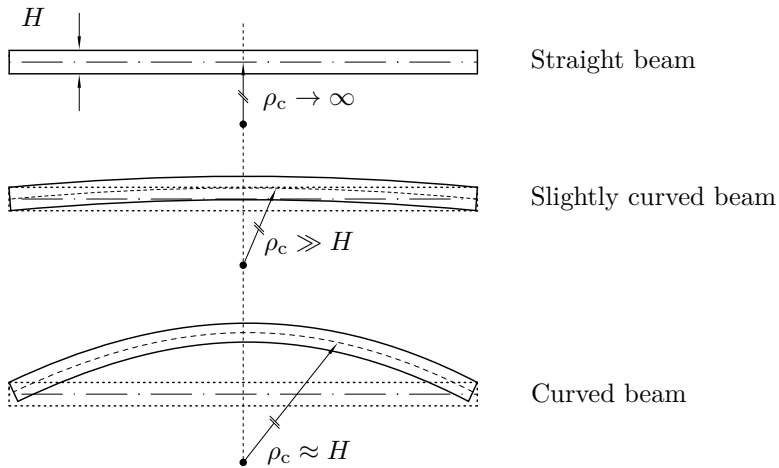
Figure 2.8: Classification of beams with respect to geometry

Deformation due to bending In general, there are three different theories with which the deflection of a beam can be described. They differ mainly in the state of the beam which is used to establish the equilibrium conditions.

- Theory of *first* order: The equilibrium conditions are established on the undeformed system.

- Theory of *second* order: The equilibrium conditions are established on the slightly deformed system.

- Theory of *third* order: The equilibrium conditions are established on the strongly deformed system.

For most problems where small deformations are expected, theory of first order is used. If high axial forces prevail, theory of second order can be used in order to identify critical loads in the context of stability considerations. In special cases, the third-order theory is applied to describe large deformations.

Deformation due to shear stresses   In reality, it can be observed that the beam cross-section is distorted due to the shear stresses. If this effect is taken into account, the beam is referred to as a *shear-soft* beam. If this effect is neglected, the beam is referred to as a *shear-resistant* beam.

Based on the mentioned characteristics, both the beam and the prevailing bending problem can be classified.

General Assumptions in Beam Theory

When setting up a physical model, assumptions are often made which may differ from the actual circumstances, but which facilitate the modeling process. Within the field of technical beam theory, the prerequisites necessary for its application are formulated by [25, p. 98] as follows.

- In unloaded condition, the beam axis is straight or only slightly curved.

- Only slender beams are considered, i.e. the beam length is at least five times greater than its height or width.

- The cross-sectional shape is retained in the unloaded state, i.e. the cross-section is true to form.

- The occurring deflections are small (maximum deflection to be less than 1/500 of the beam length).

- The applied material is homogeneous within the cross-section, isotropic and linear-elastic.

- The cross-sectional area is constant or only slightly changing along the beam axis.

- External loads as well as supporting reactions do not lead to rotations of the cross-section about the beam axis.

Fundamental Equations of Technical Bending Theory

Considering an infinitesimal beam element (see figure 2.9 (b)), possessing a specific YOUNG's Modulus E and subjected to a line load $q_3(x_1)$, the fundamental equation (eq. 2.9) of bending theory can be derived. With this it is possible to establish a relation between the applied loads

(a) Overall deflection of the beam

(b) Infinitesimal beam element
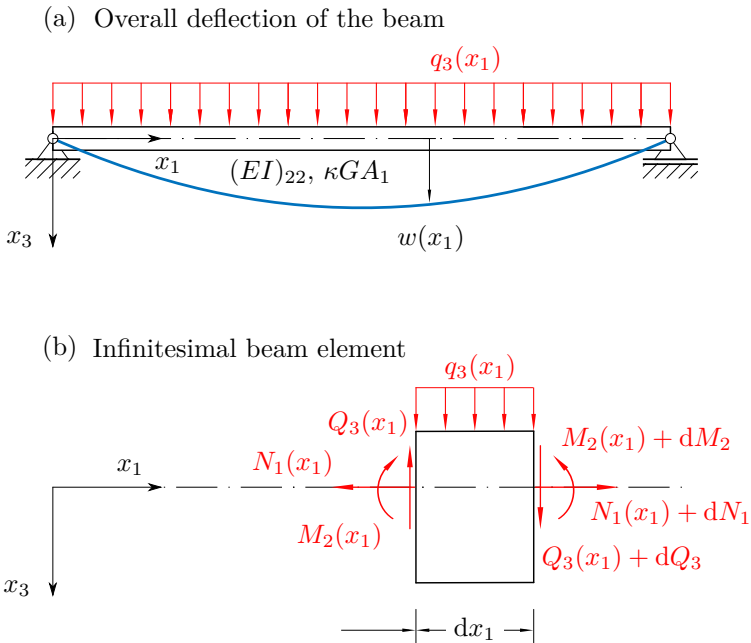
Figure 2.9: Basic deflection of a beam

and the deflection $w(x_1)$ of the beam in x_3-direction at x_1 (see figure 2.9

(a)) described by eq. (2.9). For a detailed description of the derivation, reference is made to technical literature such as [2].

$$(EI)_{22}\frac{\mathrm{d}^4 w}{\mathrm{d}x_1^4} = q_3(x_1) - \frac{(EI)_{22}}{\kappa G A_1}\frac{\mathrm{d}^2 q_3(x_1)}{\mathrm{d}x_1^2} \tag{2.9}$$

In this context, other quantities arise which will be briefly explained. The so-called moment of inertia I [mm^4] is an area moment of second order in the physical sense and is used as a geometric quantity to describe the deformation behavior of a beam[4]. It depends essentially on the shape of the cross-section and on the orientation of the reference axes [2, p. 92]. For any cross-section of area A in the $x_2 x_3$-plane, the second moments of area are calculated as follows

$$I_{22} = \int x_3^2 \mathrm{d}A + \bar{x}_3^2 A \tag{2.10}$$

$$I_{33} = \int x_2^2 \mathrm{d}A + \bar{x}_2^2 A \tag{2.11}$$

where $\bar{x}_2$ and $\bar{x}_3$ represent the orthogonal distance from the centroid to the considered bending axes by means of the *parallel axes theorem* (see for detailed description [25, p. 75]). Furthermore, the following second moments of area can be found

$$I_{23} = I_{32} = -\int x_2 x_3 \mathrm{d}A - \bar{x}_2 \bar{x}_3 A \tag{2.12}$$

which are called moments of deviations. They are of importance for cross-sections that are not axisymmetrical. For axisymmetric cross-sections, however, they vanish if the axes run through the center of area.

Equation (2.9) considers the additional tilting of the cross-section due to the shear stresses. In this context, the Shear Modulus G [N/mm^2]

---

[4] The product (EI) is briefly denoted by the *flexural stiffness* of the beam.

occurs, which is a material parameter similar to YOUNG's Modulus and can be related to it with the aid of POISSON's ratio ν.

$$G = \frac{E}{2(1 + \nu)} \tag{2.13}$$

In the course of modeling, it is assumed that the shear stress is constantly distributed over the cross-section, however this does not correspond to reality. In order to correct this mistake, a dimensionless shear correction factor κ is introduced which can be used to calculate an average shear stress distribution. The factor κ also depends on the shape of the cross-section under consideration.

With the assumptions made, eq. (2.9) can be used to describe the behavior of shear-soft beams. A beam with these properties is also called TIMOSHENKO beam, it is especially discussed in [26] and [27]. In case that a shear-resistant beam is considered, the denominator $\kappa G A_1$ strives against infinity and the second term vanishes. The equation then simplifies to

$$(EI)_{22} \frac{\mathrm{d}^4 w}{\mathrm{d}x_1^4} = q_3(x_1). \tag{2.14}$$

The differential equation is allocated to classical bending theory, developed by L. EULER and J. I. BERNOULLI and can be interpreted as a special case of the TIMOSHENKO beam. The theory according to TIMOSHENKO is particularly suitable for describing the deformation behavior of compact beams, since the shear influence on the deformation increases here. However, for many technical applications it can be shown that the application of the EULER-BERNOULLI equation (2.14) provides sufficiently accurate results. Since the main girder of a bridge crane can usually be traced back to a sufficiently slender beam, the application of eq. (2.14) is justified.

2.2.3 Elastic Stability

If a slender component is axially loaded in tension, it is possible to establish a clear relationship between the load and the deformation. It is

assumed, that the occurring deformations are small so that an establishment of the equilibrium conditions considering the undeformed system is still permissible. Once the component is loaded in compression, this is not always possible. It turns out that other states of equilibrium exist into which the component can switch. These states can be investigated using a stability analysis of the system. Here, knowledge about the load at which deflections occur in adjacent equilibrium positions is of great importance. Against the background of technical applications, it provides information about the condition at which the elastic stability starts to fail. In such a case, the elastic structure usually responds with an abrupt and large deflection, as it can be observed, for example, when a beam buckles [2, p. 263]. In the course of the investigation of equilibrium conditions in elastostatics, only *time-invariant* mechanical systems are considered, which further means that the applied loads do not depend on time [28, p. 271].

Buckling of Beams

Previously it was shown that different theories are available to describe the deformations of an elastic system. In order to interpret the deflection of a shear-resistant beam under axial load, the second order theory can be used. It is assumed, that the beam is ideally straight and that
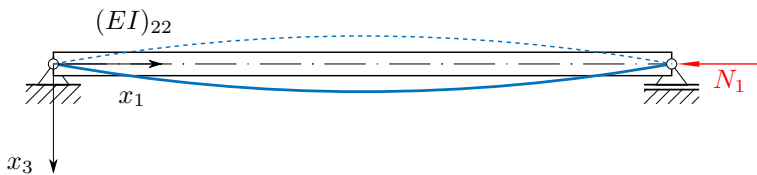
Figure 2.10: Buckling of a (slender) beam

the normal force is applied directly in the centroid of the cross-section. Then, the equilibrium conditions are established at the slightly deformed

system, which in turn leads to a homogeneous differential equation of fourth order, see eq. (2.15).

$$(EI)_{22}\frac{\mathrm{d}^4w}{\mathrm{d}x_1^4} + N_1\frac{\mathrm{d}^2w}{\mathrm{d}x_1^2} = 0 \qquad (2.15)$$

With the factor $\alpha^2 = N_1/(EI)_{22}$ and using an exponential ansatz, the solution of the differential equation can be determined. This results in the common expression

$$w = \mathrm{C}_1\cos(\alpha x_1) + \mathrm{C}_2\sin(\alpha x_1) + \mathrm{C}_3\alpha x_1 + \mathrm{C}_4. \qquad (2.16)$$

An adjustment to the prevailing boundary conditions results in a linear, homogeneous system of equations. To obtain nontrivial solutions, the determinant of the coefficient matrix must be zero. This is then the subject of a so-called *eigenvalue problem*. The solutions correspond to the critical loads, also known as buckling loads [29, p. 296]. Due to the characteristic of an eigenvalue problem, the direction of the deflection is not determined. This circumstance is depicted in figure 2.10 by the upper dashed line which indicates that both directions are possible. It can be stated in this context that buckling is a purely mathematical problem, since in reality there are no ideally straight components. Furthermore, these are always additionally loaded by their self-weight. Nevertheless, the real critical loads can be sufficiently estimated by application of the mathematical basics presented.

Buckling of Plates

A plate describes a flat load-bearing component whose lateral dimensions are much greater than its thickness (clearly visible in figure 2.11) and is, by definition, loaded transversely to its plane. However, if forces occur in the plane alone, a stability problem can occur in analogy to buckling of beams where the elastic structure fails. This phenomenon is called *plate buckling* and must be taken into account for example in lightweight constructions. In contrast to a beam, on an infinitesimal plate element the equilibria of forces and moments are set up in two spatial directions. Assuming sufficiently small deformations, the buck-
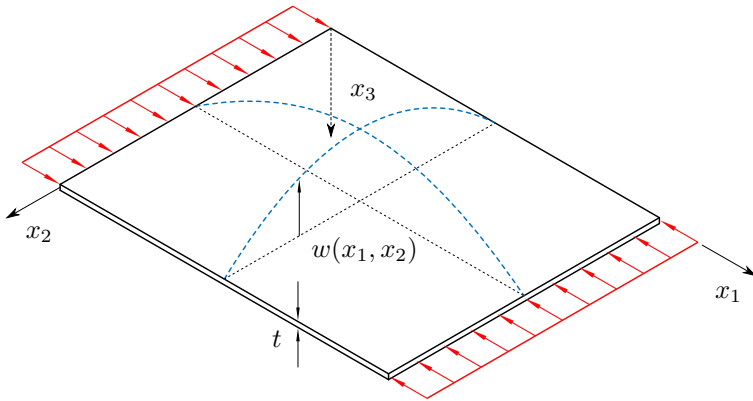
Figure 2.11: Exemplary buckling of a plate

ling equation can be identified by means of several simplifications, such as the neglect of terms of higher order. Due to the two spatial directions under consideration, the equation is a partial differential equation of the fourth order, which can only be solved analytically in certain cases. The solutions mark the critical loads at which the plate begins to buckle. Here as well, the boundary conditions in terms of supporting of the plate must be taken into account accordingly [29, p. 310–314]. In analogy to the beam, the *plate stiffness* K is introduced as a parameter, which includes both the geometry (thickness of the plate t) and the material properties. It is defined as

$$K = \frac{Et^3}{12(1 - \nu^2)} \tag{2.17}$$

and shows that the stiffness of the plate increases significantly as its thickness increases. The field of the stability of elastic structures is intensively discussed in [26] and [30].

2.2.4 Transfer of the Basics to Crane Construction

The fundamentals presented in the previous section are widely used, since they can be applied to describe the real circumstances with sufficient accuracy and thus also predict them. For this reason, they are used in the design and dimensioning of components and systems, including crane construction. In the following, it will be clarified to what extent the components of a conventional bridge crane can be modeled on the basis of engineering mechanics.

Due to the geometrical conditions and the orientation of the load action, the main girders of a bridge crane are usually modeled as straight beams. In section 2.1.1 two major cross-sections of the main girder applied in crane construction were introduced. In terms of the influence of shear stresses on the deflection it is assumed, that their impact on the deflection of thin-walled hollow cross-sections are minor in comparison to compact cross-sections. In [2, p. 155] it is indicated that the deflection caused by shear stresses can be neglected for compact beams with a length five times higher than their height. For crane constructions this approach is applicable as well.

Here, the load is transmitted almost point-like via the wheels of the traveling trolley to the crane bridge. In this context, a main feature of conventional bridge cranes is the fact, that they are not loaded by a normal force but only by the load of the goods to be transported and their self-weight. All loads then act orthogonally to the beam axis.

The ends of the crane bridge (respectively of the beam) are in turn fixed to the endcarriages, which move on the crane runway with a certain amount of clearance. This clearance allows the beam to rotate about this support point under load. For this reason, the supporting condition of the beam can be traced back to a simple support which prevents its vertical lowering. Furthermore, excessive bending of the structure does not occur due to its stiffness, that means that in general the equilibrium conditions are established on the undeformed system.

Cranes are generally steel-based structures. For this reason, the previously illustrated basics of strength theory are applied in order to determine the stress states caused by external loads. To describe the defor-

mation behavior, the beam theory according to Euler-Bernoulli is used [1, p. 145].

2.3 Application of Segmented Supporting Structures in Crane Construction

A specific literature review revealed, that the use of segmented overhead cranes is largely unexplored. So far, current research refers to continuous beam systems that are not subject to prestressing and are therefore structural *passive*. In this context, we define the attribute passive in such a way that the structure is only designed to withstand nominal external loads that stress the material. Conversely, *active* (or reinforced) means that additional external loads are applied to the structure, which have a positive influence on the material stresses and deformations resulting from the nominal loads by reducing them, see figure 2.12. Here, the aim is to achieve the most efficient utilization of the material. The
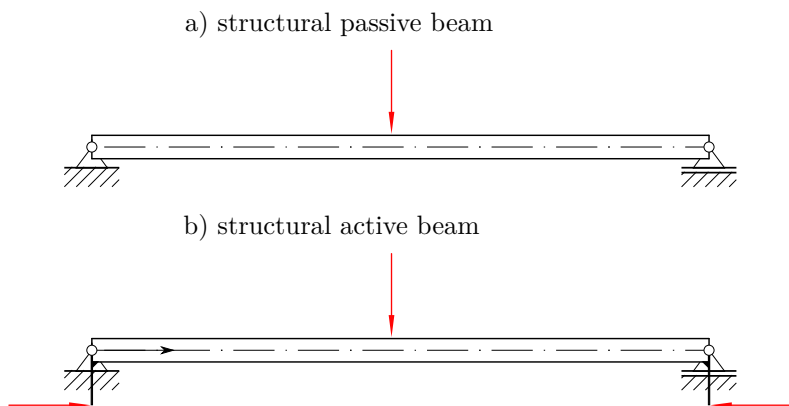
Figure 2.12: Structural passive and active beam

only comparable concept is the one according to S. Bolender et al. that was developed as a modular system. It is motivated by the usage of standardized individual parts and the associated reduction of produc-

tion costs. The modular bridge crane is designed as a two-dimensional truss consisting of an upper and a lower chord. The trolley travels on the outer edges of the hollow sections of the lower chord. Additional connecting elements at the junctions of the truss facilitate assembly and guarantee a form fit connection at the joints. A total amount of eight tension rods run in pairs in the hollow profiles of the upper and lower chord and transmit the prestressing force to the individual segments via stop pieces when tensioning. This closes the contact surfaces and the structure is able to transmit bending moments. Only then it is load-bearing. The tension rods, consisting of steel bars bolted together by means of threaded rods, run inside the hollow profiles, they are shown as red dashed lines in figure 2.13. When designing the modular bridge
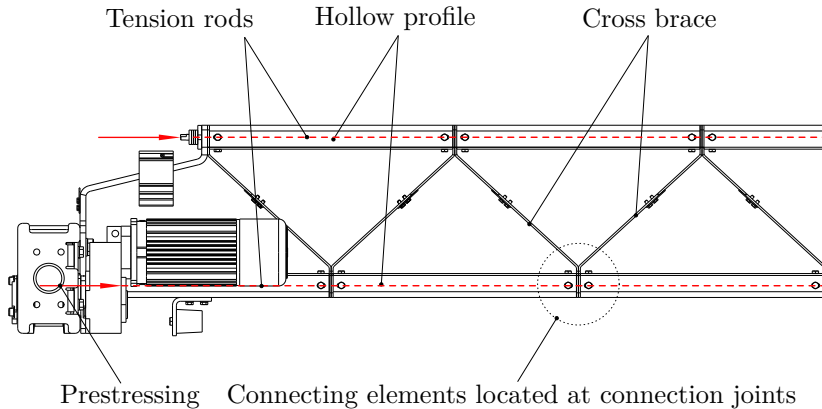
Figure 2.13: Detailed view of the scalable, modular, segmented crane [3]

crane, the so-called *limit state method* was used for the verification of the static strength. In this method, all occurring loads are multiplied by an individual partial safety factor and a dynamic coefficient. The verification of the elastic stability was also carried out according to the common rules.

In order to validate the concept, FE analyses were carried out with the ABAQUS© code using a crane (total span width 6.10 m, load capacity 3.20 t, total weight without endcarriages approx. 520.00 kg) as an

example. The analysis showed, that both the deformations and the mechanical stresses did not exceed the defined limits and thus the concept was classified as suitable [3].

2.3.1 Prestressed Girders

The analysis of the state of research in the previous section showed that, with the exception of [3], no prestressed crane girders have been investigated so far. Nevertheless, the technique of prestressing has been known for a long time and is mainly used in bridge construction and further applications related to civil engineering. The application of prestressed concrete is mentioned here as an essential representative. In the following, the current research results in the field of eccentrically prestressed steel beams will be examined in more detail.

Already in the year 1950, G. MAGNEL demonstrated with a prestressed beam made of mild steel that weight savings could be achieved by prestressing the beam compared to a conventional beam. Although the argumentation is based on simplified assumptions (e.g. stability problems are neglected), it could be shown that costs and weight of the considered structure can be reduced. At that time, for example, an economic benefit was already predicted by G. MAGNEL for the prestressing of steel structures. In his publication, areas of civil engineering are listed as application cases, such as airplane hangars as a practical example [31]. His research results are also motivation for the transfer of prestressing techniques into crane construction.

Based on this, B. M. AYYUB et al. (1990) investigated the influence of prestressing on the structural properties of a composite beam (beam consisting of I-shaped steel beam and concrete slab). Special attention was paid to the choice and arrangement of the tensile members. Table 2.1 gives an overview of the tensile members investigated in [4]. The arrangements of the single configurations are depicted in figure 2.14. It should be mentioned in this context, that in the configurations shown, the tendons undergoe an increase in axial force, taking the self-weight into account, since they are in contact with the beam and are subject to additional elongation due to the deformation of the girder. The

Table 2.1: Considered configurations in [4]

Characteristics	Beam A	Beam B	Beam C
Straight tendon	●	●	
Draped tendon			●
Strand		●	●
Bar	●		
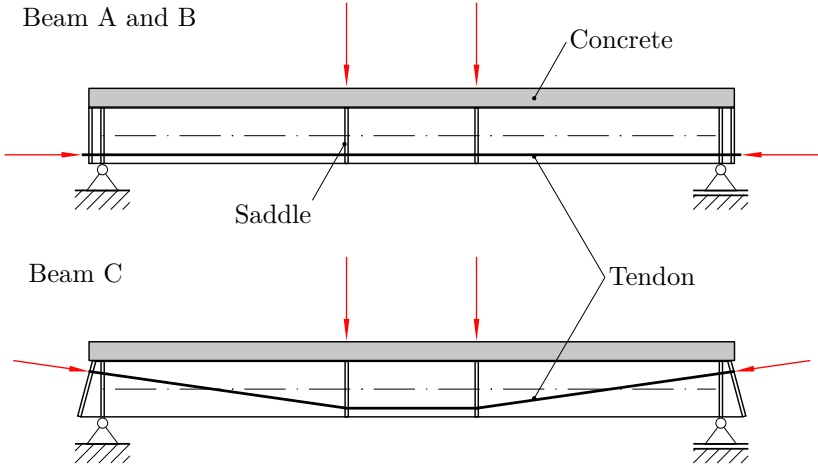
Figure 2.14: Considered configurations of tensile members according to [4], beam type specified in table 2.1

authors use the strain energy equation approach according to P. G. HOADLEY [32] in order to determine the normal force increase.

A final evaluation of the different concepts lead to the conclusion that the use of straight tendons is recommended due to the fact that they result in higher yield loads and lower construction cost. In addition, the authors recommend the use of strands instead of bars due to their higher strength-to-weight-ratio [4].

A similar investigation was performed by B. BELLETTI and A. GASPERI (2010). The subject of the research work here was an I-shaped steel beam of medium span width (from 35.00 m up to 45.00 m) as a load-bearing element in a roof construction. Steel cables eccentrically arranged to the centroid axis were also used as tensile members with special focus on the arrangement of deviators [33].

The coupling between the tensile member and the steel beam was further investigated in detail over several years by J. GOSAYE et al. A thin-walled cold-formed steel beam with an enclosed steel cable was considered as a reference structure. Particularly noteworthy are the analytical approaches to describe the mechanical behavior, which were also validated numerically and experimentally. Here, a key feature was also that the steel cable was connected to the beam via collars. In [34] and [35], for example, the authors aptly stated, that due to the additional obstruction in lateral direction, the underlying buckling load was increased. The reason for this is that the effective buckling length is reduced and the beam therefore only buckles in its second eigenmode. For the mathematical description of the shortening or compression, the authors use the compatibility condition that a resultant elongation occurs due to the bracing of the member. In that case, the elongation is the same for both components. By considering the respective stiffness, the deformation behavior and thus possible operating states can be described. The possible states considered are listed below.

- Case 1: The beam fails first
- Case 2: The tensile member fails first
- Case 3: Beam and tensile member fail simultaneously

Accordingly, it has already been established that the failure of the overall structure depends on the strength properties of all components involved, further both the steel beam and the tensile member.

N. HADJIPANTELIS et. al. (2018) showed against this background that the prestressing of an open thin-walled profile made of cold-formed steel with a steel cable can delay instability phenomena (such as local buckling) and thus increase the overall load-bearing capacity. The prestress-

ing induces initial stresses in the material, which counteract those of the actual load and thus reduce them [36]. In their following paper [37] the authors also formulate criteria regarding the serviceability of the structure. These mainly cover the limitation of excessive deflections of the beam and compliance with material strength values.

2.4 Structural Optimization of Box Section Girders

The dimensioning regulations presented in the previous section 2.1.2 serve to evaluate a designed crane bridge in terms of the extent to which it meets the defined criteria. Limit values are defined which must be complied with in order to exclude the possibility of structural failure. If we now assume that for given boundary conditions, such as a defined span width and / or a defined load, there are several possibilities for the construction of the crane bridge, then these possibilities can be examined against the background of certain aspects. For instance, if two different crane bridges are taken into account, which both meet all defined constraints, they may differ in their resulting weight. In the context of an *optimization* procedure, the best solution can be identified from the set of all possible solutions that fulfill all constraints [38, p. 2]. This particular solution is then called the *optimum*, which means that no better solution exists besides it. The quantity that is to be optimized is mathematically formulated as the *objective function f* and subject to defined *constraints*. These constraints may be formulated as functions or as fixed values. In this context, a fundamental distinction is made between *linear* and *nonlinear* optimization: while in linear optimization all involved functions are linear, in nonlinear optimization some or even all underlying functions are nonlinear. Another difference is the number of existing objective functions. If the underlying problem is reduced to only one objective function, it is called a *single-criterion* optimization problem. If several objective functions occur, they are combined in a vector and are subject to a *multi-criteria* optimization problem [39, p. 99].

As M. GOLDER has already revealed in his work [1], the crane bridge contributes the largest share to the total weight of the entire structure. Against the background of material and manufacturing costs, a reduction in its weight has a positive effect on the overall costs. As a result, efforts are being made in current research in order to reduce the weight of the crane bridge.

2.4.1 Basics of Nonlinear Optimization

In the section on the fundamentals of engineering mechanics (see section 2.2), it has already been shown that most of the relationships in strength theory and beam theory are nonlinear in their nature. Optimization tasks, which have to consider these properties in the context of constraints, are therefore also to be classified as nonlinear. For this reason, the essential basics of nonlinear optimization are summarized in the following. For the short notation of a nonlinear optimization problem, we introduce the acronym NLP (nonlinear program).

Definitions and Characteristics

In literature, there are different notations for optimization problems. In the further course of the work, we introduce the following notation to represent the form of a single-criterion NLP with constraints. According to this notation, the function $f : \mathbb{R}^n \to \mathbb{R}$ is to be minimized regarding a set of given constraints determined by the functions g_γ (*inequality* constraints) and h_ψ (*equality* constraints) with $g_\gamma, h_\psi : \mathbb{R}^n \to \mathbb{R}$.

$$
\begin{aligned}
&\min_{\mathbf{x}\,\in\,\mathbb{R}^n} \quad f(\mathbf{x}) \\
&\text{s.t.} \qquad g_\gamma(\mathbf{x}) \leq 0, \quad \gamma \in \mathbf{\Gamma}, \\
&\qquad\qquad h_\psi(\mathbf{x}) = 0, \quad \psi \in \mathbf{\Psi}
\end{aligned}
\tag{2.18}
$$

Here, the corresponding index sets are defined as

$$
\mathbf{\Gamma} = \{1, \ldots, p\} \qquad\qquad \mathbf{\Psi} = \{1, \ldots, q\}
$$

while $p, q \in \mathbb{N} \cup \{0\}$ applies. The vector $\mathbf{x}$ summarizes all parameters $x_1, \ldots, x_n$ on which the objective function f depends.

$$\mathbf{x} = [x_1, \ldots, x_n]^{\mathrm{T}} \tag{2.19}$$

Moreover, it is obvious that due to the presence of the constraints g_γ and h_ψ, the set $\mathbf{M}$ of admissible points is limited. Rather, the set is then described as follows [38, p. 112].

$$\mathbf{M} = \{\mathbf{x} \in \mathbb{R}^n \,|\, g_\gamma(\mathbf{x}) \leq 0, \gamma \in \mathbf{\Gamma}, h_\psi(\mathbf{x}) = 0, \psi \in \mathbf{\Psi}\} \tag{2.20}$$

Convexity The solvability of an optimization problem, the properties of the solutions as well as the applicable methods are strongly related to the properties of the underlying functions and sets. In this context, the term of the so-called *convexity* is of particular importance. A set $\mathbf{C} \subseteq \mathbb{R}^n$ is called convex if

$$\forall \mathbf{x}, \mathbf{y} \in \mathbf{C}, \lambda \in (0, 1): \quad (1 - \lambda)\mathbf{x} + \lambda \mathbf{y} \in \mathbf{C} \tag{2.21}$$

applies. Figuratively speaking, this means that the connecting line between the two points $\mathbf{x}$ and $\mathbf{y}$ must always lie in the set $\mathbf{C}$, see figure 2.15. If this is not the case, we speak of a *concave* set. On the other

Convex set **Concave set**
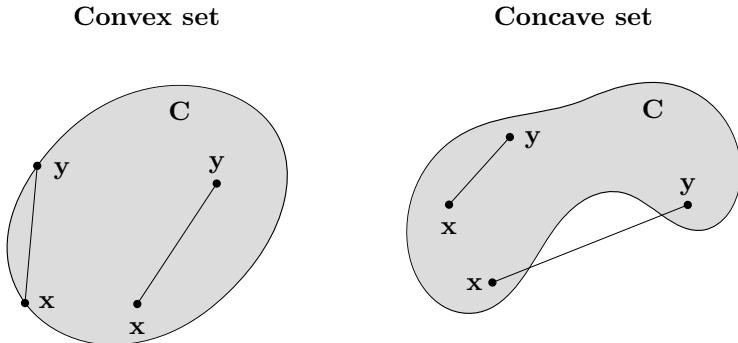
Figure 2.15: Illustration of a convex and a concave set in $\mathbb{R}^2$ [5, p. 39]

hand, a function $f : \mathbf{C} \to \mathbb{R}$ is defined as convex on the convex set $\mathbf{C} \subseteq \mathbb{R}^n$ if the following condition is true.

$$\forall\, \mathbf{x}, \mathbf{y} \in \mathbf{C}, \lambda \in (0,1): \quad f((1-\lambda)\mathbf{x} + \lambda\mathbf{y}) \leq (1-\lambda)f(\mathbf{x}) + \lambda f(\mathbf{y}) \tag{2.22}$$

Graphically interpreted this means that the function graph always runs under all its secants. On this basis, optimization problems can also be classified with respect to their convexity. A special property relates to the relationship between local and global minima. Furthermore, for a convex optimization problem (i.e. both the set $\mathbf{C}$ and the objective function f are convex), it applies that every local minimum point is simultaneously a global minimum point [5, p. 38–41].

Selection of Solution Procedures

In comparison to linear optimization problems the solution of NLP is much more complex and usually requires numerical methods. A large number of procedures exists for this purpose. It is essential to formulate the NLP correctly, identify its type and then to determine an appropriate strategy in order to solve it. In the following a selection of suitable solution methods relevant for the work are presented.

Gradient method The *gradient method* is a numerical method that can be applied in order to approximate the solution of NLP with a continuous objective function and without constraints. The basic idea behind the method is that starting from an initial point the direction of the strongest slope is determined. The target is then to identify a (local) minimum of the function.

$$\min_{\mathbf{x} \in \mathbb{R}^n} \quad f(\mathbf{x}) \tag{2.23}$$

In order to determine the slope, the gradient $\mathbf{d}$ is calculated at an initial point $\mathbf{x}_0$.

$$\mathbf{d}_0 = -\nabla f(\mathbf{x}_0) \tag{2.24}$$

By application of an appropriate increment t_0, the following point to be evaluated is then determined by

$$\mathbf{x}_1 = \mathbf{x}_0 + t_0 \, \mathbf{d}_0. \tag{2.25}$$

In this connection, the increment is to be selected in such a way that the following applies

$$f(\mathbf{x}_1) < f(\mathbf{x}_0). \tag{2.26}$$

A major requirement for the condition 2.26 is that the gradient exists, i.e.

$$\|\mathbf{d}_0\| > 0. \tag{2.27}$$

This method will be executed until the gradient is less than a defined value at which the operation is to be terminated. The challenge here is to select an increment t_0 that allows to find satisfying solutions. However, this can be difficult to solve under certain circumstances. For this reason, in literature such as [39] it is recommended to reduce the increment iteratively as well.

An alternative to the gradient method is the NELDER-MEAD method. The main difference is that the gradient of the objective function does not have to be determined explicitly. Furthermore, the procedure is also suitable for functions which are not continuously differentiable and therefore does not place any requirements on the objective function [39, p. 120–123].

In this context, it should be noted once again that with the help of numerical methods, optimal solutions can only be approximated, i.e. the statement that the solution found by the algorithm is also the best one does not apply.

Karush-Kuhn-Tucker Conditions In unconstrained nonlinear optimization, the absence of a descent direction is the necessary optimality condition for a point $\bar{\mathbf{x}}$ to be considered as a local minimum [38, p. 127]. In the constrained case, on the other hand, additional requirements are imposed on the set $\mathbf{M}$ described by the constraints. These re-

quirements are referred to as *constraint qualifications*, an important representative is the so-called Mangasarian-Fromowitz constraint qualification (MFCQ). In this context, a point $\bar{\mathbf{x}} \in \mathbf{M}$ satisfies the MFCQ provided the following conditions apply [38, p. 156]:

- the vectors $\nabla h_\psi(\bar{\mathbf{x}})$, $\psi \in \boldsymbol{\Psi}$ are linearly independent and

- a vector $\mathbf{s}^* \in \mathbb{R}^n$ exists with $\langle \nabla g_\gamma(\bar{\mathbf{x}}), \mathbf{s}^* \rangle < 0$, $\gamma \in \boldsymbol{\Gamma}_0(\bar{\mathbf{x}})$ and $\langle \nabla h_\psi(\bar{\mathbf{x}}), \mathbf{s}^* \rangle = 0$, $\psi \in \boldsymbol{\Psi}$.

Here, $\boldsymbol{\Gamma}_0(\bar{\mathbf{x}})$ describes the *active index set* (see [38, p. 113]) and is defined by

$$\boldsymbol{\Gamma}_0(\bar{\mathbf{x}}) = \{\gamma \in \boldsymbol{\Gamma} \,|\, g_\gamma(\bar{\mathbf{x}}) = 0\}. \qquad (2.28)$$

On this basis, the basic theorem of Karush-Kuhn-Tucker can be formulated. This states that if $\bar{\mathbf{x}}$ is a local minimum point of the underlying optimization problem, the functions f, g_γ, $\gamma \in \boldsymbol{\Gamma}_0(\bar{\mathbf{x}})$ and h_ψ, $\psi \in \boldsymbol{\Psi}$ are continuously differentiable, and the MFCQ holds, then multipliers $\lambda_\gamma \geq 0$, $\gamma \in \boldsymbol{\Gamma}_0(\bar{\mathbf{x}})$ and $\mu_\psi \in \mathbb{R}$, $\psi \in \boldsymbol{\Psi}$ exist with

$$\nabla f(\bar{\mathbf{x}}) + \sum_{\gamma \in \boldsymbol{\Gamma}_0(\bar{\mathbf{x}})} \lambda_\gamma \nabla g_\gamma(\bar{\mathbf{x}}) + \sum_{\psi \in \boldsymbol{\Psi}} \mu_\psi \nabla h_\psi(\bar{\mathbf{x}}) = 0. \qquad (2.29)$$

These multipliers λ_γ are called KKT multipliers (in the literature also called Lagrange multipliers) and can be chosen in such a way that $|\{\gamma \in \boldsymbol{\Gamma}_0(\bar{\mathbf{x}}) \,|\, \lambda_\gamma > 0\}| \leq n - q$ applies. The corresponding point is called KKT point and must comply with the following conditions.

$$\nabla f(\bar{\mathbf{x}}) + \sum_{\gamma \in \boldsymbol{\Gamma}_0(\bar{\mathbf{x}})} \lambda_\gamma \nabla g_\gamma(\bar{\mathbf{x}}) + \sum_{\psi \in \boldsymbol{\Psi}} \mu_\psi \nabla h_\psi(\bar{\mathbf{x}}) = 0$$

$$g_\gamma(\bar{\mathbf{x}}) \leq 0, \, \gamma \in \boldsymbol{\Gamma}$$

$$h_\psi(\bar{\mathbf{x}}) = 0, \psi \in \boldsymbol{\Psi}$$

$$\lambda_\gamma \geq 0, \, \gamma \in \boldsymbol{\Gamma}_0(\bar{\mathbf{x}})$$

Often, however, the active index set is not known. To overcome this circumstance, artificial multipliers λ_γ, $\gamma \in \boldsymbol{\Gamma} \backslash \boldsymbol{\Gamma}_0(\bar{\mathbf{x}})$ are introduced, which

disappear again by adding another constraint. Then, one obtains the new system of equations [38, p. 160–161].

$$\nabla f(\bar{\mathbf{x}}) + \sum_{\gamma \in \mathbf{\Gamma}} \lambda_\gamma \nabla g_\gamma(\bar{\mathbf{x}}) + \sum_{\psi \in \mathbf{\Psi}} \mu_\psi \nabla h_\psi(\bar{\mathbf{x}}) = 0$$

$$g_\gamma(\bar{\mathbf{x}}) \leq 0, \, \gamma \in \mathbf{\Gamma}$$
$$h_\psi(\bar{\mathbf{x}}) = 0, \psi \in \mathbf{\Psi}$$
$$\lambda_\gamma \geq 0, \, \gamma \in \mathbf{\Gamma}$$
$$\lambda_\gamma \cdot g_\gamma(\bar{\mathbf{x}}) = 0, \, \gamma \in \mathbf{\Gamma}$$

Thus, the calculation of a KKT point offers the possibility to obtain an analytical solution of the problem. However, the constraint qualifications described at the beginning must be fulfilled so that this point is also a minimum point. A detailed discussion of this method can be found in specific literature such as [5] or [40].

It remains to be said that the calculation of such a point is largely determined by the complexity of the optimization problem. This includes the number of equations, the number of variables and the general (analytical) solvability of the equation system. Thus, the calculation of a KKT point can often only be performed for simplified problems.

Branch and Bound   The calculation of optimization problems can be extremely computationally intensive, especially if the number of parameters to be considered increases and thus the number of possible combinations. In such a case, the so-called *Branch and Bound* method can be used to exclude combinations on the basis of case distinctions and thus limit the solution space. An essential prerequisite for the application of this technique is the understanding of the problem under consideration.

The Branch and Bound method aims to divide the problem to be solved into subproblems and hence identify irrelevant solutions at an early stage. Usually this technique is used for integer linear programs. These are especially discussed in [5].

2.4.2 Current Optimization Approaches in Crane Construction

After the basics of nonlinear optimization have been highlighted, the following section discusses the current optimization strategies in research to reduce the weight of the main girder of overhead cranes. Special attention is paid to the algorithms used, the considered structure and the defined constraints.

To calculate the optimum cross-section of a crane bridge, G. Pavlovic et al. (2013) provide an analytical optimization approach based on the method of Lagrange multipliers [6]. Thereby, a box section is considered under the assumption that the rail, the trolley travels on, is placed above the web plate. The general setup is depicted in figure 2.16. Furthermore, a fixed mounted crane cab is taken into account,
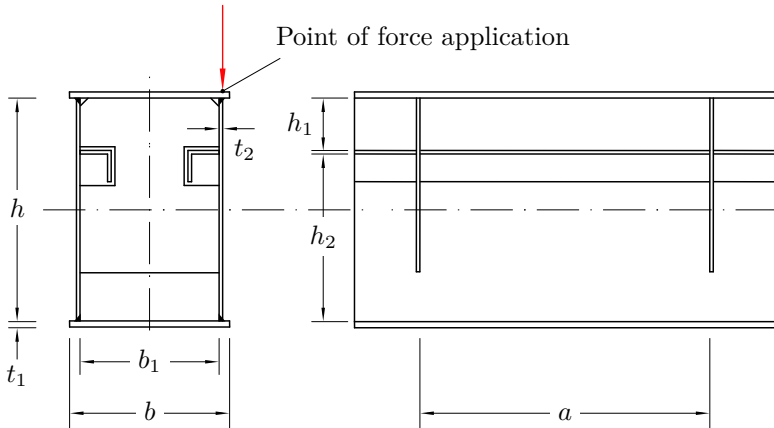
Figure 2.16: Considered box section in [6] and [7]

see figure 2.17. Its weight acts as an additional transverse force F_g. As already mentioned before, the application of Lagrange multipliers is only suitable for a certain amount of functions of moderate complexity. This is achieved by considering only one constraint and two parameters to be optimized. These are in particular the external width and the
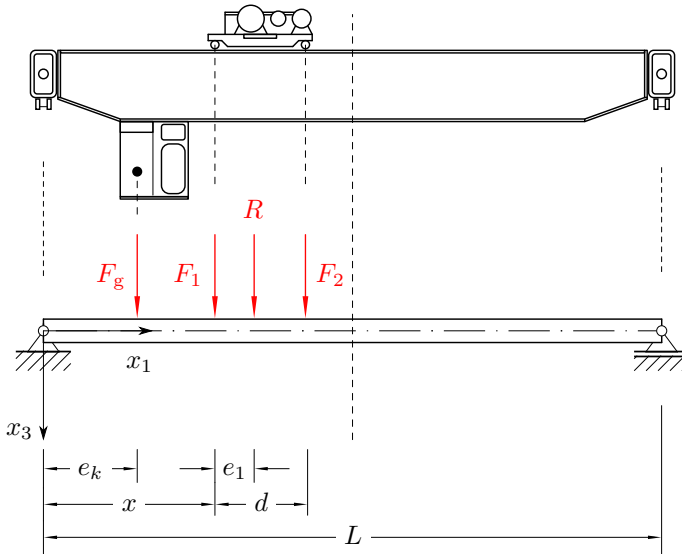
Figure 2.17: Considered crane configuration in [6] and [7]

external height of the box section, all other occurring parameters are set as constants. While the objective function is established with regard to the resulting cross-section, the underlying constraint function refers to the compliance with the specified strength values, i.e. that the MISES stress must not be exceeded. To determine the MISES stress, for the sake of simplicity, only the normal stresses occurring in oblique bending are considered. The aspect of limited deflection of the beam is not taken into account.

Starting from the approach in [6], M. SAVKOVIC et al. (2013) extend the problem by the constraints of dynamic stiffness and maximum allowable deflection of the crane bridge. The prevention of local plate buckling is added as another constraint. Again, the LAGRANGE multiplier method is used as a solution procedure and leads to an analytical expression. With the help of the optimization process, material savings between 4.90 % and 29.40 % can be achieved in comparison to the considered real reference cranes [7].

In addition to the classical analytical methods, efforts have recently been made to use alternative approaches in order to optimize box section profiles in crane construction. These include, in particular, biologically inspired algorithms that have clear parallels to nature. The advantage is that a large number of complex constraints can be taken into account, but the underlying numerical procedure can only approximate a solution. For the sake of completeness, some results regarding the application of these types of algorithms are presented hereafter.

The Particle Swarm Optimization (PSO) is based on the idea of imitating the behavior of swarm animals (such as fish or birds) when generating solutions. It is assumed that in a D-dimensional search space $S \subseteq \mathbb{R}^D$ a swarm consists of N particles. The particles themselves possess no volume and no weight, but they are characterized by a velocity and carry a potential solution with them. Meanwhile the particles collect *experiences* regarding suitable flight directions and exchange these with each other. On this basis, the speed and direction of the swarm are dynamically adjusted [41].

In their work, C. Sun et al. (2011) investigate a modified approach for the implementation of a PSO (MPSO) with feasibility-based rules for optimizing the self-weight of a box section girder. The feasibility-based rules cover in particular the following aspects:

- A feasible solution is preferred to an infeasible solution.

- In case of two feasible solutions the one producing better results regarding the objective function is preferred.

- In case of two infeasible solutions the one violating less the constraints is preferred.

As constraint functions, the authors define the compliance with the limit values regarding the Mises stress, the dynamic stiffness, the maximum allowed deflections in x_3- and x_2-direction as well as the local stresses due to wheel load imposition. In this context, further constraints regarding geometric parameters are defined. Comparing the results with an enumeration algorithm, the authors conclude that the MPSO performs
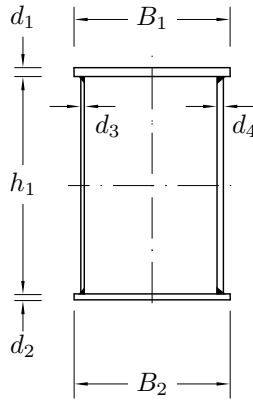
Figure 2.18: Box section and relevant design parameters considered in [8]

better in terms of weight reduction coming along with simultaneous reduction of the computing time [8].

Beside the PSO, other algorithms exist, which are inspired by the behavior of swarm animals. These include, for instance, the *Firefly* algorithm (FA), the *Bat* algorithm (BA) and the *Cuckoo Search* algorithm (CSA). The algorithms mentioned work basically on the same principle and are similar to the PSO. Here, too, the behavior of swarm animals is taken as a reference in order to be able to approximately determine the global minimum of the given optimization problem.

These algorithms are compared in [10] by M. SAVKOVIC et al. and evaluated with respect to their performance. In contrast to most of the work in the field, which deals with the optimization of double girder bridge cranes, the focus here is on a single girder bridge crane, with a bottom chord designed trolley. The constraint functions are determined by the criteria of strength, the elastic stability of plates, the lateral stability of the entire girder as well as the constraint regarding the dynamic stiffness. In conclusion to their work, the authors summarize that the application of the above-mentioned algorithms is justified and that, compared to solutions made in practice, material savings between

16 % and 39 % can be achieved. In this context, the FA gives the best results in terms of material savings.

Further work in this field is included in [42]. The basic idea here is mainly the combination or modification of existing algorithms in order to increase the degree of material savings.

2.5   Summary of the State of Research

The regulations currently used in crane construction define various limit values and provide methods to ensure safe operation of the crane system and thus exclude any danger to people and the environment. By definition, however, the regulations mentioned are limited to structurally passive components only. Conversely, this means that there are no design regulations for a segmented and eccentrically prestressed crane girder and that this girder configuration has not been investigated so far. The only comparable concept to be mentioned is the work done by S. BOLENDER et al., which focuses on a prestressed, segmented crane bridge. The general structure is based on a truss construction, whereby the individual components are plugged and braced together. Hereby, the tension members run in the hollow profiles of the upper and lower chord.

The prestressing technique is mainly used in the field of civil engineering, for example in roof constructions or bridge building. Mainly composite structures are investigated, whereas pure prestressed steel beams are rarely considered. In the literature, the clear advantages are the weight savings that can be achieved by using prestressed beams, but the additional forces which are applied increase the complexity of the system and the occurrence of additional failure mechanisms, such as local plate buckling or buckling of the entire beam. Due to a high strength-to-weight ratio, steel cables are recommended as the traction element, in contrast to steel bars. In this context, the literature has already pointed out that both the beam and the tension member must be considered when analyzing the performance. From this follows, that the possible failure mechanisms based on the traction element must also be taken into account.

Since the main girder of a bridge crane is the heaviest component, a number of different approaches are currently being taken into account to minimize its resulting total weight. Due to the characteristics of the underlying equations, this task falls into the domain of nonlinear optimization. In literature, the LAGRANGE multiplier method is often used as an analytical approach. However, their possibilities for application are limited. If the complexity as well as the number of constraint functions increases, the resulting system of equations can only be solved with great effort or not at all. This results in the application of alternative optimization strategies, with the help of which the complexity remains controllable and at the same time minima can be approximated. It turns out, that for the optimization problems in crane construction mainly biologically inspired algorithms are used, which imitate the behavior of swarm animals. Furthermore, it can be shown that these methods can be used to approximately solve non-linear optimization problems with a high degree of complexity. In this context, it must be noted that the constraint functions selected in the literature vary greatly and that there is no uniform understanding of the boundary conditions to be observed. The reason for this is, on the one hand, the reference structure under consideration (for example, constraints in the design of a double girder bridge crane differ from those of a single girder bridge crane) and, on the other hand, the selection of the optimization strategy. As mentioned above, some optimization methods are linked to a certain degree of complexity.

By studying the current state of research, both the structure and the understanding of the behavior of an eccentrically prestressed and segmented girder for use in crane construction can be identified as a research gap and as a mostly undiscovered field. Up to now, there is no comparison construction, that can be used as a starting point for the research work. This also means that no optimization methods for reducing the total weight have been investigated so far. Hence, this thesis aims to contribute to the design and optimization of prestressed, segmented girders in crane construction.

3 Constructive Implementation

You can tell a really good idea by the
fact that its realization seemed
impossible from the start.
- A. EINSTEIN

The following chapter focuses on the description of the new kind of bridge crane girder. First of all, basic requirements are formulated, which are used as guidelines for the design. Based on this, the components involved and their particular functions are explained in more detail, whereby these can be divided into two categories. One category includes all components that are assigned to the main girder, the other category includes all components that are related to the traction mechanism. Subsequently, the preliminary planned manufacturing processes for the production of the components and the materials used are introduced. The chapter ends with the presentation of the entire construction and the assembly sequences.

3.1 Requirements on the Construction

In the context of a new design, it is essential to formulate requirements in advance that must be met against the background of a target-oriented approach. These serve at the same time as guidelines for the construction. As mentioned at the beginning, the system is examined with regard to static loads, therefore constraints relating to the dynamic behavior are neglected. The requirements are further divided into *fixed requirements* (**FR**) and *desired requirements* (**DR**).

FR1: Compliance with specified strength values of the materials being applied

As in conventional crane construction, it is essential that the strength values of the materials are maintained. This means that the mechanical stresses that occur must not exceed the defined yield stress. The aim is therefore to ensure that the loads always remain in the linear-elastic range in order to exclude permanent damage.

FR2: Ensuring the elastic stability

Due to the preload, high axial pressure forces are applied to the structure. Thus, it must be ensured that no stability failure with regard to the elastic stability occurs, such as global buckling of the entire girder or local buckling of thin plates.

FR3: Maintaining maximum permissible deformations

Limit values for maximum permissible deflections have been established in crane construction, which are specified in the current regulations. These values are also taken into account for the design of the segmented, prestressed girder.

FR4: Continuous component bonding

In contrast to a conventional beam, the segmented beam is characterized by the fact that it consists of individual segments that are pressed together at the connection joints by pretensioning the tensile member. Here, it must be ensured that sufficient compressive stress is always present in the profiles and that no gaping occurs. This would disrupt the component bonding and safe operation cannot be guaranteed any longer.

FR5: Possibility of dismantling all components

The segmentation concept offers the advantage that temporarily used cranes can be again dismantled into their individual parts after the end of their operation. The aim is therefore to design the structure in such a way that dismantling is possible.

DR1: Transportability of all components on EUR-pallets

Following on from the earlier requirement, the construction method can also be based on the dimensions of common transportation means, such as EUR-pallets. For this reason, the components must not exceed the dimensions of a standardized EUR-pallet.

DR2: Simple construction and only a small number of components installed

The last requirement refers to a comparatively simple structure. This includes, among other things, easy manufacturability of the components as well as a small total number of parts.

At this point it should be mentioned that the defined requirements do not claim to be complete. Rather, they represent the fundamental aspects that the structure must fulfill against the background of static loads and a safe operation.

3.2   Functional Design

In comparison to a conventional crane girder, the segmented girder can only transmit shear forces and moments in case that the single segments are sufficiently pressed together at their connection joints. Four different types of components are used in this context, with each component performing a different task. Figure 3.1 shows the conceptual design of the segmented beam. The basic approach is to divide the crane bridge into discrete segments of a certain length, the so-called *main segments*.
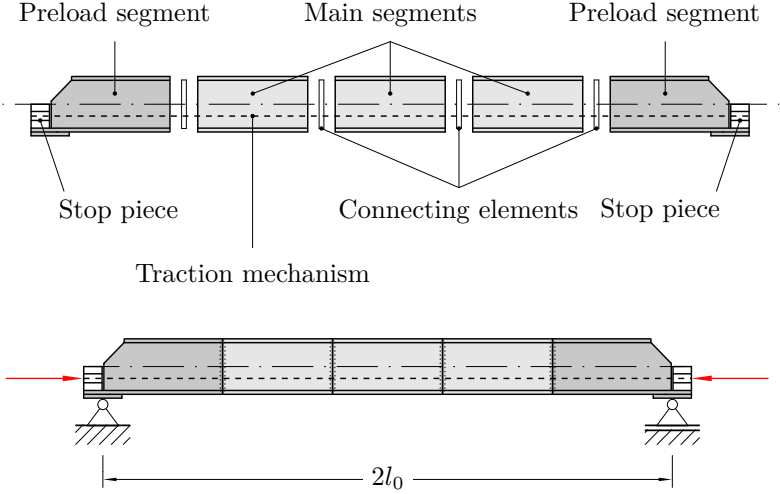
Figure 3.1: Conceptual design of the segmented, prestressed crane bridge

In turn, *connecting elements* are used at the connection joints, which mainly facilitate the assembly and ensure a form-fit component bonding. Furthermore, *preload segments* are added at the ends of the girder. They possess a local special design due to the application of the prestressing force. The preload segments are further abutted by the *stop pieces*. These are in direct contact with the traction mechanism and transmit the prestressing force as a compressive force to the segments. The traction mechanism runs in the cavities of the main segments (respectively preload segments) and is arranged eccentrically to the centroid axis of the main girder. The pre-deformation can be achieved by the induced initial bending moment due to the eccentrically acting prestressing force.

In this context, it is useful to parameterize the individual components of the crane girder, whereby a certain number of primary parameters are defined. These mainly comprise the geometrical dimensions of the main segment. Here, all geometrical parameters possess the unit [mm], unless otherwise specified.

3.2.1 Segmentation Strategy

The crane bridge is geometrically decisively defined by its span width. Due to the symmetry of the structure, we denote half the span width as l_0 and define it as the *span width*[1] in the following course of the work. If we first imagine a conventional crane bridge, whose span width can be manufactured as desired, we are now faced with the challenge of defining a general procedure for a segmented crane bridge, according to which the individual components can be manufactured and assembled so that their total length in the prestressed state matches the span width as well.

The segmentation strategy is responsible for accomplishing this task. Different approaches to segmentation exist, so it is reasonable to define a number of boundary conditions or key performance indicators in advance to guide the strategy development.

Small Number of Individual Parts

Against the background of manufacturing and arising costs, it is preferable to reduce the overall design to a small number of individual parts. At the same time, the number of variants is reduced.

Small Number of Connection Joints

According to figure 3.1 the construction resembles the principle of a braced sleeve. If contact surfaces are pressed together in a bolted connection, the microscopic roughness of the materials will flatten out. This results in a loss of prestressing force, which must be taken into account when calculating the required prestressing force. As the number of joints decreases, so does the influence of the loss of pretensioning force. Therefore, the lowest possible number of joints should be preferred.

---

[1] The real span width is then represented by $2l_0$.

These two aspects form the core of the proposed segmentation strategies, which are presented below. The basic objective is to set the length of the main segments to a defined value and only adjust the length of the adjacent preload segments. In principle, this means that only two segment types occur, which already limits the number of variants. A further advantage is that the dimensions of the associated steel bars and threaded rods, which together form the traction mechanism, are also limited to two variants each.

We define l_{s} as the length of a main segment and l_{s}^* as the length of the according preload segments which may vary with respect to the underlying segmentation type. In this connection, l_{r} represents the length of a common steel rod and equals the length of the main segment. Additionally, l_{r}^* denotes the lengths of the additional rods which penetrate the through-holes of the stop pieces.

Segmentation Type 1: Integer and odd Number of Main Segments

In case that the length of the girder can be represented as the sum of an odd multiple of the length of the main segments l_{s} and the defined maximum length of the preload segments, segmentation type 1 is given. It can be seen as a standard case that does not require any further
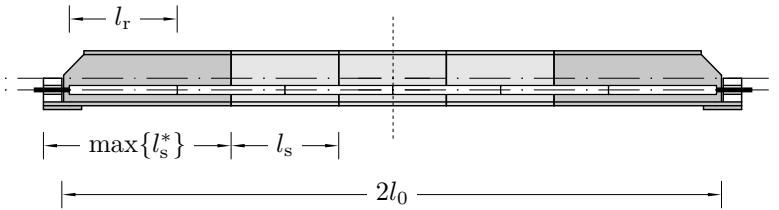
Figure 3.2: Segmentation type 1

adjustments, see figure 3.2. Furthermore, no additional steel bars and threaded rods are necessary.

Segmentation Type 2: Integer and Even Number of Main Segments

Segmentation type 2 is present as soon as the entire length can be expressed as the sum of an integer even multiple of the length of the main segments and the defined maximum length of the preload segments. In
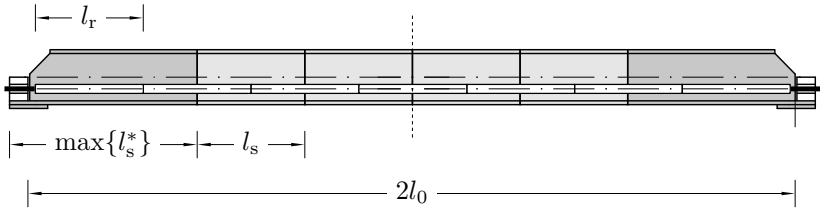
Figure 3.3: Segmentation type 2

figure 3.3 it can be seen that here, compared to segmentation type 1, the crucial connection joint lies exactly in the symmetry axis of the girder. With regard to the requirement that the beam must not gape, this type of segmentation imposes increased restrictions on the calculation of the necessary prestressing force.

Segmentation Type 3: Non-integer and Even Multiple of Main Segment Length

If the entire length of the crane bridge cannot be represented in terms of segmentation type 1 or 2, a further classification must be made. Segmentation type 3 occurs as soon as the entire length can be expressed as the sum of an odd multiple of l_s with a remainder $\bar{m} \in (0, 1)$ and the defined maximum length of the preload segment, see figure 3.4. Here, the lengths of the preload segments are to be adjusted. For this, at first the remainder is divided into two parts and added to the preload segments. Since they now exceed their defined maximum lengths, each of them are to be shortened by the half length of a main segment $l_s/2$. This again gives a new main segment and in total an even number of main segments. Due to the adjusted lengths of the preload segments, additional steel bars are necessary as well.
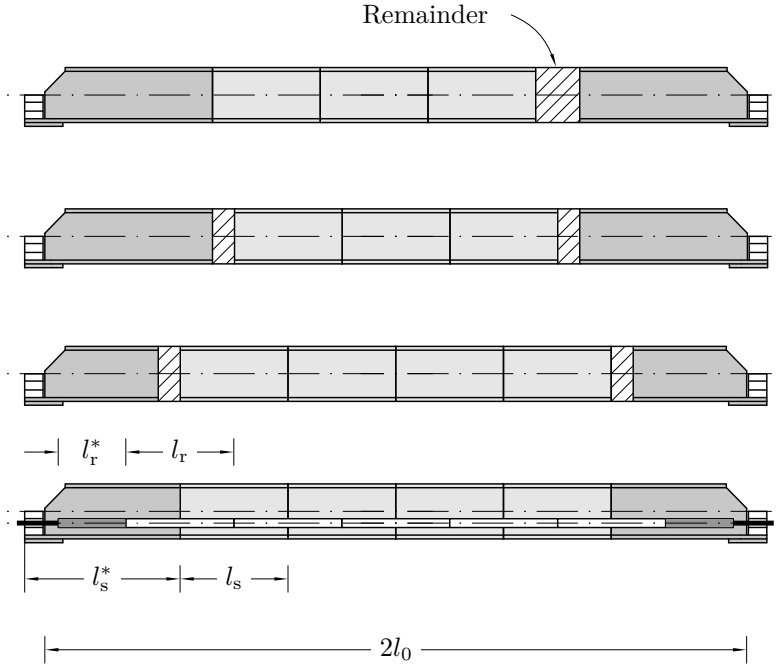
Figure 3.4: Segmentation type 3

Segmentation Type 4: Non-integer and odd Multiple of Main Segment Length

Segmentation type 4 is similar to type 3, the only difference is that the entire length can be expressed at first as an even multiple of the main segment length with a remainder $\bar{m}$ and the defined maximum lengths of the preload segments. Again, the lengths of the preload segments are to be adjusted while the same procedure is applied. In contrast to segmentation type 3, we obtain in total an odd multiple of main segments.

Remainder
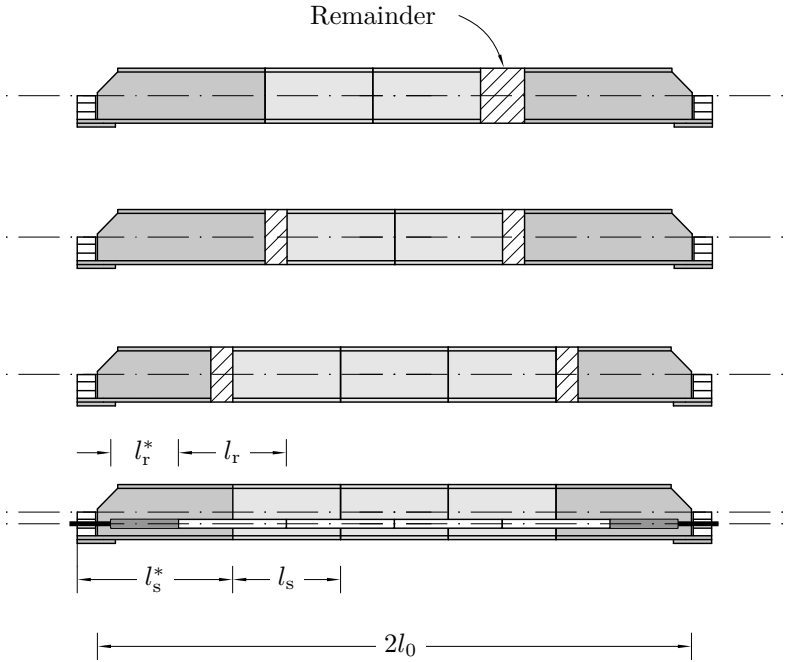
Figure 3.5: Segmentation type 4

Finally, the calculation steps are summarized for the segmentation strategies. For this purpose, we first introduce the dimensionless quantity λ, which is used as a multiple of the length of a main segment to determine the length of the stop piece l_{st}.

$$l_{\text{st}} = \lambda l_{\text{s}}, \quad \lambda \in (0, 1) \tag{3.1}$$

The number of main segments n_{s} is then to be determined as follows.

$$n_{\text{s}} = 2 \left(\lambda + \frac{l_0}{l_{\text{s}}} - \frac{\max\{l_{\text{s}}^*\}}{l_{\text{s}}} \right) \tag{3.2}$$

Table 3.1: Corresponding quantities with respect to the segmentation type

Segmentation Type	$n_{\mathrm{s}}\,[-]$, $k \in \mathbb{N}\backslash\{0\}$	$\hat{n}_{\mathrm{s}}\,[-]$	$l_{\mathrm{s}}^*\,[\mathrm{mm}]$
Type 1	$2k-1$	n_{s}	$\max\{l_{\mathrm{s}}^*\}$
Type 2	$2k$	n_{s}	$\max\{l_{\mathrm{s}}^*\}$
Type 3	$2k+\bar{m}$	$\lfloor n_{\mathrm{s}}\rfloor + 1$	$l_0 - \hat{n}_{\mathrm{s}}l_{\mathrm{s}}/2 + \lambda l_{\mathrm{s}}$
Type 4	$2k-1+\bar{m}$	$\lfloor n_{\mathrm{s}}\rfloor + 1$	$l_0 - \hat{n}_{\mathrm{s}}l_{\mathrm{s}}/2 + \lambda l_{\mathrm{s}}$

By considering the according case distinctions, the characteristics of each segmentation strategy can be defined, see table 3.1. Here, the quantity $\hat{n}_{\mathrm{s}}$ describes the adjusted number of main segments.

3.2.2 Initial Estimation of the Underlying Global Load Profile

Compared to conventional crane bridges, the segmented crane bridge has a different load profile due to the additional axial compressive stress. It makes sense to subject the girder to an initial theoretical analysis in advance in order to predict heavily loaded areas. For this purpose, we consider the global normal stress σ_{11} in x_1-direction, since this will represent the essential part of the total load. Figure 3.6 shows qualitatively the expected load profile of the beam being loaded at $x_1 = l_0$. It can be seen that the normal stress is composed of a total of four components. First, the profile is subjected to purely axial compression (a), which we assume to be constantly distributed over the cross-sectional area. The eccentrically arranged traction mechanism generates an additional initial bending moment (b). This leads to a negative deflection, i.e. a deformation of the beam in negative x_3-direction. As a result of this bending, the upper chord is then subjected to tensile stress and the compressive stress prevailing there is first reduced. On the other hand, the compressive stress in the bottom chord increases due to superposition of the additional part of the bending. If the beam is now subjected to the design load (c) in the next step, positive deflection occurs, i.e. the beam then tends to deflect in the positive x_3-direction.
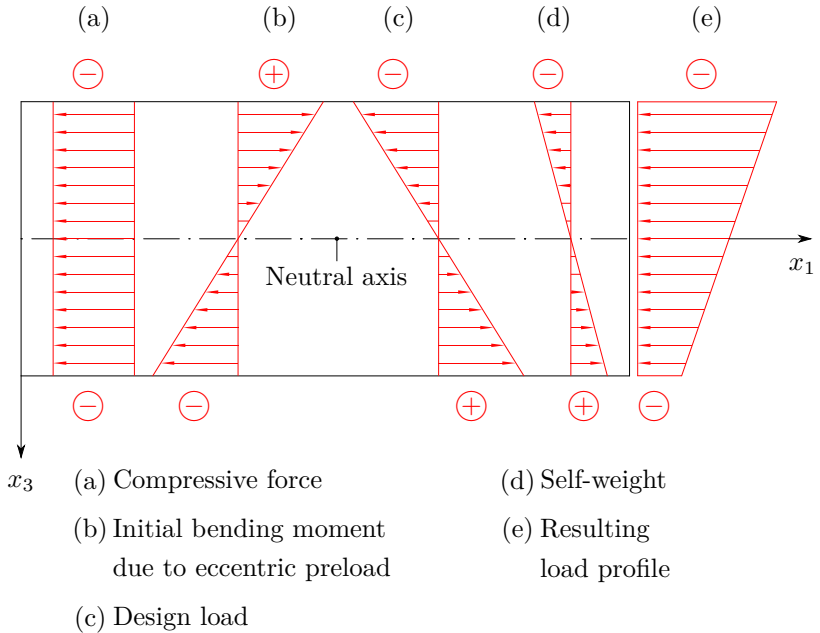
Figure 3.6: Expected load profile regarding a load application at $x_1 = l_0$

This causes the compressive stress in the upper chord to increase again, while the compressive stress prevailing in the bottom chord is reduced. The design load is additionally superimposed by the load due to the self-weight (d). Although the magnitude of this load is smaller, it must be taken into account, especially for beams with large span widths. If all the components shown are superimposed, a resulting load profile (e) is obtained. From this we can already derive the following findings in advance:

- The compressive stresses in the bottom chord must not be completely relieved, otherwise the beam would start to gape since the girder is not capable of absorbing tensile stresses due to the loose component bond.

- Considering that there is always a compressive stress and the girder does not gape, the upper chord tends to be more heavily loaded in the case of central application (i.e. in the middle of the girder at $x_1 = l_0$) of the design load compared to the lower chord. This is an important finding, especially in the context of the strength values to be maintained and the local elastic stability.

- If the design load acts close to one of the supports, the profile is subjected to greater shear stresses due to the increase in the shear force.
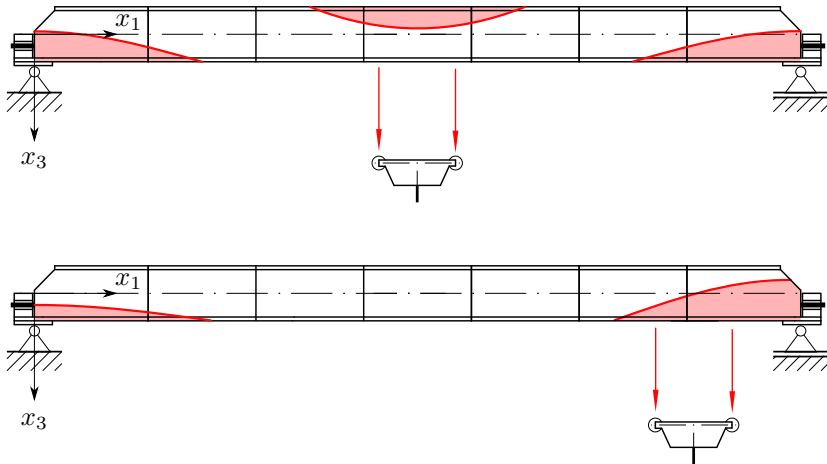
Figure 3.7: Estimated highly loaded areas during operation

On this basis, we can now derive an initial estimation of the global heavily stressed areas. These vary depending on the position of the trolley and must therefore be considered collectively. The areas identified are highlighted in red in figure 3.7.
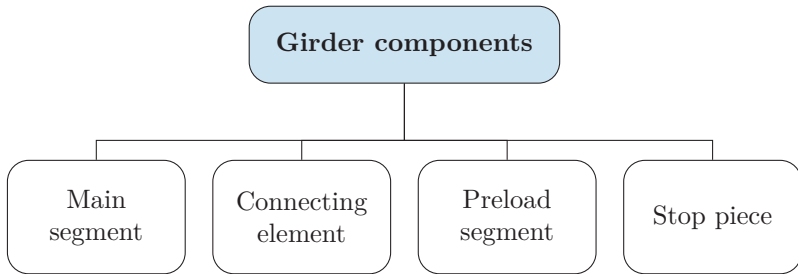
Figure 3.8: Girder components

3.3 Design of the Prestressed and Segmented Bridge Crane Girder

This section deals with the description of the structural design of the individual components, which together form the crane girder. These can be roughly divided into components allocated to the girder and components allocated to the traction mechanism. In this connection, special attention is paid to their geometries and respective functions.

3.3.1 Girder Components

The crane girder itself consists of in total four separate components, see figure 3.8. As soon as they are connected with each other, they form the main girder of the bridge crane.

Main Segment

The main segment possessing a defined length l_s is designed as a box section with two web plates of width t arranged parallel to each other. The upper and lower chords are welded to the web plates. The parameter c takes into account the resulting horizontal length of the weld seam. Here, the length of the main segment equals, with regard to the desired requirement **DR1**, the width of a standard EUR-pallet, i.e.

$l_\mathrm{s} = 800.00\,\mathrm{mm}$. In addition, there are vertically arranged recesses at the ends, which are intended as positioning aids for the connecting element (see figure 3.15) to be inserted. Figure 3.9 illustrates the major dimensions to be taken into account. The outer geometry is completely axisymmetrically designed and has a total external height of $2h$ and a total external width of $2b$. With the introduction of the dimensionless ratios

$$\eta = \frac{h_0}{h},\ \eta \in (0,1) \qquad\qquad \beta = \frac{b_0}{b},\ \beta \in (0,1) \qquad (3.3)$$

the inner height h_0 and the inner width b_0 can be expressed by a multiple of the external height, respectively the external width. A stabilizing bulkhead plate is welded in the middle of the main segment. This possesses a recess through which the traction mechanism can travel. The traction mechanism is in turn arranged with the eccentricity ϵ to the centroid axis. Parameters s_2 and s_3 are placeholders to reserve a certain amount of space for the traction mechanism. Recesses are also provided at the outer edges of the bulkhead plate in order to avoid overlapping of the adjacent weld seams with regard to a construction suitable for welding [43, p. 151]. In addition, the main segment possesses an upper as well as a bottom support which are planned for the establishment of a connection between the main segment and the connecting element. It should be emphasized in this connection that, strictly speaking, the coordinate system drawn in, does not coincide with the centroid, since it is shifted in the x_3-direction due to the bulkhead plate being asymmetrical to the x_2-axis. However, this influence is negligible compared to the remaining beam due to the small total volume of the bulkhead plate. Therefore, it is assumed with respect to the further course that the centroid is located in the origin of the drawn coordinate system.

The overall construction is designed for a trolley with a bottom chord running gear. The wheels of the trolley travel on the plate of the bottom chord, whereby an idealized concentrated force R_3 is introduced via this plate. Here, it is assumed that a completely symmetrically distributed load is present. This means that the load attached to the trolley is distributed evenly over its four wheels. It is further assumed that the wheels of the trolley have a total width of $2b_\mathrm{w}$ and that the load is introduced exactly in the middle of the wheel.
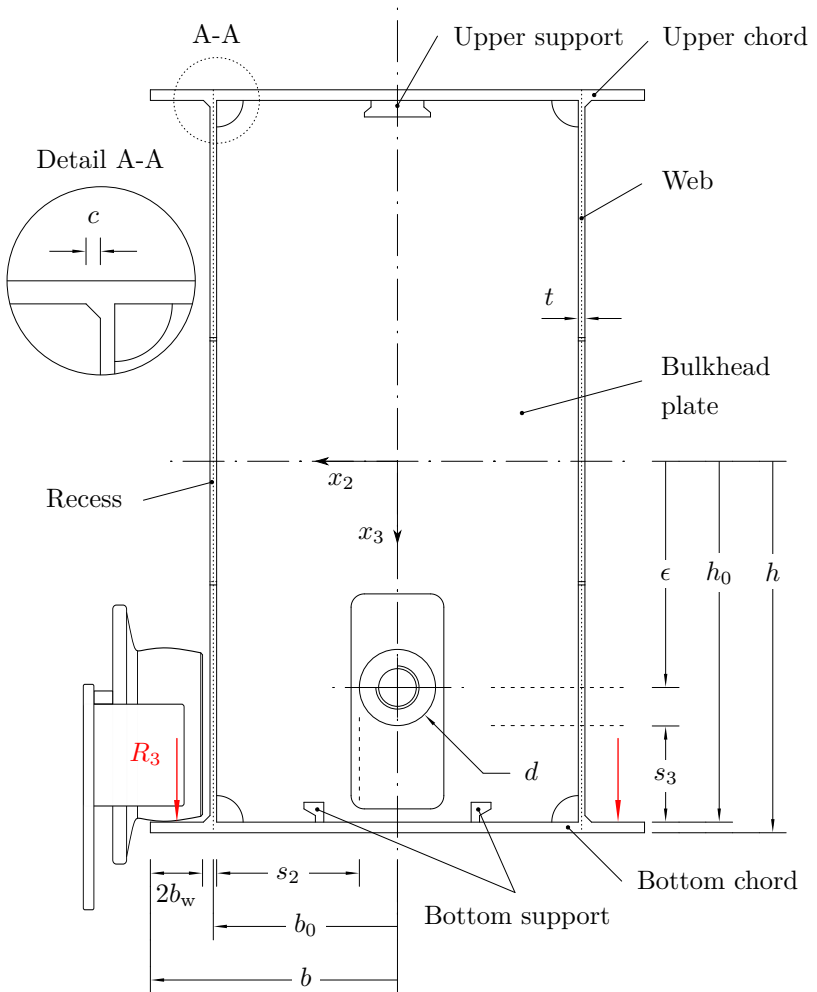
Figure 3.9: Dimensions of the main segment (front view)

It can already be derived from the figures shown that the main segment is described by a thin-walled, slender geometry. This circumstance is especially noticeable in the case of larger dimensions. Since a contin-
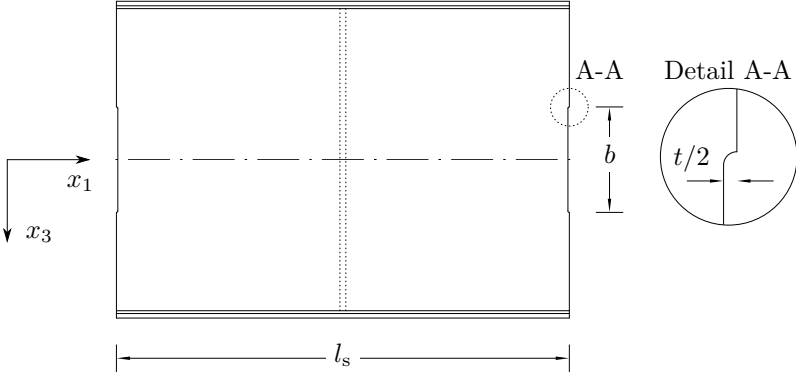
Figure 3.10: Dimensions of the main segment (side view)

uous component bond is required, they must be pressed together by a compressive force. Here, the web plates in particular, as well as the top and bottom chord plates, are exposed to the risk of local failure of elastic stability. For local reinforcement of the plates, different types of stiffening ribs will be qualitatively investigated in the following. These are shown in figure 3.11 and are welded to the plates. The areas highlighted in blue indicate the attached stiffening ribs. In order to be able to make a qualitative comparison, the total additional area is kept constant, i.e. each type has the same amount of additional area available. This allows a statement to be made about which surface distribution provides the greatest stiffening effect in principle. Of great interest here is how much the value of the first eigenvalue can be increased in contrast to that of the untreated profile which is denoted by N_c^* in the following. With the help of the ABAQUS$^©$ code, stability analyses are carried out for all profile types. Here, we assume steel as the underlying material ($E = 2.10 \cdot 10^5$ N/mm^2, $\nu = 0.30$). The inner edges of the segments are simply and rotatably supported, which suitably represents the situation in later use, see figure 3.12. The segment is then subjected to a surface load which is assumed to be distributed uniformly over the entire cross-section. The result of the stability analysis of the reference segment is shown in figure 3.13. It can be clearly seen that the lateral web

Shape A

Shape B
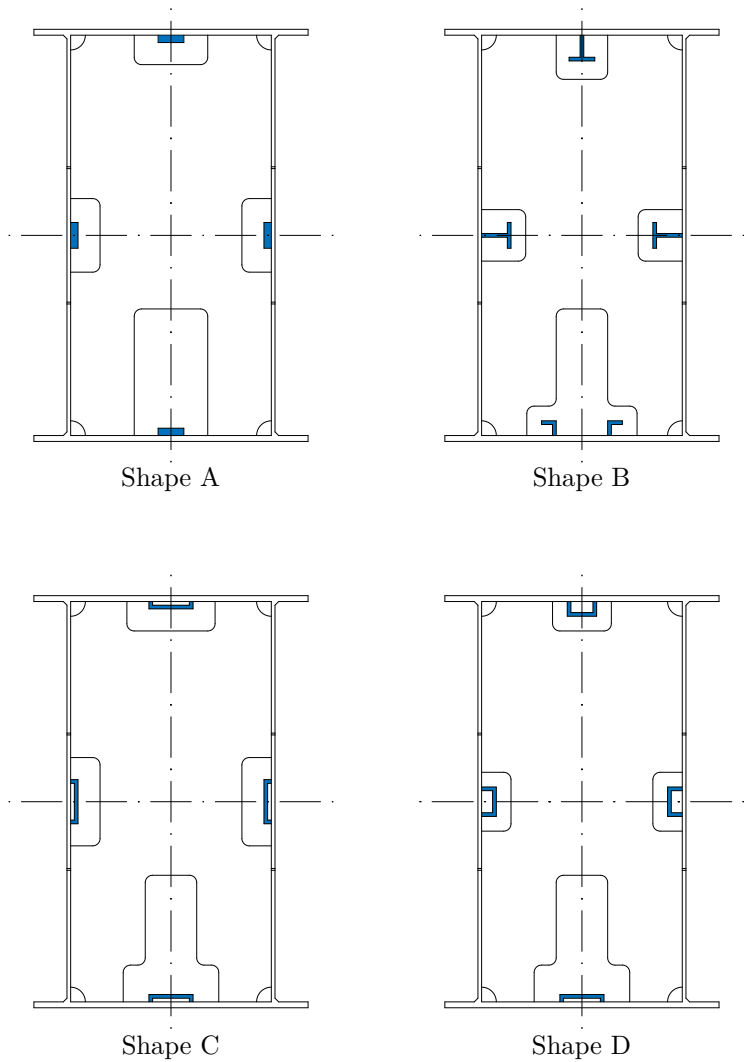
Shape C

Shape D

Figure 3.11: Different shape designs of stiffening ribs in order to reinforce the plates

Simply supported edges

Load application
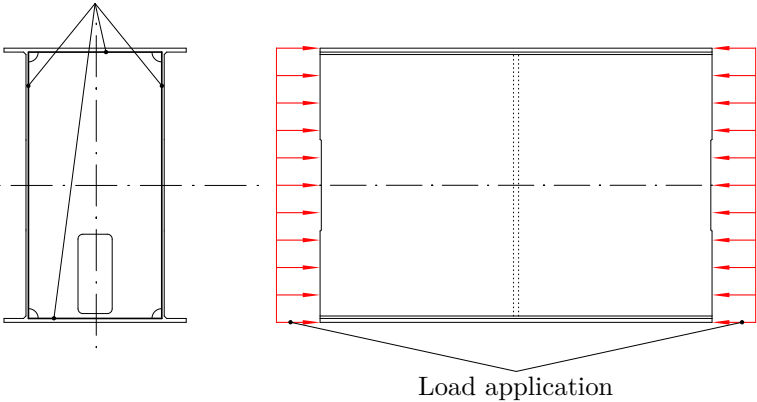
Figure 3.12: Supporting conditions during stability analyses

Buckling of
web plate
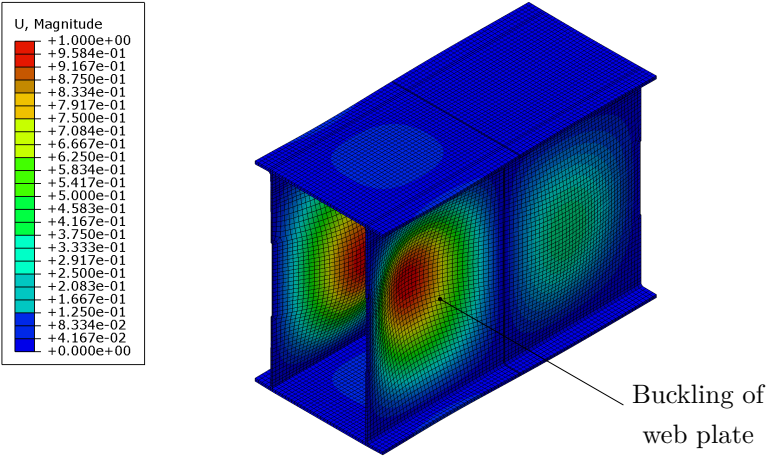
Figure 3.13: Different approaches in order to reinforce critical plates

plates tend to buckle and are therefore also the vulnerable component zones. Accordingly, it is advisable to reinforce the area in the form of stiffening ribs. Stability analyses are also carried out for the individual

Table 3.2: Resulting reinforcement factors with regard to the first buckling mode

Shape Type	First eigenvalue N_c [kN]	$N_c/N_c^* - 1$
Reference shape	$1.2786 \cdot 10^3$	0.0000
Shape A	$2.6412 \cdot 10^3$	1.0657
Shape B	$3.4057 \cdot 10^3$	1.6635
Shape C	$2.9035 \cdot 10^3$	1.2708
Shape D	$3.4165 \cdot 10^3$	1.6720

types; an evaluation is given in table 3.2. While type A provides the smallest reinforcement effect, the largest increase in the first eigenvalue can be achieved with the aid of type D. This is due in particular to the fact that, among other things, the original buckling field is reduced by the parallel webs. Furthermore, the greater extensions of the ribs to the inside of the profile have a positive effect compared to type C, since this increases the stiffness of the plate in x_2-direction and thus hinders the plate in its deflection in the preferred direction. This is also the main reason for the strengthening effect of type B. Based on the results,
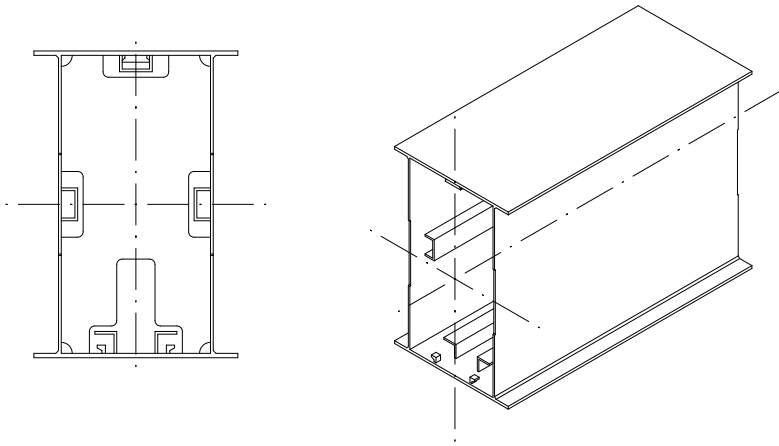
Figure 3.14: Final design of the main segment

type D is selected to reinforce the side web plates and the upper chord plate. For the bottom chord plate, the shape of type B is planned, as this provides a greater effect in comparison to type D. Due to the space required by the traction mechanism, the design of the shape of the ribs is much more limited in this area. Figure 3.14 shows the final design of the main segment. Here, the parameters depicted in figure 3.9 are valid as well. However, the dimensions of the stiffening ribs are to be designed individually.

Connecting Element

Connecting elements are used at the joints to ensure a form-fit connecting between the segments and fulfill basically the function of a removable bulkhead plate. Here, the alignment pins also serve to transmit shear forces. One connecting element is plate-shaped and possesses a geometrically identical recess as the one in the main segment, since here too, it must be guaranteed that the tensile member can pass the connecting element without being disturbed. The external dimensions correspond exactly to the internal dimensions of the main segment, thus enabling the connecting elements to be inserted, see figure 3.15. On the sides, there are elongated plates in horizontal direction, on which again spigots are attached. These engage with the according negatives in the web plates of the main segments. The outer edges of a connecting element are bevelled to provide again space for the adjacent welding seams of the main segment. The assembly procedure is shown in figure 3.16.

Preload Segment

The preload segment is similar in shape to the main segment and also possesses a bulkhead plate[2] for additional stabilization. The internal dimensions correspond to those of the main segment, see figure 3.17. Basically, the preload segment consists of an upper and a lower chord, which are connected by two vertically arranged web plates. It has a

---

[2] The exact location of the bulkhead plate depends on the total length of the preload segment and must be positioned individually.
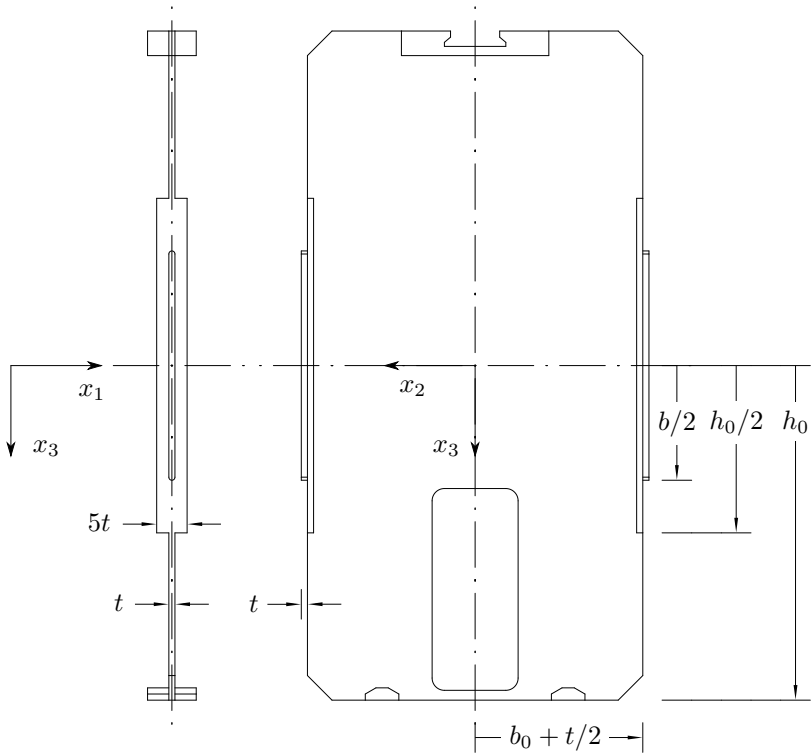
Figure 3.15: Major dimensions of the connecting element

total length of l_s^* and can be divided into two sections by design. The force application area requires a special local design due to the high pretensioning forces. In this area, local stress increases take place. For this reason, it is reasonable to extend the area in this region on which the forces can be distributed. SAINT-VENANT's principle states that an increase in stress appears in the area where the load is applied, however, these rapidly diminish with increasing distance from the point of force application [44, p. 92]. This effect is preliminary taken into account by the reinforcing plates shown in figure 3.18, which possess a length h measured from the contact surface. In total, the resulting width for a

Connecting element

Main segments
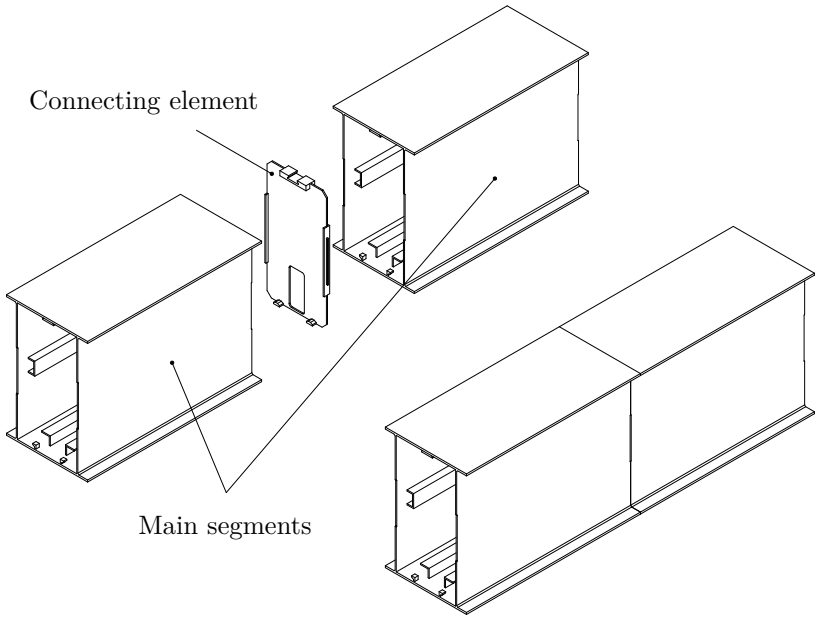
Figure 3.16: Insertion of the connecting element

web is increased to $3t$. In the lower area of the reinforcement plates the contact surface is bevelled by an estimated angle of $20°$ and is similar to a relief notch in its function. Through preliminary FE analyses, it was shown that under this angle, the local stresses can be largely reduced. The aim here is to make the flow of force smoother (see figure 3.18, detail A-A). In the upper area, the web plates are beveled by an angle of $45°$ to additionally stiffen the structure in this zone and approximately align with the resulting pressure cone. In the force application area, the connection to the endcarriages results in a high force development due to the shear force. For this reason, an auxiliary web plate can be optionally welded on at this point, offset by $90°$ to the x_1-axis, in order to be able to absorb the transverse forces accordingly. An additional plate of the same thickness is welded to the bottom chord. According
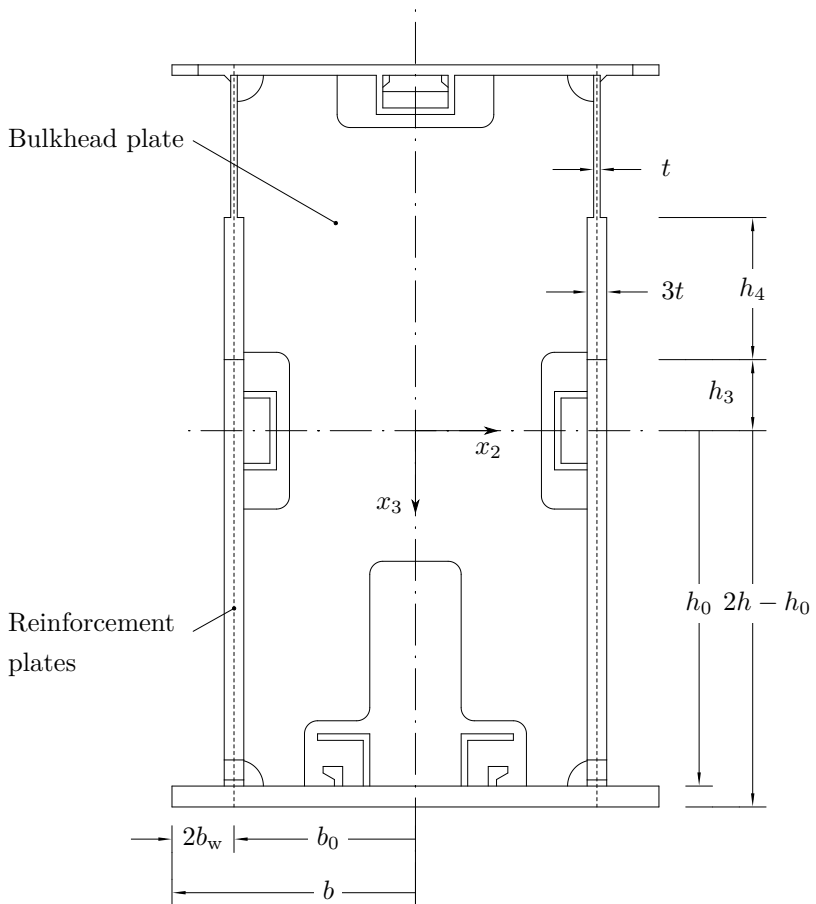
Figure 3.17: Dimensions of the preload segment (front view)

to DIN EN 1993-6 this is recommended to reduce the influence of the local load introduction by the trolley wheels [9, p. 24]. The free end is designed in the same way as the main segment. It also provides a recess in the web plates for the insertion of a connecting element.
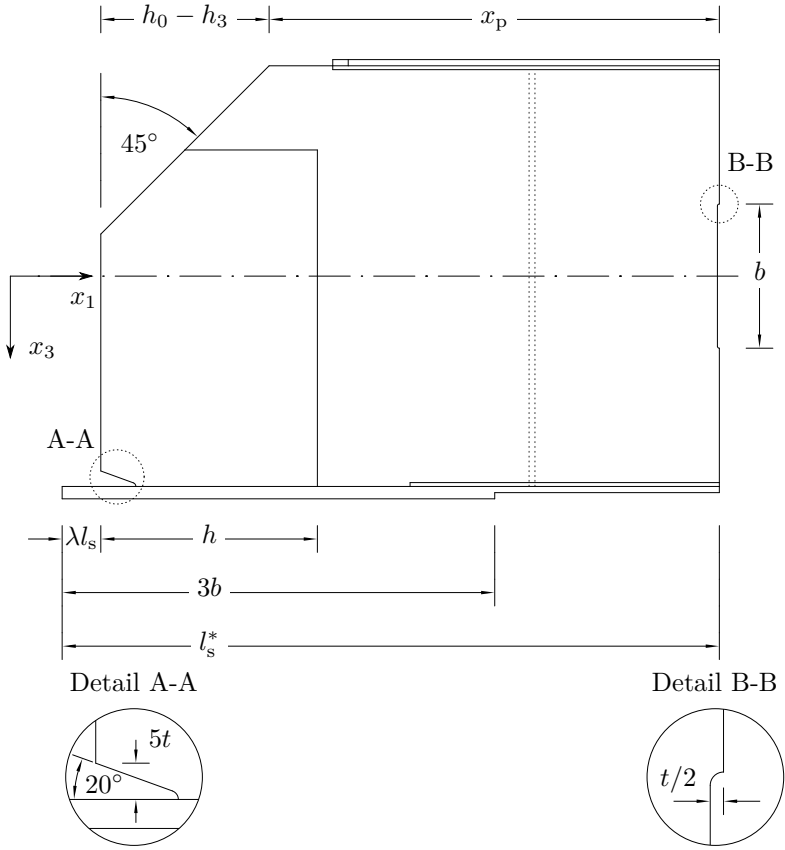
Figure 3.18: Dimensions of the preload segment (side view)

Stop Piece

Compared to the other components, the stop piece is both compact and robust, as the direct application of force occurs here due to the preload. The total length is λl_s and corresponds to a multiple of the defined segment length, see figure 3.19. The flat contact surface is identical to that of the preload segment and forms the contact surface for transmitting
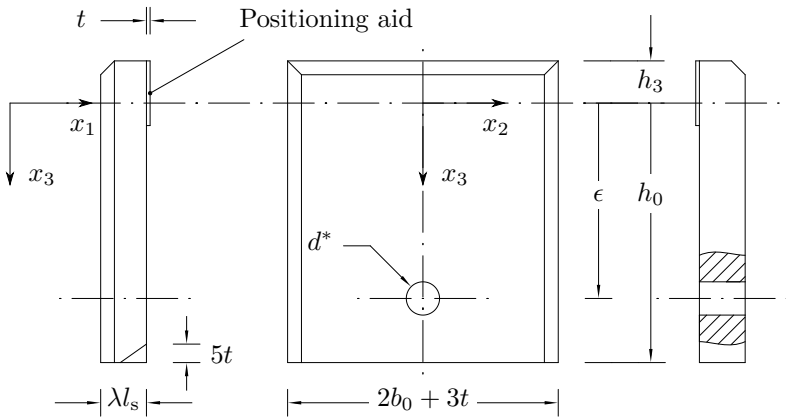
Figure 3.19: Major dimension of the stop piece

the compressive forces. As with the preload segment, the lower area is bevelled to make the force flow at the transition zone smoother. This results in a tapered shape of the stop piece, which serves to increase its rigidity. A through-hole is provided eccentrically so that the threaded rod of the traction mechanism can pass through the stop piece. The diameter d^* of the hole depends on the nominal diameter of the threaded rod.

3.3.2 Traction Mechanism

The traction mechanism consists of a combination of steel bars and threaded rods that are connected to each other to form a long bolt and correspond to the concept presented in [3]. In addition, these are further divided into additional and common threaded rods as well as additional and common steel bars, see figure 3.20. The threaded rods have a metric ISO thread and the material selected for the round steels is 42CrMoS4 (material number 1.7227), as this has a comparatively high yield strength of about $720 \, \text{N/mm}^2$ [45, p. 149]. According to VDI 2230, a minimum length of the engaged thread of approximately $0.7 \, d_\text{N}$ (d_N as the nominal diameter) is recommended considering 42CrMoS4,

71
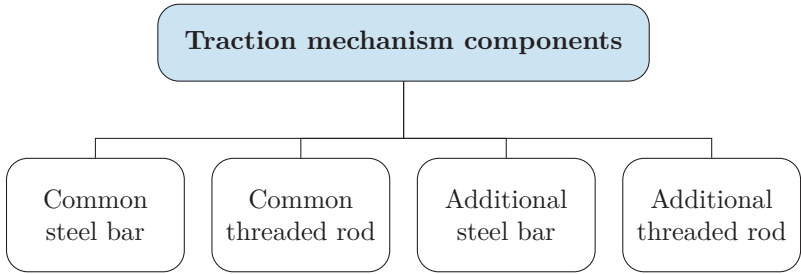
Figure 3.20: Components of the traction mechanism

however, $1.1\,d_{\mathrm{N}}$ is selected for the connection in order to facilitate the mounting [11, p. 101]. Basically there are common round steels with
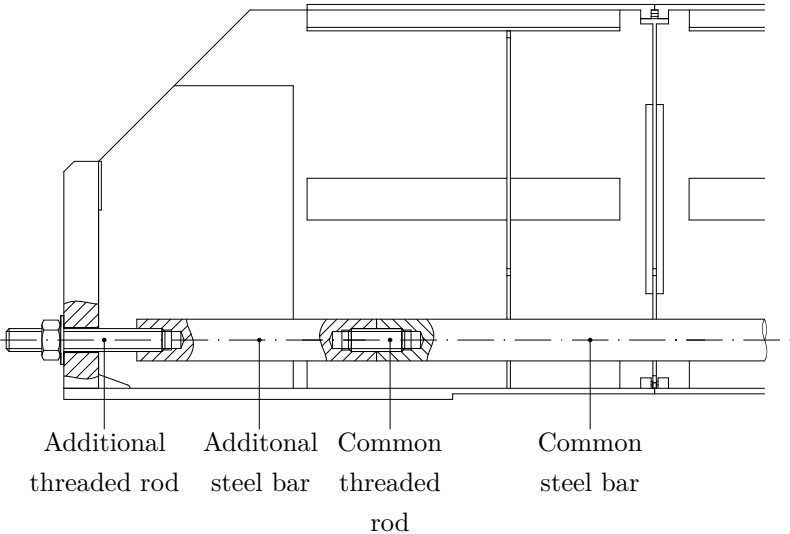
Figure 3.21: Section view of the preload zone

a length l_{r} and the matching common threaded rods with a length of $2.2\,d_{\mathrm{N}}$. This combination is used in the inner region of the structure. At the outer areas additional steel bars and the according additional

threaded rods are used, each with an individual length l_r^*. The threaded rods penetrate the stop pieces at the ends through their through-holes and are fastened with a shim and nut, see figure 3.21.

By tightening the nuts, the desired prestressing force is applied, which acts as a tensile force in the traction mechanism and in turn as a compressive force in the segments through contact with the stop piece. Here, figure 3.22 shows a qualitative course of the force flow. It can be seen how the tensile force is transmitted to the preload segment via the nut and the shim and then acts here as a compressive force. While the upper part provides a comparatively large area to which the force can be distributed, stress concentrations are to be expected in the lower area. This is due on the one hand to the smaller area and on the other hand to the transition from the web plate to the welded-on lower chord plate. This area is additionally highlighted in the figure 3.22. Finally,

Area of stress concentration
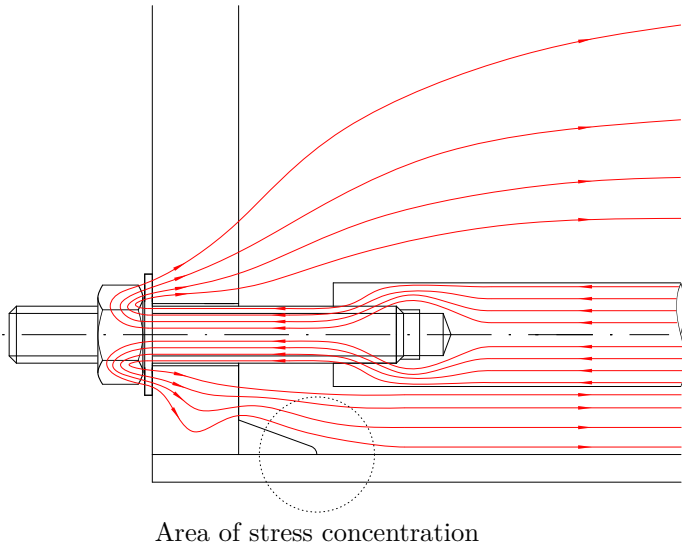
Figure 3.22: Section view of the preload zone, expected stress concentrations

the traction mechanisms relevant for the work are summarized in table A.1.

3.3.3 Entire Construction

In the previous section, all the components involved in the construction of the segmented crane bridge were presented. These can be divided into two groups: the girder components and the traction mechanism components. For practical application, it is planned that first the traction mechanism is assembled and then the girder components are threaded onto it. Finally, the prestressing force is applied and the girder is ready for use. The entire construction is shown as an example in figure 3.23.
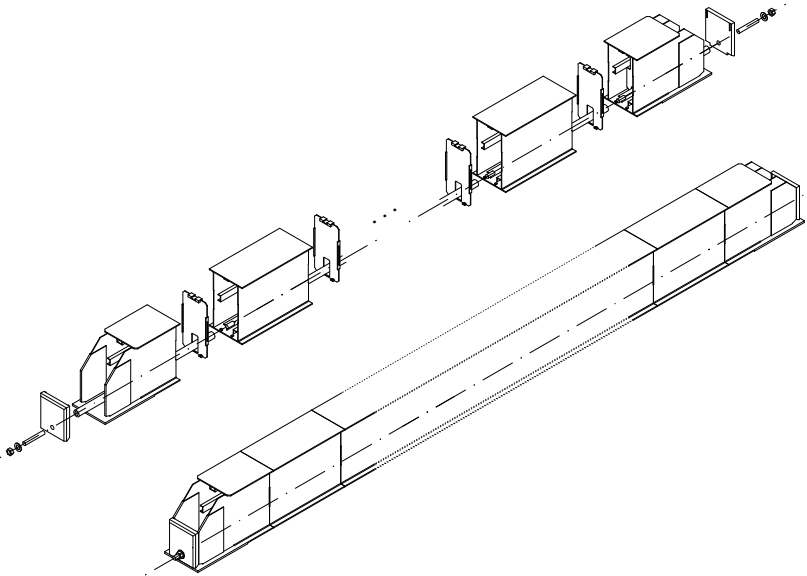
Figure 3.23: Assembly sequence

It can be seen how the initially individual, loose components are assembled into a plug-in construction and then braced together. Disassembly after operation time then follows in reverse order.

4 Dimensioning and Development of Constraint Functions

> *Mathematics is the only perfect way*
> *to fool yourself.*
> - A. Einstein

A general design proposal for the segmented and prestressed crane girder is now available based on the work carried out in the previous chapter 3. The involved components are given and their key dimensions are suitably parameterized. It is now of particular interest to work out, which boundary conditions the design must fulfill or which limit values must be observed in order to consider a real application. Based on already known design specifications in crane construction, the system has to be examined in this context to determine which additional constraints occur due to the novel type of design in contrast to conventional bridge cranes. The basis for this is *modeling*, the focus of which is the abstraction of the predicted behavior and the underlying properties of the system in the form of a mechanical substitute model. The corresponding implementation in a mathematical model is carried out on the basis of the fundamentals presented in chapter 2.

4.1 Initial Considerations and Basic Models

It is well known that physical models do not represent the true facts of the situation, they rather describe the observations or experiences made with sufficient accuracy. If they are of satisfying quality, they can be used to make statements about the physical behavior of the system under consideration. With regard to the segmented girder, a

mechanical substitute model is worked out in the following, which forms the foundation for the later dimensioning task.

4.1.1 Assumptions

Within the course of the modeling, it is basically assumed that the entire segmented crane bridge can be represented as a continuous beam of a total span width denoted by $2l_0$, in case it is always under compressive stress in the upper and lower chord. This ensures the component bonding and prevents any gaping according to requirement **FR4**. In addition, the beam is simply supported.

Furthermore, it possesses cross-sectional quantities determined by its geometry. Local changes in geometry are neglected, including the specific design of the preload segment, the connecting elements as well as the welded-in bulkhead plates, however they possess a positive[1] influence on the stiffness. The tensile member is also modeled as a continuous beam with a circular cross-sectional area, a disturbance of the stresses at the connection joint is neglected as well.

Moreover, a homogeneously distributed material with isotropic and linear elastic behavior is assumed. The materials listed in DIN EN 13001-3-1, which are used in crane construction, serve as guidelines [15, p. 13].

In contrast to the loads considered in literature, the modeling assumes the self-weight of the crane bridge as a constantly distributed line load μ. With the area of the cross-section A_1 and a constant density ρ, we then obtain

$$\mu = \rho A_1 \mathrm{g} \tag{4.1}$$

for the continuously distributed self-weight. Regarding to the achievable pre-deformations caused by the eccentrically applied prestressing force, the self-weight plays a significant role since its influence increases with increasing dimensions of the crane bridge. With the aid of the pre-

---

[1] In terms of providing additional stiffness.

deformation the initially straight beam can be transformed to a slightly curved beam, according to section 2.2.2.

In addition to its self-weight, the crane bridge is subjected to external loads which are transmitted to the lower chord at points via the wheels (total wheel base assumed to be $2l_w$) of the trolley. If there is no further information available, it is assumed, that the self-weight m_t of the traveling trolley is a multiple α_w of the nominal load m_0, i.e. $m_w = \alpha_w\, m_0$ with $\alpha_w \in (0,1)$. This leads to the resulting force in x_3-direction

$$F_3 = (m_0 + m_w)\mathrm{g} = (1 + \alpha_w)\, m_0\mathrm{g} \tag{4.2}$$

whereby it is additionally postulated that the total load is distributed evenly over all four wheels. Then, it follows for a force transmitted by one wheel

$$R_3 = \frac{F_3}{4}. \tag{4.3}$$

The even distribution also leads to the circumstance that no torsional moments occur about the x_1-axis. In case of a (rigid) bumper impact it is assumed, that the resulting force acting due to the acceleration in x_2-direction is determined by $F_2 = \lambda_2\, F_3$ with $\lambda_2 \in (0,1)$. This force is also assumed to be distributed equally over all four wheels of the traveling trolley.

$$R_2 = \frac{F_2}{4} \tag{4.4}$$

It should be mentioned that the estimation of the forces acting on the girder during a bumper impact strongly depend on the material of the bumpers and the velocity of the traveling bridge crane. For this reason, this general assumption is made to enable a consideration of the additional load.

On this basis, the crane bridge can be modeled within the framework of beam theory. As a modeling strategy the linear beam theory of first order is applied in analogy to literature [37], since small deflections of the main girder in comparison to its total span width are expected. However, the beam theory of second order is applied to estimate the

deflection of the tensile member running inside. Due to its low flexural stiffness the impact of the tension forces increases.

4.1.2 Mechanical Model

With the aid of the elaborated assumptions it is now possible to graphically represent the corresponding mechanical substitute model, which is shown in figure 4.1. Here, the schematically depicted traveling trolley is
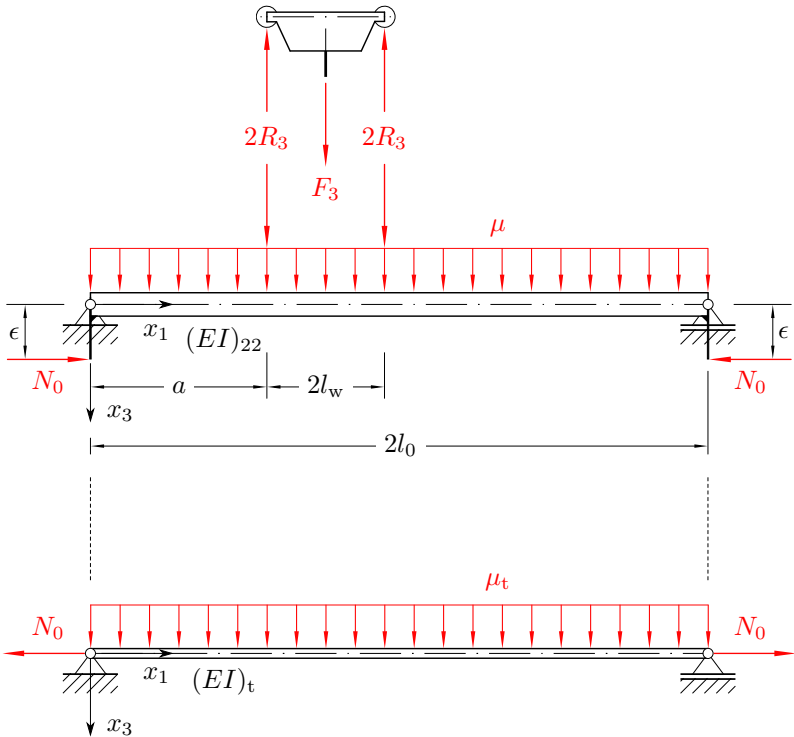
Figure 4.1: Basic mechanical model

separated from the beam by means of a theoretical cut to visualize the

acting forces. Since the situation can be referred to a two-dimensional problem due to the symmetry, the forces induced via the wheels result in $2R_3$. In order to allow the possibility of different trolley positions represented by the model, it is positioned at an arbitrary position a along the x_1-axis. In this connection, the first wheel of the traveling trolley is the reference point with respect to the underlying coordinate system.

The beam has a total length of $2l_0$ according to the span width and a flexural stiffness $(EI)_{22}$ with respect to the x_2-axis, respectively $(EI)_{33}$ in terms of bending about the x_3-axis. In addition to the loads in x_3-direction by the nominal load, the beam is also loaded along the x_1-axis by the prestressing force N_0. The prestressing force is caused by tightening of the tensile member, which is then loaded in x_1-direction on tension. The axial force thus acts as an internal force in the entire system. The tensile member is considered to be a beam as well with a flexural stiffness[2] $(EI)_t$, which is loaded in x_3-direction purely by its distributed self-weight μ_t. In this context, it is also required that the tensile member is only connected to the beam at the supporting points in the through-holes of the stop pieces. Since the contact area of the shim is negligible compared to the span width, we additionally assume that the transmittable moment at this point is also very small and has no significant relevance for the deformations that occur. If we now neglect this moment, the tensile member is rotatable mounted inside the stop pieces and thus simply supported as well. This leads to the circumstance that both components are not coupled with each other in terms of a bending moment and that they can be considered separately against the background of their deflections.

4.2 Geometric Quantities

Within the mechanical substitute system, geometrical quantities appear which characterize the individual components regarding to their specific shape. These are of particular importance with respect to the determi-

---

[2] Independent from the axes due to its circular cross-section.

nation of the deformation behavior and the mechanical stresses. In this context, the dimensions of the weld seams are neglected.

Cross-sectional Area of the Main Girder

As shown in figure 3.9, the cross-section of the main girder can be interpreted as a surface composed of individual discrete geometries. Accordingly, the following relationship results for the entire area.

$$A_1 = 4(b - (b - t)\eta)h$$
$$A_1 = \theta_1 h, \quad \theta_1 = f(\eta, b) \tag{4.5}$$

Here, the factor θ_1 is introduced in order to separate the external height h from the other parameters and will be used in the further course of the work.

Second Moments of Area

In case of bending about the x_2- or x_3-axis, the respective second moments of area must be known to determine both the deflections occurring and the bending stresses associated with them. Due to the axial symmetry, the deviation moments disappear. In terms of bending about the x_2-axis, the corresponding second moment of area of the surface is to be calculated according to eq. (4.6).

$$I_{22} = \frac{4}{3}(b - (b - t)\eta^3)h^3$$
$$I_{22} = \theta_{22}h^3, \quad \theta_{22} = f(\eta, b) \tag{4.6}$$

For bending about the x_3-axis the moment of inertia follows to

$$I_{33} = \left(\frac{8}{6}(1 - \eta)b^3 + 4t\eta\beta^2 b^2 + \frac{1}{3}\eta t^3\right)h$$
$$I_{33} = \theta_{33}h, \quad \theta_{33} = f(\eta, b, \beta). \tag{4.7}$$

As with the determination of the cross-sectional area A_1, we interpret the cross-section in such a way that it is composed of individual areas. Here, the auxiliary factors θ_{22} and θ_{33} are introduced as well to separate the external height h.

First Moments of Area

During operation the girder is loaded by a force perpendicular to the centroid axis. Although the normal stresses dominate in terms of magnitude, the associated shear stresses due to bending must also be taken into account for the sake of completeness. When calculating the corresponding shear stresses, the so-called first moments of area appear in addition to the second moments of inertia. For bending about the x_2-axis, the maximum first moment of area is to be calculated as follows.

$$S_2(x_3) = \begin{cases} bh^2 + (t-b)(\eta h)^2 - tx_3^2 & 0 \leq x_3 \leq \eta h \\ b(h^2 - x_3^2) & \eta h \leq x_3 \leq h \end{cases} \tag{4.8}$$

Similarly, the first moment of area in case of bending about the x_3-axis is given by the equations below.

$$S_3(x_2) = \begin{cases} (h - \eta h)(b^2 - x_2^2) + 2\eta h \beta bt & 0 \leq x_2 \leq \beta b - t/2 \\ (h - \eta h)b^2 + \left(\beta b + \dfrac{t}{2}\right)\eta h - hx_2^2 & \beta b - t/2 \leq x_2 \leq \beta b + t/2 \\ (h - \eta h)(b^2 - x_2^2) & \beta b + t/2 \leq x_2 \leq b \end{cases} \tag{4.9}$$

In contrast to the second moments of area, these depend on the individual position within the $x_2 x_3$-plane and are defined in sections due to the abrupt changes in geometry.

4.3 Occurring Loads

The investigation of the occurring loads is of great importance for the dimensioning. They decisively define which internal mechanical stresses

act in the material. As is well known, the internal bending moments must be determined for the normal stresses and the shear forces for the assigned shear stresses. These are to be derived in the following sections.

4.3.1 Bending Moments and Shear Forces

First of all, bending about the x_2-axis is considered. Here, the free body diagram of the girder with all occurring forces in figure 4.2 serves as the baseline situation. In this context, we introduce another dimensionless
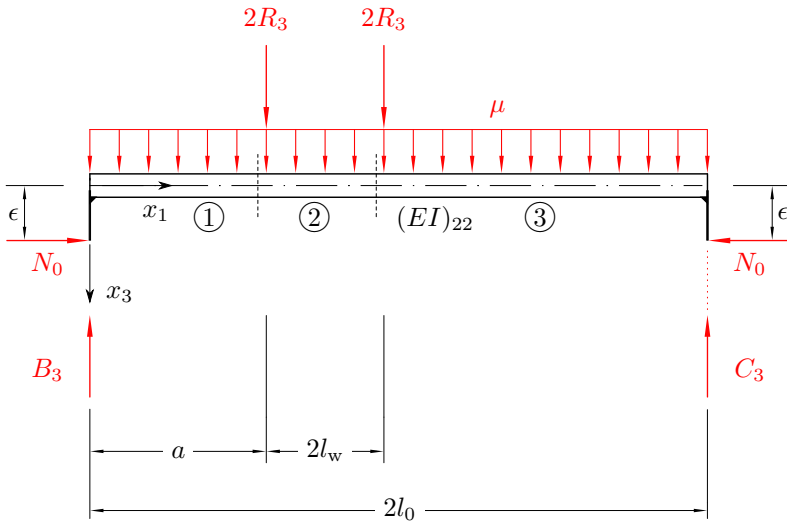
Figure 4.2: Free body diagram of the girder in terms of bending about the x_2-axis

variable denoted by α_1 that indicates the ratio between the wheelbase of the traveling trolley and the span width.

$$\alpha_1 = \frac{l_w}{l_0} \tag{4.10}$$

The concentrated forces applied due to the wheel contacts lead to a load profile of the beam defined in sections. The sections "1", "2" and "3" are determined accordingly by two theoretical cuts (represented in figure 4.2 by vertical dashed lines). After the supporting forces B_3 and C_3 have been calculated and the equilibria of forces and moments have been established, we obtain the following expressions for the load curves by performing several transformations. For the shear force we find:

$$Q_{31}(x_1) = 2R_3 \left(2 - \frac{\alpha_1 l_0 + a}{l_0} \right) + \mu(l_0 - x_1)$$

$$Q_{32}(x_1) = 2R_3 \left(1 - \frac{\alpha_1 l_0 + a}{l_0} \right) + \mu(l_0 - x_1)$$

$$Q_{33}(x_1) = -2R_3 \frac{\alpha_1 l_0 + a}{l_0} + \mu(l_0 - x_1) \tag{4.11}$$

while its single components are valid in the following sections.

$$Q_3(x_1) = \begin{cases} Q_{31}(x_1) & 0 \leq x_1 \leq a \\ Q_{32}(x_1) & a \leq x_1 \leq a + 2\alpha_1 l_0 \\ Q_{33}(x_1) & a + 2\alpha_1 l_0 \leq x_1 \leq 2l_0 \end{cases}$$

In the context of the moment curve, we define the *initial bending moment* M_0 induced by the eccentrically tightening of the traction mechanism.

$$M_0 = N_0 \epsilon \tag{4.12}$$

Then the components of the moment curve are defined by eq. (4.13)

$$M_{21}(x_1) = -\frac{1}{2}\mu x_1^2 + \left(\mu l_0 + 2R_3 \left(2 - \frac{\alpha_1 l_0 + a}{l_0} \right) \right) x_1 - M_0$$

$$M_{22}(x_1) = -\frac{1}{2}\mu x_1^2 + \left(\mu l_0 + 2R_3 \left(1 - \frac{\alpha_1 l_0 + a}{l_0} \right) \right) x_1 + 2R_3 a - M_0$$

$$M_{23}(x_1) = -\frac{1}{2}\mu x_1^2 + \left(\mu l_0 + 2R_3 \frac{\alpha_1 l_0 + a}{l_0} \right) x_1 + 4R_3(\alpha_1 l_0 + a) - M_0$$

$$\tag{4.13}$$

83

and are analogously to the shear force valid in the same sections.

$$
M_2(x_1) = \begin{cases} M_{21}(x_1) & 0 \le x_1 \le a \\ M_{22}(x_1) & a \le x_1 \le a + 2\alpha_1 l_0 \\ M_{23}(x_1) & a + 2\alpha_1 l_0 \le x_1 \le 2l_0 \end{cases}
$$

As soon as the girder undergoes a bending about the x_3-axis due to a bumper impact, the same procedure is executed according to figure 4.3 in order to identify the load profile. For the shear force we find:
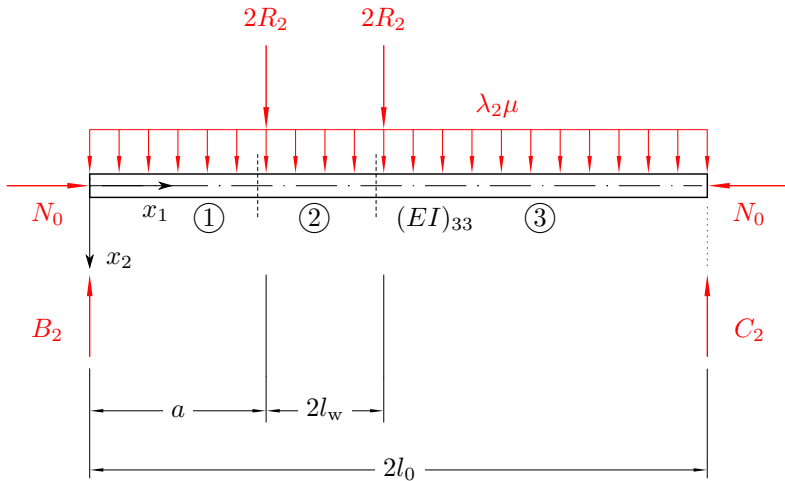
Figure 4.3: Free body diagram of the girder in terms of bending about the x_3-axis

$$
Q_{21}(x_1) = 2R_2 \left(2 - \frac{\alpha_1 l_0 + a}{l_0} \right) + \lambda_2 \mu(l_0 - x_1)
$$

$$
Q_{22}(x_1) = 2R_2 \left(1 - \frac{\alpha_1 l_0 + a}{l_0} \right) + \lambda_2 \mu(l_0 - x_1)
$$

$$
Q_{23}(x_1) = -2R_2 \frac{\alpha_1 l_0 + a}{l_0} + \lambda_2 \mu(l_0 - x_1) \tag{4.14}
$$

and for the bending moment:

$$M_{31}(x_1) = -\frac{1}{2}\lambda_2\mu x_1^2 + \left(\lambda_2\mu l_0 + 2R_2\left(2 - \frac{\alpha_1 l_0 + a}{l_0}\right)\right)x_1$$

$$M_{32}(x_1) = -\frac{1}{2}\lambda_2\mu x_1^2 + \left(\lambda_2\mu l_0 + 2R_2\left(1 - \frac{\alpha_1 l_0 + a}{l_0}\right)\right)x_1 + 2R_2 a$$

$$M_{33}(x_1) = -\frac{1}{2}\lambda_2\mu x_1^2 + \left(\lambda_2\mu l_0 + 2R_2\frac{\alpha_1 l_0 + a}{l_0}\right)x_1 + 4R_2(\alpha_1 l_0 + a).$$

$$(4.15)$$

Both curves are valid in the same individual ranges as in case of bending about the x_2-axis. Thus, the load profiles are clearly determined and can be used to calculate the internal mechanical stresses. Concluding, figure 4.4 shows qualitatively the traveling trolley running on the lower chord and the corresponding load curves for different positions a_i in terms of bending about the x_2-axis.

4.3.2 Determination of the Initial Bending Moment

The previously introduced initial bending moment M_0 is a key element in the further course of the work. Different pre-deformations can be achieved depending on the prestressing force. However, the challenge is to provide a correspondence between the deformation and M_0. An approach to get this problem solved is the application of the beam theory and the consideration of the resulting deflection during operation. As already pointed out, the common regulations in crane construction provide limit values for the maximum deflection of the crane girder [23]. The highest value will occur, once the traveling trolley is positioned directly in the middle of the beam. In that case, we can utilize the system symmetry. Here, figure 4.5 illustrates the situation as well as the corresponding freebody diagram containing the involved forces and moments.

By establishing the equilibria of forces and moments, the supporting reaction B_3 can be determined. Due to the concentrated force induced by $2R_3$, the beam deflections are again defined in certain areas. However, only the second section at the position $x_3 = l_0$ is relevant, since the
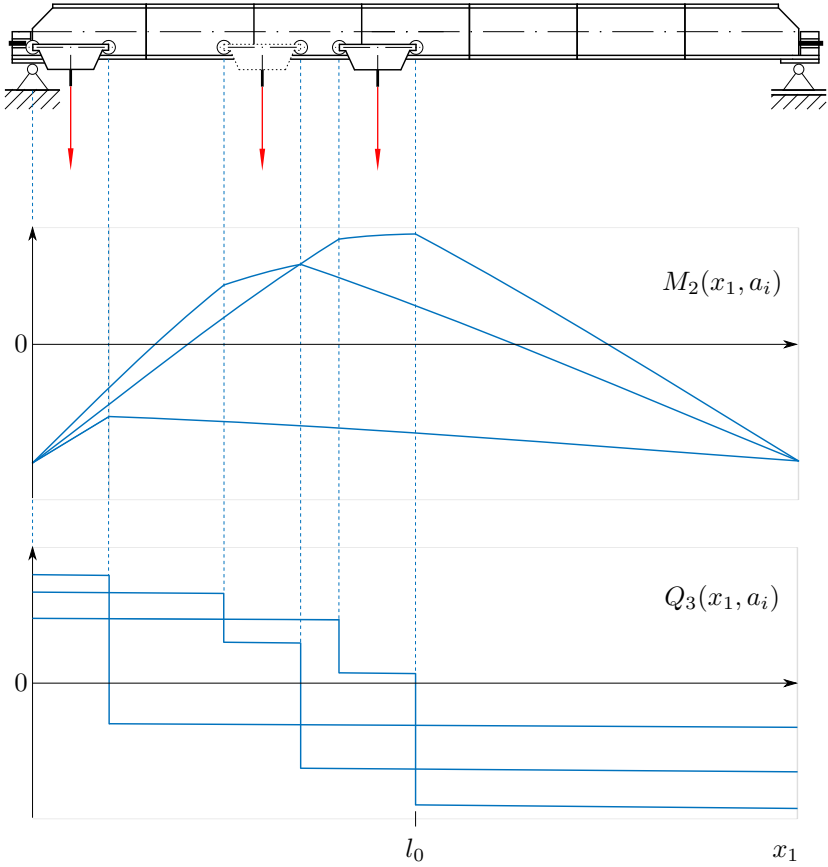
Figure 4.4: Qualitatively depicted load curves considering bending about the x_2-axis

maximum deflection appears here. Considering the following boundary conditions

$$w(0) \stackrel{!}{=} 0 \qquad\qquad w'(l_0) \stackrel{!}{=} 0$$
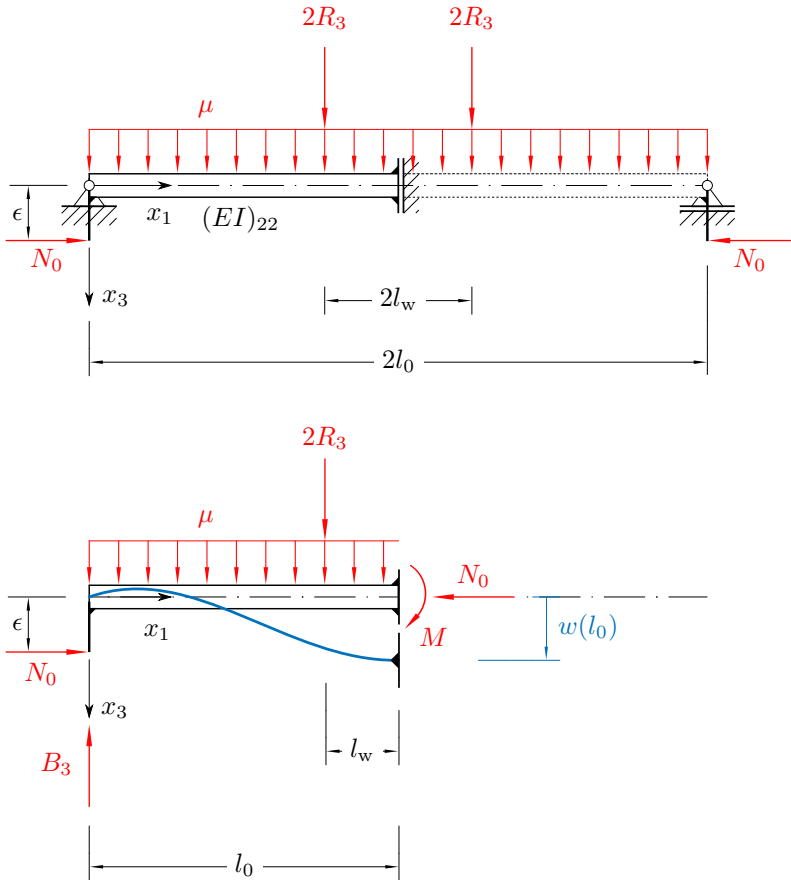
Figure 4.5: Maximum deflection during operation in x_3-direction

the differential equations as well as the appearing integration constants can be solved. Then, we obtain for the second section at $x_1 = l_0$ the following relation.

$$(EI)_{22}w(l_0) = \frac{5}{24}\mu l_0^4 + R_3 l_0(1 - \alpha_1) - \frac{1}{2}M_0 l_0^2 - \frac{1}{3}R_3 l_0^3(1 - \alpha_1)^3$$

(4.16)

87

We now require, that the occurring deflection is determined by

$$w(l_0) = \delta l_0 \tag{4.17}$$

where $\delta \in [0, 1)$ describes the dimensionless ratio between the maximum deflection $w(l_0)$ and the span width l_0. Subsequently, eq. (4.16) can be rearranged with respect to the initial bending moment M_0 which leads to the desired relation.

$$M_0 = \frac{5}{12}\mu l_0^2 + \frac{2}{3}(\alpha_1^3 - 3\alpha_1^2 + 2)R_3 l_0 - (EI)_{22}\frac{2\delta}{l_0} \tag{4.18}$$

With eq. (4.12) and eq. (4.18) a relation between the axial prestressing force N_0, the eccentricity ϵ and the occurring deformation determined by δl_0 is now available. It can be seen that the initial bending moment decreases with an increasing flexural stiffness denoted by $(EI)_{22}$. This circumstance is discussed in chapter 5 in more detail. On the other hand it takes greater values once the ratio δ decreases.

4.3.3 Investigation of the Maximum Bending Moment

Figure 4.6 shows the crane bridge under vertical load induced by the traveling trolley and the corresponding, qualitatively represented course of the bending moment, whereby a different load over the wheels is now considered. The factor $\rho_3 \geq 1$ takes this circumstance into account. Here, an alternative normal force N_0^* is also assumed, which leads to the initial bending moment M_0^*. This differs due to the position of the maximum deflection of the beam.

Based on the characteristics of the section-wise defined moment curve $M_2(x_1)$, it can be seen that the maximum bending moment will occur in case of vertical load application at the edge of section "2" and depends significantly on the reference position a of the left wheel. Since the initial bending moment primarily determines the extent to which the entire function graph is shifted in a negative direction, it is neglected at first.
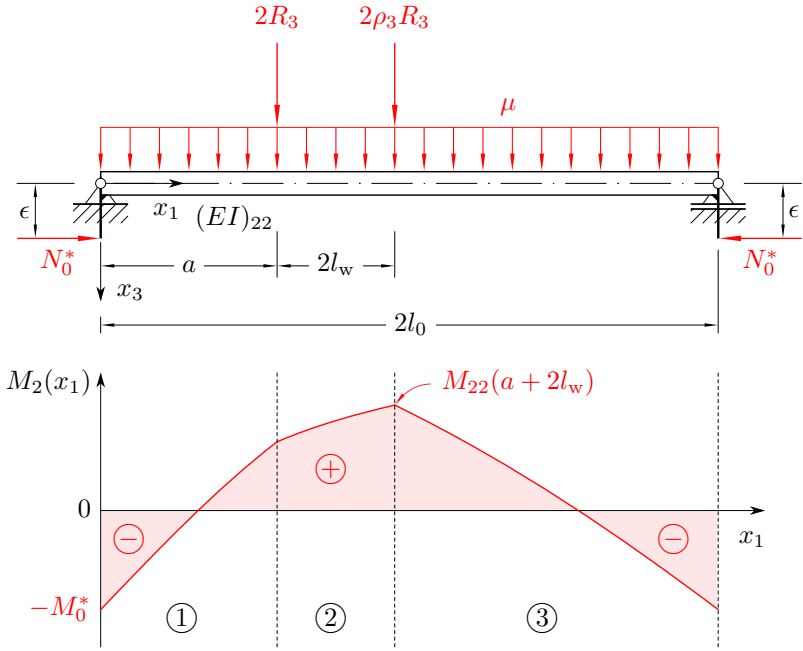
Figure 4.6: Maximum bending moment during vertical load application

In the following, it is of interest at which a' the bending moment becomes maximum and which value $M'_{22}(a')$ it takes. For this purpose, the support reactions and the internal forces are determined again. For the support force $B_3(a)$ at $x_1 = 0$, we obtain the following expression under consideration of the equilibrium conditions.

$$B_3(a) = \left(2 - \frac{a}{l_0} + \left(2 - \frac{a}{l_0} - 2\alpha_1 \right) \rho_3 \right) R_3 + \mu l_0 \tag{4.19}$$

Furthermore the corresponding bending moment at $x_1 = a + 2l_\mathrm{w} = (a/l_0 + 2\alpha_1)l_0$ follows to

$$M_{22}(a) = -\frac{1}{2}\mu l_0^2 \left(\frac{a}{l_0} + 2\alpha_1\right)^2 + B_3 \cdot \left(\frac{a}{l_0} + 2\alpha_1\right) l_0 - 4R_3\alpha_1 l_0.$$
(4.20)

The determination of a' leads to a non-restricted extreme value problem. In this framework it is required that for a certain a' the derivative of the term of the moment curve becomes exactly zero, i.e.

$$\frac{\mathrm{d}M_{22}(a)}{\mathrm{d}a} \stackrel{!}{=} 0.$$
(4.21)

By calculating of the derivative and some transformations one obtains

$$a' = \frac{(2 + (2 - \alpha_1)\rho_3 - 2\alpha_1(1 + \rho_3)) R_3 l_0 + \mu l_0^2(1 - 2\alpha_1)}{2(1 + \rho_3)R_3 + \mu l_0}$$
(4.22)

$$\left(\frac{a'}{l_0}\right) = \frac{(2 + (2 - \alpha_1)\rho_3 - 2\alpha_1(1 + \rho_3)) R_3 + \mu l_0(1 - 2\alpha_1)}{2(1 + \rho_3)R_3 + \mu l_0}$$
(4.23)

for the position of the left wheel of the traveling trolley at which the bending moment becomes maximum[3]. The value for the corresponding bending moment is given by

$$M'_{22}(a') = \frac{(2(1 + \rho_3 - \alpha_1)R_3 + \mu l_0)^2}{4(1 + \rho_3)R_3 + 2\mu l_0}l_0.$$
(4.24)

With the help of the derived equations, it is then to be investigated to what extent the maximum bending moment $M'_{22}(a')$ exceeds the bending moment at $x_1 = (1-\alpha_1)l_0$ considering an exactly central trolley position. For this purpose, we introduce the dimensionless factor ϕ,

---

[3] Since it is already known that this is a maximum, an investigation of the extremum using the second derivative can be dispensed with.
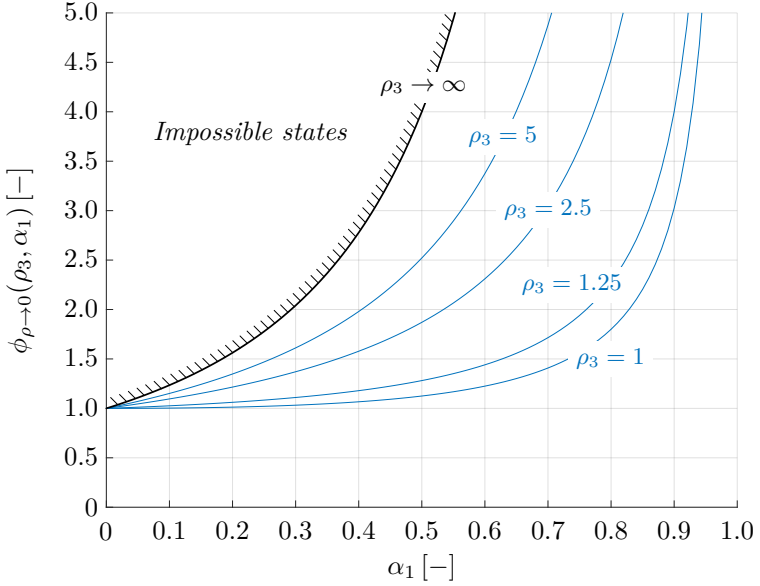
Figure 4.7: Amplification factor for different ρ_3

which is defined as follows.

$$\phi = \frac{M'_{22}(a')}{M_{22}((1 - \alpha_1)l_0)} \tag{4.25}$$

With eq. (4.20) one thus obtains the following expression.

$$\phi = \frac{(2(1 + \rho_3 - \alpha_1)R_3 + \mu l_0)^2}{(2(1 + \rho_3)R_3 + \mu l_0)\left((2R_3 + \mu l_0)(1 - \alpha_1^2) + 2\rho_3 R_3(1 - \alpha_1)^2\right)} \tag{4.26}$$

Neglecting the self-weight of the girder leads to

$$\phi_{\rho \to 0} = \frac{(1 + \rho_3 - \alpha_1)^2}{(1 + \rho_3)(1 + (1 - \alpha_1)^2\rho_3 - \alpha_1^2)} \tag{4.27}$$

which then only depends on ρ_3 and α_1. In the same course follows

$$\left(\frac{a'}{l_0}\right)_{\rho\to 0} = 1 - \frac{1 + 2\rho_3}{1 + \rho_3}\alpha_1 \tag{4.28}$$

for the corresponding (dimensionless) position of the left wheel of the traveling trolley.

The function plot of $\phi_{\rho\to 0}$ is shown in figure 4.7 for different values of ρ_3. By taking a limit value ($\rho_3 \to \infty$), it can be seen that the amplification factor is limited. Furthermore, it turns out that $\phi_{\rho\to 0}$ provides small function values for small values of α_1. Thus, it can be shown that in the symmetrical load case ($\rho_3 = 1$) for an $\alpha_1 = 0.1^4$, the maximum moment is 1.0028 times higher than the bending moment $M_{22}((1 - \alpha_1)l_0)$ at central trolley position. This means an increase of $\approx 0.3\%$, which reveals that due to the further consideration of the safety factor γ_{M1}, the bending moment $M_{22}((1 - \alpha_1)l_0)$ can be assumed in terms of dimensioning.

Further Findings

So far, the initial bending moment has been neglected and it has been assumed that the maximum bending moment occurs at a'. This is valid if

$$M'_{22}(a') \geq M_0^* \tag{4.29}$$

is fulfilled, otherwise the maximum bending moment occurs at $x_1 = 0$. Due to the complexity of the term and the large number of parameters, no general statement can be made as to whether this condition always applies. Only for special cases such statements are possible.

Against this background, the case $\rho_3 = 1$ is considered at first, then $M_0^* = M_0$ is just valid and eq. (4.18) can be used. Furthermore $\rho \to 0$ is again taken into account. By introducing the factor $\omega^* = (EI)_{22}/(R_3 l_0^2)$

---

[4] Based on empirical values for usual ratios of the wheelbase to the span width of the crane bridge.

and performing several transformations, this leads to the following condition.

$$3\omega^*\delta \geq \alpha_1^3 - \frac{15}{4}\alpha_1^2 + 3\alpha_1 - 1 \qquad (4.30)$$

$$f^\delta(\omega^*, \delta) \geq f^{\alpha_1}(\alpha_1) \qquad (4.31)$$

In the context of a proof it is to be verified whether this condition is always true.

Proof. Let $\delta \in [0,1)$, $\alpha_1 \in (0,1)$ and $\omega^* > 0$, then applies

$$\forall \delta \in [0,1) \wedge \omega^* > 0 : f^\delta(\omega^*, \delta) \geq 0.$$

An evaluation at the interval boundaries gives $f^{\alpha_1}(0) < 0$ and $f^{\alpha_1}(1) < 0$. To examine whether $f^{\alpha_1}(\alpha_1)$ provides positive function values for $\alpha_1 \in (0,1)$, the extreme points are analyzed. Using the first derivative

$$\frac{\mathrm{d}f^{\alpha_1}(\alpha_1)}{\mathrm{d}\alpha_1} = 3\alpha_1^2 - \frac{15}{2}\alpha_1 + 3$$

one obtains by setting $\mathrm{d}f^{\alpha_1}(\alpha_1)/\mathrm{d}\alpha_1 = 0$ the extreme points

$$\alpha_{11} = 2 \wedge \alpha_{12} = \frac{1}{2}.$$

Here, only α_{12} is decisive, since this point lies in the interval of α_1. An analysis of the second derivative

$$\frac{\mathrm{d}^2 f^{\alpha_1}(\alpha_1)}{\mathrm{d}\alpha_1^2} = 6\alpha_1 - \frac{15}{2}$$

at $\alpha_1 = 1/2$ provides the following result.

$$\left.\frac{\mathrm{d}^2 f^{\alpha_1}(\alpha_1)}{\mathrm{d}\alpha_1^2}\right|_{\alpha_1=1/2} = -\frac{9}{2} < 0$$

It concludes that the extreme point is a maximum of $f^{\alpha_1}(\alpha_1)$ on the interval and that it is also negative. Consequently applies

$$\forall\,\alpha_1 \in (0,1) : f^{\alpha_1}(\alpha_1) < 0.$$

Since zero is not a negative number, it can be shown that the following condition is always satisfied.

$$f^{\delta}(\omega^*,\delta) > f^{\alpha_1}(\alpha_1) \tag{4.32}$$

$\square$

The proof indicates that even the strict inequality holds, i.e. that $M'_{22}(a') > M_0$ for $\rho_3 = 1$ and $\rho \to 0$ is always true.

4.4 Identification of Relevant Constraint Functions

In chapter 3 preliminary requirements were defined, which serve as guidelines for the construction. Taking into account the design of the segmented bridge crane girder, further constraints can be determined. These mainly cover the following areas:

- geometry,
- mechanical stresses,
- occurring deformations,
- permissible prestressing,
- elastic stability of the structure,
- serviceability and
- contour accuracy.

As part of the development of the constraint functions we will discover, that the previously defined term for the initial bending moment plays an essential role.

4.4.1 Constraint Functions Related to Geometry

Figure 4.8 shows the frontal section view of the main segment and all relevant parameters to be taken into account. Here, the distances s_2 [mm] and s_3 [mm] are introduced as additional quantities in terms of space reservation. First of all, geometrical conditions must be maintained in order to enable the depicted configuration. For instance, there is a minimum value for the inner width of the segment that must be achieved to enable the traction equipment to fit inside. From figure 4.8 we obtain the first geometric constraint defined by ineq. (4.34).

$$\beta b \geq \frac{1}{2}(d+t) + s_2 \tag{4.33}$$

$$g_1 = \beta b - \frac{1}{2}(d+t) - s_2 \geq 0 \tag{4.34}$$

Thus, a lower limit for the inner width is already determined. However, the wheel of the trolley must fit on the bottom flange. The weld seam is geometrically considered as well. Assuming that it is set up at an angle of about 45° with respect to the bottom chord, the horizontal length of the weld seam according to [43, p. 169] is estimated at

$$c = \sqrt{2} \cdot 0.70\, t = \sqrt{0.98}\, t. \tag{4.35}$$

This means that for a given half width b, the inner width is additionally limited upwards. We obtain

$$b - 2b_{\mathrm{w}} - \left(\sqrt{0.98} + \frac{1}{2}\right) t \geq \beta b \tag{4.36}$$

$$g_2 = b - 2b_{\mathrm{w}} - \left(\sqrt{0.98} + \frac{1}{2}\right) t - \beta b \geq 0 \tag{4.37}$$

from figure 4.8. In this context, first geometric constraints for the vertical dimensions can be set up in addition to the width ratios. Against
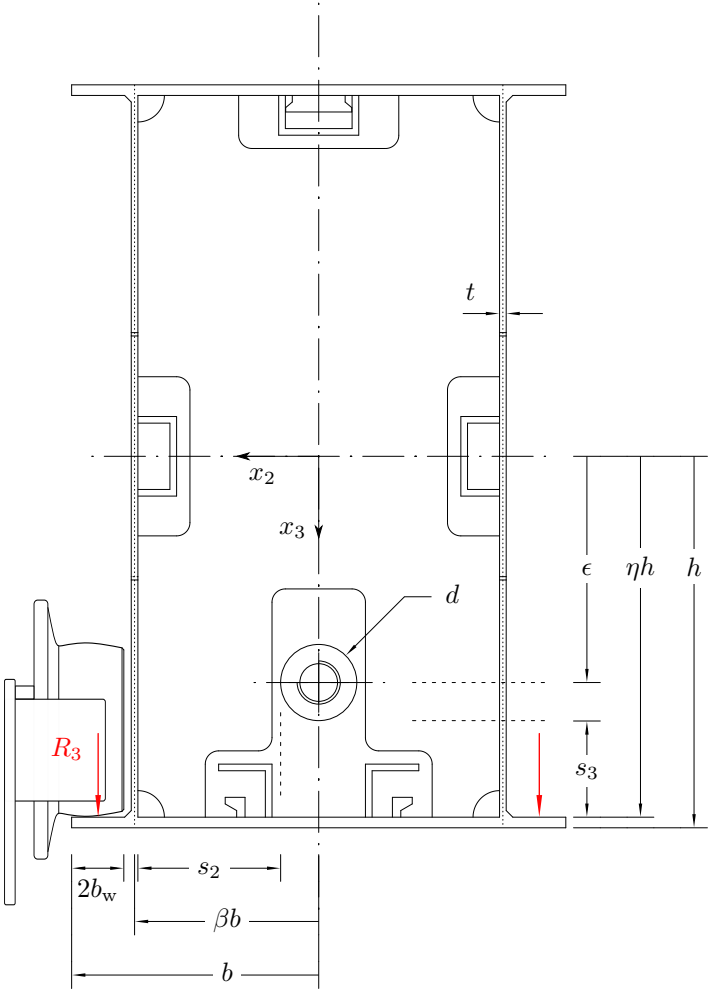
Figure 4.8: Section view of the main segment

the background of manufacturability, we require that the thickness of

the bottom chord must at least correspond to the web thickness t. It follows from this for the outer height

$$h \geq \eta h + t. \tag{4.38}$$

Furthermore, we limit the outer height h upwards in order to exclude technically unfeasible solutions. The threshold value is set to $\lambda_{\mathrm{h}} l_0$ with $\lambda_{\mathrm{h}} \in (0, 1)$ as a dimensionless constant. The upper limit then given by the following inequation.

$$\lambda_{\mathrm{h}} l_0 \geq h \tag{4.39}$$

$$g_3 = \lambda_{\mathrm{h}} l_0 - h \geq 0 \tag{4.40}$$

If we now postulate that this limit is reached (i.e. $h = \lambda_{\mathrm{h}} l_0$) we find with the aid of ineq. (4.38) that the height ratio is also limited upwards.

$$1 - \frac{t}{\lambda_{\mathrm{h}} l_0} \geq \eta$$

$$g_4 = 1 - \frac{t}{\lambda_{\mathrm{h}} l_0} - \eta \geq 0 \tag{4.41}$$

Furthermore, in chapter 3 it was explained, that the end of the preload segment is chamfered, see figure 3.18. This must be considered as well, since the bevelled web plates also limit the height upwards when the preload segment is fixed in length. Against this background the corresponding inequation must apply.

$$\lambda l_{\mathrm{s}} + \eta h - h_3 + x_{\mathrm{p}} \leq l_{\mathrm{s}}^* \tag{4.42}$$

In this context, we define the dimensionless ratio λ_3

$$\lambda_3 = \frac{h_3}{\eta h} \tag{4.43}$$

and find by several transformations a further upper limit for the outer height h.

$$\frac{l_{\mathrm{s}}^* - \lambda l_{\mathrm{s}} - x_{\mathrm{p}}}{(1 - \lambda_3)\eta} \geq h \tag{4.44}$$

$$g_5 = \frac{l_{\mathrm{s}}^* - \lambda l_{\mathrm{s}} - x_{\mathrm{p}}}{(1 - \lambda_3)\eta} - h \geq 0 \tag{4.45}$$

In this way, the geometric constraints to be fulfilled are identified and clearly defined.

4.4.2 Constraint Functions Related to Stresses

One of the most important aspects of dimensioning is the compliance with specific strength values of the materials being used. For this reason, it is necessary to develop suitable mathematical relations which represent this requirement accordingly. The MISES yield criterion is of great importance in this context. As is well known, the MISES stress is applied in order to transform the individual components of the stress tensor determined by eq. (2.3) at a certain point into a uniaxial stress state. This allows the critical points in particular, which are subject to the highest loads, to be evaluated with regard to exceeding the yield strength. However, these points must be identified at first. Taking into account the previously depicted load curves (see figure 4.4), figure 4.9 shows the girder and the two trolley positions A and B that lead to the highest loads in each case. Since further local stresses are caused by the load introduction of the wheels, these must be taken into account additionally. Here, reference is made to [9]. The outer edge of the flange and the location of the point load are to be considered. The identified points can be clearly described with the help of the underlying coordinate system and the defined parameters. By application of the convention

$$\boldsymbol{p}_\xi = x_{\xi 1}\boldsymbol{e}_1 + x_{\xi 2}\boldsymbol{e}_2 + x_{\xi 3}\boldsymbol{e}_3 \tag{4.46}$$
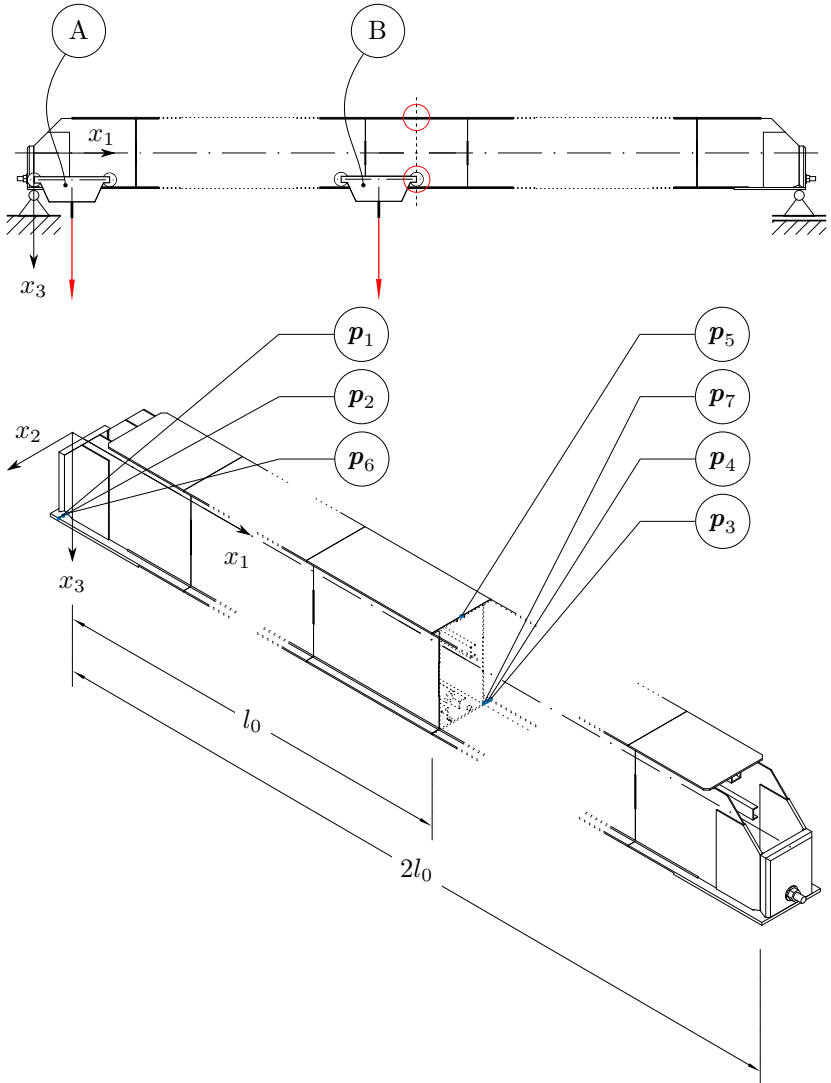
Figure 4.9: Operating conditions and identification of critical points in terms of mechanical stresses

they are defined as follows.

$$
\begin{aligned}
\boldsymbol{p}_1 &= & +\, b\, \boldsymbol{e}_2 & & +h\, \boldsymbol{e}_3 & & (4.47)\\
\boldsymbol{p}_2 &= & +\, (b - b_\mathrm{w})\, \boldsymbol{e}_2 & & +h\, \boldsymbol{e}_3 & & (4.48)\\
\boldsymbol{p}_3 &= l_0\, \boldsymbol{e}_1 & -\, b\, \boldsymbol{e}_2 & & +h\, \boldsymbol{e}_3 & & (4.49)\\
\boldsymbol{p}_4 &= l_0\, \boldsymbol{e}_1 & -\, (b - b_\mathrm{w})\, \boldsymbol{e}_2 & & +h\, \boldsymbol{e}_3 & & (4.50)\\
\boldsymbol{p}_5 &= l_0\, \boldsymbol{e}_1 & & & -h\, \boldsymbol{e}_3 & & (4.51)\\
\boldsymbol{p}_6 &= & (\beta b + t/2)\, \boldsymbol{e}_2 & & +h\, \boldsymbol{e}_3 & & (4.52)\\
\boldsymbol{p}_7 &= l_0\, \boldsymbol{e}_1 & -\, (\beta b + t/2)\, \boldsymbol{e}_2 & & +h\, \boldsymbol{e}_3 & & (4.53)
\end{aligned}
$$

Based on the critical points, the constraints taking into account the MISES stresses are established. Against the background of the situation described, the general MISES stress with respect to a certain point $\boldsymbol{p}_\xi$ with $\xi \in \{1, \dots, 7\}$ can be represented. Here, normal stresses in x_3-direction are neglected and we obtain

$$
\sigma_{\mathrm{M},\xi} = \sqrt{\sigma_{11}^2 + \sigma_{22}^2 - \sigma_{11}\sigma_{22} + 3(\tau_{13}^2 + \tau_{23}^2)}.
$$

In this connection, the individual components are defined by the following expressions

$$
\sigma_{11}(\boldsymbol{p}_\xi, \epsilon) = -\frac{N_0}{A_1} + \frac{M_2(x_{\xi 1}, \epsilon)}{I_{22}} x_{\xi 3} - \frac{M_3(x_{\xi 1})}{I_{33}} x_{\xi 2} + \hat{\sigma}_{11}^*(\boldsymbol{p}_\xi)
$$

$$
\hat{\sigma}_{11}^*(\boldsymbol{p}_\xi) = \lambda_\sigma^* \hat{\sigma}_{11}(x_{\xi 2}) \quad \forall\, \xi \in \{1, \dots, 7\} \backslash \{5\}
$$

$$
\sigma_{22}(\boldsymbol{p}_\xi) = \lambda_\sigma^* \hat{\sigma}_{22}(x_{\xi 2}) \quad \forall\, \xi \in \{1, \dots, 7\} \backslash \{5\}
$$

$$
\tau_{13}(\boldsymbol{p}_\xi) = \frac{Q_3(x_{\xi 1}) S_2(x_{\xi 3})}{I_{22}\gamma(x_{\xi 3})}
$$

$$
\tau_{23}(\boldsymbol{p}_\xi) = \frac{Q_2(x_{\xi 1}) S_3(x_{\xi 2})}{I_{33}\gamma(x_{\xi 2})}
$$

with $\gamma(x_{\xi 3})$ (respectively $\gamma(x_{\xi 2})$) representing the current width of the profile. It should be mentioned, that the normal stresses in x_1-direction must also be superimposed on the compressive stress due to prestressing and the local stress in x_1-direction due to the wheel-flange contact depicted in figure 4.10. The normal stress component in x_2-direction
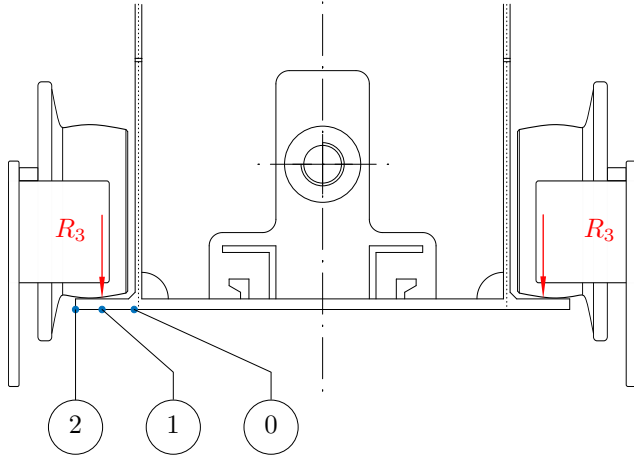
Figure 4.10: Local stresses defined in [9], parallel flange considered

is caused purely by the local stress. The local stresses are determined by [9] with respect to their location and are to be multiplied by an additional factor λ_σ^* according to [46]. By definition of

$$\vartheta = \frac{b_{\mathrm{w}}}{2(b-t)} \tag{4.54}$$

they result in

$$\hat{\sigma}_{11,i} = c_{11,i} \frac{R_3}{h^2(1-\eta)^2} \tag{4.55}$$

$$\hat{\sigma}_{22,i} = c_{22,i} \frac{R_3}{h^2(1-\eta)^2}. \tag{4.56}$$

The coefficients $c_{11,i}$ and $c_{22,i}$ are to be set with respect to the considered location $i \in \{0, 1, 2\}$ on the x_2-axis. For local stresses in x_1-direction they are defined by

$$c_{11,0} = 0.050 - 0.580\,\vartheta + 0.148\,\mathrm{e}^{3.015\,\vartheta}$$
$$c_{11,1} = 2.230 - 1.490\,\vartheta + 1.390\,\mathrm{e}^{-18.33\,\vartheta}$$
$$c_{11,2} = 0.730 - 1.580\,\vartheta + 2.910\,\mathrm{e}^{-6.000\,\vartheta}$$

and in terms of local stresses in x_2-direction by

$$c_{22,0} = -2.110 + 1.977\,\vartheta + 0.0076\,\mathrm{e}^{6.530\,\vartheta}$$
$$c_{22,1} = 10.108 - 7.408\vartheta + 10.108\mathrm{e}^{-1.364\,\vartheta}$$
$$c_{22,2} = 0$$

according to [9]. Here, position "0" represents the transition zone between the web plate and the bottom chord, "1" the location of the wheel-flange contact and "2" the outer flange edge (see figure 4.10). We now require that the resulting equivalent stress must not exceed the yield strength f_y. In this case, the subsequent inequation must apply.

$$f_\mathrm{y}^2 \geq \sigma_{11}^2 + \sigma_{22}^2 - \sigma_{11}\sigma_{22} + 3(\tau_{13}^2 + \tau_{23}^2)$$

By introducing the parameter ψ_σ, defined as

$$\psi_\sigma = \sigma_{22}^2 + 3(\tau_{13}^2 + \tau_{23}^2) - f_\mathrm{y}^2 \tag{4.57}$$

and several transformations, we finally obtain the new relation

$$\sigma_{11}^2 - \sigma_{11}\sigma_{22} + \psi_\sigma \leq 0 \tag{4.58}$$

which is a quadratic inequation that can be solved by conventional methods. It follows

$$\sigma_{11} \leq \frac{\sigma_{22}}{2}\left(1 \pm \sqrt{1 - \frac{4\psi_\sigma}{\sigma_{22}^2}}\right).$$

Once the expression for the normal stress in x_1-direction is applied, we find

$$-\frac{N_0}{A_1} + \frac{M_2}{I_{22}}x_{\xi 3} - \frac{M_3}{I_{33}}x_{\xi 2} + \lambda_\sigma^* \hat{\sigma}_{11}^2 \leq \frac{\sigma_{22}}{2}\left(1 \pm \sqrt{1 - \frac{4\psi_\sigma}{\sigma_{22}^2}}\right).$$

With eq. (4.12) the term of the pure normal stress due to compression can be extended accordingly with the eccentricity ϵ.

$$-\frac{N_0\epsilon}{A_1\epsilon} + \frac{M_2}{I_{22}}x_{\xi 3} - \frac{M_3}{I_{33}}x_{\xi 2} + \lambda_\sigma^* \hat{\sigma}_{11}^2 \leq \frac{\sigma_{22}}{2}\left(1 \pm \sqrt{1 - \frac{4\psi_\sigma}{\sigma_{22}^2}}\right)$$

This leads to the fact that the eccentricity ϵ now occurs explicitly in the inequality and can be solved accordingly. The solution of the quadratic inequation produces two possible results. It can be shown that the negative one only gives reasonable solutions. One obtains

$$\epsilon^\sigma(\boldsymbol{p}_\xi) = \frac{M_0}{A_1}\left(\frac{M_2}{I_{22}}x_{\xi 3} - \frac{M_3}{I_{33}}x_{\xi 2} - \frac{1}{2}\left(\hat{\sigma}_{22} - \sqrt{\hat{\sigma}_{22}^2 - 4\psi_\sigma}\right) + \lambda_\sigma^* \hat{\sigma}_{11}\right)^{-1}$$
(4.59)

which defines clearly the limit condition for compliance with the strength values of the material. Moreover, the eccentricity must be of a minimum value to prevent material failure by exceeding the yield stress. In this context, the vector $\boldsymbol{p}_\xi$ designates the point under consideration with its corresponding coordinates. Considering ineq. (4.59) and the crucial points, we obtain the following set of constraint functions.

$$g_6 = \epsilon - \epsilon^\sigma(\boldsymbol{p}_1) \geq 0 \qquad\qquad (4.60)$$
$$g_7 = \epsilon - \epsilon^\sigma(\boldsymbol{p}_2) \geq 0 \qquad\qquad (4.61)$$
$$g_8 = \epsilon - \epsilon^\sigma(\boldsymbol{p}_3) \geq 0 \qquad\qquad (4.62)$$
$$g_9 = \epsilon - \epsilon^\sigma(\boldsymbol{p}_4) \geq 0 \qquad\qquad (4.63)$$
$$g_{10} = \epsilon - \epsilon^\sigma(\boldsymbol{p}_5) \geq 0 \qquad\qquad (4.64)$$
$$g_{11} = \epsilon - \epsilon^\sigma(\boldsymbol{p}_6) \geq 0 \qquad\qquad (4.65)$$
$$g_{12} = \epsilon - \epsilon^\sigma(\boldsymbol{p}_7) \geq 0 \qquad\qquad (4.66)$$

4.4.3 Constraint Functions Related to Occurring Deformations

The common rules in crane construction limit the permissible deformations of a crane bridge during operation [23]. These primarily relate to the total deflection of the girder. In terms of a segmented crane bridge we additionally require that no contact between the traction equipment and the main segment occurs in normal operation. Thus, we remain consistent in our assumption that both components can be considered independently of each other. Otherwise, a force would act between the contact partners, coupling both system components. We consider the

a) undeformed state   b) deformed state
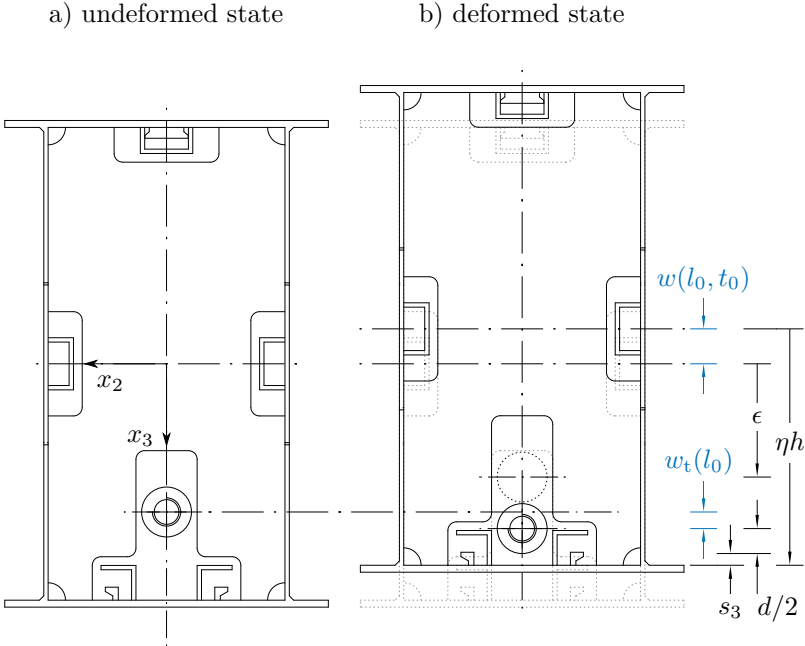
Figure 4.11: Undeformed and deformed state of the girder and the traction mechanism

case in which the beam and the traction mechanism come closest. This is the situation with prestressing. The beam will deflect upwards in negative x_3-direction due to the eccentrically acting axial force, while the tensile member will deflect downwards due to gravity. Figure 4.11 illustrates the deformed state of the system. The deformation of the traction mechanism is denoted by $w_t(l_0)$, the deflection of the beam is denoted by $w(l_0, t_0)$. Both deformations are taken into account at $x_1 = l_0$. The additional parameter t_0 indicates that the state of prestressing is considered. As long as no contact appears, the dimensions and deformations indicate that the inner height ηh must be of a minimum value. This results in the following relation.

$$\eta h \geq \epsilon + \frac{d}{2} + w_t(l_0) + |w(l_0, t_0)| + s_3 \qquad (4.67)$$

Here, the absolute deflection of the girder at prestressing is taken into account since it takes negative values due to the pre-deformation. With the aid of eq. (4.16), the deflection can be determined by neglecting the nominal load represented by $2R_3$.

$$w(l_0, t_0) = \frac{1}{(EI)_{22}} \left(\frac{5}{24} \mu l_0^4 - \frac{1}{2} M_0 l_0^2 \right) \qquad (4.68)$$

On the other hand, the computation of $w_t(l_0)$ is more complex due to the influence of the axial force taken into consideration. Figure 4.12 depicts the freebody diagram of the traction mechanism supported inside the girder. After computation of the supporting reaction A_3, the equilibrium conditions can be established with respect to the beam theory of second order, i.e. the slightly deformed system is subject to the mathematical modeling. With $\mu_t = \rho A_t g$ we find for the bending moment

$$M_2(x_1) = -\frac{1}{2} \mu_t x_1^2 + \mu_t l_0 x_1 - N_0 w_t.$$
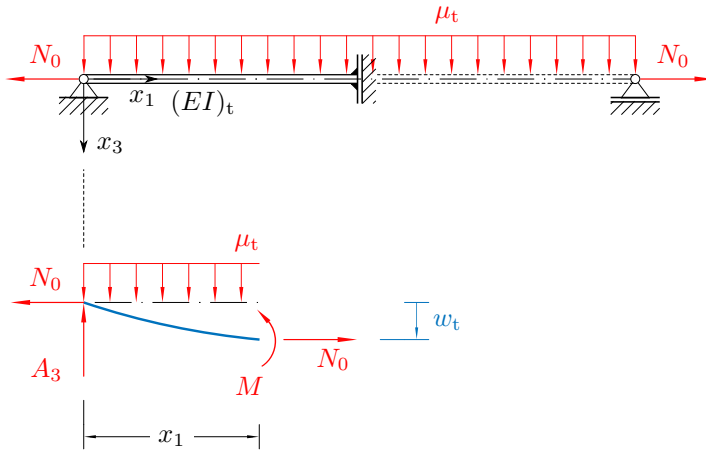
Figure 4.12: Freebody diagram of the traction mechanism

The underlying equation is specified as an inhomogeneous differential equation of second order.

$$(EI)_t \frac{\mathrm{d}^2 w_t}{\mathrm{d}x_1^2} = \frac{1}{2}\mu_t x_1^2 - \mu_t l_0 x_1 + N_0 w_t$$

By introduction of $\alpha^2 = N_0/(EI)_t$ and several transformations, we obtain the expression

$$\frac{\mathrm{d}^2 w_t}{\mathrm{d}x_1^2} - \alpha^2 w_t = \frac{1}{2}\frac{\mu_t \alpha^2}{N_0}x_1^2 - \frac{\mu_t l_0 \alpha^2}{N_0}x_1.$$

The entire solution consists of two individual parts: the *homogeneous* and the *particular* solution. The homogeneous solution $w_{t,h}$ can be found by application of an exponential ansatz and results in

$$w_{t,h} = C_1 e^{\alpha x_1} + C_2 e^{-\alpha x_1}.$$

However, the particular solution requires an individual approach which takes the characteristic of the inhomogeneous term into account. Since it is a quadratic function, we select a quadratic ansatz as well and find

$$w_{\mathrm{p}} = -\frac{1}{2}\frac{\mu_{\mathrm{t}}}{N_0}x_1^2 + \frac{\mu_{\mathrm{t}}l_0}{N_0}x_1 - \frac{\mu_{\mathrm{t}}}{\alpha^2 N_0}$$

for the particular solution w_{p} after comparison of the coefficients. Now the entire solution is fully defined, the remaining coefficients C_1 and C_2 can be determined through the boundary conditions

$$w_{\mathrm{t}}(0) \overset{!}{=} 0 \qquad\qquad w_{\mathrm{t}}'(l_0) \overset{!}{=} 0$$

and provide the term describing the deflection of the traction mechanism at $x_1 = l_0$.

$$w_{\mathrm{t}}(N_0, l_0) = \frac{2\mu_{\mathrm{t}}\mathrm{e}^{\alpha l_0}}{\alpha^2 N_0(1 + \mathrm{e}^{2\alpha l_0})} + \frac{1}{2}\frac{\mu_{\mathrm{t}}l_0^2}{N_0} - \frac{\mu_{\mathrm{t}}}{\alpha^2 N_0} \tag{4.69}$$

The normal force is still unknown but it is already obvious that the deflection of the traction mechanism becomes minimal with increasing prestressing force. The lowest possible deflection of the traction mechanism should be aimed for, since the required internal height also decreases and thus the resulting total weight. For this reason, the maximum permissible prestressing force denoted by $\gamma_{\mathrm{M2}} N$ is selected[5]. Against this background the relevant deflection follows to

$$w_{\mathrm{t}}(l_0) = \frac{2\gamma_{\mathrm{M2}}\mu_{\mathrm{t}}\mathrm{e}^{\alpha l_0}}{\alpha^2 N(1 + \mathrm{e}^{2\alpha l_0})} + \frac{\gamma_{\mathrm{M2}}}{2}\frac{\mu_{\mathrm{t}}l_0^2}{N} - \frac{\gamma_{\mathrm{M2}}\mu_{\mathrm{t}}}{\alpha^2 N}. \tag{4.70}$$

With eq. (4.70) and (4.68) the constraint function with regard to the deformation behavior can be formulated. Due to the fact that ϵ occurs

---

[5] With N as the maximum assembly preload of the considered bolt.

explicitly here as well, the term can also be rearranged according to the eccentricity. By additional application of eq. (4.18), we obtain

$$\epsilon^\eta = \eta h - \frac{d}{2} - w_t(l_0) - \frac{R_3 l_0^3}{3(EI)_{22}}(\alpha_1^3 - 3\alpha_1^2 + 2) + \delta l_0 - s_3 \qquad (4.71)$$

for the limit of the eccentricity. A rearrangement gives the implicit form of the constraint function.

$$g_{13} = \epsilon^\eta - \epsilon \geq 0 \qquad (4.72)$$

The developed constraint function limits the eccentricity upwards.

In addition to the deformations in x_3-direction, deflections of the system in x_2-direction occur as well during a bumper impact. However, since this is an exceptional case, we neglect the requirement that there must be no contact between the tensile member and the girder. Thus, the problem is reduced to a bending problem considering only the girder. Figure 4.13 shows the free body diagram in terms of bending about the x_3-axis. The maximum deflection will arise once the traveling trolley is located in the middle of the beam. In that case the symmetry of the system can be again utilized which leads to a beam divided into two sections due to the concentrated force $2R_2$. With eq. (2.14) the differential equation can be established, taking into account the corresponding boundary conditions

$$v(0) = 0 \qquad\qquad v'(l_0) = 0$$

in order to determine the integration constants. Then we obtain for the deflection v at $x_1 = l_0$:

$$(EI)_{33}v(l_0) = \frac{5}{24}\lambda_2\mu l_0^4 + \frac{1}{3}R_2(1 - \alpha_1)\left(3 - (1 - \alpha_1)^2\right)l_0^3. \qquad (4.73)$$

In order to prevent the beam from excessive bending in case of a bumper impact, a limit value is established which must not be exceeded.

$$v(l_0) \leq \delta_2 l_0 \qquad (4.74)$$
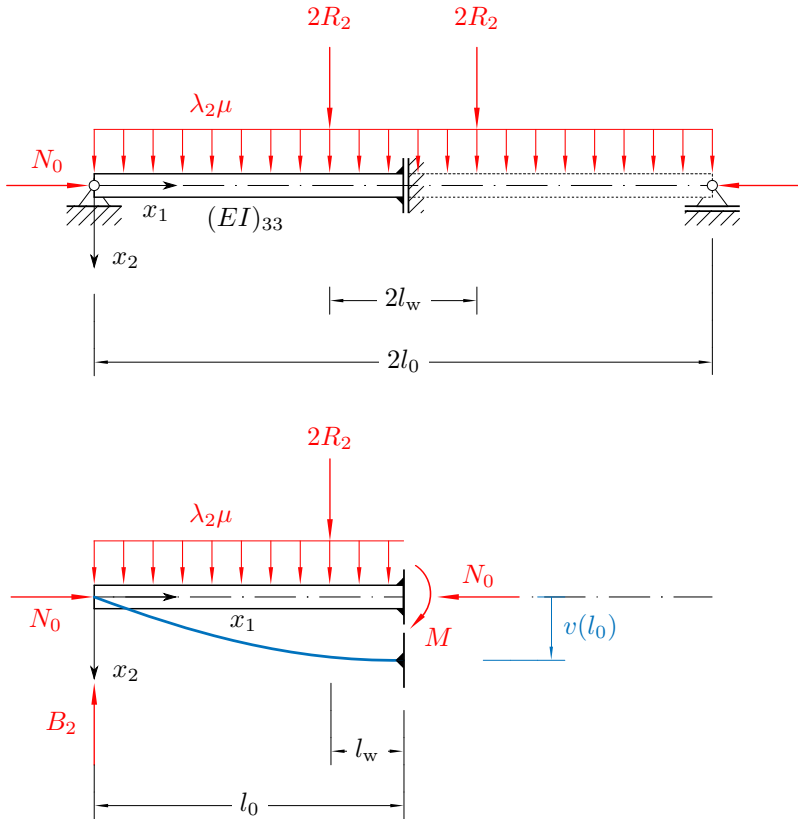
Figure 4.13: Deflection due to bumper impact in x_2-direction

Here, δ_2 represents the ratio between the deflection $v(l_0)$ and the span width l_0. Subsequently, we obtain the following inequation.

$$(EI)_{33}\delta_2 l_0 \geq \frac{5}{24}\lambda_2\rho A_1 g l_0^4 + \frac{1}{3}R_2(1 - \alpha_1)\left(3 - (1 - \alpha_1)^2\right)l_0^3 \quad (4.75)$$

It is now of interest to extract a constraint regarding the geometrical properties of the beam. Here, the main quantities describing the stiffness

of the beam are the second moment of inertia with respect to the x_3-axis I_{33} and the cross-sectional area A_1. With the relations defined by eq. (4.7) and eq. (4.5) it is now possible to restate ineq. (4.75) and the constraint to be fulfilled by h can be identified.

$$h^\delta = \frac{8R_2(1-\alpha_1)(3-(1-\alpha_1)^2)l_0^3}{24E\theta_{33}\delta_2 l_0 - 5\lambda_2\rho g\theta_1 l_0^4}$$

$$g_{14} = h - h^\delta \geq 0 \tag{4.76}$$

It limits the external height downwards, i.e. that a minimum outer height must be available in order to prevent the girder from excessive bending in case of a bumper impact.

4.4.4 Constraint Functions Related to Permissible Prestressing

It is obvious that the tensile member cannot be loaded arbitrarily and its strength values must not be exceeded either. For this purpose, we are guided by the maximum permitted assembly forces according to VDI 2230 [11, p. 109]. In addition, a safety factor for the bolted joints is introduced with respect to DIN EN 1993-6 and denoted by γ_{M2} [9, p. 26].

Again, on the basis of eq. (4.12) the following constraint can be developed.

$$\epsilon^N = \frac{\gamma_{M2}M_0}{N}$$

$$g_{15} = \epsilon - \epsilon^N \geq 0 \tag{4.77}$$

Here, N describes the maximum permissible prestressing force acting in the respective threaded rod.

4.4.5 Constraint Functions Related to Elastic Stability

Due to the axial forces resulting from prestressing, the girder is exposed to high compressive forces and stresses. In this connection, it is manda-

tory that no local buckling of thin plates or even a global buckling of the structure occurs. Following the analytical approach given by eq. (2.16), DIN EN 13001-3-1 provides a procedure to prove the elastic stability of the components. At first, the global buckling in the x_1x_2-plane is considered.

According to DIN EN 13001-3-1 it is required that an acting normal force N_1 along the x_1-axis is smaller than a defined limit value [15].

$$N_1 \leq \frac{\kappa f_{\mathrm{y}} A_1}{\gamma_{\mathrm{M1}}} \tag{4.78}$$

This allows to be extended again by the eccentricity ϵ and we obtain by application of eq. (4.12) and consideration, that the prestressing force N_0 equals the maximum force N_1, the corresponding inequation.

$$\epsilon \geq \frac{\gamma_{\mathrm{M1}}}{\kappa f_{\mathrm{y}} A_1} M_0$$

In this context, κ appears as an additional factor, which must be determined depending on the slenderness ratio λ_{s}. Taking into account the geometrical quantities eq. (4.7) and eq. (4.5), it is to be calculated by

$$\lambda_{\mathrm{s}} = \frac{2l_0}{\pi} \sqrt{\frac{f_{\mathrm{y}}\theta_1}{E\theta_{33}}} \tag{4.79}$$

The factor κ now depends on the slenderness ratio. For $\lambda_{\mathrm{s}} \leq 0.20\,\mathrm{mm}$ follows

$$\kappa = 1.00$$

while for a $\lambda_{\mathrm{s}} \geq 0.20\,\mathrm{mm}$

$$\kappa = \frac{1}{\xi_{\mathrm{s}} + \sqrt{\xi_{\mathrm{s}}^2 - \lambda_{\mathrm{s}}^2}}$$

applies. Considering $\alpha_{\mathrm{s}} = 0.34$, the factor ξ_{s} is to be determined by

$$\xi_{\mathrm{s}} = 0.50(1 + \alpha_{\mathrm{s}}(\lambda_{\mathrm{s}} - 0.20) + \lambda_{\mathrm{s}}^2)$$

Once these different cases are taken into account, we obtain the following constraint function

$$\epsilon^{\mathrm{g}} = \frac{\gamma_{\mathrm{M1}} M_0}{f_{\mathrm{y}} A_1} \begin{cases} 1.0 & \lambda_{\mathrm{s}} \leq 0.2 \, \mathrm{mm} \\ \xi_{\mathrm{s}} + \sqrt{\xi_{\mathrm{s}}^2 - \lambda_{\mathrm{s}}^2} & \lambda_{\mathrm{s}} > 0.2 \, \mathrm{mm} \end{cases}$$

$$g_{16} = \epsilon - \epsilon^{\mathrm{g}} \geq 0 \tag{4.80}$$

which specifies the lower limit of the eccentricity in order to prevent the girder from global buckling with respect to the x_3-axis.

In addition to global buckling, local plate buckling is also a possible stability failure of the structure, which must also be avoided. For this, we assume that the vertically arranged web plates are the critical components as already explained in section 3.3.1. Moreover, we require that the uniformly distributed normal stress in x_1-direction dominates. Furthermore, it is assumed that the webs are simply supported and that they are divided into two parts due to the bulkhead plates inside the segments. According to DIN EN 13001-3-1 it is required that the normal compressive stress is limited to a specific value.

$$\sigma_{11} \leq \frac{\kappa_x f_{\mathrm{y}}}{\gamma_{\mathrm{M1}}} \tag{4.81}$$

Taking into account that the normal stress is uniformly distributed, ineq. (4.81) can be restated as follows.

$$\frac{N_1}{A_1} \leq \frac{\kappa_x f_{\mathrm{y}}}{\gamma_{\mathrm{M1}}}. \tag{4.82}$$

Again, we consider the limit state in which $N_0 = N_1$ applies and obtain for the eccentricity

$$\epsilon \geq \frac{\gamma_{\mathrm{M1}} M_0}{\kappa_x f_{\mathrm{y}} A_1}. \tag{4.83}$$

The parameter κ_x depends on the dimensionless slenderness ratio λ_x, which is defined as

$$\lambda_x = \sqrt{\frac{f_\mathrm{y}}{\kappa_{\sigma,x}\sigma_\mathrm{e}}}$$

with the buckling factor $\kappa_{\sigma,x}$ (to be set as $\kappa_{\sigma,x} = 4.0$, see [15]) and the related buckling stress

$$\sigma_\mathrm{e} = \frac{\pi^2 E}{12(1-\nu^2)} \left(\frac{t}{l_\mathrm{c}}\right)^2.$$

The dimensionless slenderness ratio is determined by

$$\lambda_x = \frac{l_\mathrm{c}}{\pi t}\sqrt{\frac{3f_\mathrm{y}}{E}(1-\nu^2)}. \tag{4.84}$$

Hereby, the quantity l_c describes the length of the crucial section and is defined as

$$l_\mathrm{c} = \frac{1}{2}\max\{l_\mathrm{s}; (l_\mathrm{s}^* - \lambda l_\mathrm{s})\}. \tag{4.85}$$

It mainly depends on the underlying type of segmentation and the resulting lengths of the preload segment and the main segment. In this context, figure 4.14 shows the difference between the individual web plate lengths. In this connection, eq. (4.84) indicates that λ_x takes the highest values with increasing l_c. Based on DIN EN 13001-3-1 the limit value for the eccentricity is then defined as follows

$$\epsilon^\mathrm{l} = \frac{\gamma_{\mathrm{M}1} M_0}{f_\mathrm{y} A_1} \begin{cases} 1.0 & \lambda_x \leq 0.7 \\ (1.474 - 0.677\,\lambda_x)^{-1} & 0.7 < \lambda_x < 1.291 \\ \lambda_x^2 & \lambda_x \geq 1.291 \end{cases}$$

$$g_{17} = \epsilon - \epsilon^\mathrm{l} \geq 0. \tag{4.86}$$

Inequation (4.80) and ineq. (4.86) determine the limit values of the eccentricity ϵ in order prevent failures in terms of elastic stability.
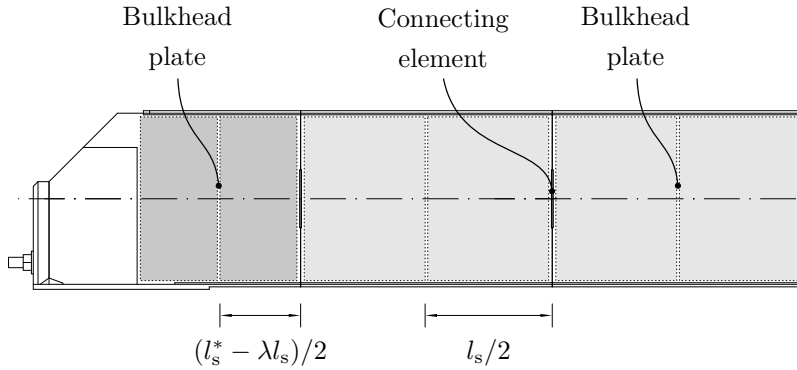
Figure 4.14: Identification of the underlying crucial plate length

4.4.6 Constraint Functions Related to Serviceability

Against the background of a segmented and prestressed girder in crane construction, we define *serviceability* to mean that the structure always retains its shape. More precisely, this means that the prestressing forces are high enough and provide sufficient surface pressure at the connection joints to prevent relative movements between the individual components due to excessive shear forces.

If we now consider, that a specific compressive force N_μ is required in order to achieve a sufficient surface pressure, it must to be lower than the maximum permissible preload N of the bolted connection. Previously, it has already been defined that the prestressing force N_0 must not be greater than N, which in turn means

$$N_\mu \leq N_0 \leq N.$$

We now postulate that the prestressing force is already sufficient and ensures the serviceability of the crane girder. Then applies the following requirement.

$$N_0 \geq N_\mu \tag{4.87}$$

Again, ineq. (4.87) is capable to be extended with the eccentricity and we obtain the according inequation.

$$N_0 \epsilon \geq N_\mu \epsilon$$

$$\epsilon^\mu = \frac{M_0}{N_\mu}$$

$$g_{18} = \epsilon^\mu - \epsilon \geq 0 \tag{4.88}$$

It is now necessary to quantify the required normal force N_μ while VDI 2230 forms the basis for the calculation. The standard provides a procedure consisting of several steps in order to estimate the required assembly preload for the considered bolted connection [11, p. 29–38]. Usually, the following aspects below must be taken into account:

- required minimum assembly preload,

- axial working load,

- changes in preload and

- thermally induced stresses.

Changes in temperature are neglected, for this reason thermally induced stresses acting on the bolted connection are neglected as well. The same applies for the axial working load. This leads to the fact that the required minimum assembly preload N_μ can be separated into two components - N_μ^Q and N_μ^s.

$$N_\mu = N_\mu^Q + N_\mu^s \tag{4.89}$$

The first component N_μ^Q describes the ability of transmitting bending moments and shear forces without any relative movements occurring between the contact partners (minimum clamp load). Due to the bolted connection used, additional pretensioning force losses due to surfaces roughness must be taken into account, which are designated with N_μ^s.

In order to determine N_μ^Q, we at first identify the location of the highest shear forces. These occur at $x_1 = 0$[6] and equal position "A" in figure 4.9. Taking into account a friction coefficient of $\mu_T = 0.14$ (considering dry steel-steel contact according to [11]) and a number n_c of connection joints of the girder we obtain

$$N_\mu^Q = \frac{\sqrt{Q_3^2(0) + Q_2^2(0)}}{n_c \mu_T}.$$ (4.90)

In doing so, the number of connection joints depends on the considered type of configuration (see section 3.2.1). Eq. (4.90) determines the minimum clamp load, which must be applied.

In order to estimate the changes in preload due to embedding of the contact surfaces, the amounts of embedding f_Z (assumed to be $3\,\mu$m for all contacts [11, p. 73]) as well as the axial resiliences of the bolt δ_S and the plates δ_P being pressed together must be taken into account. Then for the preload loss

$$N_\mu^s = \frac{f_Z}{\delta_S + \delta_P}$$ (4.91)

applies. The resiliences $\delta_{S,i}$ [mm/N] relevant for the bolted connection can be divided into four groups. These comprise the resiliences relating to the common rods δ_r, the additional rods δ_r^* as well as the resiliences of the connection areas δ_c and of the bolted areas δ_b. Here, figures 4.15 and 4.16 depict the considered lengths of the involved components. The resiliences are to be calculated individually [11, p. 39–41], see table 4.1, while the according values for the cross-section at the minor diameter A_{d3} are to be taken from [11, p. 125]. We obtain the overall resilience of the bolted connection by summarizing all sub-resiliences since they are connected to each other in series.

$$\delta_S = \sum_i \delta_{S,i}$$ (4.92)

---

[6] To be seen as a conservative approach since the wheel of the traveling trolley cannot reach this location in reality but it is limited by its specific start dimension.
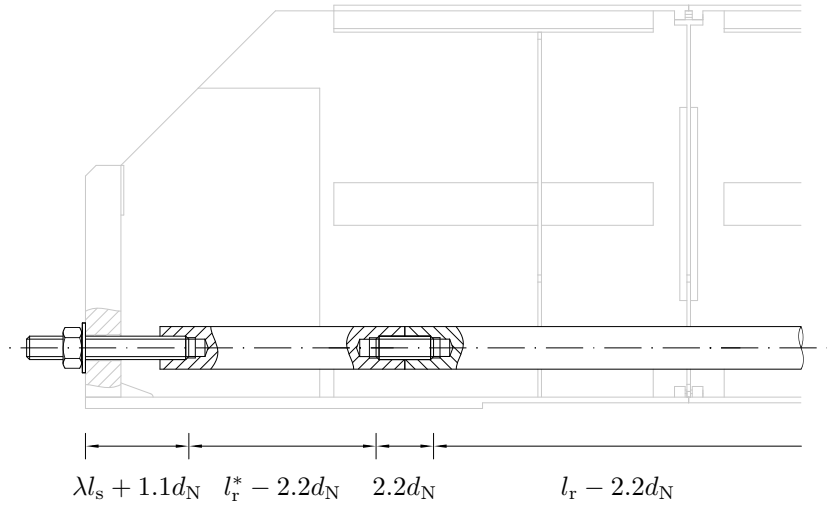
Figure 4.15: Corresponding lengths of the bolted area
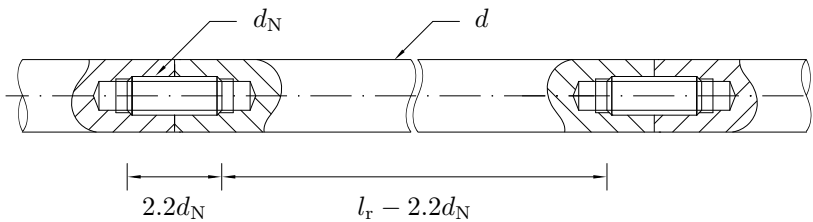
Figure 4.16: Corresponding lengths regarding the common rod connections

In addition to the bolted connection, the plates, represented by the segments of the girder, also possess a resilience. Under the assumption of a uniformly distributed pressure profile over the cross-section, it is calculated by

$$\delta_{\mathrm{P}} = \frac{2l_0}{EA_1}. \tag{4.93}$$

117

Table 4.1: Calculation of resiliences

Resilience	Calculation
δ_{r}	$(4l_{\mathrm{r}} - 8.8d_{\mathrm{N}})/(E\pi d^2)$
δ_{r}^*	$(4l_{\mathrm{r}}^* - 8.8d_{\mathrm{N}})/(E\pi d^2)$
δ_{c}	$2\left(1.1d_{\mathrm{N}}/(EA_{d3}) + 1.32/(E\pi d_{\mathrm{N}})\right)$
δ_{b}	$1.1d_{\mathrm{N}}/(EA_{d3}) + 4\lambda l_{\mathrm{s}}/(E\pi d_{\mathrm{N}}^2) + 1.32/(E\pi d_{\mathrm{N}})$

The entire amount of the single resiliences depends on the span width and with it on the segmentation type.

With the definition of N_μ^{s} and N_μ^Q, the quantity N_μ is completely determined and therefore also the constraint function eq. (4.88).

4.4.7 Constraint Functions Related to Contour Accuracy

A further aspect regarding the preliminary requirements defined in section 3.1 covers the continuous component bonding. More precisely, this means that no gaping between the single segments at their connection joints occurs. For this purpose, it is necessary to define a constraint function which must be met in order to prevent the structure from gaping.

Here, the prestressing is a key element. It closes the contact surfaces at the connection joints and, if the surface pressure is sufficient, allows the structure to transmit shear forces and bending moments. In this context, the necessary normal force is given by the minimum clamp load N_μ^Q (see eq. (4.90)). In order to avoid gaping, it is obligatory that the girder is always under compressive stress. Due to the loose bond, it is not able to absorb tensile stresses. For this reason, the critical point that is most at risk with regard to the occurrence of tensile stresses must be identified at first.

As is generally known, tensile stresses occur at a beam, which is subject to bending about the x_2-axis, in the lower chord. This is a normal state

during operation of the crane. The girder might be loaded by bending moments about the x_3-axis as well in case of a bumper impact. Then *oblique bending* arises which means that additional stress components in x_1-direction appear which are to be superimposed. In that case the point $\boldsymbol{p}_8$ located at the edge of the lower chord is the most crucial. Its coordinates are defined by

$$\boldsymbol{p}_8 = x_{\mathrm{c}}\,\boldsymbol{e}_1 + b\,\boldsymbol{e}_2 + h\,\boldsymbol{e}_3. \tag{4.94}$$

Here, x_{c} describes the location of the crucial connection joint in x_1-direction. Furthermore, it depends on the type of segmentation. We now require that the dominating normal stress σ_{11} must be always negative and define a minimum value denoted by $\lambda_\gamma^* f_{\mathrm{y}}$ with the dimensionless factor $\lambda_\gamma^* \in (0,1)$. Then, the following inequation must apply.

$$\sigma_{11} \leq -\lambda_\gamma^* f_{\mathrm{y}} \tag{4.95}$$

By application of the definition regarding the normal stress follows

$$-\frac{N_0}{A_1} + \frac{M_2}{I_{22}}x_3 - \frac{M_3}{I_{33}}x_2 + \lambda_\sigma^*\,\hat{\sigma}_{11} \leq -\lambda_\gamma^* f_{\mathrm{y}}.$$

Again, the first term representing the additional compressive force in the inequation allows to be extended with the eccentricity ϵ. Furthermore, the local stress due to the wheel-flange contact is taken into account. We obtain

$$-\frac{N_0\epsilon}{A_1\epsilon} + \frac{M_2}{I_{22}}x_3 - \frac{M_3}{I_{33}}x_2 + \lambda_\sigma^*\,\hat{\sigma}_{11} \leq -\lambda_\gamma^* f_{\mathrm{y}}$$

while further rearranging leads to the constraint function which must be met.

$$\epsilon^\gamma(\boldsymbol{p}_8) = \frac{M_0}{A_1}\left(\frac{M_2}{I_{22}}x_3 - \frac{M_3}{I_{33}}x_2 - \lambda_\sigma\hat{\sigma}_{11} + \lambda_\gamma^* f_{\mathrm{y}}\right)^{-1}$$

$$g_{19} = \epsilon^\gamma(\boldsymbol{p}_8) - \epsilon \geq 0 \tag{4.96}$$

Table 4.2: Summary of constraint functions

Constraint g_γ	According implicit function	
g_1	$\beta b - (d+t)/2 - s_2$	≥ 0
g_2	$b - 2b_\mathrm{w} - (\sqrt{0.98} + 1/2)t - \beta b$	≥ 0
g_3	$\lambda_\mathrm{h} l_0 - h$	≥ 0
g_4	$1 - t/(\lambda_\mathrm{h} l_0) - \eta$	≥ 0
g_5	$(l_\mathrm{s}^* - \lambda l_\mathrm{s} - x_\mathrm{p})/(\eta(1 - \lambda_3)) - h$	≥ 0
g_6	$\epsilon - \epsilon^\sigma(\boldsymbol{p}_1)$	≥ 0
g_7	$\epsilon - \epsilon^\sigma(\boldsymbol{p}_2)$	≥ 0
g_8	$\epsilon - \epsilon^\sigma(\boldsymbol{p}_3)$	≥ 0
g_9	$\epsilon - \epsilon^\sigma(\boldsymbol{p}_4)$	≥ 0
g_{10}	$\epsilon - \epsilon^\sigma(\boldsymbol{p}_5)$	≥ 0
g_{11}	$\epsilon - \epsilon^\sigma(\boldsymbol{p}_6)$	≥ 0
g_{12}	$\epsilon - \epsilon^\sigma(\boldsymbol{p}_7)$	≥ 0
g_{13}	$\epsilon^\eta - \epsilon$	≥ 0
g_{14}	$h - h^\delta$	≥ 0
g_{15}	$\epsilon - \epsilon^N$	≥ 0
g_{16}	$\epsilon - \epsilon^\mathrm{g}$	≥ 0
g_{17}	$\epsilon - \epsilon^\mathrm{l}$	≥ 0
g_{18}	$\epsilon^\mu - \epsilon$	≥ 0
g_{19}	$\epsilon^\gamma(\boldsymbol{p}_8) - \epsilon$	≥ 0

4.5   Summary of Constraint Functions

In this chapter the underlying constraint functions were elaborated. These define limit values which must be met by certain geometrical quantities of the structure. In this context, a major result is that most of the constraint functions can be expressed by a functional relation between the eccentricity ϵ and the remaining quantities. This circumstance will be a key feature subsequently. In table 4.2 all constraint functions are summarized.

5 Structural Optimization

*Dare to know. Have the courage to
use your own intelligence.*
- I. KANT

In the previous chapter, the essential constraints that must be fulfilled by the segmented, prestressed girder in order to be considered as a suitable solution against the background of elastostatic behavior were identified. Assuming that a finite number of possible solutions exists, they can be distinguished by their characteristics. These include, for instance, the deformations or the mechanical stresses, which give different values depending on the solution. However, as often proven in literature, the solution, where the total weight of the crane bridge becomes minimal, is mostly desired. This means that the task is to *optimize* the crane bridge with respect to its self-weight while at the same time the defined constraints are all met.

The following chapter deals with the treatment of the underlying optimization problem and the development of a possible solution strategy in order to identify solutions with minimum weight. This strategy is implemented in a numerical algorithm, which is then to be evaluated regarding its properties.

5.1 Analyses and Definitions

In the beginning, the developed functions and involved design variables are interpreted and analyzed with regard to their mathematical characteristics. This step forms the basis for the subsequent identification of appropriate solution approaches.

5.1.1 Establishment of the Optimization Program

To clearly define the optimization program it is necessary to specify at first the objective function f that has to be optimized. In analogy to the optimization approaches described in literature (see section 2.4), we select the cross-sectional area of the main segment as the objective function as well. A decisive difference in contrast to conventional beams
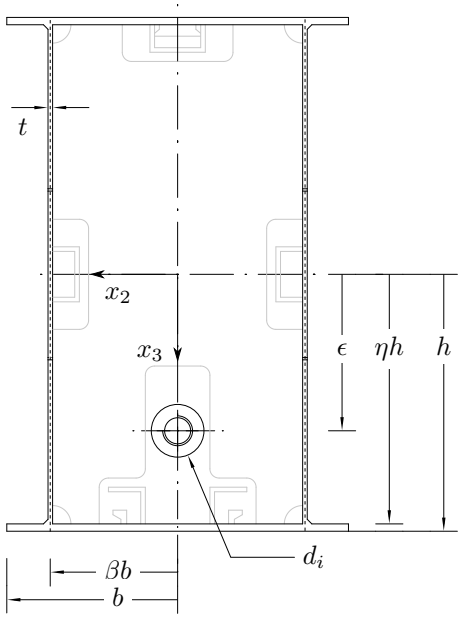
Figure 5.1: Considered cross-section in terms of optimization

is that in addition to the segment dimensions, the cross-section of the steel bar (determined by d_i) assigned to the tensile member is also included in the resulting surface area. Especially with larger diameters of the tensile member, its additional mass can no longer be neglected and must therefore be taken into account. Here, the index i already indicates that an individual steel bar from a set of available traction mechanisms is considered. Figure 5.1 shows the cross-section which forms the ba-

sis for the establishment of the objective function. In comparison to figure 4.8, local peculiarities such as the dimensions of the weld seam or the bulkhead plate are neglected. Taking into account the geometrical quantities, the surface area can be determined. In this connection, we further consider the web thickness t to be constant[1]. The objective function is then defined as

$$f(b, \eta, h, d_i) = 4(b - (b - t)\eta)h + \frac{\pi}{4}d_i^2. \tag{5.1}$$

We can already state that not all geometrical parameters, that define the shape of the main girder, appear in the objective function. For example, the width ratio β and the eccentricity ϵ also determine the shape, but have no influence on the calculation of the surface area. The same applies for the deflection ratio δ. Another special feature is, that not all variables are distributed continuously. Due to given dimensions of the threaded rods, the resulting diameter d_i of a steel bar is to be considered as a discrete quantity. In this context, we define the set of discrete traction mechanisms as $\{\boldsymbol{D}\}$ consisting of in total n elements. In addition, $\{\boldsymbol{D}\}$ includes all corresponding quantities relating to a specific traction mechanism such as the nominal diameter $d_{\mathrm{N},i}$ of the bolt or the maximum permissible assembly preload N_i, see table A.1. Furthermore, we note the specific sets of the individual dimensioned design variables

$$h \in \boldsymbol{\Omega}^h, \ \boldsymbol{\Omega}^h := \{h \in \mathbb{R}_+ \mid 0 < h\}$$
$$b \in \boldsymbol{\Omega}^b, \ \boldsymbol{\Omega}^b := \{b \in \mathbb{R}_+ \mid 0 < b\}$$
$$\epsilon \in \boldsymbol{\Omega}^\epsilon, \ \boldsymbol{\Omega}^\epsilon := \{\epsilon \in \mathbb{R}_+ \mid 0 < \epsilon\}$$

and those of the dimensionless parameters

$$\eta \in \boldsymbol{\Omega}^\eta, \ \boldsymbol{\Omega}^\eta := \{\eta \in \mathbb{R}_+ \mid 0 < \eta < 1\}$$
$$\beta \in \boldsymbol{\Omega}^\beta, \ \boldsymbol{\Omega}^\beta := \{\beta \in \mathbb{R}_+ \mid 0 < \beta < 1\}$$
$$\delta \in \boldsymbol{\Omega}^\delta, \ \boldsymbol{\Omega}^\delta := \{\delta \in \mathbb{R}_+ \mid 0 \le \delta < 1\}.$$

---

[1] According to commercial available steel plates.

The combinations of the subsets

$$\boldsymbol{\Omega}_1 := \boldsymbol{\Omega}^h \times \boldsymbol{\Omega}^b \times \boldsymbol{\Omega}^\eta, \; \boldsymbol{\Omega}_1 \subseteq \mathbb{R}^3_+ \backslash \{\boldsymbol{0}\}$$
$$\boldsymbol{\Omega}_2 := \boldsymbol{\Omega}^\eta \times \boldsymbol{\Omega}^\beta \times \boldsymbol{\Omega}^\delta, \; \boldsymbol{\Omega}_2 \subseteq \mathbb{R}^3_+$$

leads to the entire set $\boldsymbol{\Omega}$.

$$\boldsymbol{\Omega} := \boldsymbol{\Omega}_1 \times \boldsymbol{\Omega}_2, \; \boldsymbol{\Omega} \subseteq \mathbb{R}^6_+ \tag{5.2}$$

A vector $\mathbf{y}$ containing all continuously distributed design variables is then defined as follows.

$$\mathbf{y} := \begin{bmatrix} h & b & \epsilon & \eta & \beta & \delta \end{bmatrix}^{\mathrm{T}} \tag{5.3}$$

By introducing the additional vector $\mathbf{x}$

$$\mathbf{x} := \begin{bmatrix} h & b & \eta \end{bmatrix}^{\mathrm{T}}, \quad \mathbf{x} \subseteq \mathbf{y} \tag{5.4}$$

the underlying optimization program $\mathcal{P}(d_i)$ for a fixed d_i can be described as follows

$$\begin{aligned} \min_{\mathbf{y} \in \boldsymbol{\Omega}(d_i), \, d_i \in \{\boldsymbol{D}\}} & \quad f(\mathbf{x}, d_i) \\ \text{s.t.} & \quad g_\gamma(\mathbf{y}, d_i) \geq 0, \quad \gamma \in \boldsymbol{\Gamma} \end{aligned} \tag{5.5}$$

where $\boldsymbol{\Omega}(d_i)$ represents the set of possible $\mathbf{y}$ determined by the constraint functions $g_\gamma(\mathbf{y}, d_i)$ and the index set $\boldsymbol{\Gamma}$.

$$\boldsymbol{\Omega}(d_i) = \{\mathbf{y} \in \mathbb{R}^6_+, d_i \in \{\boldsymbol{D}\} \,|\, g_\gamma(\mathbf{y}, d_i) \geq 0, \, \gamma \in \boldsymbol{\Gamma}\} \tag{5.6}$$

A point $\mathbf{y}'_i \in \boldsymbol{\Omega}(d_i)$ is referred to as an *optimal* point in case that no other point exists, which gives better results for the value of the objective function. Taking into account the dedicated additional vector defined by eq. (5.4) and its corresponding optimal point $\mathbf{x}'_i \subseteq \mathbf{y}'_i$, it applies

$$f(\mathbf{x}, d_i) \geq f(\mathbf{x}'_i, d_i), \quad \forall \mathbf{x} \subseteq \mathbf{y} \in \boldsymbol{\Omega}(d_i). \tag{5.7}$$

The aggregation of all optimization programs with respect to the individual traction mechanisms gives the new set

$$\boldsymbol{P} = \{\mathcal{P}_1(d_1), \ldots, \mathcal{P}_i(d_i), \ldots, \mathcal{P}_n(d_n)\} \tag{5.8}$$

with the sets containing the optimal points $\mathbf{Y}'$ and the corresponding values of the objective functions $\boldsymbol{f}$.

$$\mathbf{Y}' = \{\mathbf{y}'_1, \ldots, \mathbf{y}'_i, \ldots, \mathbf{y}'_n\} \tag{5.9}$$

$$\boldsymbol{f} = \{f(\mathbf{x}'_1, d_1), \ldots, f(\mathbf{x}'_i, d_i), \ldots, f(\mathbf{x}'_n, d_n)\},\ \mathbf{x}'_i \subseteq \mathbf{y}'_i \tag{5.10}$$

Here, the overall desired solution is just that input combination consisting of $\mathbf{x}'_c$ and d', which leads to the smallest value of the set $\boldsymbol{f}$. Moreover, in this case the following applies

$$[\mathbf{x}'_c \quad d']^{\mathrm{T}} \longmapsto \boldsymbol{f}(\mathbf{x}'_c, d') \Longrightarrow \min\{\boldsymbol{f}\},\ \mathbf{x}'_c \subseteq \mathbf{y}'_c \in \mathbf{Y}',\ d' \in \{\boldsymbol{D}\} \tag{5.11}$$

where $\mathbf{y}'_c$ contains all required values in order to obtain the best solution.

In summary it can be stated, that the underlying problem is a multidimensional, non-smooth (due to the appearance of the discrete and not continuously differentiable quantity d_i) and nonlinear optimization program, where both the objective function and the constraints are nonlinear. These are further characterized by the fact that only inequality conditions occur.

5.1.2 Initial Investigations

In order to develop a suitable solution strategy, the key properties of the optimization problem are to be investigated in advance. The first subsection discusses the basic solvability of the problem. Subsequently, the possible critical points and their properties are examined in more detail.

Solvability

To verify the solvability, we first consider the *semi-constrained* optimization program, i.e. we already take into account the constraint that $\mathbf{x} \subseteq \mathbf{y} \in \mathbb{R}_+^6$ applies. For a fixed $b > 0$ and $1 > \eta > 0$, we obtain for a selectable $h > 0$ the following illustration of the objective function $f(\mathbf{x}, d_i)$, qualitatively shown in figure 5.2 (a). Forming the lower level
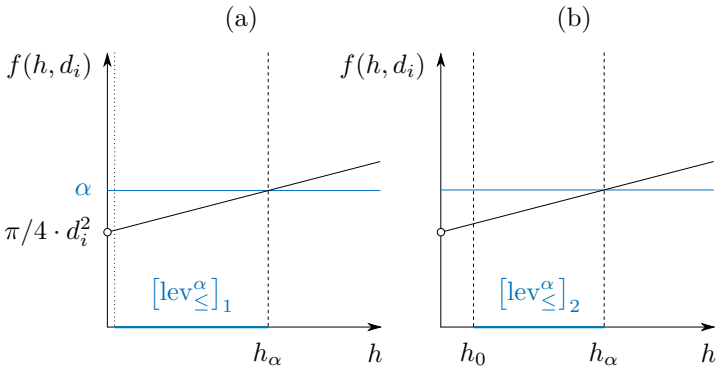
Figure 5.2: Lower level sets

set of f on $\mathbb{R}_+$ to a level $\alpha > \pi/4 \cdot d_i^2$, $\alpha \in \mathbb{R}_+$ gives

$$\left[\text{lev}_{\leq}^\alpha (f, \mathbb{R}_+) \right]_1 = \{ h \in \mathbb{R}_+ \,|\, 0 < f(h) \leq h_\alpha \}. \tag{5.12}$$

Although the interval is non-empty, it is not compact due to the lack of closure, since its complement $(-\infty, 0] \cup (h_\alpha, \infty)$ is not open. With respect to the extended theorem of WEIERSTRASS, the statement that the set $\mathbf{S}$ of all global minimal points, defined as

$$\mathbf{S} := \{ \mathbf{x}' \subseteq \mathbf{y}', \, \mathbf{y}' \in \mathbf{\Omega} \,|\, \forall \, [\mathbf{x} \subseteq \mathbf{y}], \, \mathbf{y} \in \mathbf{\Omega} : f(\mathbf{x}) \geq f(\mathbf{x}') \} \tag{5.13}$$

is non-empty and compact cannot be satisfied [5, p. 23]. Thus the sufficient condition for the solvability of the optimization problem is violated.

In turn, we now consider the optimization problem constrained by the set $\mathbf{\Omega}(d_i)$ and assume that a minimum height h_0 must be guaranteed, see figure 5.2 (b). Then, the lower level set is determined by

$$\left[\operatorname{lev}_{\leq}^{\alpha}(f, \mathbb{R}_+)\right]_2 = \{h \in \mathbb{R}_+ \mid h_0 \leq f(h) \leq h_{\alpha}\}. \tag{5.14}$$

In contrast to eq. (5.12) it is closed and compact. Hence, we can conclude that now the extended theorem of WEIERSTRASS applies and the optimization problem is solvable. Accordingly, the constraint of the problem is essential for its solvability.

Properties of the Functions Involved

In addition to the necessary optimality criterion of first order in non-constrained optimization, which requires that $\nabla f(\mathbf{x}_{\mathrm{c}}) = \mathbf{0}$ applies at a critical point $\mathbf{x}_{\mathrm{c}}$, the necessary second-order optimality criterion must be satisfied as well. This just implies that in case of a local minimum point the HESSIAN matrix $\mathbf{H}_f(\mathbf{x}_{\mathrm{c}})$ must be positive semi-definite. For this purpose we verify the eigenvalues of $\mathbf{H}_f(\mathbf{x}_{\mathrm{c}})$ for non-negativity. In this context, the HESSIAN matrix follows to

$$\mathbf{H}_f(\mathbf{x}_{\mathrm{c}}) = \begin{bmatrix} 0 & -4h_{\mathrm{c}} & 4 - 4\eta_{\mathrm{c}} \\ -4h_{\mathrm{c}} & 0 & 4t - 4b_{\mathrm{c}} \\ 4 - 4\eta_{\mathrm{c}} & 4t - 4b_{\mathrm{c}} & 0 \end{bmatrix}. \tag{5.15}$$

By application of the *characteristic polynomial*

$$\chi(\lambda) := \det\left(\lambda \mathbf{I}_1 - \mathbf{H}_f(\mathbf{x}_{\mathrm{c}})\right)$$

we obtain

$$\chi(\lambda) = \lambda^3 - p\lambda - q \tag{5.16}$$

with the coefficients

$$p = 16(h_{\mathrm{c}}^2 + b_{\mathrm{c}}^2 + \eta_{\mathrm{c}}^2 + t^2 + 1 - 2b_{\mathrm{c}}t - 2\eta_{\mathrm{c}})$$
$$q = 128h_{\mathrm{c}}(1 - \eta_{\mathrm{c}})(b_{\mathrm{c}} - t).$$

Table 5.1: Possible conditions and corresponding characteristics of critical points

Condition	Definiteness	Critical point
$p\sqrt{p} < \cos(\pi/6)q$	Positive definite	Strict local minimum
$p\sqrt{p} \geq \cos(\pi/6)q$	Indefinite	Saddle point

It is a polynomial of third degree where λ denotes the eigenvalues to be calculated by establishing $\chi(\lambda) = 0$. They represent the roots of the function. As $h_c > t$, $b_c > t$ and $1 > \eta_c > 0$ applies, it can be stated that the coefficients p and q are both > 0. Since q is negative in eq. (5.16), we can already conclude that, due to the characteristics of the function, there is a positive root (and thus a positive eigenvalue) in every case. It is now to be examined whether also negative eigenvalues can occur. In this specific case, the associated function value to the extremum at $\lambda = -\sqrt{p/3}$ must be positive, i.e $\chi(-\sqrt{p/3}) > 0$. According to the *intermediate value theorem* of real analysis, there is then at least one root in the interval $[-\sqrt{p/3}, 0]$, see [47, p. 336]. This special case is also called BOLZANO's theorem [48, p. 248]. Insertion of $\lambda = -\sqrt{p/3}$ into eq. (5.16) leads to the following condition which must apply.

$$p\sqrt{p} \overset{!}{\geq} \cos\left(\frac{\pi}{6}\right) q$$

Due to the complexity of the expression, it is not possible to determine in general terms whether this condition is always satisfied. Moreover, a critical point must be examined with regard to the case distinctions listed in table 5.1. However, we can still rule out the possibility that a strict local minimum occurs via the properties of the objective function. In case of a *strict* local minimum, the objective function must be strictly convex. Figure 5.2 shows that the underlying objective function is a straight line and thus forms a special case, since the function is both convex and concave. Accordingly, the requirement of strict convexity can be excluded, which leads to the statement that each critical point must be a saddle point for a fixed d_i.

Interpretation of the Solution Space

After the solvability of the optimization problem has been investigated and the type of critical points has been determined, the permissible solution space shall finally be interpreted in the last section. Since this
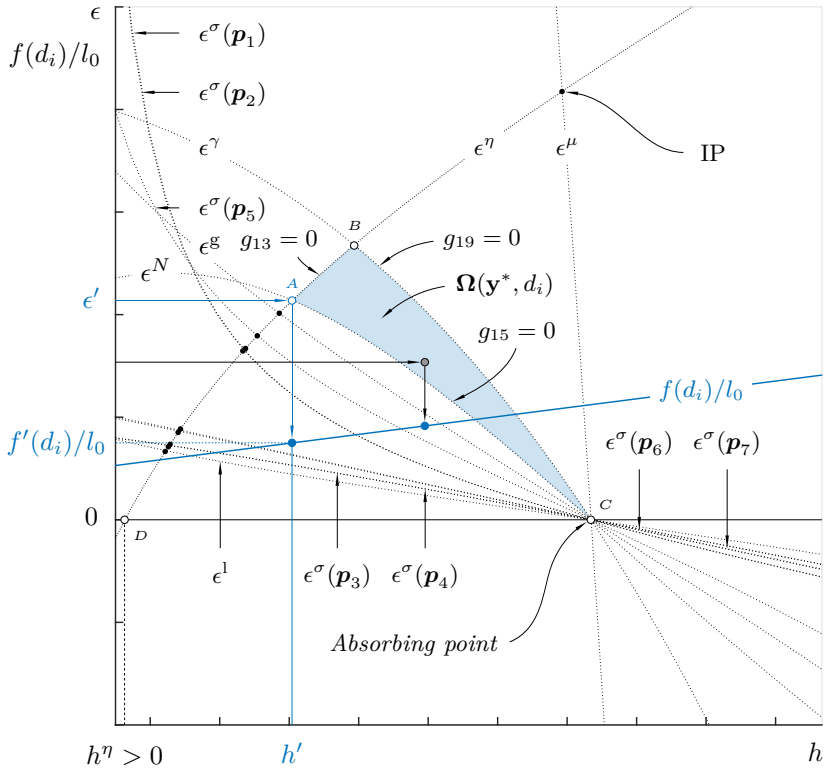
Figure 5.3: Qualitative illustration of the solution space (assuming $\delta > 0$)

extends over a six-dimensional space and therefore does not allow a

complete graphical representation, we assume that a permissible point combination exists denoted by

$$\mathbf{y}^* = [b^* \quad \eta^* \quad \beta^* \quad \delta^*]^{\mathrm{T}}, \quad \mathbf{y}^* \subseteq \mathbf{y} \in \mathbf{\Omega}(d_i). \tag{5.17}$$

Here, we benefit from the findings of the previous chapter 4. There it was shown that almost all constraints can be represented as functional relations between the eccentricity ϵ and the height h and do not necessarily require an implicit representation. With the help of this property, the constraint functions can now be visualized and are depicted in figure 5.3. At this point it should be mentioned that the illustration is valid for a $\delta > 0$ and describes the resulting set in a qualitative form. By which constraints the set is limited cannot be defined in a general way, rather this depends on the further parameters of the function (such as nominal load m_0 and span width l_0 for instance). However, we will see in the further course of the work that the knowledge of the shape of the set will be of minor importance. Furthermore, figure 5.3 represents a possible solution space on which the essential properties are to be demonstrated.

The corresponding compact set of points $\mathbf{\Omega}(\mathbf{y}^*, d_i) \subseteq \mathbf{\Omega}(d_i)$ containing all permissible combinations of ϵ and h is then to be identified by the application of the developed inequality conditions. In particular, the intersection points (IP) of the individual functions are analyzed. Here, the set is constrained by three curves (AB, BC and CA), while all points on these lines are *active* in their respective inequality constraints.

There are a number of further peculiarities in this context, which will be discussed in more detail. From figure 5.3 it can be noticed that, except for the function ϵ^η, all other constraint functions intersect the abscissa at a designated point C. All these functions have in common that they can be represented as the product of two functions, namely the initial bending moment M_0 and a respective individual term (see chapter 4). Accordingly, point C just corresponds to the associated root of the term of the initial bending moment. A key feature of this point is that due to the root the eccentricity vanishes here. This circumstance can be interpreted to mean that at this particular height the girder is just stiff enough to maintain the required deflection ratio $\delta > 0$ at nominal load. Here, h reaches its maximum value. For this reason, point C will be

referred to as the *absorbing point* in the following, which, however, can only occur for deflection ratios $\delta > 0$. Point B, in turn, represents the point of maximum eccentricity which can be applied without violating the boundary conditions.

Against the background of the actual optimization problem, point A is of great importance. On the one hand, it limits the set as a vertex and, on the other hand, it just corresponds to the minimum height h' for $\mathbf{y}^*$ which satisfies all constraints. With the according value for the eccentricity ϵ', the desired profile geometry of minimum weight is then exactly described. The additional, qualitative course of the objective function normalized to the span width $f(d_i)/l_0$ clarifies this, since it just reaches its permissible minimum value $f(d_i)'/l_0$.

5.1.3 Key Findings

The investigation of the underlying optimization program performed in the previous section revealed important information which are to be summarized in brief below:

1. The optimization problem is solvable only in case that the problem is constrained.

2. Every critical point of the semi-constrained optimization problem is a saddle point.

3. The critical points, which provide minimal values for the objective function, are located on the edge of the set determined by the constraints.

5.2 Solution Approach

Due to the complexity and number of nonlinear constraint functions, the optimization problem cannot be solved analytically in its entirety. In case of the KKT conditions (see section 2.4), the resulting system of equations could not be solved with a justified effort. Furthermore, the method has to be executed for all (discrete) values d_i of $\{\boldsymbol{D}\}$. Finally,

these circumstances require the application of a numerical method for the *approximate solution* of the optimization problem.

Since the segmented crane bridge is a new kind of structure, the primary goal here is to gain a thorough understanding of the characteristics of the system within the solution process. This also means that conclusions are to be drawn as to which constraints dominate or which constraints are responsible for the fact that no solution can be found. For this reason, the attempt is made to use as much information as possible that is already available in advance to develop a suitable solution method based on it. An essential point is to identify paths or parameter combinations in time, which do not lead to a solution and to separate them accordingly to make the procedure efficient.

5.2.1 Discretization of Continuously Distributed Variables

In the previous section it was shown that if a point $\mathbf{y}^*$ is assumed to satisfy the boundary conditions and leads to a solution, the associated solution set $\mathbf{\Omega}(\mathbf{y}^*, d_i)$ can be represented graphically. The main advantage of this is that the functions then depend only on the variable h, while the remaining parameters can be considered constant. A determination of the minimum height h' (for the point $\mathbf{y}^*$) is then comparatively simple, since it is located on the edge of the set and can be identified via the calculation of the intersection points of the functions. The according eccentricity then corresponds to the function value at this point. The handling of the problem is simplified by this approach considerably. Nevertheless, no statement can yet be made as to whether there are other points that lead to better results.

Furthermore, so far we do not have any information regarding the "determination" of such a possible point $\mathbf{y}^*$. In addition, the design variables, which the point $\mathbf{y}^*$ contains, are continuously distributed, accordingly also infinitely many combinations are possible. In order to summarize all these points, we introduce in this context the new subset $\mathbf{\Lambda}^*(d_i)$, which contains all possible combinations of the remaining variables. For this

purpose, the new index set $\bar{\mathbf{\Gamma}} \subseteq \mathbf{\Gamma}$ is first introduced, for whose elements the following condition applies.

$$\forall \bar{\gamma} \in \bar{\mathbf{\Gamma}} \, : \, g_{\bar{\gamma}} \neq f(h, \epsilon) \tag{5.18}$$

Here, $\bar{\mathbf{\Gamma}}$ then takes into account only those constraint functions that do not contain either h or ϵ. The set of all permissible point combinations $\mathbf{\Lambda}^*(d_i)$ is then defined by

$$\mathbf{\Lambda}^*(d_i) = \{\mathbf{y}^* \in \mathbb{R}_+^4, d_i \in \{\boldsymbol{D}\} \,|\, g_{\bar{\gamma}}(\mathbf{y}^*, d_i) \geq 0, \bar{\gamma} \in \bar{\mathbf{\Gamma}}\}. \tag{5.19}$$

Here, it is to be highlighted that this point is assigned to a fixed $d_i \in \{\boldsymbol{D}\}$ and thus all variables except h and ϵ are exactly defined.

It is easy to see that examining each point individually would not be purposeful. For this reason, we apply the strategy of *discretization* to break down the infinite, continuously distributed number of combinations to a finite (discrete) number. In this process, we facilitate the handling of the problem, but accept a loss of information, since not all points will be considered, but rather a selection. In this context, we define another subset $\mathbb{L}^*(d_i) \subseteq \mathbf{\Lambda}^*(d_i)$ containing a finite amount of points from $\mathbf{\Lambda}^*(d_i)$. Figure 5.4 represents the discretization qualitatively. Here, it can be seen that all points from $\mathbb{L}^*(d_i)$ are also contained in $\mathbf{\Lambda}^*(d_i)$. However, the same statement does not apply vice versa. In the further course of the work it is task to identify such a set $\mathbb{L}^*(d_i)$.

5.2.2 Verification of the Existence of Suitable Design Variable Combinations

The idea of discretization now lays the foundation for the development of a first procedure, with the help of which a suitable point combination can be identified, which allows the solvability of the optimization problem in principle. Here, we again profit from the already defined constraints.
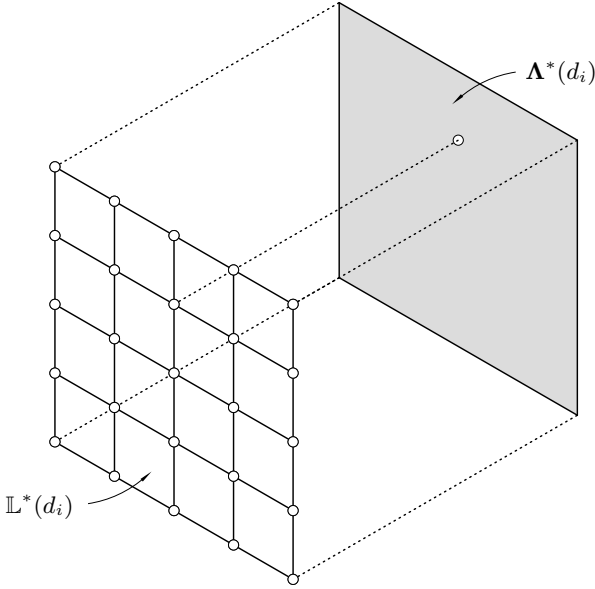
Figure 5.4: Discretization strategy

First, we decompose the intervals defined at the beginning for the height ratio $\mathbf{\Omega}^\eta$ and the deflection ratio $\mathbf{\Omega}^\delta$ (see section 5.1.1) into associated discrete intervals

$$\bar{\mathbf{C}}_i^\delta(d_i) = [\delta_{i1}, \ldots, \delta_{ij}, \ldots, \delta_{io}], \quad \bar{\mathbf{C}}_i^\delta(d_i) \subseteq \mathbf{\Omega}^\delta \qquad (5.20)$$

$$\bar{\mathbf{C}}_i^\eta(d_i) = [\eta_{i1}, \ldots, \eta_{ik}, \ldots, \eta_{ip}], \quad \bar{\mathbf{C}}_i^\eta(d_i) \subseteq \mathbf{\Omega}^\eta \qquad (5.21)$$

with $1 \leq j \leq o$ and $1 \leq k \leq p$. The maximum value of $\bar{\mathbf{C}}_i^\eta(d_i)$ can be determined by consideration of constraint g_4.

$$\max\{\bar{\mathbf{C}}_i^\eta(d_i)\} \stackrel{!}{=} 1 - \frac{t}{\lambda_\mathrm{h} l_0} \qquad (5.22)$$

By combining them, we obtain a new two-dimensional interval.

$$\bar{\mathbf{C}}_i^{(1)}(d_i) = \bar{\mathbf{C}}_i^\delta(d_i) \times \bar{\mathbf{C}}_i^\eta(d_i), \quad \bar{\mathbf{C}}_i^{(1)}(d_i) \subseteq \mathbb{R}_+^2 \qquad (5.23)$$

At any point $\bar{\mathbf{c}}_{ijk}^{(1)} = [\delta_{ij}, \eta_{ik}]$ of this interval under certain circumstances another interval can be spanned, which is assigned to this point. Here, we first also decompose the set $\mathbf{\Omega}^b$ into a discrete interval of considerable values for the width b with $1 \leq l \leq q$.

$$\bar{\mathbf{C}}_{ijk}^b(d_i) = [b_{ijk1}, \ldots, b_{ijkl}, \ldots, b_{ijkq}], \quad \bar{\mathbf{c}}_{ijk}^b(d_i) \subseteq \mathbf{\Omega}^b \qquad (5.24)$$

From the constraints g_1 and g_2 we can see that the width b and the width ratio β are functionally related. For this reason, the outstanding interval cannot be simply set up, rather this relationship must be taken into account. Since we take the interval of the width as given, we rearrange the constraint in order to identify the functional relationship. Thus we obtain the (functionally) bounded and initially continuous interval $\mathbf{C}_{ijkl}^\beta(b_{ijkl}, d_i)$.

$$\mathbf{C}_{ijkl}^\beta(b_{ijkl}, d_i) = \left[\frac{d_i + t + 2s_2}{2b_{ijkl}}, 1 - 2\frac{b_{\mathrm{w}}}{b_{ijkl}} - \left(\sqrt{0.98} + \frac{1}{2} \right) \frac{t}{b_{ijkl}} \right]$$

For this interval to be generated, the following inequality condition must be satisfied.

$$\frac{d_i + t + 2s_2}{2b_{ijkl}} \overset{!}{\leq} 1 - 2\frac{b_{\mathrm{w}}}{b_{ijkl}} - \left(\sqrt{0.98} + \frac{1}{2} \right) \frac{t}{b_{ijkl}} \qquad (5.25)$$

A further discretization then leads to the assigned interval for a specific $b_{ijkl} \in \bar{\mathbf{C}}_{ijk}^b(d_i)$.

$$\bar{\mathbf{C}}_{ijkl}^\beta(b_{ijkl}, d_i) = [\beta_{ijkl1}, \ldots, \beta_{ijklm}, \ldots, \beta_{ijklr}], \quad \bar{\mathbf{C}}_{ijkl}^\beta(b_{ijkl}, d_i) \subseteq \mathbf{\Omega}^\beta \qquad (5.26)$$

The two new intervals can also be formed to a two-dimensional interval as follows.

$$\bar{\mathbf{C}}_{ijk}^{(2)}(d_i) = \bar{\mathbf{C}}_{ijk}^b(d_i) \times \bar{\mathbf{C}}_{ijkl}^\beta(\bar{\mathbf{C}}_{ijk}^b, d_i), \quad \bar{\mathbf{C}}_{ijk}^{(2)}(d_i) \subseteq \mathbb{R}_+^2 \qquad (5.27)$$

Table 5.2: Approaches to determine suitable parameter combinations

Name	Description	Characteristic
LOA	Local optimization approach	Separation of entire problem into single problems $P_i(d_i)$
GOA	Global optimization approach	Consideration of entire problem

By combining the intervals $\bar{\mathbf{C}}_i^{(1)}(d_i)$ and $\bar{\mathbf{C}}_{ijk}^{(2)}(d_i)$ the entire space can be represented now by a further combination. We obtain

$$\bar{\mathbf{C}}_i(d_i) = \bar{\mathbf{C}}_i^{(1)}(d_i) \times \bar{\mathbf{C}}_{ijk}^{(2)}(d_i), \quad \bar{\mathbf{C}}_i(d_i) \subseteq \mathbb{R}_+^4 \tag{5.28}$$

while a point from this interval is then described by

$$\bar{\mathbf{c}}_{ijklm}(d_i) = [\delta_{ij}, \eta_{ik}, b_{ijkl}, \beta_{ijklm}(b_{ijkl})], \quad \bar{\mathbf{c}}_{ijklm}(d_i) \in \bar{\mathbf{C}}_i(d_i). \tag{5.29}$$

The procedure is qualitatively illustrated in figure 5.5.

Global Approach for the Identification of Suitable Design Variable Combinations

Up to now, the entire optimization problem was separated into subproblems and considered locally in each case. A certain diameter $d_i \in \{\boldsymbol{D}\}$ served as a reference point.

In the following, an alternative, global approach will be developed, which basically follows the same procedure, but additionally includes the set $\{\boldsymbol{D}\}$ in the determination of suitable parameter combinations. In order to be able to distinguish between both approaches, we will use the terms LOA and GOA in the further course of the work, see table 5.2. The optimization problem determined by eq. (5.5) in section 5.1.1 remains in its definition, only the introduced index i disappears, since
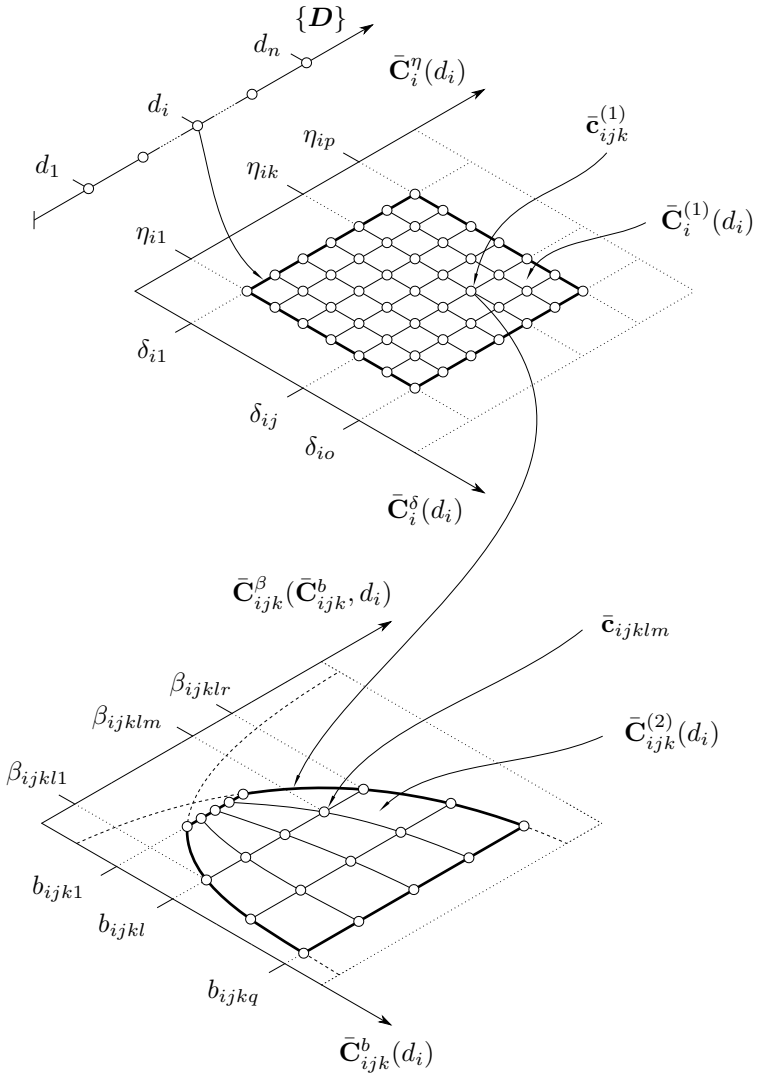
Figure 5.5: LOA - Identification of possible combinations of design variables

we now no longer consider the problem at a fixed d_i. Moreover, we then obtain the new expression

$$
\begin{aligned}
&\min_{\mathbf{y} \in \mathbf{\Omega},\, d \in \{\boldsymbol{D}\}} && f(\mathbf{x}, d) \\
&\quad\text{s.t.} && g_\gamma(\mathbf{y}, d) \geq 0, \quad \gamma \in \mathbf{\Gamma}
\end{aligned}
\tag{5.30}
$$

with the corresponding set

$$
\mathbf{\Omega} = \{\mathbf{y} \in \mathbb{R}_+^6, d \in \{\boldsymbol{D}\} \,|\, g_\gamma(\mathbf{y}, d) \geq 0,\, \gamma \in \mathbf{\Gamma}\}.
\tag{5.31}
$$

Accordingly, we consider d as an additional parameter to be varied. We proceed analogously to the previous section and first address the identification of suitable combinations of design variables. In contrast to the LOA, we consider a different sequence in the first step and create a discrete, three-dimensional space described by the intervals with respect to the deflection ratio $\bar{\mathbf{B}}^\delta$, height ratio $\bar{\mathbf{B}}^\eta$ and width $\bar{\mathbf{B}}^b$.

$$
\bar{\mathbf{B}}^\delta = [\delta_1, \ldots, \delta_j, \ldots, \delta_o], \quad \bar{\mathbf{B}}^\delta \subseteq \mathbf{\Omega}^\delta
\tag{5.32}
$$

$$
\bar{\mathbf{B}}^\eta = [\eta_1, \ldots, \eta_k, \ldots, \eta_p], \quad \bar{\mathbf{B}}^\eta \subseteq \mathbf{\Omega}^\eta
\tag{5.33}
$$

$$
\bar{\mathbf{B}}^b = [b_1, \ldots, b_l, \ldots, b_q], \quad \bar{\mathbf{B}}^b \subseteq \mathbf{\Omega}^b
\tag{5.34}
$$

The maximum value of $\bar{\mathbf{B}}^\eta$ is to be calculated analogously to eq. (5.22). Combining of the single intervals leads to the new three-dimensional interval $\bar{\mathbf{B}}^{(1)}$.

$$
\bar{\mathbf{B}}^{(1)} = \bar{\mathbf{B}}^\delta \times \bar{\mathbf{B}}^\eta \times \bar{\mathbf{B}}^b, \quad \bar{\mathbf{B}}^{(1)} \subseteq \mathbb{R}_+^3
\tag{5.35}
$$

Again, under certain circumstances, a new interval can be created at a point $\bar{\mathbf{b}}_{jkl}^{(1)} = [\delta_j, \eta_k, b_l]$ with $\bar{\mathbf{b}}_{jkl}^{(1)} \in \bar{\mathbf{B}}^{(1)}$. Since we assume a fixed width b_l at this point, an essential prerequisite for the creation of a new interval is, that minimum one traction mechanism (mainly determined by the diameter d) of the given set $\{\boldsymbol{D}\}$ fits into the segment, respectively into the connecting element. For this reason it is mandatory, that a subset $\{\boldsymbol{D}\}_{jkl}^*$ of $\{\boldsymbol{D}\}$ exists which contains all possible traction mechanisms that are suitable to be inserted while $\{\boldsymbol{D}\}_{jkl}^*$ must contain at least one traction mechanism. Otherwise the restricted geometry does not allow the insertion. Again, we use the constraint functions g_1 and g_2 with

respect to geometry and establish the following condition, which must be fulfilled[2].

$$\exists! \{\boldsymbol{D}\}^*_{jkl} \subseteq \{\boldsymbol{D}\}, \forall d_{jkli} \in \{\boldsymbol{D}\}^*_{jkl}:$$
$$0 \leq d_{jkli} \leq 2b_l - 4b_{\mathrm{w}} - (\sqrt{3.92} + 2)t - 2s_2 \qquad (5.36)$$

The resulting set $\{\boldsymbol{D}\}^*_{jkl}$ at the point $\bar{\mathbf{b}}^{(1)}_{jkl}$ can be interpreted as an interval as well while the total number of elements n_{jkl} depends on the width b_l, i.e. $n_{jkl} = f(b_l)$.

$$\{\boldsymbol{D}\}^*_{jkl} = [d_{jkl1}, \ldots, d_{jkli}, \ldots, d_{jkln}], \quad \{\boldsymbol{D}\}^*_{jkl} \in \{\boldsymbol{D}\} \qquad (5.37)$$

In addition, for each $d_{jkli} \in \{\boldsymbol{D}\}^*_{jkl}$ a range of possible inner widths can be determined. In comparison to the interval $\mathbf{B}^{(1)}$, here the quantities are functionally related. Taking into account g_1 and g_2 it can be determined that the minimum value of the possible width ratio depends on the diameter of the respective steel bar. On the other hand, the maximum value of the range only depends on the outer width b_l. Again, we formulate the corresponding interval $\mathbf{B}^\beta_{jkli}$.

$$\mathbf{B}^\beta_{jkli}(b_l, d_{jkli}) = \left[\frac{d_{jkli} + t + 2s_2}{2b_l}, 1 - 2\frac{b_{\mathrm{w}}}{b_l} - \left(\sqrt{0.98} + \frac{1}{2} \right) \frac{t}{b_l} \right] \quad (5.38)$$

In analogy to the ineq. (5.25), the following condition must also be fulfilled.

$$\frac{d_{jkli} + t + 2s_2}{2b_l} \overset{!}{\leq} 1 - 2\frac{b_{\mathrm{w}}}{b_l} - \left(\sqrt{0.98} + \frac{1}{2} \right) \frac{t}{b_l} \qquad (5.39)$$

A discretization leads to the corresponding interval for the width ratio.

$$\bar{\mathbf{B}}^\beta_{jkli}(b_l, d_{jkli}) = [\beta_{jkli1}, \ldots, \beta_{jklim}, \ldots, \beta_{jklir}], \quad \bar{\mathbf{B}}^\beta_{jkli} \subseteq \boldsymbol{\Omega}^\beta \quad (5.40)$$

The generated intervals are further combined to

$$\bar{\mathbf{B}}^{(2)}_{jkl} = \{\boldsymbol{D}\}^*_{jkl} \times \bar{\mathbf{B}}^\beta_{jkli}(b_l, d_{jkli}), \quad \bar{\mathbf{B}}^{(2)}_{jkl} \subseteq \mathbb{R}^2_+ \qquad (5.41)$$

---

[2] Here, the index i for the diameter d is kept.

which gives by a further combination the entire space.

$$\bar{\mathbf{B}} = \bar{\mathbf{B}}^{(1)} \times \bar{\mathbf{B}}^{(2)}_{jkl}, \quad \bar{\mathbf{B}} \subseteq \mathbb{R}^5_+ \tag{5.42}$$

A point $\bar{\mathbf{b}}_{jklim}$ of $\bar{\mathbf{B}}$ is then described as follows,

$$\bar{\mathbf{b}}_{jklim} = [\delta_j, \eta_k, b_l, d_{jkli}(b_l), \beta_{jklim}(b_l, d_{jklim})], \quad \bar{\mathbf{b}}_{jklim} \in \mathbf{B} \tag{5.43}$$

with figure 5.6 illustrating the approach.

It has been shown for both strategies that the discretization leads to a space $\bar{\mathbf{C}}_i(d_i) \subseteq \mathbb{R}^4_+$ (LOA), respectively $\bar{\mathbf{B}} \subseteq \mathbb{R}^5_+$ (GOA), of discrete combination possibilities, whose cardinality in turn depends on the fineness of the discretization. We now generally refer to such a space as $\bar{\mathbf{X}} \subseteq \mathbb{R}^v_+$ with $v \in \{4, 5\}$. If there exists at least one point $\bar{\mathbf{x}}^*$ from $\bar{\mathbf{X}}$ that satisfies all constraints $g_{\bar{\gamma}}$ with according index set $\bar{\mathbf{\Gamma}}$ assigned to it, then it is also an element of $\mathbb{L}^* \subseteq \mathbf{\Lambda}^* \subseteq \mathbb{R}^v_+$ and the generation of the remaining space is possible. At this moment it should already be pointed out that the existence of $\bar{\mathbf{x}}^*$ depends decisively on the initially chosen intervals and the fineness of the discretization. Consequently, this is a *necessary* condition for the numerical computation of a solution and summarized in lemma 5.2.1.

Lemma 5.2.1. *Let $\bar{\mathbf{X}} \subseteq \mathbb{R}^v_+$ be the set of discrete point combinations and $\mathbb{L}^* \subseteq \mathbf{\Lambda}^* \subseteq \mathbb{R}^v_+$ the discrete set of points, which fulfill all the corresponding constraints $g_{\bar{\gamma}}$. If $\bar{\mathbf{X}} \cap \mathbf{\Lambda}^* \neq \emptyset$ then $\mathbb{L}^* \neq \emptyset$ and it applies:*

$$\exists \bar{\mathbf{x}}^* \in \bar{\mathbf{X}} \subseteq \mathbb{R}^v_+ : g_{\bar{\gamma}}(\bar{\mathbf{x}}^*) \geq 0, \bar{\gamma} \in \bar{\mathbf{\Gamma}}.$$

This condition is depicted in figure 5.7. Whether a solution of the entire optimization problem can also be found at this point remains unanswered for the moment. Moreover, this criterion implies that by the existence of a suitable combination of variables $\bar{\mathbf{x}}^*$, the set $\mathbb{L}^*$ can be identified since it is not empty. This is an essential condition for the further calculation of a solution.
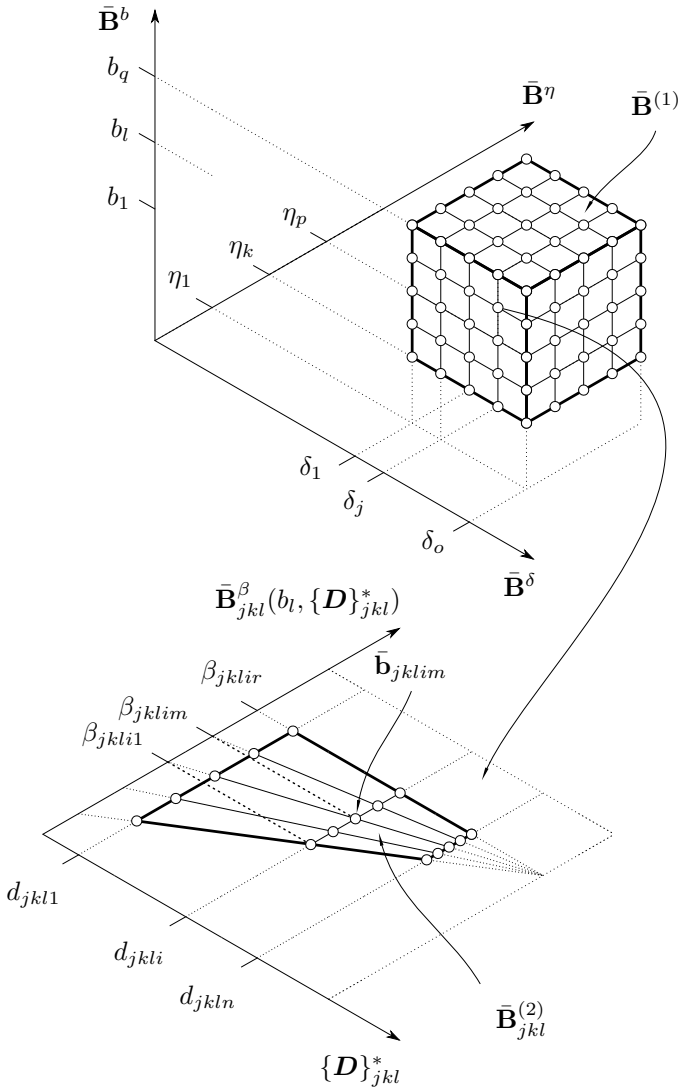
Figure 5.6: GOA - Identification of possible combinations of design variables

$$\bar{\mathbf{X}} \cap \mathbf{\Lambda}^* = \emptyset \qquad \bar{\mathbf{X}} \cap \mathbf{\Lambda}^* \neq \emptyset \qquad \bar{\mathbf{X}} \cap \mathbf{\Lambda}^* \neq \emptyset$$

$$|\mathbb{L}^*| = 0 \qquad\qquad |\mathbb{L}^*| = 1 \qquad\qquad |\mathbb{L}^*| > 1$$
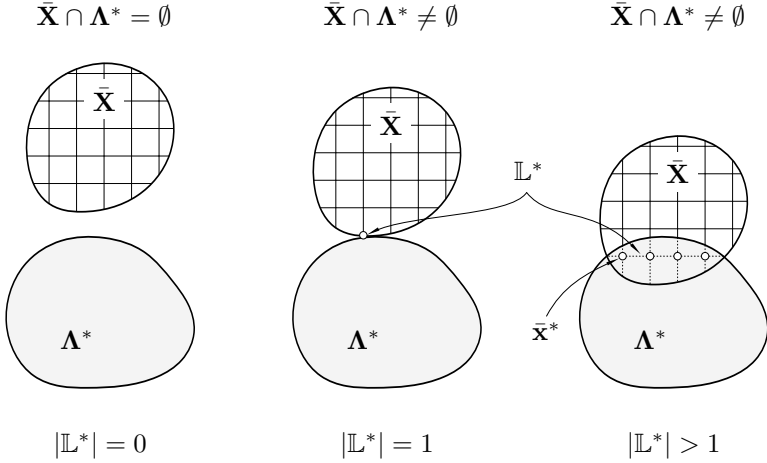
Figure 5.7: Discretization and corresponding sets

5.2.3 Identification of Local Critical Points

After the first solvability condition has been formulated, the remaining part of the optimization problem will be investigated in the following section. In this context, we require that lemma (5.2.1) is true, i.e. $\mathbb{L}^* \neq \emptyset$, and that at least one suitable variable combination $\bar{\mathbf{x}}^*_{i...m}$ exists on which the further computation can be performed. Whether this combination is determined by the LOA or GOA strategy is not important at this point. The entire index $(i...m)$ refers to the fact that, except for the eccentricity ϵ and the height h, all other design variables are now known. For the sake of completeness, we use this accordingly for the occurring quantities. The task is now to determine $\epsilon_{i...m}$ and $h_{i...m}$ associated with the point $\bar{\mathbf{x}}^*_{i...m}$ while it is of particular interest for which values $\epsilon'_{i...m}$ and $h'_{i...m}$ the objective function value at the point becomes minimum. For this purpose, it is reasonable to follow up the strategy of using available information and successively limit the possible range of $h_{i...m}$ with regard to the defined constraints (see summary table 4.2).

In the following, we will formulate important relations and conditions as lemmas and always assume their validity. On this basis, the entire solution strategy can be developed.

Successive Interval Limitation

In order to prevent the girder from exceeding a maximum permissible deflection in x_2-direction, the beam must possess a minimum outer height. The corresponding constraint is determined by g_{14}. The external height is additionally limited downwards, which can be identified by rearranging eq. (4.38). Here, only the maximum value given by the constraints is of interest. Then, the interval $\boldsymbol{I}_{i\ldots m}$ of possible external heights $h_{i\ldots m}$ follows to

$$\boldsymbol{I}_{i\ldots m} = \left[\max\left\{\frac{t}{1-\eta_j}; h_{i\ldots m}^{\delta}\right\}, \min\left\{\frac{l_{\mathrm{s}}^* - \lambda l_{\mathrm{s}} - x_{\mathrm{p}}}{\eta_j(1-\lambda_3)}; \lambda_{\mathrm{h}} l_0\right\}\right] \quad (5.44)$$

while the smaller value given by g_3 and g_5 define the upper limit. In figure 5.3 it was qualitatively shown that in the case of a deflection ratio $\delta > 0$ the maximum value of the height is limited by the absorbing point. This point just corresponds to the root of the term of the initial bending moment M_0. In order to examine whether a root exists, the following condition must apply with respect to the intermediate value theorem.

Lemma 5.2.2. *Let* $M_{0,i\ldots m}(\min\{\boldsymbol{I}_{i\ldots m}\}) > 0$, $M_{0,i\ldots m}(\max\{\boldsymbol{I}_{i\ldots m}\}) < 0$, *then applies:* $\exists! \, h_{i\ldots m}^M \in \boldsymbol{I}_{i\ldots m} : M_{0,i\ldots m}(h_{i\ldots m}^M) = 0$ *and* $h_{i\ldots m}^M := \max\{\boldsymbol{I}_{i\ldots m}\}$.

In case that lemma 5.2.2 applies, the upper limit of $\boldsymbol{I}_{i\ldots m}$ is to be adjusted and we obtain

$$\boldsymbol{I}_{i\ldots m} = \left[\max\left\{\frac{t}{1-\eta_j}; h_{i\ldots m}^{\delta}\right\}, h_{i\ldots m}^M\right]. \quad (5.45)$$

The interval defined by eq. (5.44), respectively eq. (5.45), forms the basis for the subsequent investigation of the remaining constraint functions. From figure 5.3 we further see that the function ϵ^η intersects the

143

abscissa, denoted by point D. When this is the case, the intersection point limits the interval downwards and the current lower limit is given by the root. Unless there is an intersection point in the interval, we require that only positive function values for ϵ^η exist on the interval, i.e. only positive values for the eccentricity. This circumstance results in the following requirements.

Lemma 5.2.3. *Let $\epsilon^\eta(\min\{\boldsymbol{I}_{i\dots m}\}) > 0$, $\epsilon^\eta(\max\{\boldsymbol{I}_{i\dots m}\}) > 0$, then all function values $\epsilon^\eta_{i\dots m}$ on the interval are positive and constraint g_{13} is fulfilled.*

Lemma 5.2.4. *Let $\epsilon^\eta(\min\{\boldsymbol{I}_{i\dots m}\}) < 0$, $\epsilon^\eta(\max\{\boldsymbol{I}_{i\dots m}\}) > 0$, then both negative and positive function values occur and it applies: $\exists! \, h^\eta_{i\dots m} \in \boldsymbol{I}_{i\dots m} : \epsilon^\eta_{i\dots m}(h^\eta_{i\dots m}) = 0$ and $h^\eta_{i\dots m} := \min\{\boldsymbol{I}_{i\dots m}\}$ and constraint g_{13} is fulfilled.*

By graphical analysis of the constraint functions with regard to the mechanical stresses it can be seen that they tend to form poles within the interval, with positive values for the eccentricity only existing right to the pole, see figure 5.8. Taking into account eq. (4.59), the according
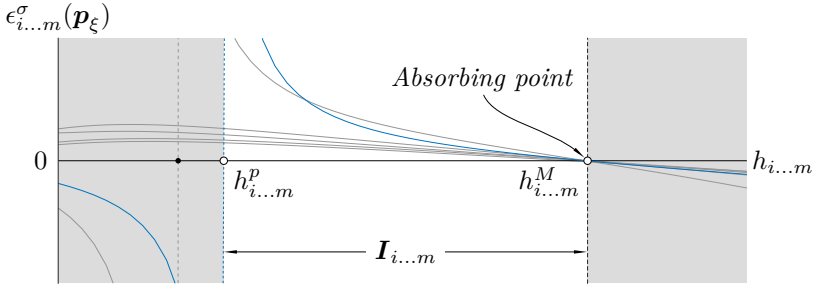
Figure 5.8: Qualitative representation of the poles

equations $P^\sigma_{i\dots m,\xi}$ describing the poles are determined by

$$P^\sigma_{i\dots m,\xi} = \frac{M_2}{I_{22}}p_{\xi 3} - \frac{M_3}{I_{33}}p_{\xi 2} - \frac{\sigma_{22}}{2} + \sqrt{\frac{\sigma_{22}^2}{4} - \psi_\sigma + \lambda^*_\sigma \hat{\sigma}_{11}}. \qquad (5.46)$$

First and foremost, we require that only positive function values of $P^\sigma_{i\ldots m,\xi}$ exist on the interval, then we can rule out the possibility that the interval is bounded by a pole. If this is not the case, then the root must be identified again via the intermediate value theorem. Moreover, we formulate the following conditions.

Lemma 5.2.5. *Let* $P^\sigma_{i\ldots m,\xi}(\min\{\boldsymbol{I}_{i\ldots m}\}) > 0$, $P^\sigma_{i\ldots m,\xi}(\max\{\boldsymbol{I}_{i\ldots m}\}) > 0$, *then all function values on the interval are positive.*

Lemma 5.2.6. *Let* $P^\sigma_{i\ldots m,\xi}(\min\{\boldsymbol{I}_{i\ldots m}\}) > 0$, $P^\sigma_{i\ldots m,\xi}(\min\{\boldsymbol{I}_{i\ldots m}\}) < 0$, *then both negative and positive function values occur and it applies:* $\exists! \, h^p_{i\ldots m,\xi} \in \boldsymbol{I}_{i\ldots m} : P^\sigma_{i\ldots m,\xi}(h^p_{i\ldots m,\xi}) = 0$.

Since lemma (5.2.5), respectively lemma (5.2.6), refers to a certain point $\boldsymbol{p}_\xi$ we tighten it by introducing the set $\{\boldsymbol{P}\}^\sigma_{i\ldots m}$ containing all roots $h^p_{i\ldots m,\xi}$ and obtain the condition

$$\max\{\{\boldsymbol{P}\}^\sigma_{i\ldots m}\} := \min\{\boldsymbol{I}_{i\ldots m}\} \tag{5.47}$$

in case that the set exists, i.e. $\{\boldsymbol{P}\}^\sigma_{i\ldots m} \neq \emptyset$. In figure 5.8 the function with the relevant pole is highlighted in blue while the gray areas mark the non-permissible interval ranges.

At this stage the interval is adjusted where only positive values for the eccentricity are given, determined by eq. (4.71). In the following, it is to be verified whether the contained combinations of $\epsilon_{i\ldots m}$ and $h_{i\ldots m}$ satisfy the remaining constraints. By rearranging the equations, we find that the remaining functions limit the eccentricity either upwards or downwards. For this reason, it makes sense to sort them accordingly. At first we consider the constraints that limit $\epsilon_{i\ldots m}$ downwards and establish auxiliary functions which are defined as follows:

$$D^{(1)}_{i\ldots m}(h_{i\ldots m}) := \epsilon^\eta_{i\ldots m} - \epsilon^{\mathrm{l}}_{i\ldots m} \tag{5.48}$$

$$D^{(2)}_{i\ldots m}(h_{i\ldots m}) := \epsilon^\eta_{i\ldots m} - \epsilon^{\mathrm{g}}_{i\ldots m} \tag{5.49}$$

$$D^{(3)}_{i\ldots m,\xi}(h_{i\ldots m}) := \epsilon^\eta_{i\ldots m} - \epsilon^\sigma_{i\ldots m,\xi}(\boldsymbol{p}_\xi), \quad \xi \in \{1,\ldots,7\} \tag{5.50}$$

$$D^{(4)}_{i\ldots m}(h_{i\ldots m}) := \epsilon^\eta_{i\ldots m} - \epsilon^N_{i\ldots m} \tag{5.51}$$

In this connection, it is of particular interest, whether for the specific auxiliary functions roots exist. These mark the significant points where both boundary conditions are fulfilled, on which the auxiliary functions are based on. Since the $\epsilon_{i...m}^{\eta}$ limits the eccentricity upwards and the remaining functions limit the eccentricity downwards, we can state as a first requirement regarding solvability that all function values of the auxiliary functions must be positive. Otherwise, the boundary conditions would be violated. In case that a root of an auxiliary function exists, both positive and negative function values occur. Again, the root then marks the new lower boundary of the interval. On this basis, we derive the corresponding lemmas in the following.

Lemma 5.2.7. *Let $\forall\, h_{i...m} \in \boldsymbol{I}_{i...m} :\, D_{i...m}^{(1)}(h_{i...m}) > 0$, then the constraints g_{13} and g_{17} are fulfilled.*

Lemma 5.2.8. *Let $D_{i...m}^{(1)}(\min\{\boldsymbol{I}\}_{i...m}) < 0$, $D_{i...m}^{(1)}(\max\{\boldsymbol{I}\}_{i...m}) > 0$, then applies: $\exists!\, h_{i...m}^{(1)} \in \boldsymbol{I}_{i...m} :\, D_{i...m}^{(1)}(h_{i...m}^{(2)}) = 0$ and the constraints g_{13} and g_{17} are fulfilled.*

As far as lemma (5.2.7) is not satisfied, a solution can still exist. For this, however, lemma (5.2.8) must be fulfilled. For the other auxiliary functions we proceed analogously and set up the respective conditions. One of the conditions must be true for each function. Subsequently we formulate the conditions regarding $D_{i...m}^{(2)}$.

Lemma 5.2.9. *Let $\forall\, h_{i...m} \in \boldsymbol{I}_{i...m} :\, D_{i...m}^{(2)}(h_{i...m}) > 0$, then the constraints g_{13} and g_{16} are fulfilled.*

Lemma 5.2.10. *Let $D_{i...m}^{(2)}(\min\{\boldsymbol{I}\}_{i...m}) < 0$, $D_{i...m}^{(2)}(\max\{\boldsymbol{I}\}_{i...m}) > 0$, then applies: $\exists!\, h_{i...m}^{(2)} \in \boldsymbol{I}_{i...m} :\, D_{i...m}^{(2)}(h_{i...m}^{(2)}) = 0$ and the constraints g_{13} and g_{16} are fulfilled.*

Furthermore, the conditions with regard to mechanical stresses result as follows.

Lemma 5.2.11. *Let $\forall\, h_{i...m,\xi} \in \boldsymbol{I}_{i...m}$, $\xi \in \{1,\ldots,7\} :\, D_{i...m,\xi}^{(3)}(h_{i...m,\xi}) > 0$, then the constraints g_{13} and g_6 to g_{12} are fulfilled.*

Lemma 5.2.12. *Let $D_{i\dots m,\xi}^{(3)}(\min\{\boldsymbol{I}\}_{i\dots m}) < 0$, $D_{i\dots m,\xi}^{(3)}(\max\{\boldsymbol{I}\}_{i\dots m}) > 0$, then applies: $\exists!\, h_{i\dots m,\xi}^{(3)} \in \boldsymbol{I}_{i\dots m}$, $\xi \in \{1,\dots,7\} : D_{i\dots m,\xi}^{(3)}(h_{i\dots m,\xi}^{(3)}) = 0$ and the constraints g_{13} and g_6 to g_{12} are fulfilled.*

The remaining conditions comprise the constraint with regard to the maximum assembly preload that can be applied to the traction mechanism.

Lemma 5.2.13. *Let $\forall\, h_{i\dots m} \in \boldsymbol{I}_{i\dots m} : D_{i\dots m}^{(4)}(h_{i\dots m}) > 0$, then the constraints g_{13} and g_{15} are fulfilled.*

Lemma 5.2.14. *Let $D_{i\dots m}^{(4)}(\min\{\boldsymbol{I}\}_{i\dots m}) < 0$, $D_{i\dots m}^{(4)}(\max\{\boldsymbol{I}\}_{i\dots m}) > 0$, then applies: $\exists!\, h_{i\dots m}^{(4)} \in \boldsymbol{I}_{i\dots m} : D_{i\dots m}^{(4)}(h_{i\dots m}^{(4)}) = 0$ and the constraints g_{13} and g_{15} are fulfilled.*

All occurring roots can be summarized into a new set denoted by $\{\boldsymbol{R}\}_{i\dots m}$, whereby all of them limit the range of possible solutions downwards. Then, the current lower limit of the interval $\boldsymbol{I}_{i\dots m}$ is represented by the maximum value of $\{\boldsymbol{R}\}_{i\dots m}$. We obtain

$$\max\{\{\boldsymbol{R}\}_{i\dots m}\} \coloneqq \min\{\boldsymbol{I}_{i\dots m}\} \tag{5.52}$$

for the lower limit of the current interval. In case that no roots occur, the respective alternative conditions must be fulfilled and the lower limit of $\boldsymbol{I}_{i\dots m}$ remains unmodified.

The last step contains the investigation of the constraint functions limiting the eccentricity upwards. Analogously to the previous section the auxiliary functions

$$U_{i\dots m}^{(5)}(h_{i\dots m}) \coloneqq \epsilon_{i\dots m}^{\eta} - \epsilon_{i\dots m}^{\mu} \tag{5.53}$$

$$U_{i\dots m}^{(6)}(h_{i\dots m}) \coloneqq \epsilon_{i\dots m}^{\eta} - \epsilon_{i\dots m}^{\gamma} \tag{5.54}$$

with respect to the constraints g_{18} and g_{19} are defined. Here, the same conditions apply and we formulate the respective requirements.

Lemma 5.2.15. *Let $\forall\, h_{i\dots m} \in \boldsymbol{I}_{i\dots m} : U_{i\dots m}^{(5)}(h_{i\dots m}) > 0$, then the constraints g_{13} and g_{18} are fulfilled.*

147

Lemma 5.2.16. *Let* $U_{i...m}^{(5)}(\min\{\boldsymbol{I}_{i...m}\}) < 0$, $U_{i...m}^{(5)}(\max\{\boldsymbol{I}_{i...m}\}) > 0$, *then applies:* $\exists!\, h_{i...m}^{(5)} \in \boldsymbol{I}_{i...m} \,:\, D_{i...m}^{(5)}(h_{i...m}^{(5)}) = 0$ *and the constraints* g_{13} *and* g_{18} *are fulfilled.*

The last conditions concerning the solvability include the constraints concerning the contour accuracy. We define them according to the same scheme.

Lemma 5.2.17. *Let* $\forall\, h_{i...m} \in \boldsymbol{I}_{i...m} \,:\, U_{i...m}^{(6)}(h_{i...m}) > 0$, *then the constraints* g_{13} *and* g_{19} *are fulfilled.*

Lemma 5.2.18. *Let* $U_{i...m}^{(6)}(\min\{\boldsymbol{I}_{i...m}\}) < 0$, $U_{i...m}^{(6)}(\max\{\boldsymbol{I}_{i...m}\}) > 0$, *then applies:* $\exists!\, h_{i...m}^{(6)} \in \boldsymbol{I}_{i...m} \,:\, D_{i...m}^{(6)}(h_{i...m}^{(6)}) = 0$ *and the constraints* g_{13} *and* g_{19} *are fulfilled.*

Exactly as executed before, the two possible occurring roots can be grouped to a set $\{\boldsymbol{R}\}_{i...m}^{*}$ while now its minimum value determines the upper limit of the interval $\boldsymbol{I}_{i...m}$. Then the following condition applies.

$$\min\{\{\boldsymbol{R}\}_{i...m}^{*}\} \coloneqq \max\{\boldsymbol{I}_{i...m}\} \tag{5.55}$$

Determination of the Local Critical Point

With the help of the successive reduction of the interval $\boldsymbol{I}_{i...m}$, the current lower and upper limit of the external height $h_{i...m}$ and the corresponding eccentricity $\epsilon_{i...m}$ could be determined. As a last final constraint, it must be possible to establish an interval within the defined limits. For this purpose we require

$$\min\{\boldsymbol{I}_{i...m}\} \overset{!}{\leq} \max\{\boldsymbol{I}_{i...m}\}. \tag{5.56}$$

In case of existing roots, i.e. $\{\boldsymbol{R}\}_{i...m} \neq \emptyset$ and $\{\boldsymbol{R}\}_{i...m}^{*} \neq \emptyset$, the constraint defined by eq. (5.56) above can be alternatively formulated as

$$\max\{\{\boldsymbol{R}\}_{i...m}\} \overset{!}{\leq} \min\{\{\boldsymbol{R}\}_{i...m}^{*}\}. \tag{5.57}$$

If the interval does not exist, the set $\boldsymbol{\Omega}'_{i\ldots m}(\bar{\mathbf{x}}^*_{i\ldots m}) \subseteq \boldsymbol{\Omega}_{i\ldots m}(\bar{\mathbf{x}}^*_{i\ldots m})$ containing $\epsilon_{i\ldots m}$ and $h_{i\ldots m}$ does not exist either and therefore no solution can be found. To determine the height that leads to a minimum objective function value $f'(\bar{\mathbf{x}}^*_{i\ldots m}, h'_{i\ldots m})$ at the point $\bar{\mathbf{x}}^*_{i\ldots m}$, we easily recognize that it must now be at the edge of the interval due to the inequality constraints. This finding is also consistent with the properties of the optimization problem investigated in section 5.1.3. Therefore, we can now clearly identify the minimum $h'_{i\ldots m}$, since this just corresponds to the lower limit of the interval $\boldsymbol{I}_{i\ldots m}$. With this background, we can now establish the *sufficient* condition for numerical solvability, which we will refer to as the second order criterion of numerical solvability in the following.

Lemma 5.2.19. *Let* $\min\{\boldsymbol{I}_{i\ldots}\} \leq \max\{\boldsymbol{I}_{i\ldots m}\}$*, then* $\boldsymbol{\Omega}'_{i\ldots m}(\bar{\mathbf{x}}^*_{i\ldots m}) \neq \emptyset$ *and* $h'_{i\ldots m} = \min\{\boldsymbol{I}_{i\ldots m}\}$ *and* $\epsilon'_{i\ldots m} = \epsilon^{\eta}_{i\ldots m}(h'_{i\ldots m})$.

Figure 5.9 shows the consistent interval reduction qualitatively. The vertical dashed lines represent the intersection of the individual constraint functions while the gray areas again mark the impermissible ranges. It can be clearly seen that the minimum height sought lies on the edge of the set $\boldsymbol{\Omega}'_{i\ldots m}(\bar{\mathbf{x}}_{i\ldots m})$. Furthermore, it should be noted that all values $[h_{i\ldots m}, \epsilon_{i\ldots m}] \in \boldsymbol{\Omega}_{i\ldots m}(\bar{\mathbf{x}}^*_{i\ldots m})$ also represent possible solutions, but only those are of interest that are elements of $\boldsymbol{\Omega}'_{i\ldots m}(\bar{\mathbf{x}}^*_{i\ldots m})$.

Summary of Numerical Solvability

Finally, we summarize that the numerical determination of a possible solution requires two essential conditions. These include the *First order criterion of numerical solvability* as a *necessary* condition, i.e. the existence of a permissible parameter combination $\bar{\mathbf{x}}^*_{i\ldots m}$ (see lemma (5.2.1)), and the *Second order criterion of numerical solvability* as a *sufficient* condition, according to which the existence of the set $\boldsymbol{\Omega}'_{i\ldots m}(\bar{\mathbf{x}}^*_{i\ldots m})$ is required (see lemma (5.2.19)). In this framework, the interval is successively reduced against the background of the defined inequality conditions, whereby it is then constantly verified by exclusion procedures whether the interval can be established and thus the set $\boldsymbol{\Omega}'_{i\ldots m}(\bar{\mathbf{x}}^*_{i\ldots m})$ exists. Since irrelevant areas or rather impermissible solutions are cut
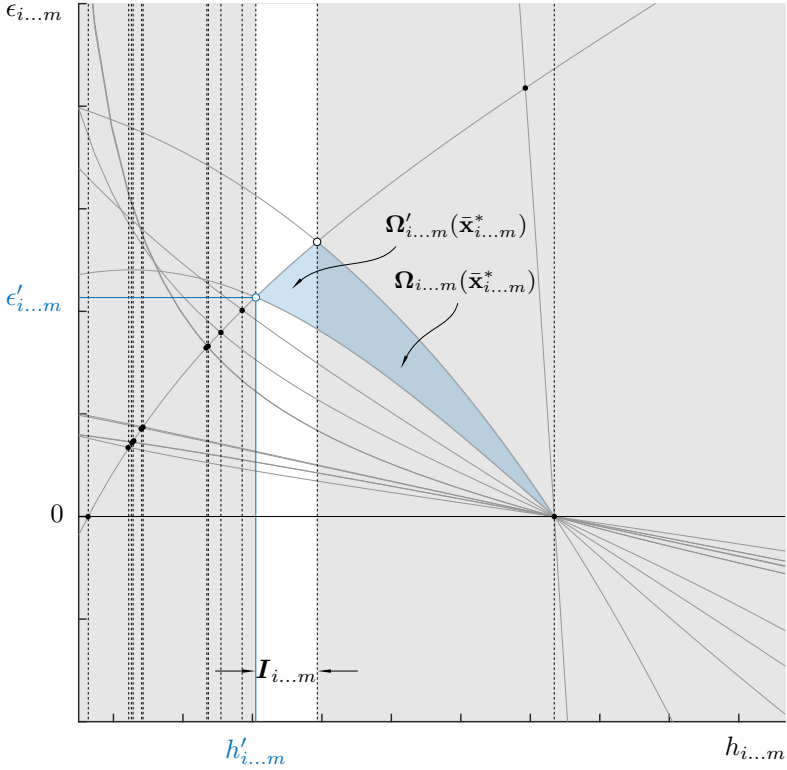
Figure 5.9: Interval limitation

off at the same time, this approach can be assigned to the method of *Branch and Bound*. The contribution of all relevant sets is graphically illustrated in figure 5.10. Here, the set $\boldsymbol{\Omega}$ denotes the set of all solutions $\mathbf{y}$ of the optimization problem, while $\bar{\mathbf{X}}$ represents the set of all discrete parameter combinations. We recognize that a fraction of $\bar{\mathbf{X}}$ must be a subset of $\boldsymbol{\Omega}$, otherwise no solutions exist. This subset is denoted by $\mathbb{L}^*$. At such a point $\bar{\mathbf{x}}^*_{i\dots m} \in \mathbb{L}^*$, the set $\boldsymbol{\Omega}_{i\dots}(\bar{\mathbf{x}}^*_{i\dots m})$ can be identified by application of the successive interval limitation, which in turn leads to the set $\boldsymbol{\Omega}'_{i\dots}(\bar{\mathbf{x}}^*_{i\dots m})$ by an interval limitation. The desired point
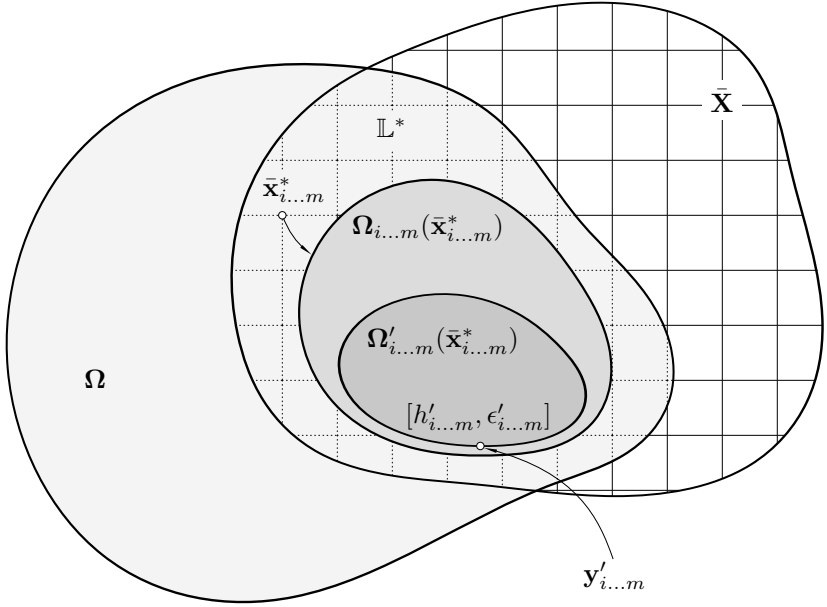
Figure 5.10: Solution approach

$[h'_{i...m}, \epsilon'_{i...m}]$ is then located on the edge of the set and results altogether in the overall point $\mathbf{y}'_{i...m}$, which is defined as follows.

$$\mathbf{y}'_{i...m} = [\bar{\mathbf{x}}^*_{i...m}, h'_{i...m}, \epsilon'_{i...m}], \quad \mathbf{y}'_{i...m} \in \mathbf{\Omega} \qquad (5.58)$$

Furthermore, figure 5.10 highlights that the discretization has a significant impact on finding a solution due to the accepted loss of information. For example, if the discretization is not fine enough, it may not be possible to identify a point $\bar{\mathbf{x}}^*_{i...m}$ that is an element of $\mathbb{L}^*$. Accordingly, in this case $\mathbb{L}^*$ does not exist either, i.e. $\mathbb{L}^* = \emptyset$, and a solution cannot be found at all.

The calculation of roots is an essential part of the procedure. Due to the high degree of complexity of the equations, it is not possible to formulate analytically closed expressions. Furthermore, a numerical procedure for the calculation of the roots is required. Since in the determination of a

151

solution, among other things, the function values at the interval boundaries are considered, the *bisection method* is used as a numerical solution procedure for the determination of roots. By a consistent interval nesting, the roots can be approximated until a defined termination criterion is reached. It is a very robust method and, compared to other methods (such as NEWTON's method), only requires statements about the function values at the interval boundaries [49, p. 185].

Analytical Examination

The numerical method provides solutions, but no statements about the characteristics of the calculated solutions. Against the background of the fundamentals of nonlinear optimization developed in chapter 2, the problem is to be investigated analytically. Due to the underlying complexity, however, assumptions and simplifications have to be made:

- The constants are selected in such a way that the problem is solvable and

- the decisive local critical point is always identified by the intersection of the functions ϵ^η and ϵ^N according to the numerical procedure presented.

The determination of this intersection leads to a polynomial of sixth degree, which is not elementary solvable. For this reason, this solution is simplifying assumed as known and denoted by $\bar{\mathbf{x}} = [\bar{\epsilon}, \bar{h}]$.

Within the graphical interpretation (see figure 5.3) it could already be determined that this point is obviously a local minimum, which - in this case - is active in the constraints g_{13} and g_{15}. It is now to be investigated whether this always holds for such an intersection. For this purpose the gradients of the involved functions are formed and it is requested that no vector $\mathbf{s}^* \in \mathbb{R}^2$ exists [38, p. 130] which solves the following system.

$$\langle \nabla f(\bar{\mathbf{x}}), \mathbf{s}^* \rangle < 0, \qquad \langle \nabla g_\gamma(\bar{\mathbf{x}}), \mathbf{s}^* \rangle < 0, \qquad \gamma \in \{13, 15\}$$

If this is true, $\bar{\mathbf{x}}$ is a local minimum point. Here, the partial derivatives are determined by

$$\frac{\partial g_{13}}{\partial h} = -\eta - \frac{R_3 l_0^3 (\alpha_1^3 - 3\alpha_1^2 + 2)}{E\theta_{22}} \frac{1}{h^4} \qquad \frac{\partial g_{13}}{\partial \epsilon} = -1$$

$$\frac{\partial g_{15}}{\partial \epsilon} = \frac{\gamma_{\text{M2}}}{N} \left(\frac{6E\theta_{22}\delta}{l_0} h^2 - \frac{5}{12} \rho g \theta_1 l_0^2 \right) \qquad \frac{\partial g_{15}}{\partial \epsilon} = 1$$

$$\frac{\partial f}{\partial h} = \theta_1 \qquad\qquad\qquad\qquad \frac{\partial f}{\partial \epsilon} = 0$$

which give the corresponding system of inequalities.

$$-\left(\eta + \frac{R_3 l_0^3}{E\theta_{22}} (\alpha_1^3 - 3\alpha_1^2 + 2) \frac{1}{h^4} \right) s_1^* + s_2^* \qquad < 0 \qquad (5.59)$$

$$\frac{\gamma_{\text{M2}}}{N} \left(\frac{5}{12} \rho g \theta_1 l_0^2 - \frac{6E\theta_{22}\delta}{l_0} \bar{h}^2 \right) s_1^* - s_2^* \qquad < 0 \qquad (5.60)$$

$$\theta_1 s_1^* \qquad < 0 \qquad (5.61)$$

By ineq. (5.61), s_1^* must be negative for the inequality to be satisfied while s_2^* is freely selectable. With $s_2^*/s_1^* = \kappa^*$, this subsequently leads to a new system of inequalities.

$$\kappa^* > \eta + \frac{R_3 l_0^3}{E\theta_{22}} (\alpha_1^3 - 3\alpha_1^2 + 2) \frac{1}{\bar{h}^4} \qquad (5.62)$$

$$\kappa^* > \frac{\gamma_{\text{M2}}}{N} \left(-\frac{5}{12} \rho g \theta_1 l_0^2 + \frac{6E\theta_{22}\delta}{l_0} \bar{h}^2 \right) \qquad (5.63)$$

Since the right term of ineq. (5.62) can only have positive values, κ^* must also be positive for the inequality to be true. Now, if the term in the parenthesis of ineq. (5.63) is ≤ 0, then the system of inequalities is satisfied in any case. But for $\bar{\mathbf{x}}$ to be a minimum point, this condition must be formulated in such a way that the system of inequalities cannot be fulfilled. This results in

$$\bar{h} > \frac{l_0}{6} \sqrt{\frac{5\rho g \theta_1 l_0}{2E\theta_{22}\delta}} \qquad (5.64)$$

as a condition for the external height.

With the help of the analytical consideration, the conclusions listed below can be drawn with respect to the previously defined assumptions.

- The existence of a minimum point does not depend on the eccentricity.

- If the self-weight is neglected ($\rho \to 0$), every point $\bar{\mathbf{x}}$ is always a minimum point, since ineq. (5.64) then reduces to the trivial condition $\bar{h} > 0$.

- Furthermore, it can be demonstrated that under the condition given by ineq. (5.64), the MFCQ is also satisfied.

- If ineq. (5.64) is fulfilled, every minimum point is also a KKT point.

5.2.4 Global Solution Approximation

The strategy developed in the previous section is able to identify points $\mathbf{y}'_{i...m} \in \mathbf{\Omega}$ that satisfy all constraints and even provide the optimal result for a fixed point $\bar{\mathbf{x}}^*_{i...m}$. However, this optimum is only limited to that local point $\bar{\mathbf{x}}^*_{i...m}$ and we cannot predict yet whether there are any "better" points in $\mathbf{\Omega}$ compared to the already determined point $\mathbf{y}'_{i...m}$. Moreover, we would have to discretize the spaces infinitely fine and compare all the points, thus obtaining the best among them. It is obvious that this approach is not reasonable on one hand and not feasible on the other hand.

Hence, we first hypothesize that a point $\mathbf{y}'_0$ with the property of satisfying all boundary conditions exists and that a better point $\mathbf{y}'_1$ is located near this point. With the help of the definition of the so-called *direction of descent* we are even able to prove this hypothesis [38, p. 30]. For this purpose, we additionally first normalize all remaining continuously differentiable and dimensioned quantities with respect to the span width l_0 and thus obtain the quantities that are decisive for the objective function.

$$\psi = \frac{h}{l_0}, \, \psi \in (0,1) \qquad \omega = \frac{b}{l_0}, \, \omega \in (0,1) \qquad \theta = \frac{t}{l_0}, \, \theta \in (0,1)$$

These can again be combined into a vector

$$\boldsymbol{\xi} := [\psi \quad \omega \quad \eta]^{\mathrm{T}} \tag{5.65}$$

which is a subset of the superior vector $\boldsymbol{\eta}$, which contains all dimensionless and continuously differentiable quantities (analogous to $\mathbf{y}$). In terms of completeness, we refer to the associated set determined by the constraint functions as $\tilde{\boldsymbol{\Omega}}$. This set is now divided into two parts: one subset $\tilde{\boldsymbol{\Omega}}^*$ refers to the equality conditions and the other subset $\tilde{\boldsymbol{\Omega}}^\circ$ refers to the strict inequality conditions. This allows a distinction to be made as to whether a point is in the set or on the edge of the set.

$$\tilde{\boldsymbol{\Omega}}^\circ = \{\boldsymbol{\eta}^\circ \in \mathbb{R}^6_+, d \in \{\boldsymbol{D}\} \,|\, \tilde{g}_\gamma(\boldsymbol{\eta}^\circ) > 0,\, \gamma \in \boldsymbol{\Gamma}\}$$
$$\tilde{\boldsymbol{\Omega}}^* = \{\boldsymbol{\eta}^* \in \mathbb{R}^6_+, d \in \{\boldsymbol{D}\} \,|\, \tilde{g}_\gamma(\boldsymbol{\eta}^*) = 0,\, \gamma \in \boldsymbol{\Gamma}\}$$

In turn, the union of the sets results in the original set and

$$\tilde{\boldsymbol{\Omega}}^\circ \cup \tilde{\boldsymbol{\Omega}}^* = \tilde{\boldsymbol{\Omega}}$$

applies. Accordingly, the new variables also lead to a new dimensionless objective function φ, which forms the basis for the following proof.

Proof. Let $\boldsymbol{\xi}_0' \subseteq \boldsymbol{\eta}_0' \in \tilde{\boldsymbol{\Omega}}^\circ$ be a critical point and $\varphi(\boldsymbol{\xi}) = 4(\omega - (\omega - \theta)\eta)\psi + \pi/4 \cdot (d/l_0)^2$ the associated objective function, where $d \in \{\boldsymbol{D}\}$ is not continuously differentiable. We assume, that apart from $\boldsymbol{\xi}_0'$ no better critical point $\boldsymbol{\xi}_1' \subseteq \boldsymbol{\eta}_1'$ exists for which applies:

$$\varphi(\boldsymbol{\xi}_1') < \varphi(\boldsymbol{\xi}_0') \tag{5.66}$$

Then also no descent direction $\mathbf{s}$ exists and it must apply:

$$\nexists \mathbf{s} \in \mathbb{R}^3 : \langle \nabla\varphi(\boldsymbol{\xi}_0'), \mathbf{s} \rangle < 0$$

Here, the scalar product leads to the following expression:

$$[\omega_0' - (\omega_0' - \theta)\eta_0']s_1 + [1 - \eta_0']\psi_0's_2 + [\theta - \omega_0']\psi_0's_3 < 0$$

We select a vector $\mathbf{s} = \begin{bmatrix} 0 & -1 & 1 \end{bmatrix}^{\mathrm{T}}$ and verify the above statement as follows.

$$-[1 - \eta_0']\psi_0' + [\theta - \omega_0']\psi_0' < 0$$
$$\eta_0' - 1 < \omega_0' - \theta$$
$$a_1 < a_2$$

By definition, $b > 2t$ applies in any case. From this follows at the same time that $\omega_0' > 2\,\theta$ and thus $a_2 > 0$ due to $\theta \in (0, 1)$. Since η_0' is always < 1, so is $a_1 < 0$. Hence, it is true that $a_2 > a_1$ and that the following statement applies

$$\exists\,\mathbf{s} \in \mathbb{R}^3 : \langle \nabla\varphi(\boldsymbol{\xi}_0'), \mathbf{s} \rangle < 0$$

which proves that at least one descent direction $\mathbf{s} \in \mathbb{R}^3$ exists. Accordingly, there exists also a better critical point $\boldsymbol{\xi}_1'$ which satisfies the statement given by ineq. (5.66). □

In the context of the proof the distinction of the sets is of relevance. Via the numerical procedure, a better point can always be approximated, provided that one is in the set. On the other hand, theoretically the case can occur that due to the discretization the best point is calculated by chance. Then there is still a descent direction, but then there is no better point which also fulfills all constraints.

The statement of the proof is also valid for the dimensioned space, i.e., in the neighborhood of a critical point $\mathbf{y}_0'$ exists a point $\mathbf{y}_1'$ which leads to a better value of the objective function. The knowledge gained by the proof is of great importance for the approximation of a solution. Since a descent direction exists, we can search for a better solution in the neighborhood of a found critical point and extend the whole procedure to a *gradient based method*. This also allows us to avoid the circumstance of having to perform an infinitely large discretization of all intervals. Rather, it can be argued that we identify first a point based on an initially coarse discretization of the entire search range and then search again for a better one in the neighborhood of this point.
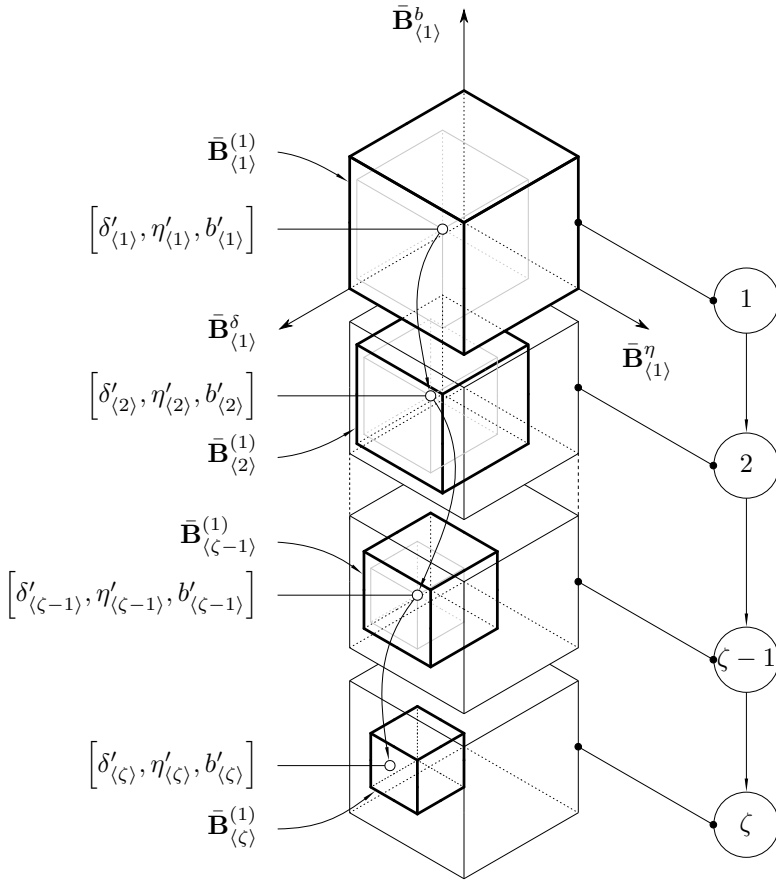
Figure 5.11: Recursive limitation of the initial search space

In the following, the procedure is developed using the GOA strategy. For the LOA the procedure is analogous only with the difference that this is done for each $d_i \in \{\boldsymbol{D}\}$ separately. In section 5.2.3 it was shown that the set $\bar{\mathbf{X}}$ with an initial discretization fineness is essential for finding a solution. After a point $\mathbf{x}'_{\langle 1 \rangle} \subseteq \mathbf{y}'_{\langle 1 \rangle}$ with $\mathbf{y}'_{\langle 1 \rangle} \in \boldsymbol{\Omega}$ has been identified by

the execution of the developed calculation steps, this then leads to the corresponding objective function value.

$$f\left(\mathbf{x}'_{\langle 1 \rangle}\right) = 4\left(b'_{\langle 1 \rangle} - \left(b'_{\langle 1 \rangle} - t\right)\eta'_{\langle 1 \rangle}\right)h'_{\langle 1 \rangle} + \frac{\pi}{4}\left(d'_{\langle 1 \rangle}\right)^2 \qquad (5.67)$$

The process of calculating a solution for a given discretization fineness is called a *recursion step* in the following. Here, the square brackets in the index indicate the current recursion step ζ. Now that we have identified the first point, we generate a new initial search space formed around the point as part of the subsequent recursion step. In particular, the values $\delta'_{\langle 1 \rangle}$, $\eta'_{\langle 1 \rangle}$ and $b'_{\langle 1 \rangle}$ are of great importance, since they are assigned to the initial search space $\bar{\mathbf{B}}^{(1)}_{\langle 1 \rangle}$. In this connection, we introduce the
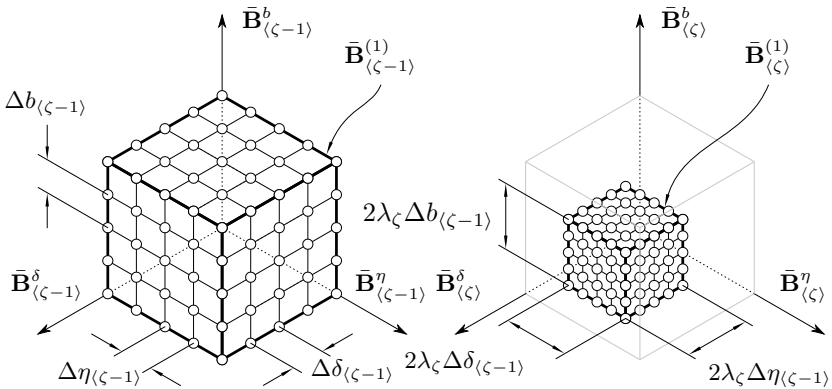
Figure 5.12: Recursive interval limitation

dimensionless factor λ_ζ called *incremental multiplier*, which is multiplied by the increment widths $\Delta\delta_{\langle\zeta-1\rangle}$, $\Delta\eta_{\langle\zeta-1\rangle}$ and $\Delta b_{\langle\zeta-1\rangle}$ of the previous calculation step in order to set up the boundaries of the current search space. Including also the traction means determined in the first step of the calculation, the algorithm is extended by the additional restriction of the possible traction means. Figure 5.13 schematically represents the containment of the given set $\{\boldsymbol{D}\}$. The position of the (local) optimum traction mechanisms $d'_{\langle 1 \rangle, i'}$ in the first calculation step is marked with i'. We then refer to this as GOA*, where in this context we introduce
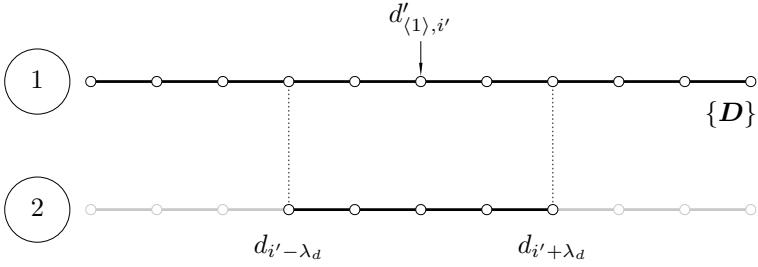
Figure 5.13: Recursive interval limitation of the traction mechanisms considered

the additional integer and dimensionless quantity $\lambda_d \in \mathbb{N}\setminus\{0\}$. This specifies the recursive restriction of the search space of the traction means.

With the help of the corresponding intervals in the recursion step $\zeta \geq 2$

$$\bar{\mathbf{B}}_{\langle\zeta\rangle}^{\delta} = \left[\delta'_{\langle\zeta-1\rangle} - \lambda_\zeta\Delta\delta_{\langle\zeta-1\rangle},\ldots,\delta'_{\langle\zeta-1\rangle} + \lambda_\zeta\Delta\delta_{\langle\zeta-1\rangle}\right], \bar{\mathbf{B}}_{\langle\zeta\rangle}^{\delta} \subseteq \bar{\mathbf{B}}_{\langle1\rangle}^{\delta}$$

$$\bar{\mathbf{B}}_{\langle\zeta\rangle}^{\eta} = \left[\eta'_{\langle\zeta-1\rangle} - \lambda_\zeta\Delta\eta_{\langle\zeta-1\rangle},\ldots,\eta'_{\langle\zeta-1\rangle} + \lambda_\zeta\Delta\eta_{\langle\zeta-1\rangle}\right], \bar{\mathbf{B}}_{\langle\zeta\rangle}^{\eta} \subseteq \bar{\mathbf{B}}_{\langle1\rangle}^{\eta}$$

$$\bar{\mathbf{B}}_{\langle\zeta\rangle}^{b} = \left[b'_{\langle\zeta-1\rangle} - \lambda_\zeta\Delta b_{\langle\zeta-1\rangle},\ldots,b'_{\langle\zeta-1\rangle} + \lambda_\zeta\Delta b_{\langle\zeta-1\rangle}\right], \bar{\mathbf{B}}_{\langle\zeta\rangle}^{b} \subseteq \bar{\mathbf{B}}_{\langle1\rangle}^{b}$$

the current initial search space can be formed as follows.

$$\bar{\mathbf{B}}_{\langle\zeta\rangle}^{(1)} = \bar{\mathbf{B}}_{\langle\zeta\rangle}^{\delta} \times \bar{\mathbf{B}}_{\langle\zeta\rangle}^{\eta} \times \bar{\mathbf{B}}_{\langle\zeta\rangle}^{b}, \quad \bar{\mathbf{B}}_{\langle\zeta\rangle}^{(1)} \subseteq \bar{\mathbf{B}}_{\langle1\rangle}^{(1)} \tag{5.68}$$

Here, we further require that the current search spaces are always a true subset of the search space in the first recursion step and thus obtain the conditions listed below.

$$\delta'_{\langle\zeta-1\rangle} - \lambda_\zeta \Delta\delta_{\langle\zeta-1\rangle} \overset{!}{\geq} \min\left\{\bar{\mathbf{B}}^\delta_{\langle 1\rangle}\right\} \tag{5.69}$$

$$\delta'_{\langle\zeta-1\rangle} + \lambda_\zeta \Delta\delta_{\langle\zeta-1\rangle} \overset{!}{\leq} \max\left\{\bar{\mathbf{B}}^\delta_{\langle 1\rangle}\right\} \tag{5.70}$$

$$\eta'_{\langle\zeta-1\rangle} - \lambda_\zeta \Delta\eta_{\langle\zeta-1\rangle} \overset{!}{\geq} \min\left\{\bar{\mathbf{B}}^\eta_{\langle 1\rangle}\right\} \tag{5.71}$$

$$\eta'_{\langle\zeta-1\rangle} + \lambda_\zeta \Delta\eta_{\langle\zeta-1\rangle} \overset{!}{\leq} \max\left\{\bar{\mathbf{B}}^\eta_{\langle 1\rangle}\right\} \tag{5.72}$$

$$b'_{\langle\zeta-1\rangle} - \lambda_\zeta \Delta\eta_{\langle\zeta-1\rangle} \overset{!}{\geq} \min\left\{\bar{\mathbf{B}}^b_{\langle 1\rangle}\right\} \tag{5.73}$$

$$b'_{\langle\zeta-1\rangle} + \lambda_\zeta \Delta\eta_{\langle\zeta-1\rangle} \overset{!}{\leq} \max\left\{\bar{\mathbf{B}}^b_{\langle 1\rangle}\right\} \tag{5.74}$$

This prevents invalid parameter combinations from being taken into account. If the limits of the current search space should exceed those of the initial search space, the following adjustments are made.

$$\delta'_{\langle\zeta-1\rangle} - \lambda_\zeta \Delta\delta_{\langle\zeta-1\rangle} < \min\left\{\bar{\mathbf{B}}^\delta_{\langle 1\rangle}\right\} \longrightarrow \min\left\{\bar{\mathbf{B}}^\delta_{\langle\zeta\rangle}\right\} \overset{!}{=} \min\left\{\bar{\mathbf{B}}^\delta_{\langle 1\rangle}\right\}$$

$$\delta'_{\langle\zeta-1\rangle} + \lambda_\zeta \Delta\delta_{\langle\zeta-1\rangle} > \max\left\{\bar{\mathbf{B}}^\delta_{\langle 1\rangle}\right\} \longrightarrow \max\left\{\bar{\mathbf{B}}^\delta_{\langle\zeta\rangle}\right\} \overset{!}{=} \max\left\{\bar{\mathbf{B}}^\delta_{\langle 1\rangle}\right\}$$

$$\eta'_{\langle\zeta-1\rangle} - \lambda_\zeta \Delta\eta_{\langle\zeta-1\rangle} < \min\left\{\bar{\mathbf{B}}^\eta_{\langle 1\rangle}\right\} \longrightarrow \min\left\{\bar{\mathbf{B}}^\eta_{\langle\zeta\rangle}\right\} \overset{!}{=} \min\left\{\bar{\mathbf{B}}^\eta_{\langle 1\rangle}\right\}$$

$$\eta'_{\langle\zeta-1\rangle} + \lambda_\zeta \Delta\eta_{\langle\zeta-1\rangle} > \max\left\{\bar{\mathbf{B}}^\eta_{\langle 1\rangle}\right\} \longrightarrow \max\left\{\bar{\mathbf{B}}^\eta_{\langle\zeta\rangle}\right\} \overset{!}{=} \max\left\{\bar{\mathbf{B}}^\eta_{\langle 1\rangle}\right\}$$

$$b'_{\langle\zeta-1\rangle} + \lambda_\zeta \Delta b_{\langle\zeta-1\rangle} > \max\left\{\bar{\mathbf{B}}^b_{\langle 1\rangle}\right\} \longrightarrow \max\left\{\bar{\mathbf{B}}^b_{\langle\zeta\rangle}\right\} \overset{!}{=} \max\left\{\bar{\mathbf{B}}^b_{\langle 1\rangle}\right\}$$

$$b'_{\langle\zeta-1\rangle} + \lambda_\zeta \Delta\eta_{\langle\zeta-1\rangle} > \max\left\{\bar{\mathbf{B}}^b_{\langle 1\rangle}\right\} \longrightarrow \max\left\{\bar{\mathbf{B}}^b_{\langle\zeta\rangle}\right\} \overset{!}{=} \max\left\{\bar{\mathbf{B}}^b_{\langle 1\rangle}\right\}$$

Furthermore, each interval is described by the respective number of elements it contains. In this context, we keep the discretization fineness which leads to the same cardinalities in each interval with respect to

the recursion step. The greater the values for $\bar{n}^\delta$, $\bar{n}^\eta$ and $\bar{n}^b$, the more finely the search space is discretized.

$$\left|\bar{\mathbf{B}}^\delta_{\langle\zeta\rangle}\right| = \left|\bar{\mathbf{B}}^\delta_{\langle1\rangle}\right| = \bar{n}^\delta \tag{5.75}$$

$$\left|\bar{\mathbf{B}}^\eta_{\langle\zeta\rangle}\right| = \left|\bar{\mathbf{B}}^\eta_{\langle1\rangle}\right| = \bar{n}^\eta \tag{5.76}$$

$$\left|\bar{\mathbf{B}}^b_{\langle\zeta\rangle}\right| = \left|\bar{\mathbf{B}}^b_{\langle1\rangle}\right| = \bar{n}^b \tag{5.77}$$

The same applies for the obtained interval of the width ratio.

$$\left|\bar{\mathbf{B}}^\beta_{jkli}(b_l, d_{jkli})_{\langle\zeta\rangle}\right| = \left|\bar{\mathbf{B}}^\beta_{jkli}(b_l, d_{jkli})_{\langle1\rangle}\right| = \bar{n}^\beta \tag{5.78}$$

while the cardinality of the set containing the applicable traction mechanisms depends on the current width within the framework of the GOA strategy.

Finally, the entire procedure is then repeated recursively until the change of the found minima becomes sufficiently small and reaches the termination criterion (similar to the *Gradient method*), defined by eq. (5.79) with $0 < \bar{\varepsilon} \ll 1$.

$$\left|\frac{f\left(\mathbf{x}'_{\langle\zeta\rangle}\right)}{f\left(\mathbf{x}'_{\langle\zeta-1\rangle}\right)} - 1\right| < \bar{\varepsilon} \wedge f\left(\mathbf{x}'_{\langle\zeta\rangle}\right) - f\left(\mathbf{x}'_{\langle\zeta-1\rangle}\right) > 0 \tag{5.79}$$

Here, the meaning of *approximation* becomes clear once again. Although we were able to show the general solvability of the optimization problem in section 5.1.2, we cannot solve the global problem exactly due to the discretization, but rather approximate the global solution until the termination criterion defined is reached. Nevertheless, we are able to determine the optimum for a fixed point $(\bar{\mathbf{x}}^*_{i...m})_{\langle\zeta\rangle}$ in each recursion step with respect to the determination criterion determined by the performed bisection method.

5.3   Algorithm Implementation and Settings

A total of three solution approaches are available, whereby the GOA*
is to be seen as a special case of the GOA. A gradient-based method
forms the basis for the approximation of a solution. In this context, the
introduced process parameters $\bar{n}^\delta$, $\bar{n}^\eta$ and $\bar{n}^b$ as well as the incremental
multiplier λ_ζ and λ_d (in case of GOA*) occur additionally. All of them
are freely selectable in each case. In the following section it is now to
be examined which quality the individual parameter settings have and
which approximate the solution best.

5.3.1   Design of Experiments

In addition to the geometric quantities mentioned, which are to be opti-
mized, a large number of other parameters have occurred in the course
so far, which were assumed to be constants, but which can also be
varied. This results in a large number of possible variations, whereby
the effort of investigating each individual combination would not be
justifiable. Here, the *Design of Experiments* (DoE) provides methods
to obtain significant results from comparatively few experiments to be
performed within the framework of a structured approach.

In the procedures for generating a suitable test field for computer ex-
periments, it is assumed that hardly any information is available in
advance. For this reason, the targeted test field is constructed in such
a way that as much information as possible can be obtained in each re-
gion of the factor space. This results in the construction of a uniformly
distributed test field that aims at minimizing the variance of the global
mean of the variables under consideration. In this context, the literature
offers different methods for constructing such a test field. We select the
Latin Hypercube method since it provides a significantly lower variance
of the global average compared to other methods, such as using a ran-
dom *Monte Carlo* field with the same number of test points [50, p. 205–
206]. In the so-called Latin Hypercube Design (LHD), an $n_r \times n_f$ matrix
$\mathbf{L}^{n_r \times n_f}$ is formed whose columns consist of a random permutation of the
numbers $\{1, 2, 3, \ldots n_r\}$. In the application of *Latin Hypercube Sampling*
(LHS), a random number from the range $[0, 1)$ is subtracted from each

Table 5.3: Investigated ranges of continuously distributed variables

Quantity	Lower limit	Upper limit	Unit
m_0	4000	16000	[kg]
l_0	2000	8000	[mm]
γ_{M1}	1.10	2.00	[$-$]
γ_{M2}	1.10	2.00	[$-$]

value of the LHD and then divided by the value n_r. Accordingly, the test field is normalized to a unit space. Commercial available software solutions, such as the MATLAB$^{©}$ code, provide predefined functions that can be used to generate an LHS. For this purpose, the quantities to be varied must first be determined, whereby we limit the number to a total of five quantities. These include m_0, l_0, γ_{M1}, γ_{M2} as well as the yield strength R_e, since these can be varied over a wide range compared to the other variables. All parameters, with the exception of R_e, can be considered to be continuously distributed in their respective ranges. The variable R_e, on the other hand, is varied discretely and is oriented to the steels used in steel construction. We keep the remaining parameters constant in the analysis. In general, the authors D. R. JONES et al. [51] recommend that the required number of test points n_T to be used can be approximately calculated based on the number of dimensions n_D as follows.

$$n_T \approx 10 \cdot n_D \tag{5.80}$$

According to J. LOEPPKY et al. [52] this approach is justifiable for $n_D \leq 5$. The LHS then leads to the resulting test points (see table A.2 and A.3). In the context of the investigation of the algorithms, the discretization is performed in such a way that the search spaces are built up as a Cartesian grid, i.e. the number of elements is equal $(\bar{n}^\delta = \bar{n}^\eta = \bar{n}^b = \bar{n}^\beta = \bar{n})$ and have in each case the same distance to each other. Here, the integer number $\bar{n}$ is varied between 6 and 10, while the incremental factor λ_ζ is varied in 0.25 steps from 0.50 to 1.50. This results in a total of 25 possible combinations $\mathbf{p} = [\bar{n}, \lambda_\zeta]$ of

parameter settings (see appendix table A.5). Indeed, also larger values are conceivable, but it must be noted that this also increases the required computing time considerably. Therefore, a compromise between the achievable approximation quality and the calculation time has to be made. For each combination, the solution is then approximated and the number of required iterations n_I is determined. The individual solutions are further compared with each other and the deviation of the other results from the minimum solution found, which is assumed as the respective benchmark, is calculated. The number of iterations in turn provides information about the time required for the approximation of the parameter combination. In case of the GOA*, λ_d is set to 2 so as not to overly constrain the surrounding search space.

5.3.2 Parameter Settings

In the following section, appropriate parameter settings are identified based on the previously constructed test points. In particular, the approximation quality and the required number of iterations are in the foreground with respect to the single algorithm strategies and the parameter combinations.

Approximation Quality

First, it is to be determined which parameter combination provides the best results on average for an algorithm strategy. For this purpose, all parameter combinations are applied for each test point T_i in order to calculate a minimum. We summarize the minima found for a test point in the set $\mathbf{f}'_i$, while

$$f'_i(\mathbf{p}) \in \mathbf{f}'_i \tag{5.81}$$

applies. Of great interest is now, which parameter combination provides the best result, which just corresponds to the smallest element of $\mathbf{f}'_i$. If we now put the remaining results in relation to the smallest element,

we can determine the relative deviations $\Delta f_i'(\mathbf{p})$. This is then to be calculated as follows for a certain parameter combination.

$$\Delta f_i'(\mathbf{p}) = \frac{f_i'(\mathbf{p})}{\min\{\mathbf{f}_i'\}} - 1 \tag{5.82}$$

This procedure is then performed for all n test points, from which we can determine the expected value $\bar{\mu}$ of the relative deviation $\Delta f'(\mathbf{p})$ as a function of the applied parameter combination $\mathbf{p}$.

$$\bar{\mu}(\Delta f'(\mathbf{p})) = \frac{1}{n} \sum_{i=1}^{n} \Delta f_i'(\mathbf{p}) \tag{5.83}$$

By comparing all the expected values, it is then possible to identify the parameter combination that, on average, provides the best solution among all the combinations considered. Additionally, the corresponding standard deviation of the sample with respect to the investigated relative deviation determined by

$$\bar{\sigma}(\Delta f'(\mathbf{p})) = \sqrt{\frac{1}{n-1} \sum_{i=1}^{n} (\Delta f_i'(\mathbf{p}) - \bar{\mu}(\Delta f'(\mathbf{p})))^2} \tag{5.84}$$

gives information about the variation of $\Delta f_i'(\mathbf{p})$ [53, p. 132]. The course of expected values of the relative deviations over the individual parameter combinations with respect to the single algorithms is illustrated in figure 5.14. Here, GOA and GOA* provide identical results. It can be seen that the relative deviation from the locally found minimum generally decreases as the number of elements increases. This is obvious, since we have already demonstrated in the previous section that the discrete space becomes more and more similar to the continuum if the number of elements is increased accordingly. We can also notice that for all investigated element numbers the best solution is found on average for the largest λ_ζ. Here also the standard deviation is the smallest.

For the applied sample size n, CHEBYSHEV's inequality, determined by

$$\Pr(|\Delta f'(\mathbf{p}) - \bar{\mu}(\Delta f'(\mathbf{p}))| \geq \varepsilon_x) \leq \frac{\bar{\sigma}^2(\Delta f'(\mathbf{p}))}{n\,\varepsilon_x^2} \tag{5.85}$$

165
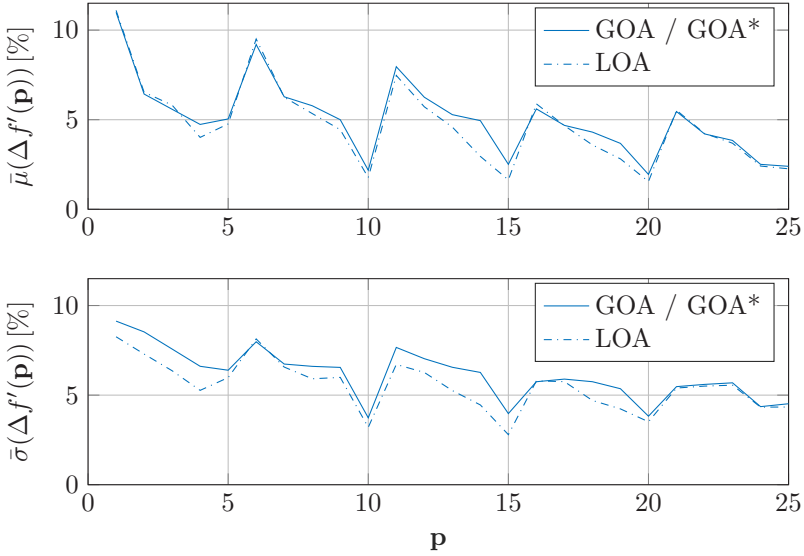
Figure 5.14: Expected values and according standard deviations in terms of relative deviations

can now be used to estimate the probability that the random variable under consideration deviates from its expected value by more than a certain threshold value ε_x [54, p. 201–202]. Based on the obtained results, the threshold value can now be determined for each parameter combination. These indicate that the calculated expected values lie within the respective ranges with a certain probability. This range is then defined as follows

$$\mathrm{Pr} = [\bar{\mu}(\Delta f'(\mathbf{p}) - \varepsilon_x, \bar{\mu}(\Delta f'(\mathbf{p})) + \varepsilon_x] \tag{5.86}$$

and depends significantly on the required probability. For this we select 95% and thus obtain the corresponding ranges for the parameter combinations considered. It should be noted that negative lower bounds are set to zero, since zero already represents the best result and therefore no negative deviations can exist. The results are summarized in tables A.6, A.7 and A.8.

Calculation Time

The calculation time is estimated by the number of iterations required on average. Here, we proceed in the same way as in the previous section. Their development is shown in figure 5.15 and it can be seen that the expected values increase approximately linearly over the parameter combinations considered. On the other hand, it can still be observed
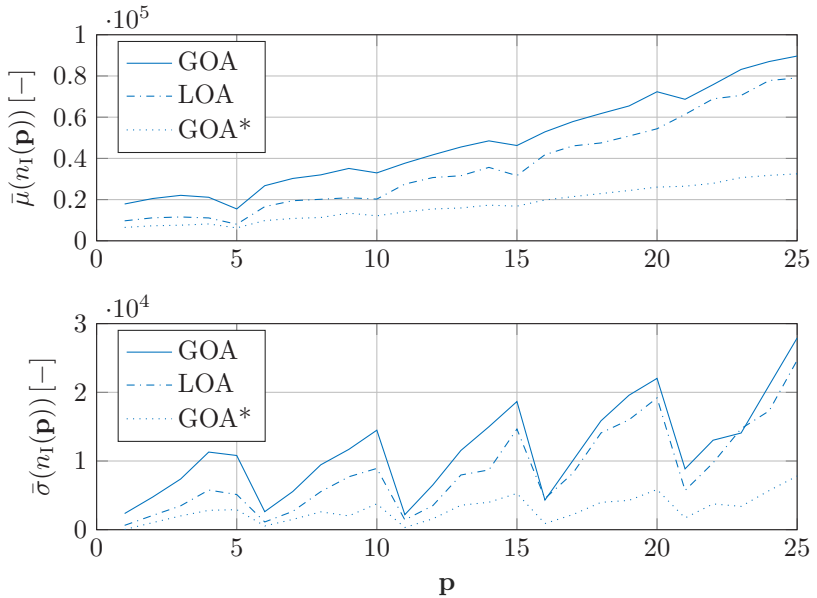
Figure 5.15: Expected values and according standard deviations in terms of necessary iterations

that the standard deviation for small values of λ_ζ are also low. This increases significantly for larger λ_ζ and thus also the possible variation. Overall, both the expected values and the standard deviations of the GOA* are the lowest, so this strategy is the fastest way to calculate a solution. On this basis, the most appropriate parameter combinations can be identified for each algorithm strategy. The essential criterion is primarily the expected value of the relative deviation. The lower this value, the more likely we can assume that this parameter combination

Table 5.4: Suitable parameter combinations with respect to the selected strategy

Strategy	$\bar{n}\,[-]$	$\lambda_\zeta\,[-]$	$\bar{\mu}(n_\mathrm{I})\,[-]$	$\bar{\mu}(\Delta f')\,[\%]$	$\mathrm{Pr}_{0.95}(\Delta f')\,[\%]$
LOA	9	1.50	54369	1.5492	$[0.00, 3.51]$
GOA	9	1.50	72343	1.9456	$[0.00, 4.36]$
GOA*	9	1.50	25950	1.9456	$[0.00, 4.36]$

provides the best result compared to the other combinations. Nevertheless, it should be noted that a trade-off is required in terms of the computational time involved. The most suitable parameter combinations found in each case are summarized in 5.4. Subsequently, it is to
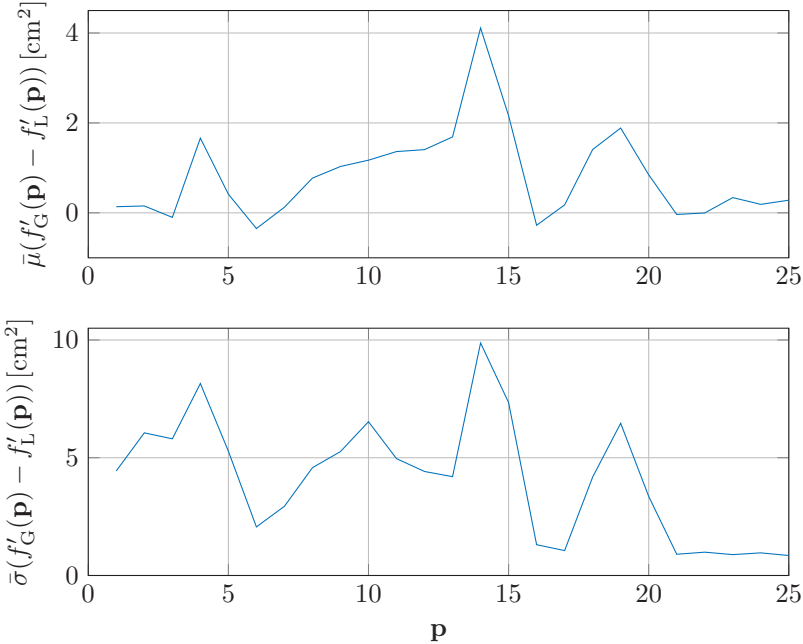
Figure 5.16: Comparison of algorithm strategies

be determined which algorithm strategy is capable of delivering the best results depending on the parameter combinations considered. For this purpose, the differences of the calculated minima are formed for each test point and each parameter combination. The determinations of the expected value of the differences and the associated standard deviation are then carried out in analogy to the previous procedure. Figure 5.16 shows the results with $f'_G(\mathbf{p})$ representing the results obtained by the GOA algorithm and $f'_L(\mathbf{p})$ the results with respect to the LOA algorithm. Here, a negative expected value means that for the considered parameter combination on average the GOA algorithm provides a better result, for a positive expected value accordingly the LOA algorithm. It can be seen that with an increasing number of elements, the results become more and more similar. In this context, the value of the standard deviation also decreases. Until then, it can be observed that on average the LOA delivers better results.

5.3.3 Summary of Parameter Settings

At the end of this section, the main findings will be summarized once again in a condensed form. These concern in particular the implementation of the algorithms and the expected results.

- All in all, the GOA requires the most computation time, while the GOA* is capable of computing a solution the fastest.

- Compared to the other strategies, the LOA delivers the best results. However, the quality of the results equalizes with increasing discretization fineness, i.e. a higher number of elements $\bar{n}$ and a higher incremental multiplier λ_ζ.

- To calculate a configuration it is recommended to use the GOA* with $\bar{n} = 9$ and $\lambda_\zeta = 1.50$ as parameter settings. With an average number of 25950 iterations, it provides the fastest solution. By examining the parameter settings, it was shown that $\mathbf{p}_{20}$ has the lowest relative deviation on average. Using CHEBYSHEV's inequality, it is shown that with a probability of 95%, the relative deviation lies in a range between 0.00% and 4.36%.

6   Algorithm Results and Validation

So far, the basic principles for the design and weight optimization of a segmented, prestressed crane bridge girder have been worked out theoretically. Accordingly, at this point we have calculation rules at our disposal with which we can calculate the geometric quantities and the necessary prestressing force of the associated girder on the basis of given values such as the nominal load or the span width. Particularly against the background of neglecting geometrical peculiarities or idealizations with regard to the loads, we are forced to recognize that up to now, however, we have not been able to make any statements with regard to the practical suitability of the constructions. Although configurations are calculated that comply with the defined boundary conditions, these are based on the simplified models developed, which are not capable of describing reality in its entirety due to the high degree of complexity. Instead, it is now necessary to verify whether the estimates and neglect assumptions made are justified. This then provides the answer to the question of the extent to which the calculation models and the optimization procedure can be used to design and construct a segmented, prestressed crane girder.

6.1   FE Analyses

The current state of the literature shows that FE analyses are widely used as a common tool for validation in the field of crane design. This

is especially due to the fact that cranes usually have large dimensions and therefore real experiments can only be performed for selected applications.

The aim of this section is to demonstrate the suitability of the developed computation and optimization method using selected examples. The single girder bridge cranes studied by M. SAVKOVIC et al. [10], which were calculated using biologically inspired optimization algorithms, serve as reference structures. Here, figure 6.1 illustrates the considered cross-section with the specific parameters to be optimized. They are summarized in a vector
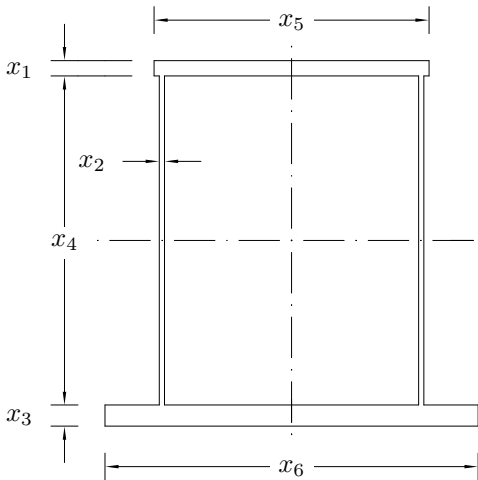
Figure 6.1: Considered design by M. SAVKOVIC et al. [10]

$$\mathbf{x} = \begin{bmatrix} x_1 & x_2 & x_3 & x_4 & x_5 & x_6 \end{bmatrix}^{\mathrm{T}} \tag{6.1}$$

and lead to the corresponding objective function.

$$f(\mathbf{x}) = 2x_4x_2 + x_5x_1 + x_6x_3 \tag{6.2}$$

In contrast to the developed optimization problem of this thesis, the consideration according to [10] leads to a six-dimensional optimization

Table 6.1: Input parameters, based on [10]

Parameters		Config. 1	Config. 2	Config. 3
m_0	[kg]	5000.00	8000.00	10000.00
l_0	[mm]	7600.00	7550.00	8400.00
m_t	[kg]	610.00	600.00	880.00
$2l_\mathrm{w}$	[mm]	708.00	600.00	600.00
R_e	[N/mm^2]	335	335	335
E	[N/mm^2]	$2.11 \cdot 10^5$	$2.11 \cdot 10^5$	$2.11 \cdot 10^5$
γ_{M1}	[$-$]	1.50	1.50	1.50
γ_{M2}	[$-$]	1.25	1.25	1.25

problem in which all quantities are continuously distributed. Furthermore, additional quantities such as the maximum permissible deflection ratio δ do not influence the objective function, since this is a purely passive structure whose deflection can only be affected by design. In total, twenty constraint functions are taken into account by the authors.

Although there are differences in the cross-sectional profile considered and in the constraints (for example, the common dynamic limits in crane construction are taken into account), the configurations are nevertheless appropriate for making an initial comparison with regard to weight optimization and performance of the developed algorithms.

6.1.1 Considered Reference Configurations

Based on [10], real crane systems are used as reference configurations, whose resulting cross-sectional areas are specified. Furthermore, information is available regarding the traveling trolley, i.e. the self-weight as well as the wheelbase are known. Additional parameters, which are assumed to be constant, can be taken from table 6.1. It should be noted that the value γ_{M2} is only used for the segmented prestressed bridge girder, since it primarily refers to the bolted connection. The remaining parameters necessary for the calculation are considered as constants

and are to be taken from table A.4. As recommended in section 5.3.3,

Table 6.2: GOA* Algorithm results according to the considered configurations

Quantity		Config. 1	Config. 2	Config. 3
Segmentation type	$[-]$	4	2	4
n_{s}	$[-]$	17	16	19
l_{s}^*	[mm]	850.00	1200.00	850.00
l_{r}^*	[mm]	400.00	750.00	400.00
ζ'	$[-]$	11	11	7
n_{I}	$[-]$	28998	28998	5868
λ_ζ'	$[-]$	1.50	1.50	1.25
$\bar{n}'$	$[-]$	9	9	6
h'	[mm]	280.10	353.10	534.70
h_0'	[mm]	272.10	344.20	528.80
b'	[mm]	186.50	194.70	200.90
b_0'	[mm]	139.00	147.20	153.40
ϵ'	[mm]	202.70	269.50	440.20
d'	[mm]	60.00	70.00	80.00
N_0'	[kN]	413.90	486.00	583.90
η'	$[-]$	0.9714	0.9748	0.9890
β'	$[-]$	0.7453	0.7560	0.7636
ϵ'/h'	$[-]$	0.7237	0.7632	0.8233
δ'	[%]	0.2329	0.1704	0.0650

the GOA* algorithm is used for calculation. The entire spectrum of possible parameter settings is examined in order to determine the best solution. Here, the results are summarized in table 6.2 and show that, as already predicted, the parameter combination $\mathbf{p}_{20}$ produces the best results with the exception of configuration 3. Here, the best solution is found with $\mathbf{p}_4$. Furthermore, figure 6.2 shows the convergence behavior of the algorithm with respect to the individual configurations.

Table 6.3: Comparison of computational results

Results		Config. 1	Config. 2	Config. 3
Real solution	[cm^2]	177.2000	248.8000	262.4000
Best result FA	[cm^2]	138.3252	160.6526	186.1351
Worst result FA	[cm^2]	216.2055	241.4631	286.6161
Mean FA	[cm^2]	149.6354	172.0198	198.9969
Standard deviation FA	[cm^2]	14.8068	15.1253	15.5601
Standard deviation FA	[%]	9.8953	8.7928	7.8193
Best result BA	[cm^2]	142.3196	169.9500	194.6763
Worst result BA	[cm^2]	345.0764	513.6837	481.4968
Mean BA	[cm^2]	142.7343	170.4467	195.2616
Standard deviation BA	[cm^2]	7.2298	11.2392	10.7403
Standard deviation BA	[%]	5.0652	6.5940	5.5005
Best result CSA	[cm^2]	140.3409	162.5000	190.6222
Worst result CSA	[cm^2]	194.8671	226.5248	241.0208
Mean CSA	[cm^2]	152.3099	174.4944	203.2311
Standard deviation CSA	[cm^2]	13.7967	6.9632	13.5137
Standard deviation CSA	[%]	9.0583	3.9905	6.6494
Best result GOA*	[cm^2]	142.3473	176.6377	203.4379
Worst result GOA*	[cm^2]	151.1405	191.4117	228.3735
Mean GOA*	[cm^2]	145.8671	181.1306	215.6813
Standard deviation GOA*	[cm^2]	2.3228	4.3189	6.0699
Standard deviation GOA*	[%]	1.5924	2.3844	2.8143
Max. weight savings FA	[%]	21.94	35.43	29.06
Max. weight savings BA	[%]	19.68	31.69	25.81
Max. weight savings CSA	[%]	20.80	34.69	27.35
Max. weight savings GOA*	[%]	19.65	29.00	22.47

Table 6.4: Share of the tensile member on the total cross-sectional area

Quantity		Config. 1	Config. 2	Config. 3
f'_s	[cm^2]	128.32	157.313	178.71
f'_d	[cm^2]	28.27	38.48	50.27
f'_d/f'	[%]	19.84	21.80	24.66

Due to the implemented gradient-based method, the striving towards a limit value can be clearly seen, which just represents the approximated solution. Subsequently, the solutions found will be compared with the real and the optimized solutions from [10]. First of all, it can be stated that a weight reduction can be achieved by the developed concept of the segmented, prestressed girder and the associated optimization algorithm GOA*. For configuration 2, the largest overall weight saving can be achieved with 29.00 % compared to the real solution. In contrast, the algorithms for optimizing the conventional cross-section profile according to figure 6.1 achieve a weight saving of up to 35.43 %. The calculations for configuration 1 show that all percentage weight savings differ only slightly and lie in a range between 19.65 % and 21.94 %. Here, the FA delivers the best result. For configuration 3, although the GOA* also achieves a weight reduction of 22.47 %, this is below the maximum weight savings achieved by the algorithms used in [10]. Against this background, the calculated cross-sectional areas are examined in detail in order to identify further lightweight design potential of the segmented, prestressed beam. For this purpose, the value of the objective function is divided into two parts: firstly, the part relating to the segment cross-section f'_s and secondly, the part f'_d comprising the tensile member. The results can be taken from table 6.4. We can clearly see that the pure segment profile is smaller in cross-sectional area than the profiles calculated by M. SAVKOVIC et al. in table 6.3. The tensile member, on the other hand, occupies up to 24.66 % of the total cross-section and is accordingly responsible for the additional weight increase. This suggests that the lightweight potential of the structure can be further exploited by using alternative tensile means. For example, steel cables offer a greater strength-to-weight-ratio as shown in [4] and
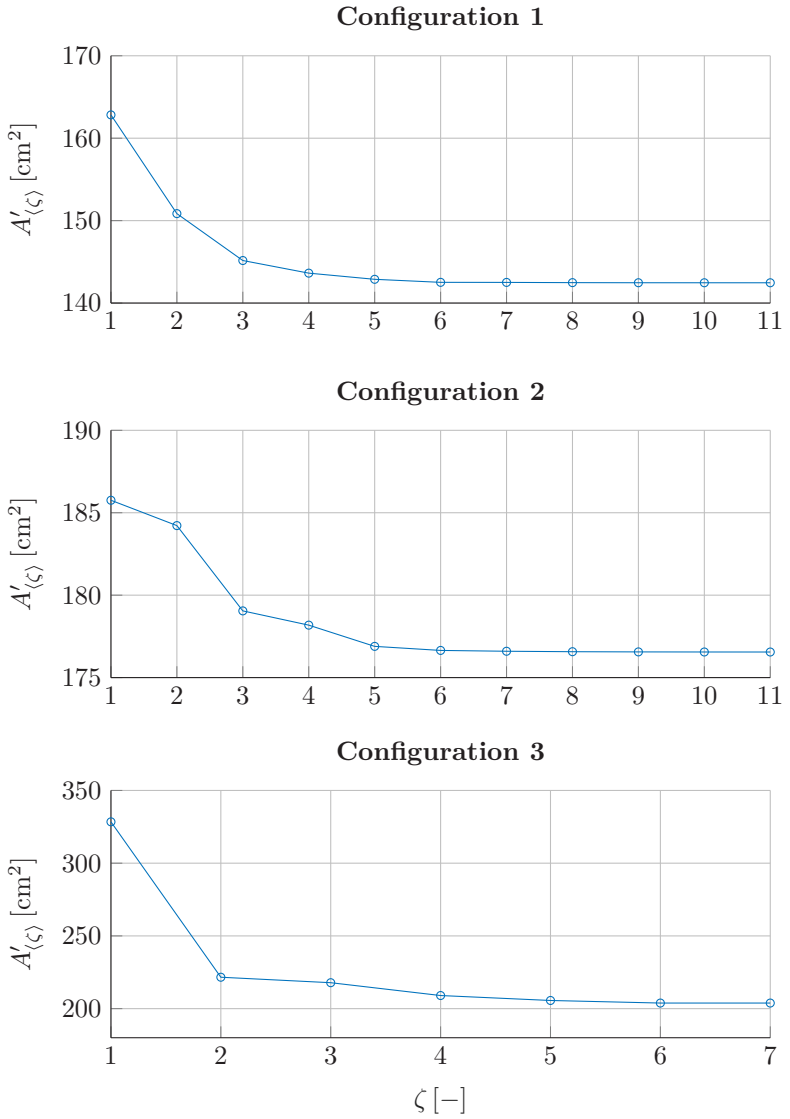
Figure 6.2: Calculated minimum cross-sectional areas depending on the recursion step

are accordingly conceivable as an alternative. However, the design of the force application requires additional design effort, as steel cables are significantly more complex with regard to the attachment possibilities.

6.1.2 Simulation Setup

Through the calculations of the objective function values, the geometric parameters of the best solutions found are also known, on the basis of which the profiles can be designed. These then are to be taken for the subsequent validation with the ABAQUS© code.

Material Properties

As stated in the first chapter, the focus of the work is on the investigation of the elastostatic behavior of the developed structure. Within the framework of the FE analyses, the material properties of the components must first be defined. In addition to the parameters given in table 6.1, the common characteristic values of steel are used to define POISSON's ratio and the density (see table A.4). Furthermore, a coefficient of friction of $\mu_f = 0.14$ is assumed for all contact pairs except for the tensile member. The contacts within the tensile member, on the other hand, are connected as a *tie constraint* in order to simulate the engagement of the threads. For additional information on the meshing strategies, see tables A.9, A.10 and A.11.

Load Cases and Boundary Conditions

To imitate the real situation, a simple support of the crane bridge is assumed. Here, *analytical rigids*[1] serve as support points. As in reality, the crane bridge is first prestressed by tightening the tensile member to press the contact surfaces together and establish functionality. The pretensioning force is simulated with the aid of the load type *bolt load* in

---

[1] Extruded ideal rigid surfaces based on parameterized curves.

order to simulate the prestressing as accurately as possible. The entire load, consisting of the traveling trolley's self-weight and the nominal load, is then applied. In this context, the wheels of the trolley are also represented as analytical rigids. Three positions of the trolley in particular are examined:

Case 1   The trolley rests exactly in the middle of the crane bridge. Here, the largest deflection of the girder occurs.

Case 2   The focus here is on examining the critical joint. If this is exactly at $x_1 = l_0$, the load is applied so that the front wheel of the trolley is at $x_1 = l_0$ as well. If the joint is at $x_1 = l_0 - l_s/2$, the load is applied via the rear wheel of the trolley. These arrangements of the load applications are based on the moment curves from figure 4.4 in section 4.3.

Case 3   In the last case to be investigated, the traveling trolley is as close as possible to one of the support points. A fixed value of 500.00 mm is assumed as the start dimension.

Simulation Steps

The entire simulation is divided into a total of three steps, which are chronologically structured. The steps are executed taking into account geometric nonlinearities with an initial increment width of 0.10 and a damping factor of 0.0002 (default value) for automatic stabilization of the calculation. First, the prestressing force is applied, followed by the application of the nominal load. In the last step, the structure is loaded by the self-weight of the components involved.

6.1.3 Simulation Results

In the following section, the results of the FE analyses are presented and discussed. In particular, the focus is on the investigation of the global

179

stresses and the deformations that occur. Another aspect includes the evaluation of the elastic stability of the structures. Here, figure 6.3

Configuration 1
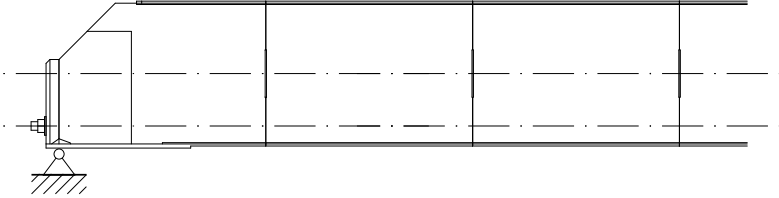
Configuration 2
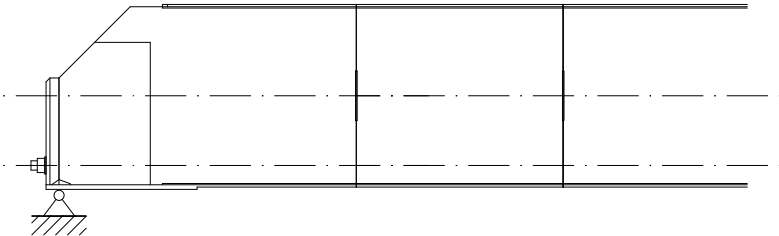
Figure 6.3: Calculated configurations 1 and 2

shows a comparison of the first two calculated configurations.

Reference Configuration 1

The results of the simulation for the first configuration show that no global yielding of the material used occurs within the structure. This is true for all load cases considered. The predicted stresses of the GOA* algorithm are higher for the majority of the examined points and can therefore be classified as comparatively conservative, see table 6.5. Point 7, which is located directly in the transition zone between the flange and the web plate, is a special feature in this context. At this point, the weld seam was geometrically considered and modeled as a chamfer. In the context of the FE calculation, this sharp edge near the load application is predestined for the occurrence of a *numerical singularity*. This

Table 6.5: Configuration 1 - FEA results

Quantity		Case 1	Case 2	Case 3	GOA*
$\sigma_{\mathrm{M}}(\boldsymbol{p}_1)$	[N/mm^2]	33.5996	33.6539	56.5147	71.3500
$\sigma_{\mathrm{M}}(\boldsymbol{p}_2)$	[N/mm^2]	38.3868	38.4459	64.3911	71.6063
$\sigma_{\mathrm{M}}(\boldsymbol{p}_3)$	[N/mm^2]	17.5207	7.2601	34.3911	73.2939
$\sigma_{\mathrm{M}}(\boldsymbol{p}_4)$	[N/mm^2]	47.6560	18.8571	34.5662	69.0044
$\sigma_{\mathrm{M}}(\boldsymbol{p}_5)$	[N/mm^2]	57.2901	56.8118	31.6458	65.4196
$\sigma_{\mathrm{M}}(\boldsymbol{p}_6)$	[N/mm^2]	38.9530	39.0181	69.1993	73.6556
$\sigma_{\mathrm{M}}(\boldsymbol{p}_7)$	[N/mm^2]	117.6485	180.2482	34.5345	62.1294
$\sigma_{11}(\boldsymbol{p}_8)$	[N/mm^2]	-5.3714	-2.6247	-33.2297	-2.3132
$w(t_1, l_0)$	[mm]	1.6371	1.6263	-2.1130	17.7019
$w_{\mathrm{t}}(l_0)$	[mm]	0.2413	0.2351	0.2350	14.8515

is characterized by the fact that the state variables to be determined and their derivatives are no longer limited and therefore the stresses in this area reach very large values [55, p. 276]. The deformations are also smaller than the deflections calculated by GOA* algorithm. The reason for this is in particular the neglect of the welded-in bulkhead plates and the connecting elements in the course of the establishment of the underlying mechanical substitute model. These components also contribute an additional share to the stiffness of the structure. Here, a further weight saving can be achieved by using an alternative, analytical model to predict the deflections which is based on taking into account the influence of the bulkhead plates and connecting elements on the lowering of the girder. The same applies to the deformation of the tensile member. It turns out that here the calculated deformations are higher than the results of the simulation as well. One approach is to model the deflection taking into account other support conditions. A simple support was assumed in advance; here, it must be investigated to what extent a clamped-clamped support better describes the deflection of the tensile member. However, it should be noted that, strictly speaking, both systems are then coupled with each other by the mo-

ment occurring in the support. The extent to which this effect has an influence is also the subject of the investigation.

With regard to elastic stability, it can be stated that no global or local failure due to buckling or plate buckling occurs. An indicator for this is that the calculation converges in every step and that no negative eigenvalues of the stiffness matrix appear. In this context, the occurrence of negative eigenvalues signifies the reaching of a bifurcation point, i.e., the structure leaves the primary path of the load-deformation relationship and moves into an adjacent one. The structure is then in the post-buckling state.
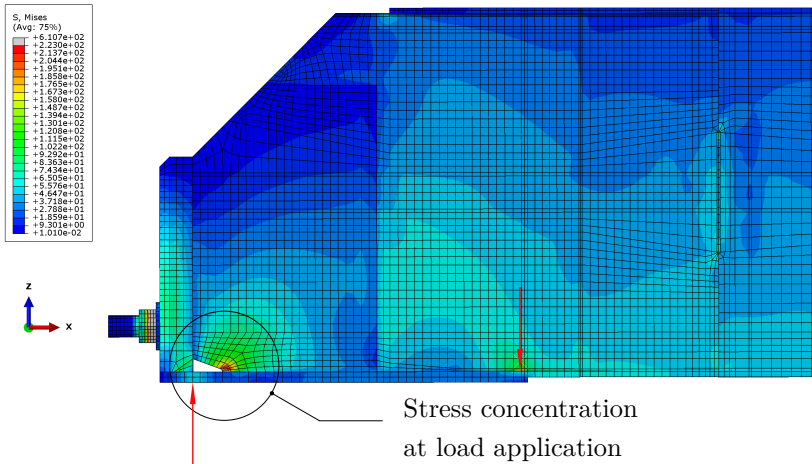
Figure 6.4: Side view of config. 1 at case 3, $f_y = 223.00\,\mathrm{N/mm}^2$

Locally, it can be observed that the pressure cone formed on the preload segment runs at an approximate angle of 60°, see figure 6.4. Accordingly, further material could be saved by adapting the chamfer of the preload segment to this angle. However, it should be stated that the stiffness of the structure in the x_3-direction must still be ensured. This concerns in particular the consideration of the approach dimension of the trolley and thus how close the trolley can be to one of the support points. Figure 6.5 shows an isometric view of the force application area. It can
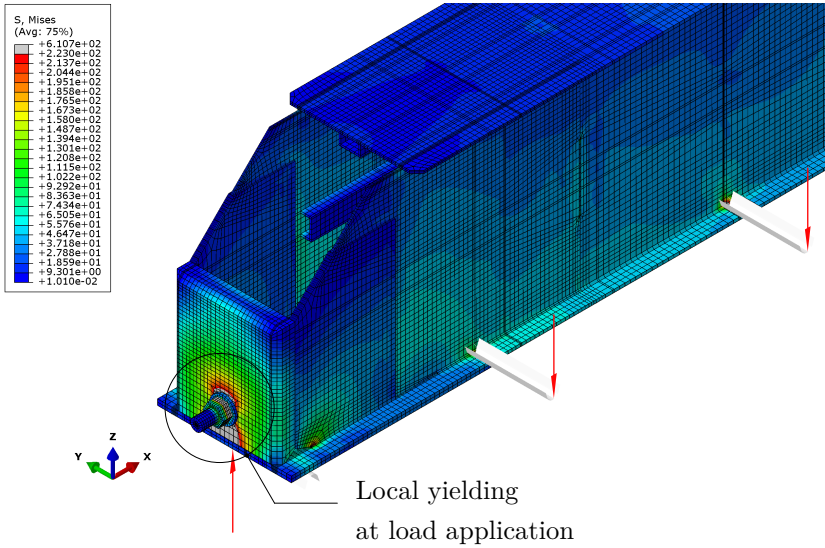
Figure 6.5: Isometric view of config. 1 at case 3, $f_y = 223.00 \, \text{N/mm}^2$

be seen that local yielding of the material starts in the area of axial load application. In practice, it can also be expected that the shim also digs into the material of the stop piece, but this effect is quite acceptable and does not damage the stop piece to such an extent that it can no longer perform its function.

Reference Configuration 2

The FE analysis for configuration 2 leads to similar results which are summarized in table 6.6. Here, too, there is no global yielding of the material, which means that it is capable of withstanding the external loads. With regard to the area of axial load application, it can also be observed that the material starts to yield locally, see figure 6.6. At the joints, an increase in mechanical stress can still be noticed on the flanks of the connecting element which is shown in figure 6.7. However, these do not lead to f_y being exceeded.

Table 6.6: Configuration 2 - FEA results

Quantity		Case 1	Case 2	Case 3	GOA*
$\sigma_{\mathrm{M}}(\boldsymbol{p}_1)$	[N/mm^2]	38.8783	39.6090	68.6581	71.2977
$\sigma_{\mathrm{M}}(\boldsymbol{p}_2)$	[N/mm^2]	46.0451	46.9403	84.1333	71.6195
$\sigma_{\mathrm{M}}(\boldsymbol{p}_3)$	[N/mm^2]	15.2575	15.9199	36.1986	72.7173
$\sigma_{\mathrm{M}}(\boldsymbol{p}_4)$	[N/mm^2]	25.5460	67.1511	36.3037	68.5660
$\sigma_{\mathrm{M}}(\boldsymbol{p}_5)$	[N/mm^2]	61.3213	61.0693	30.3648	62.6766
$\sigma_{\mathrm{M}}(\boldsymbol{p}_6)$	[N/mm^2]	53.7810	55.0570	108.1574	73.6454
$\sigma_{\mathrm{M}}(\boldsymbol{p}_7)$	[N/mm^2]	113.4754	156.5457	36.1774	61.7099
$\sigma_{11}(\boldsymbol{p}_8)$	[N/mm^2]	-9.3599	-4.9086	-36.1965	-2.3015
$w(t_1, l_0)$	[mm]	1.6843	2.0631	-2.8456	12.8628
$w_{\mathrm{t}}(l_0)$	[mm]	0.2301	0.2303	0.2302	16.7568

Stress concentration
at connection area
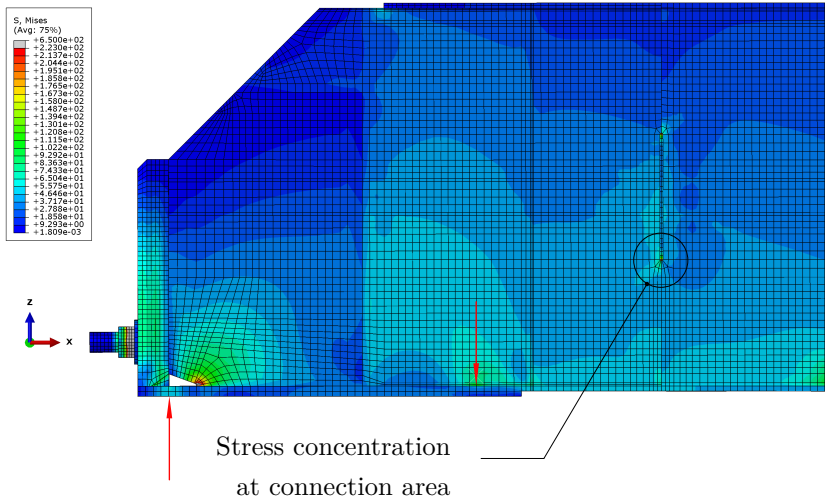
Figure 6.6: Side view of config. 2 at case 3, $f_{\mathrm{y}} = 223.00\,\mathrm{N/mm}^2$
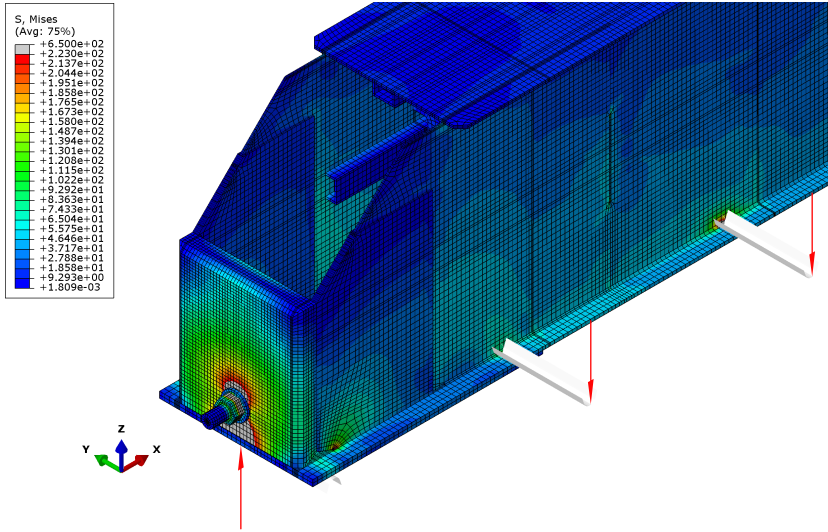
Figure 6.7: Isometric view of config. 2 at case 3, $f_y = 223.00 \, \text{N/mm}^2$

Reference Configuration 3

The simulation of configuration 3 shows that the joints of the bottom chord tend to undergo severe deformations at high prestressing forces in the load application area. Furthermore, the occurrence of negative eigenvalues of the stiffness matrix can be observed in the simulation, which is a clear indication of the post-buckling condition. A schematic representation of the deformation behavior is shown in figure 6.8. Thus, the originally envisaged connection design does not provide sufficient structural resistance for prestressing forces above 480 kN. The reason for this is the comparatively high moment in combination with the compressive stress acting in this area. Accordingly, an alternative arrangement and design of the stiffening plates are required to ensure sufficient stiffness against local deformation even at higher prestressing forces. Against this background, an alternative design is developed. It turns out that the structure must have greater stiffness in the x_3-direction. For this purpose, the bottom chord plate is provided with an additional

a) Rigid model　　　　　　　b) Deformed state
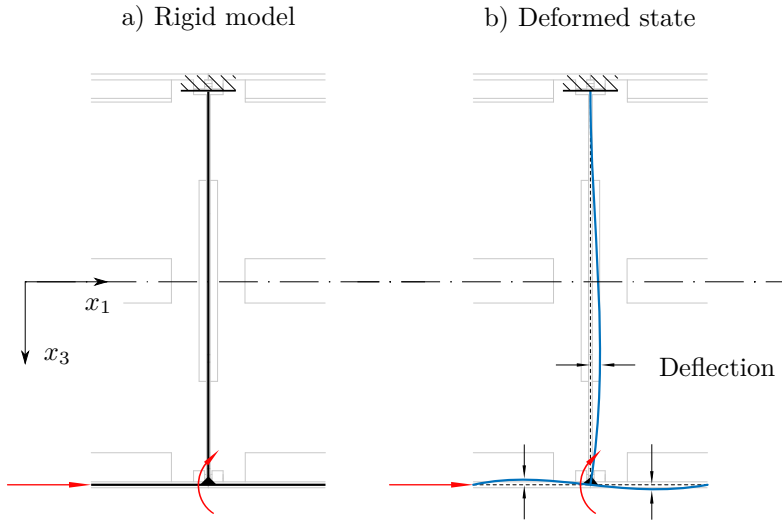
Figure 6.8: Qualitative illustration of the deformation of the connecting areas

web plate on the underside as depicted in figure 6.9 where the new features are highlighted in blue. The evaluation of the influence of the web geometry in subsection 3.3.1 has already shown that significant stiffening effects can be achieved in this way. It should also be noted that sufficient space has to be available for the traveling trolley, otherwise it will be obstructed by the strut. The originally free-standing stiffening struts are moved to the inner edges and attached to the web plates by a material bond, thus forming two inner, small box sections. This arrangement also enables us to enlarge the stiffening plates, since they do not interfere with the space requirements of the tensile member. This arrangement is also used for the preload segment, where the bottom chord plate is reinforced over the entire length and width. In addition to the stiffness issue of the segments, the connecting mechanism plays a further central role. In this context, an alternative design of the connecting element is developed as well. Figure 6.8 illustrates that the moment is transmitted to the connecting element at the joint, which then also tends to deform about the x_2- axis if the stiffness is insufficient. To
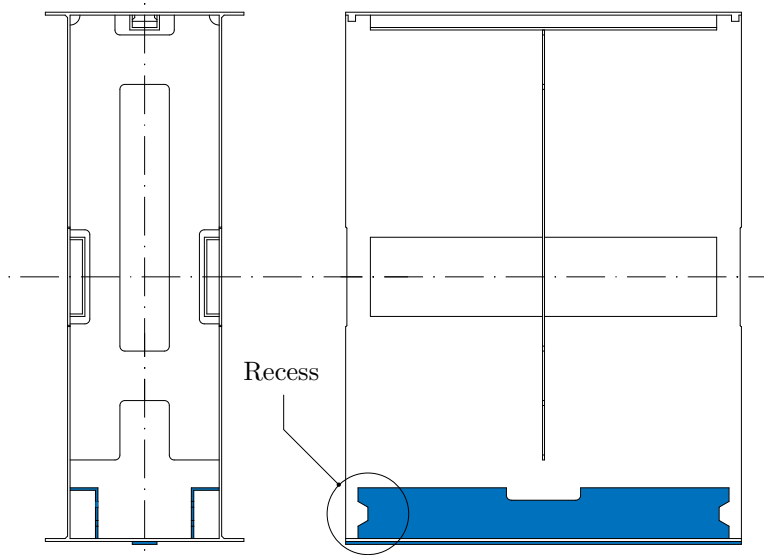
Figure 6.9: Structural improved main segment

counteract this, reinforcement in the x_1-direction is required, i.e. it is reasonable to also equip the connecting element with stiffening plates, which at the same time provide alignment pins for the insert in the segments. These pins are tapered in order to generate a centering effect for easier assembly. The corresponding recesses are located in the new designed stiffening plates of the main segment. This technique simultaneously creates a form-fit connection and, through contact, hinders the tendency of the bottom chord plate to deflect under the axial load. Due to the high prestressing forces, it is necessary to also structurally reinforce the stop piece. Its length is doubled by assuming $\lambda = 1/8$, which allows better control of the local stresses in the load application area. In addition, the stop piece is recessed to further reduce its weight, see figure 6.12.

The subsequent simulation of the configuration shows that the issues described at the beginning with regard to the local stability of the structure can be solved by the alternative design. No negative eigenvalues
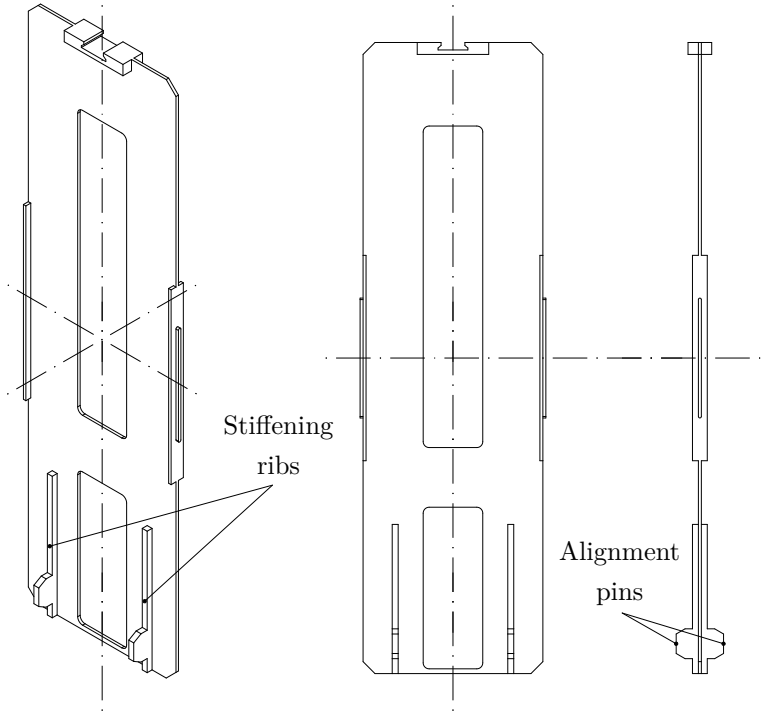
Figure 6.10: Structural improved connecting element

of the stiffness matrix appear in the calculation, consequently the beam does not reach the state of post-buckling in the course of prestressing. Furthermore, the reinforcement of the area of axial load application has a positive effect on the local stresses. Both the stop piece and the contact area are less stressed, which is illustrated in figure 6.13. However, it can still be observed that the applied simulation strategy leads to a local deformation of the bottom flange plate of the preload segment at the point of support at high shear forces (especially in case 3). The reason for this is the modeling of the support point as an *analytical rigid*, i.e. an ideal stiff parameterized curve that stresses the beam by a line load. This results in the bottom chord plate tending to wrap around this support point due to shear forces, see figure 6.14. In reality, how-

188

Detail A-A

A-A
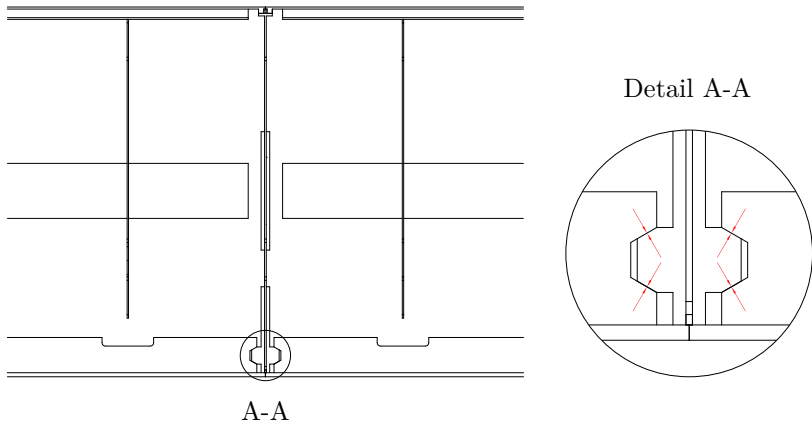
Figure 6.11: Detailed view of the connecting zone

ever, such a condition is not to be expected, since the attachment zone of the endcarriages distributes the shear force over a larger area, which reduces the impact of the shear force. An evaluation of the mechanical stresses shows that no global yielding occurs, so this calculated configuration is also able to withstand the acting loads. The same applies to the deformations; here, the respective limit values are complied with as well. The respective results are listed in table 6.7.

6.2 Derivation of Design Notes

The evaluation of the FE analyses carried out in the previous section allow the derivation of several design recommendations, that can be used for a future further development of the construction. These refer to different components and sections within the segmented prestressed girder.

189

Recess

Adjusted design of
the stop piece
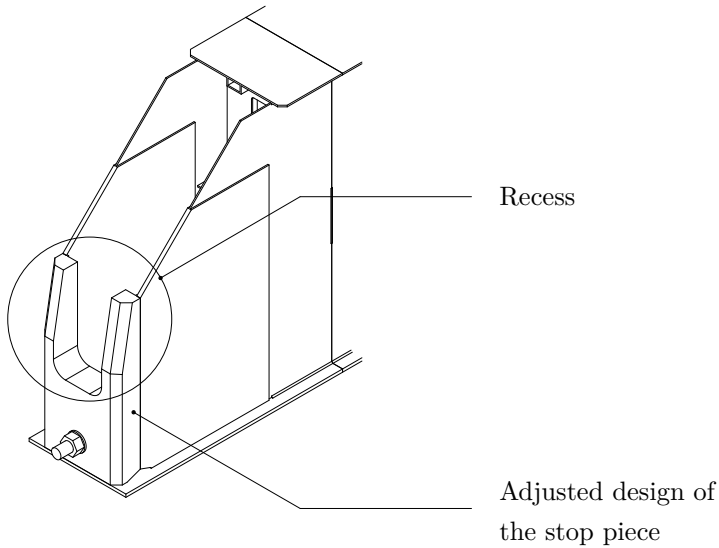
Figure 6.12: Isometric view of the improved reference configuration 3

6.2.1 Design of Connection Joints and the Connecting Element

With the aid of the FE analyses, it was possible to determine that the joining technique proposed at the beginning does not ensure sufficient structural resistance at high prestressing forces. This applies in particular to the lower chord plate of the segments. In this context, the alternative design demonstrated on reference configuration 3 achieves higher stiffness due to the inner box sections and the additional web attached to the underside of the bottom chord plate. The connecting element is also structurally reinforced in this context. It is therefore recommended to consider this alternative design for prestressing forces above 480 kN.
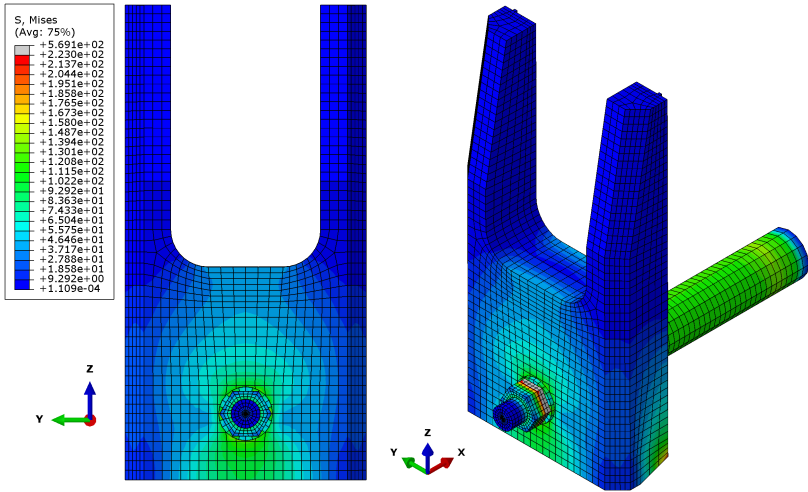
Figure 6.13: Stop piece of the improved reference configuration 3

6.2.2 Design of the Preload Segment

Due to the axial load application, the preload segment is subjected to high mechanical stresses, which in turn require a special local design. The proposed design is capable of withstanding the stresses globally. Local stress concentrations occur especially close to the load application area, but these can be eliminated by further improvements of the design. The designed relief notch plays a central role. Here, the simulations have shown that stress concentrations can be reduced by a smoother design of the force flow. Nevertheless, this zone is locally highly stressed compared to the rest of the preload segment structure. It is therefore recommended to further improve the notch geometry with regard to stress reduction. However, the manufacturability must remain guaranteed.

Reinforcing the bottom chord plate, as suggested in subsection 3.3.1, benefits the structural resistance, but for higher preload forces it is recommended to reinforce the bottom chord plate along its entire length as demonstrated by reference configuration 3.

191

S, Mises
(Avg: 75%)
+6.561e+02
+2.230e+02
+2.137e+02
+2.044e+02
+1.951e+02
+1.858e+02
+1.765e+02
+1.673e+02
+1.580e+02
+1.487e+02
+1.394e+02
+1.301e+02
+1.208e+02
+1.115e+02
+1.022e+02
+9.292e+01
+8.363e+01
+7.433e+01
+6.504e+01
+5.575e+01
+4.646e+01
+3.717e+01
+2.788e+01
+1.858e+01
+9.292e+00
+1.109e-04

Local deformation of bottom chord plate
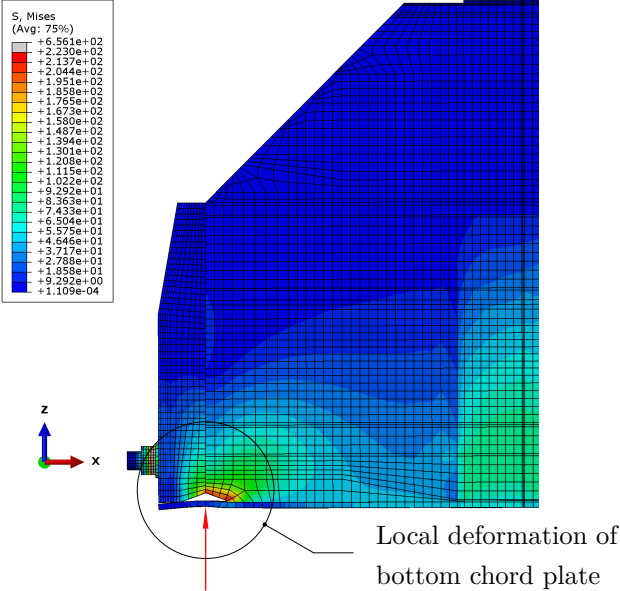
Figure 6.14: Local deformation of the bottom chord plate at the support

6.2.3 Design of the Stop Piece

In addition to the preload segment, the stop piece also has a key role to perform, as it is directly responsible for transmitting the preload force to the girder structure. It is recommended that the stop piece is also subjected to an individual design procedure and that it is dimensioned according to the axial force acting on it. It also makes sense to optimize the geometry in order to reduce the local stress concentrations.

6.3 Answering the Research Guiding Questions

On the basis of the results and findings carried out, answers as well as explanation approaches can be given to the research guiding questions defined at the beginning of this thesis.

Table 6.7: Configuration 3 - FEA results

Quantity		Case 1	Case 2	Case 3	GOA*
$\sigma_{\mathrm{M}}(\boldsymbol{p}_1)$	[N/mm^2]	16.4937	16.6883	36.4034	90.3507
$\sigma_{\mathrm{M}}(\boldsymbol{p}_2)$	[N/mm^2]	42.2620	42.6138	53.2017	90.7879
$\sigma_{\mathrm{M}}(\boldsymbol{p}_3)$	[N/mm^2]	32.1557	46.3286	57.8338	59.1903
$\sigma_{\mathrm{M}}(\boldsymbol{p}_4)$	[N/mm^2]	39.0421	32.8190	57.6719	54.7441
$\sigma_{\mathrm{M}}(\boldsymbol{p}_5)$	[N/mm^2]	47.0998	46.3377	3.4687	47.3376
$\sigma_{\mathrm{M}}(\boldsymbol{p}_6)$	[N/mm^2]	79.3355	80.0270	147.4901	93.8574
$\sigma_{\mathrm{M}}(\boldsymbol{p}_7)$	[N/mm^2]	71.3802	70.4254	57.4054	47.5779
$\sigma_{11}(\boldsymbol{p}_8)$	[N/mm^2]	-20.1425	-8.0183	-58.1233	-22.0697
$w(t_1, l_0)$	[mm]	0.7226	0.7212	-3.2828	5.4580
$w_{\mathrm{t}}(l_0)$	[mm]	0.2348	0.2347	0.2350	3.5644

Question 1

The primary challenges in terms of design cover the enabling of a continuous component bonding and at the same time the possibility of non-destructive dismantling in order to transport the single elements on appropriate conveying aids, such as EUR-pallets. In addition, space must be provided for the traction mechanism running inside the hollow profiles.

To overcome these issues, a possible solution is to divide the bridge crane into individual, discrete components and apply different segmentation techniques (presented in section 3.2.1) which depend on the desired total span width. The corresponding calculation bases are shown in table 3.1. Here, two major types of segments are introduced, the *main segment* and the *preload segment*. By considering a box section, the approach differs significantly in terms of geometry as well as segmentation from that demonstrated by S. BOLENDER et al. in [3].

In contrast to conventional bridge cranes, the segments of the novel structure are exposed to high axial forces acting in the webs due to the

prestressing. For this reason, bulkhead plates as well as stiffening plates are to be additionally added in order to reduce the effective length of the plates which are at risk of local buckling. On the other hand, the preload segments must be designed individually since here high axial loads due to the prestressing are applied. It is recommended to reinforce these areas by additional plates and chamfer the web to enhance the stiffness.

The developed stop pieces are placed on a flat plate allocated to the preload segment. It is necessary to design them compactly since they must transmit the prestressing forces in a comparatively small area.

As a further key feature of the design, the novel connecting elements are to be mentioned. These facilitate on the one hand the joining of the segments due to their positive fit and on the other hand they contribute to increasing the elastic stability by supporting the plates. In this sense, they are a kind of removeable bulkhead plate. Therefore, the connecting elements represent an important integral component which take on several tasks.

Question 2

The implementation of a dimensioning and optimization procedure requires at first both the identification and mathematical formulation of constraint functions. Essential for this is the availability of an appropriate substitute mechanical model. Due to the novel type of structure, also new constraints occur, which are to be taken into account. In this context, the avoidance of gaping regarding to the initial loose component bond as well as the appearance of the traction mechanism are to be pointed out.

Using the beam theory of first order, it could be shown within this work, that it is possible to express the eccentricity ϵ explicitly by using the found relation 4.12. This circumstance plays a major role with respect to the subsequently optimization procedure since it significantly influences the treatment of the constraint functions. For this reason, the constraint functions differ strongly from those of conventional girders against the background of the mathematical characteristics which are considered

for instance in [10], [42] and [7]. So far, the structure developed in this thesis is not yet known in crane construction.

Against this background, the corresponding optimization problem can be formulated whose objective function covers the minimization of the resulting area of the cross-section geometry, see chapter 5. Due to the large number of nonlinear relations, this is a nonlinear optimization problem. In addition, the problem becomes *non-smooth* due to the variable d which is not continuously differentiable. However, the complexity and high number of constraints do not allow a purely analytical solution of the problem. For this reason, a numerical method is necessary in order to approximate a solution.

In this thesis, a total of three solution methods are developed, whereby the GOA* represents an extension of the GOA. These methods differ in the respective treatment of the occurring variables, but they have in common that the information known in advance is smartly utilized to exclude already non-permissible parameter combinations according to the Branch and Bound method. In addition, the individual steps of the methods are based on manageable analytical relations. This also allows an interpretation of the physical behavior of the structure (for example, the identification of the *absorbing point* in section 5.1.1) and thus stands out from pure search methods. The possibility of an explicit representation of the constraint functions is of decisive importance here.

The basic idea of the solution methods is to subject the continuously distributed variables (and thus also the solution space) to a rough discretization first and to identify a solution in an initial step. This can be interpreted as a point in a multidimensional space. It can now be shown on the basis of the existence of a descent direction that in the neighborhood of such a point another point exists which leads to a better solution (see section 5.2.4). This results in the motivation to re-span the initial search domain around this point and to repeat the whole process until a defined termination criterion is reached. Thus, the original solution procedure is extended to a gradient-based procedure and made more efficient. It should be noted, however, that this discretization leads to a loss of information which indicates that an optimal solution can only be approximated with the help of the methods.

Question 3

The last research question refers to the approximation quality of the developed algorithms. The basis for this are the computer experiments carried out in chapter 5, which allow the following statements:

LOA Algorithm   With an initial number of $\bar{n} = 9$ elements and an incremental multiplier of $\lambda_\zeta = 1.50$, the LOA algorithm is able to calculate the best result among all considered parameter combinations with a relative deviation of 1.55 % and an expected value of 54369 iterations. With a probability of 95 %, the relative deviation is between 0.00 % and 3.52 %.

GOA Algorithm   With an initial number of $\bar{n} = 9$ elements and an incremental multiplier of $\lambda_\zeta = 1.50$, the GOA algorithm is able to calculate the best result among all considered parameter combinations with a relative deviation of 1.95 % and an expected value of 72343 iterations. With a probability of 95 %, the relative deviation is between 0.00 % and 4.36 %.

GOA* Algorithm   With an initial number of $\bar{n} = 9$ elements and an incremental multiplier of $\lambda_\zeta = 1.50$, the GOA algorithm is able to calculate the best result among all parameter combinations with a relative deviation of 1.95 % and an expected value of 25950 iterations. With a probability of 95 %, the relative deviation is between 0.00 % and 4.36 %.

Finally in chapter 6, the developed method is demonstrated using three reference configurations as examples. With the help of detailed FE analyses, it can be shown that the method is capable of calculating the necessary dimensions of the components involved in such a way that no global yielding of the material occurs and elastic stability is ensured. Possible local special designs have to be considered in case of high prestressing forces. For this, an alternative design is additionally proposed in the thesis. Further design notes are summarized in section 6.2.

7 Conclusion and Outlook

The journey is the reward.
- CONFUCIUS

The aim of the doctoral thesis is the development of a novel type of segmented bridge crane and its optimization in terms of material savings. A detailed study of the current field of crane construction reveals that segmented girders have not been investigated so far and that the field is almost unexplored. The only comparable design is provided by S. BOLENDER et al. which refers to a truss structure. On this basis, a novel design for segmented crane girders is developed in chapter 3. Here, the need of an appropriate segmentation strategy represents the first key finding. Against the background of a planned implementation, the common design regulations must be extended considering new constraints which are identified and developed in chapter 4. Hereby, the establishment of a suitable mechanical substitute model is mandatory. The identified constraint functions form the major input for a subsequently optimization problem in chapter 5. The problems nature is characterized by a high degree of complexity. However, a detailed investigation of the mathematical properties allows the development of different solution approaches which are able to produce configurations of minimum weight in moderate computation time. Subsequently, the procedure is evaluated by means of FE analyses on three reference configurations with the result that for all calculated configurations there is no exceeding of the material's strength values and no failure of elastic stability.

The essential basics for the treatment of segmented bridge crane girders for use in material flow systems were worked out in this thesis. In particular, mechanical issues were investigated in the context of a nonlinear and non-smooth optimization problem and the mathematical character-

istics were examined in comparison to conventional crane girders. The results of this work thus serve as a foundation for a deeper investigation of this unexplored area. This includes especially the examination of the constraints with regard to the local stability as well as a further development of the design of the force application area. The complete dimensioning requires in addition statements regarding the dynamical behavior of the structure. A complete parameterization of the model as well as the inclusion of production-related boundary conditions are to be aimed at as a long-term goal.

A   Appendix

Table A.1: Considered traction mechanisms, property class 10.9 [11, p. 109–126]

Thread	d_{N} [mm]	A_{d3} [mm^2]	$N(\mu_{\mathrm{T}} = 0.14)$ [kN]	d [mm]
M8	8.00	32.84	26.60	16.00
M10	10.00	52.30	42.20	20.00
M12	12.00	84.30	61.50	25.00
M16	16.00	114.10	115.70	30.00
M18	18.00	175.10	141.00	35.00
M22	22.00	281.50	225.00	40.00
M24	24.00	324.30	260.00	45.00
M27	27.00	427.10	342.00	50.00
M33	33.00	647.20	517.00	60.00
M36	36.00	759.30	608.00	70.00
M39	39.00	913.00	729.00	80.00

Table A.2: Test points, T_1 - T_{25}

Test point	m_0 [kg]	l_0 [mm]	γ_{M1} [$-$]	γ_{M2} [$-$]	R_e [N/mm^2]
T_1	14912.69	3819.12	1.19	1.33	355.00
T_2	14542.22	6863.74	1.44	1.61	235.00
T_3	5845.16	6974.57	1.76	1.67	275.00
T_4	9305.16	6178.51	1.49	1.52	235.00
T_5	5959.66	6178.51	1.85	1.81	235.00
T_6	11199.44	7524.44	1.36	1.28	460.00
T_7	15366.35	2775.92	1.23	1.20	235.00
T_8	7407.24	5542.45	1.71	1.11	460.00
T_9	15941.17	4664.76	1.30	1.23	355.00
T_{10}	8304.61	2588.87	1.87	1.55	235.00
T_{11}	7056.84	7294.30	1.80	1.55	355.00
T_{12}	12855.35	4999.54	1.50	1.42	355.00
T_{13}	15643.91	6738.62	1.11	1.38	235.00
T_{14}	12299.47	2398.58	1.26	1.12	460.00
T_{15}	4868.49	3132.11	1.32	1.73	420.00
T_{16}	8827.18	5902.58	1.89	1.63	355.00
T_{17}	6539.07	2921.54	1.66	1.45	460.00
T_{18}	7291.88	5407.81	1.39	1.33	275.00
T_{19}	4708.44	4050.42	1.35	1.70	460.00
T_{20}	15227.40	6478.10	1.54	1.78	275.00
T_{21}	13542.60	5966.39	1.93	1.82	460.00
T_{22}	8792.98	4028.11	1.95	1.48	275.00
T_{23}	14151.45	3258.68	1.61	1.95	460.00
T_{24}	13118.17	3426.78	1.69	1.80	355.00
T_{25}	12013.38	7454.57	1.78	1.18	355.00

Table A.3: Test points, T_{26} - T_{50}

Test point	m_0 [kg]	l_0 [mm]	γ_{M1} [$-$]	γ_{M2} [$-$]	R_e [N/mm^2]
T_{26}	9182.06	4557.35	1.15	1.30	460.00
T_{27}	8500.25	4262.31	1.65	1.76	420.00
T_{28}	5043.41	4426.69	1.16	1.44	275.00
T_{29}	8003.13	7712.11	1.52	1.47	235.00
T_{30}	10935.12	2972.20	1.57	1.88	235.00
T_{31}	9871.46	7123.15	1.12	1.92	460.00
T_{32}	12600.43	2232.67	1.17	1.68	355.00
T_{33}	10507.97	3533.66	1.94	1.60	275.00
T_{34}	13920.05	6670.06	1.63	1.86	355.00
T_{35}	5236.54	3685.95	1.46	1.50	460.00
T_{36}	10056.96	5358.04	1.44	1.25	355.00
T_{37}	11486.32	4386.24	1.30	1.40	420.00
T_{38}	6728.09	2118.51	1.27	1.37	235.00
T_{39}	11749.50	5094.05	1.41	1.58	275.00
T_{40}	4314.72	5238.63	1.40	1.14	235.00
T_{41}	11749.50	5642.91	1.82	1.17	275.00
T_{42}	14672.40	3617.96	1.60	1.27	275.00
T_{43}	10270.43	4850.53	1.55	1.87	275.00
T_{44}	9746.91	6296.75	1.22	1.72	275.00
T_{45}	6279.90	7269.10	1.90	1.65	420.00
T_{46}	4136.14	2315.79	1.74	1.95	420.00
T_{47}	13142.97	2719.06	1.82	1.99	275.00
T_{48}	13688.76	5767.68	1.71	1.97	460.00
T_{49}	7604.07	6382.54	1.99	1.21	420.00
T_{50}	5539.55	7963.03	1.98	1.89	355.00

Table A.4: Constant values

Quantity	Numerical value	Unit	Description
g	9.81	$[\text{m/s}^2]$	Gravity constant
E	$2.10 \cdot 10^5$	$[\text{N/mm}^2]$	YOUNGS's Modulus
ν	0.30	$[-]$	POISSON's ratio
ρ	$7.85 \cdot 10^{-6}$	$[\text{kg/mm}^3]$	Density (steel)
b_{w}	20.00	$[\text{mm}]$	Half width of a wheel
t	5.00	$[\text{mm}]$	Web thickness
x_{p}	100.00	$[\text{mm}]$	Preload segment, upper chord
m_{t}/m_0	0.10	$[-]$	Load of traveling trolley
l_{t}/l_0	0.05	$[-]$	Wheel base of traveling trolley
F_2/F_3	0.05	$[-]$	Force due to bumper impact
s_2/t	2.00	$[-]$	Space reservation in x_2-direction
s_3/t	2.00	$[-]$	Space reservation in x_3-direction
λ	1/16	$[-]$	Stop piece, space reservation
λ_σ^*	0.75	$[-]$	Stress factor
λ_{h}	1/7	$[-]$	Ratio of maximum height
λ_3	0.20	$[-]$	Chamfer ratio
λ_γ^*	0.01	$[-]$	Ratio to avoid gaping
δ_2	1/300	$[-]$	Deflection ratio in x_2-direction
μ_{f}	0.14	$[-]$	Friction coefficient (steel-steel)
$b_{\langle 1\rangle,1}$	50.00	$[\text{mm}]$	Lower initial interval limit
$b_{\langle 1\rangle,m}/l_0$	0.01	$[-]$	Upper initial interval limit
$\eta_{\langle 1\rangle,1}$	0.90	$[-]$	Lower initial interval limit
$\delta_{\langle 1\rangle,1}$	0.00	$[-]$	Lower initial interval limit
$\delta_{\langle 1\rangle,m}$	1/250	$[-]$	Upper initial interval limit

Table A.5: Parameter combinations

Parameter combination p	Elements $\bar{n}\,[-]$	Incr. multiplier $\lambda_\varsigma\,[-]$
$\mathbf{p}_1$	6	0.50
$\mathbf{p}_2$	6	0.75
$\mathbf{p}_3$	6	1.00
$\mathbf{p}_4$	6	1.25
$\mathbf{p}_5$	6	1.50
$\mathbf{p}_6$	7	0.50
$\mathbf{p}_7$	7	0.75
$\mathbf{p}_8$	7	1.00
$\mathbf{p}_9$	7	1.25
$\mathbf{p}_{10}$	7	1.50
$\mathbf{p}_{11}$	8	0.50
$\mathbf{p}_{12}$	8	0.75
$\mathbf{p}_{13}$	8	1.00
$\mathbf{p}_{14}$	8	1.25
$\mathbf{p}_{15}$	8	1.50
$\mathbf{p}_{16}$	9	0.50
$\mathbf{p}_{17}$	9	0.75
$\mathbf{p}_{18}$	9	1.00
$\mathbf{p}_{19}$	9	1.25
$\mathbf{p}_{20}$	9	1.50
$\mathbf{p}_{21}$	10	0.50
$\mathbf{p}_{22}$	10	0.75
$\mathbf{p}_{23}$	10	1.00
$\mathbf{p}_{24}$	10	1.25
$\mathbf{p}_{25}$	10	1.50

Table A.6: GOA - Algorithm performance

$\mathbf{p}$	$\bar{\mu}(n_\mathrm{I}(\mathbf{p}))\,[-]$	$\bar{\sigma}(n_\mathrm{I}(\mathbf{p}))\,[-]$	$\bar{\mu}(f'(\mathbf{p}))\,[\%]$	$\bar{\sigma}(f'(\mathbf{p}))\,[\%]$	$\mathrm{Pr}_{0.95}(f'(\mathbf{p}))\,[\%]$
$\mathbf{p}_1$	17874	2355	10.9959	9.1309	$[5.2211, 16.7707]$
$\mathbf{p}_2$	20525	4753	6.4313	8.5290	$[1.0370, 11.8255]$
$\mathbf{p}_3$	22071	7384	5.5815	7.5715	$[0.7927, 10.3702]$
$\mathbf{p}_4$	22071	7384	4.3760	6.6092	$[0.5560, 8.9130]$
$\mathbf{p}_5$	21131	11302	5.0419	6.3899	$[1.0006, 9.0833]$
$\mathbf{p}_6$	15472	10802	9.1921	7.9780	$[4.1464, 14.2378]$
$\mathbf{p}_7$	26748	2625	6.2786	6.7347	$[2.0191, 10.5380]$
$\mathbf{p}_8$	30265	5557	5.7790	6.6062	$[1.6009, 9.9572]$
$\mathbf{p}_9$	32009	9449	5.0000	6.5473	$[0.8591, 9.1408]$
$\mathbf{p}_{10}$	35126	11692	2.1804	3.7333	$[0.0000, 4.5451]$
$\mathbf{p}_{11}$	32965	14488	7.9576	7.6622	$[3.1116, 12.8036]$
$\mathbf{p}_{12}$	37650	2197	6.2546	7.0338	$[1.8061, 10.7032]$
$\mathbf{p}_{13}$	41733	6524	5.2817	6.5542	$[1.1365, 9.4270]$
$\mathbf{p}_{14}$	45521	11536	4.9478	6.2667	$[0.9844, 8.9112]$
$\mathbf{p}_{15}$	48512	14990	2.5093	3.9695	$[0.0000, 5.0199]$
$\mathbf{p}_{16}$	46249	18658	5.6034	5.7480	$[1.9680, 9.2388]$
$\mathbf{p}_{17}$	52880	4316	4.6830	5.8945	$[0.9550, 8.4110]$
$\mathbf{p}_{18}$	57878	10089	4.3073	5.7486	$[0.6716, 7.9431]$
$\mathbf{p}_{19}$	61767	15852	3.6778	5.3573	$[0.2895, 7.0660]$
$\mathbf{p}_{20}$	65445	19578	1.9456	3.8246	$[0.0000, 4.3645]$
$\mathbf{p}_{21}$	72343	22032	5.4562	5.4740	$[1.9941, 8.9183]$
$\mathbf{p}_{22}$	68678	8857	4.2072	5.5990	$[0.6661, 7.7483]$
$\mathbf{p}_{23}$	75790	13027	3.8425	5.6868	$[0.2458, 7.4391]$
$\mathbf{p}_{24}$	83170	14075	2.5077	4.3580	$[0.0000, 5.2639]$
$\mathbf{p}_{25}$	87000	21014	2.3983	4.5196	$[0.0000, 5.2567]$

Table A.7: LOA - Algorithm performance

$\mathbf{p}$	$\bar{\mu}(n_{\mathrm{I}}(\mathbf{p}))\,[-]$	$\bar{\sigma}(n_{\mathrm{I}}(\mathbf{p}))\,[-]$	$\bar{\mu}(f'(\mathbf{p}))\,[\%]$	$\bar{\sigma}(f'(\mathbf{p}))\,[\%]$	$\mathrm{Pr}_{0.95}(f'(\mathbf{p}))\,[\%]$
$\mathbf{p}_1$	9706	634	11.1025	8.2572	[5.8802, 16.3248]
$\mathbf{p}_2$	11168	2076	6.5329	7.2934	[1.9201, 11.1456]
$\mathbf{p}_3$	11572	3478	5.8118	6.3611	[1.7884, 9.8346]
$\mathbf{p}_4$	11108	5773	4.0124	5.2660	[0.6818, 7.3429]
$\mathbf{p}_5$	8038	5120	4.7667	5.9788	[0.9854, 8.5480]
$\mathbf{p}_6$	16597	1126	9.5054	8.1366	[4.3594, 14.6514]
$\mathbf{p}_7$	19460	2668	6.2544	6.5666	[2.1014, 10.4075]
$\mathbf{p}_8$	20160	5541	5.3431	5.9125	[1.6037, 9.0824]
$\mathbf{p}_9$	20902	7704	4.4439	5.9895	[0.6558, 8.2320]
$\mathbf{p}_{10}$	20251	8922	1.7697	3.2026	[0.0000, 3.7952]
$\mathbf{p}_{11}$	27525	1428	7.4713	6.7125	[3.2260, 11.7167]
$\mathbf{p}_{12}$	30700	3511	5.7198	6.2664	[1.7566, 9.6830]
$\mathbf{p}_{13}$	31590	7964	4.5888	5.2547	[1.2654, 7.9121]
$\mathbf{p}_{14}$	35635	8706	2.9525	4.4525	[0.1365, 5.7685]
$\mathbf{p}_{15}$	31642	14648	1.6425	2.7935	[0.0000, 3.4093]
$\mathbf{p}_{16}$	41786	4536	5.8845	5.7952	[2.2193, 9.5498]
$\mathbf{p}_{17}$	46058	8239	4.6696	5.7522	[1.0316, 8.3076]
$\mathbf{p}_{18}$	47502	14085	3.5905	4.7025	[0.6164, 6.5647]
$\mathbf{p}_{19}$	50840	16003	2.8127	4.2313	[0.1365, 5.4888]
$\mathbf{p}_{20}$	54369	19189	1.5492	3.5129	[0.0000, 3.7709]
$\mathbf{p}_{21}$	61360	5717	5.5273	5.3965	[2.1143, 8.9404]
$\mathbf{p}_{22}$	68900	9732	4.2360	5.5035	[0.7553, 7.7167]
$\mathbf{p}_{23}$	70560	14711	3.6873	5.5558	[0.1736, 7.2011]
$\mathbf{p}_{24}$	77780	17296	2.4129	4.3310	[0.0000, 5.1521]
$\mathbf{p}_{25}$	79060	24672	2.2595	4.3355	[0.0000, 5.0015]

Table A.8: GOA* - Algorithm performance

$\mathbf{p}$	$\bar{\mu}(n_I(\mathbf{p}))\,[-]$	$\bar{\sigma}(n_I(\mathbf{p}))\,[-]$	$\bar{\mu}(f'(\mathbf{p}))\,[\%]$	$\bar{\sigma}(f'(\mathbf{p}))\,[\%]$	$\mathrm{Pr}_{0.95}(f'(\mathbf{p}))\,[\%]$
$\mathbf{p}_1$	17874	2355	10.9959	9.1309	$[5.2211, 16.7707]$
$\mathbf{p}_2$	20525	4753	6.4313	8.5290	$[1.0370, 11.8255]$
$\mathbf{p}_3$	22071	7384	5.5815	7.5715	$[0.7927, 10.3702]$
$\mathbf{p}_4$	22071	7384	4.3760	6.6092	$[0.5560, 8.9130]$
$\mathbf{p}_5$	21131	11302	5.0419	6.3899	$[1.0006, 9.0833]$
$\mathbf{p}_6$	15472	10802	9.1921	7.9780	$[4.1464, 14.2378]$
$\mathbf{p}_7$	26748	2625	6.2786	6.7347	$[2.0191, 10.5380]$
$\mathbf{p}_8$	30265	5557	5.7790	6.6062	$[1.6009, 9.9572]$
$\mathbf{p}_9$	32009	9449	5.0000	6.5473	$[0.8591, 9.1408]$
$\mathbf{p}_{10}$	35126	11692	2.1804	3.7333	$[0.0000, 4.5451]$
$\mathbf{p}_{11}$	32965	14488	7.9576	7.6622	$[3.1116, 12.8036]$
$\mathbf{p}_{12}$	37650	2197	6.2546	7.0338	$[1.8061, 10.7032]$
$\mathbf{p}_{13}$	41733	6524	5.2817	6.5542	$[1.1365, 9.4270]$
$\mathbf{p}_{14}$	45521	11536	4.9478	6.2667	$[0.9844, 8.9112]$
$\mathbf{p}_{15}$	48512	14990	2.5093	3.9695	$[0.0000, 5.0199]$
$\mathbf{p}_{16}$	46249	18658	5.6034	5.7480	$[1.9680, 9.2388]$
$\mathbf{p}_{17}$	52880	4316	4.6830	5.8945	$[0.9550, 8.4110]$
$\mathbf{p}_{18}$	57878	10089	4.3073	5.7486	$[0.6716, 7.9431]$
$\mathbf{p}_{19}$	61767	15852	3.6778	5.3573	$[0.2895, 7.0660]$
$\mathbf{p}_{20}$	65445	19578	1.9456	3.8246	$[0.0000, 4.3645]$
$\mathbf{p}_{21}$	72343	22032	5.4562	5.4740	$[1.9941, 8.9183]$
$\mathbf{p}_{22}$	68678	8857	4.2072	5.5990	$[0.6661, 7.7483]$
$\mathbf{p}_{23}$	75790	13027	3.8425	5.6868	$[0.2458, 7.4391]$
$\mathbf{p}_{24}$	83170	14075	2.5077	4.3580	$[0.0000, 5.2639]$
$\mathbf{p}_{25}$	87000	21014	2.3983	4.5196	$[0.0000, 5.2567]$

Table A.9: Configuration 1 - FEA settings and element properties

Component	Seed	Element	Technique	Algorithm	Shape
Nut (M33)	4	C3D8R	Structured		Hex
Shim (M33)	6	C3D8R	Structured		Hex
Additional bolt	6	C3D8R		Medial axis	Hex-dominated
Additional rod	8	C3D8R		Medial axis	Hex-dominated
Bolt	6	C3D8R		Medial axis	Hex-dominated
Common rod	8	C3D8R		Medial axis	Hex-dominated
Connecting element	12	C3D8R		Advancing front	Hex
Preload segment	12	C3D8R	Structured		Hex
Segment	15	C3D8R	Structured		Hex
Stop piece	10	C3D8R	Structured		Hex

Table A.10: Configuration 2 - FEA settings and element properties

Component	Seed	Element	Technique	Algorithm	Shape
Nut (M33)	4	C3D8R	Structured		Hex
Shim (M33)	6	C3D8R	Structured		Hex
Additional bolt	6	C3D8R		Medial axis	Hex-dominated
Additional rod	8	C3D8R		Medial axis	Hex-dominated
Bolt	6	C3D8R		Medial axis	Hex-dominated
Common rod	8	C3D8R		Medial axis	Hex-dominated
Connecting element	12	C3D8R	Structured		Hex
Preload segment	12	C3D8R	Structured		Hex
Segment	15	C3D8R	Structured		Hex
Stop piece	10	C3D8R	Structured		Hex

Table A.11: Configuration 3 - FEA settings and element properties

Component	Seed	Element	Technique	Algorithm	Shape
Nut (M39)	4	C3D8R	Structured		Hex
Shim (M39)	6	C3D8R	Structured		Hex
Additional bolt	8	C3D8R		Medial axis	Hex-dominated
Additional rod	10	C3D8R		Medial axis	Hex-dominated
Bolt	8	C3D8R		Medial axis	Hex-dominated
Common rod	10	C3D8R		Medial axis	Hex-dominated
Connecting element	12	C3D8R	Structured		Hex
Preload segment	17	C3D8R	Structured		Hex
Segment	15	C3D8R	Structured		Hex
Stop piece	15	C3D8R	Structured		Hex

Reference List

[1] Markus Golder. *Ein Beitrag zur Kostenabschätzung für Brückenkranträger in Kastenbauweise auf Basis ihrer Bemessungsgrundlagen und Dimensionierungsnachweise.* Dissertation, Universität Karlsruhe, August 2004.

[2] Dietmar Gross, Werner Hauger, Jörg Schröder, and Wall, Wolfgang A. *Technische Mechanik 2 - Elastostatik.* Springer-Lehrbuch. Springer-Verlag Berlin Heidelberg, 12th edition, 2012.

[3] Steffen Bolender, Jan Oellerich, Meike Braun, and Markus Golder. Skalierbarer modularer Brückenkranträger in Segmentbauweise. *Logistics Journal: Proceedings*, 2017(10):1–8, September 2017.

[4] Bilal M. Ayyub, Young G. Sohn, and Hamid Saadatmanesh. Prestressed Composite Girders under Positive Moment. *Journal of Structural Engineering*, 116(11):2931–2951, November 1990.

[5] Oliver Stein. *Grundzüge der Globalen Optimierung.* Springer Spektrum, Berlin, Heidelberg, 1st edition, 2018.

[6] G. Pavlovic, M. Gasic, M. Rajovic, and M. Savkovic. Optimization of the box section of the main girders of the bridge crane by using the method of Lagrange multipliers. In *International Conference Mathematical and Informational Technologies MIT*, pages 145–152, Vrnjacka Banja, Serbia, September 2013.

[7] Mile Savkovic, Milomir Gasic, Dobrivoje Catic, Ruzica Nikolic, and Goran Pavlovic. Optimization of the box section of the main girder of the bridge crane with the rail placed above the web plate. *Structural and Multidisciplinary Optimization*, 47:273–288, February 2013.

[8] Chaoli Sun, Ying Tan, Jian-Chao Zeng, Jeng-Shyang Pan, and Yuanfang Tao. The Structure Optimization of Main Beam for Bridge Crane Based on An Improved PSO. *Journal of Computers*, 6(8):1585–1590, August 2011.

[9] DIN EN 1993-6:2007+AC:2009: Eurocode 3: Design of steel structures Part 6: Crane supporting structures. *DIN Deutsches Institut für Normung e.V.* Beuth Verlag GmbH, Berlin, December 2010.

[10] Mile Savkovic, Radovan Bulatovic, Milomir Gasic, Goran Pavlovic, and Aleksandar Stepanovic. Optimization of the box section of the main girder of the single-girder bridge crane by applying biologically inspired algorithms. *Engineering Structures*, 148:452–465, October 2017.

[11] VDI 2230: Systematic calculation of highly stressed bolted joint Joints with one cylindrical bolt. *VDI Verein Deutscher Ingenieure e. V.* Beuth Verlag GmbH, Düsseldorf, November 2016.

[12] Dieter Arnold. *Intralogistik: Potentiale, Perspektiven, Prognosen.* VDI-Buch. Springer-Verlag Berlin Heidelberg, 2007.

[13] Rudolf Griemert and Peter Römisch. *Fördertechnik - Auswahl und Berechnung von Elementen und Baugruppen.* Springer Fachmedien Wiesbaden, 11th edition, 2015.

[14] Michael ten Hompel, Thorsten Schmidt, and Johannes Dregger. *Materialflusssysteme - Förder- und Lagertechnik.* VDI-Buch. Springer-Verlag Berlin Heidelberg, 4th edition, 2018.

[15] DIN EN 13001-3-1:2012+A1:2013: Cranes General design Part 3.1: Limit states and proof competence of steel structure. *DIN Deutsches Institut für Normung e.V.* Beuth Verlag GmbH, Berlin, June 2015.

[16] DIN EN 13001-3-3:2014: Cranes General design Part 3.3: Limit state and proof of competence of wheel / rail contacts. *DIN Deutsches Institut für Normung e.V.* Beuth Verlag GmbH, Berlin, February 2015.

[17] Dietmar Gross, Werner Hauger, Jörg Schröder, and Wolfgang A. Wall. *Technische Mechanik 1 - Statik.* Springer-Lehrbuch. Springer-Verlag Berlin Heidelberg, 12th edition, 2013.

[18] Rolf Mahnken. *Lehrbuch der Technischen Mechanik - Band 1: Starrkörperstatik, Grundlagen und Anwendungen.* Springer-Lehrbuch. Springer-Verlag Berlin Heidelberg, 2nd edition, 2016.

[19] Jürgen Dankert and Helga Dankert. *Technische Mechanik - Statik, Festigkeitslehre, Kinematik / Kinetik.* Springer-Lehrbuch. Springer Fachmedien Wiesbaden, 7th edition, 2013.

[20] Holger Grote. *Zum Einfluss des Beulens auf die Tragfähigkeit von Walzprofilen aus hochfestem Stahl.* Dissertation, Ruhr-Universität Bochum, February 2003.

[21] Volker Läpple. *Einführung in die Festigkeitslehre - Lehr- und Übungsbuch.* Springer-Lehrbuch. Springer Fachmedien Wiesbaden, 4th edition, 2016.

[22] S. P. Timoshenko and J. N. Goodier. *Theory of Elasticity.* Engineering Societies Monographs. McGraw Hill Education (India) Private Limited, Chennai, 3rd edition, 2018.

[23] ISO 22986:2007(E): Cranes Stiffness Bridge and gantry cranes. *ISO International Organization for Standardization.* ISO copyright office, CH-1211 Geneva 20, April 2015.

[24] Herbert A. Mang and Günter Hofstetter. *Festigkeitslehre.* Springer-Verlag Berlin Heidelberg, 4th edition, 2013.

[25] Rolf Mahnken. *Lehrbuch der Technischen Mechanik - Elastostatik, mit einer Einführung in Hybridstruktren.* Springer-Lehrbuch. Springer-Verlag Berlin Heidelberg, 2015.

[26] Stephen P. Timoshenko and James M. Gere. *Theory of Elastic Stability.* Dover Civil and Mechanical Engineering. Dover Publications, Inc., Mineola, New York, 2nd edition, 2009.

[27] Christian Spura. *Einführung in die Balkentheorie nach Timoshenko und Euler-Bernoulli.* Essentials. Springer Fachmedien Wiesbaden, 2019.

[28] Michael Riemer, Wolfgang Seemann, Jörg Wauer, and Walter Wedig. *Mathematische Methoden der Technischen Mechanik - Für Ingenieure und Naturwissenschaftler.* Springer Fachmedien Wiesbaden, 3rd edition, 2019.

[29] Dietmar Gross, Werner Hauger, and Peter Wriggers. *Technische Mechanik 4 - Hydromechanik, Elemente der Höhreren Mechanik, Numerische Methoden.* Springer-Lehrbuch. Springer-Verlag Berlin Heidelberg, 9th edition, 2014.

[30] Stephen P. Timoshenko and S. Woinowsky Krieger. *Theory of Plates and Shells.* McGraw Hill Education (India) Private Limited, Chennai, 2nd edition, 2010.

[31] G. Magnel. Prestressed Steel Structures. *The Structural Engineer*, 28:285–295, November 1950.

[32] Peter G. Hoadley. Behavior of Prestressed Composite Steel Beams. *Journal of the Structural Division*, 89(3):21–34, 1963.

[33] B. Belletti and A. Gasperi. Behavior of Prestressed Steel Beams. *Journal of Structural Engineering*, 136(9):1131–1139, September 2010.

[34] Jonathan Gosaye, Leroy Gardner, M. Ahmer Wadee, and Murray E. Ellen. Tensile performance of prestressed steel elements. *Engineering Structures*, 79:234–243, November 2014.

[35] Jonathan Gosaye, Leroy Gardner, M. Ahmer Wadee, and Murray E. Ellen. Compressive behaviour and design of prestressed steel elements. *Structures*, 5:76–87, February 2016.

[36] Nicolas Hadjipantelis, Leroy Gardner, and M. Ahmer Wadee. Prestressed cold-formed steel beams: Concept and mechanical behaviour. *Engineering Structures*, 172:1057–1072, June 2018.

[37] Nicolas Hadjipantelis, Leroy Gardner, and M. Ahmer Wadee. Design of prestressed cold-formed steel beams. *Thin-Walled Structures*, 140:565–578, April 2019.

[38] Oliver Stein. *Grundzüge der Nichtlinearen Optimierung*. Springer Spektrum, Berlin, Heidelberg, 1st edition, 2018.

[39] Daniel Scholz. *Optimierung interaktiv - Grundlagen verstehen, Modelle erforschen und Verfahren anwenden*. Springer-Verlag Berlin Heidelberg, 1st edition, 2018.

[40] Florian Jarre and Josef Stoer. *Optimierung - Einführung in mathematische Theorie und Methoden*. Masterclass. Springer-Verlag Berlin Heidelberg, 2nd edition, 2019.

[41] Yuhui Shi and B. Gireesha Obaiahnahatti. A Modified Particle Swarm Optimizer. In *1998 IEEE International Conference on Evolutionary Computation Proceedings. IEEE World Congress on Computational Intelligence (Cat. No.98TH8360), Anchorage, AK, USA*, volume 6, pages 69–73, June 1998.

[42] Xiaogang Qu, Gening Xu, Xiaoning Fan, and Xiaoheng Bi. Intelligent Optimization Methods for the Design of an Overhead Travelling Crane. *Chinese Journal of Mechanical Engineering*, 28(1):187–196, December 2015.

[43] Herbert Wittel, Dieter Muhs, Dieter Jannasch, and Joachim Voßiek. *Roloff / Matek - Normung, Berechnung, Gestaltung.* Springer Fachmedien Wiesbaden, 22nd edition, 2015.

[44] Markus Linke and Eckart Nast. *Festigkeitslehre für den Leichtbau - Ein Lehrbuch zur Technischen Mechanik.* Springer-Verlag Berlin Heidelberg, 1st edition, 2015.

[45] Roland Gomeringer, Roland Kilgus, Volker Menges, Stefan Oesterle, Thomas Rapp, Clausius Scholer, Andreas Stenzel, Andreas Stephan, and Falko Wieneke. *Tabellenbuch Metall.* Europa-Fachbuchreihe für Metallberufe. Verlag Europa Lehrmittel Nourney, Vollmer GmbH & Company KG, Haan-Gruiten, 48th edition, 2019.

[46] FEM 9.341: Series Lifting equipment Local Girder Stresses. *Federation Europeenne de la Manutention, Section IX.* VDMA Verlag GmbH, Frankfurt, 1st edition, October 1983.

[47] T. Arens, R. Busam, F. Hettlich, C. Karpfinger, H. Stachel, and K. Lichtenegger. *Grundwissen Mathematikstudium - Analysis und Lineare Algebra mit Querverbindungen.* Springer-Lehrbuch. Springer-Verlag Berlin Heidelberg, 2013.

[48] E. Zeidler, W. Hackbusch, J. Hromkovic, B. Luderer, H.R. Schwarz, J. Blath, A. Schied, S. Dempe, G. Wanka, and S. Gottwald. *Springer-Taschenbuch der Mathematik: Begründet von I.N. Bronstein und K.A. Semendjaew Weitergeführt von G. Grosche, V. Ziegler und D. Ziegler Herausgegeben von E. Zeidler.* Springer Link: Bücher. Springer Fachmedien Wiesbaden, 3rd edition, 2013.

[49] Günter Bärwolff. *Numerik für Ingenieure, Physiker und Informatiker.* Springer-Verlag Berlin Heidelberg, 3rd edition, 2020.

[50] Karl Siebertz, David van Bebber, and Thomas Hochkirchen. *Statistische Versuchsplanung - Design of Experiments (DoE).* VDI-Buch. Springer-Verlag Berlin Heidelberg, 2nd edition, 2017.

[51] D. R. Jones, M. Schonlau, and W. J. Welch. Efficient Global Optimization of Expensive Black-Box Functions. *Journal of Global Optimization*, 13(4):455–492, December 1998.

[52] Jason Loeppky, Jerome Sacks, and William Welch. Choosing the Sample Size of a Computer Experiment: A Practical Guide. *Technometrics*, 51(4):366–376, November 2009.

[53] Fernando Puente León. *Messtechnik - Systemtheorie für Ingenieure und Informatiker*. Springer-Lehrbuch. Springer-Verlag Berlin Heidelberg, 10th edition, 2015.

[54] R. Kosfeld, H.F. Eckey, and M. Türck. *Wahrscheinlichkeitsrechnung und Induktive Statistik: Grundlagen - Methoden - Beispiele*. Springer Fachmedien Wiesbaden, 3rd edition, 2019.

[55] Klaus Knothe and Heribert Wessels. *Finite Elemente - Eine Einführung für Ingenieure*. Springer-Verlag Berlin Heidelberg, 5th edition, 2017.

[56] Dieter Arnold, Axel Kuhn, Kai Furmans, Heinz Isermann, and Horst Tempelmeier. *Handbuch Logistik*. VDI-Buch. Springer-Verlag Berlin Heidelberg, 3rd edition, 2008.